Micro- to nano-scale characterisation of the morphology, structure and composition of γ′ precipitate populations in a new nickel-base superalloy



by

Chrysanthi I. Papadaki

Trinity College

University of Oxford

Department of Engineering Science

A DISSERTATION SUBMITTED FOR THE DEGREE OF
DOCTOR OF PHILOSOPHY

Michaelmas 2020

Abstract

The emerging need to reduce CO_2 emissions, while simultaneously improving the efficiency of aeroengines drives the continuous quest for new nickel-base superalloy formulations with improved thermal and mechanical properties. Aiming to expand the operational limits of superalloys outside the current envelope, higher γ′ volume fraction alloys have been developed considering the fundamental role of γ′ precipitation in the high temperature mechanical performance. The main objective of this study has been to investigate the multimodal distribution of the γ′ precipitate populations in a new high γ′ content nickel-base superalloy. Advanced experimental techniques were employed providing complementary information about the γ′ precipitate phase not only at the overall level in terms of coherency with the γ matrix, but also at very local level regarding local lattice variations between γ′ precipitate populations. Morphological, compositional and structural variations between different γ′ precipitate populations were detected and explained using thermodynamic principles. *Operando* observations revealed differences in terms of evolution (growth, dissolution) between different γ′ precipitate populations, shedding light on the underlying physical phenomena that accompany their formation. This Thesis provides useful guidelines to optimise the processing conditions to tailor the distribution of γ′ precipitate populations to obtain the desired mechanical performance. The research presented in this Thesis provides valuable findings developed for high γ′ content nickel base superalloys but with broad applicability to various precipitation-hardened alloy systems.

Acknowledgements

'Σα βγεις στον πηγαιμό για την Ιθάκη, να εύχεσαι να 'ναι μακρύς ο δρόμος,

γεμάτος περιπέτειες, γεμάτος γνώσεις.

Η Ιθάκη σ' έδωσε τ' ωραίο ταξίδι. Χωρίς αυτήν δεν θα 'βγαινες στον δρόμο.'

in Ithaca by Constantine P. Cavafy

It is often said that what matters the most in life is the journey and not the destination. About to complete my DPhil journey, I come to realise the validity of this quote; I feel grateful for this exciting adventure, for the unique experiences I had and for the hilly paths I came across. Above all, I am immensely thankful to the people that helped and supported me throughout this journey, to whom I would like to express my gratitude.

First and foremost, I would like to thank my supervisor Professor Alexander M. Korsunsky. I am deeply grateful for the opportunity he gave me to join his research group and for his valuable guidance and support throughout the course of my work. I would not exaggerate to say that he is one of the most, as I would say in Greek, 'εύστροφος' (intelligent, fast thinking) people I know. I have been impressed by his broad knowledge and inspired by his creativity, his energy, and his continuous curiosity to understand the nature.

I am also indebted to my industrial supervisor Dr Wei Li for his guidance, advice, and continuous encouragement. His expertise in the field of nickel-base superalloys has provided me with invaluable help. Moreover, I would like to thank Dr Mark Hardy and Dr Christos Argyrakis from Rolls-Royce plc for our fruitful discussions during out project meetings in Derby.

Besides my advisors, I am thankful to my Transfer and Confirmation of Status examiners Professor David Hills and Professor Clive Siviour. I appreciate their constructive feedback and I recognise their important contribution to teach me to efficiently structure,

present and defend my research. Also, special thanks go to my former supervisor Professor Spyros A. Karamanos during my studies at University of Thessaly in Greece for his great support and motivation.

I would like to acknowledge the help of Dr David Collins and Dr Chinnapat Panwisawas during the neutron diffraction experiment at ISIS Neutron and Muon Source in Oxfordshire, UK. Also, I sincerely appreciate the valuable assistance of Dr Christopher Allen and Dr Danaie Mohsen during my experimental sessions at the electron Physical Science Imaging Centre (ePSIC) at Harwell Campus. I am also thankful to Dr Paul Bagot for his support with the atom probe tomography experiments and his generous guidance offered thereafter. Special mention to Dr Andre Nemeth for his help at Begbroke Science Park, to Dr Tony Tang for helping me when struggling with the creep tests and to Dr Paraskevas Kontis for our helpful discussions on borides.

Special thanks must also go to my colleagues, current and former members of the AMK research group: Enrico Salvati, Ricky Siqi Ying, Hongjia Zhang, Leon Romano Brandt, Joris Everaerts and Fatih Uzun. It has been a pleasure to share with them long sleepless beamtimes, French wine after experiments at ESRF, memorable group dinners and an adventurous cycling trip to Stonehenge.

I cannot complete this long list without mentioning my long-lasting friends from my hometown in Crete, with special thanks to Klery, and the close friends I met in Volos during my studies at the University of Thessaly, and particularly Eleni, Stefania, Katerina and George. Also, I cannot forget the special friends I made in Oxford to whom I am deeply grateful for all the support throughout these years, namely Ariadne and Aphrodite, as well as the Oxford University Greek Society OUGS (2016-2018) and the 'FREVD' team.

Above all, my deepest appreciation and my sincere gratitude goes to my parents, Ieronymos and Athina, and my siblings, Katerina and George for their unconditional love and support ever since. Thank you for always believing in me and giving me the wings to fly. This Thesis would not have been possible without them. Words of appreciation also go to the other members of my family.

Contents

1. Abstract 3

2. Acknowledgements 5

3. Introduction 15

1.1. A Brief Historical Overview 15

1.2. The Jet Engine 16

1.2.1. Invention and Development 16

1.2.2. Basic Operation Principles 17

1.2.3. Turbine Discs 18

1.3. Physical Metallurgy of Nickel-Base Superalloys 19

1.3.1. Present Phases 20

1.4. Thermo-mechanical Processing 21

1.4.1. Processing Routes 22

1.4.2. Heat Treatment and Microstructure 23

1.5. The Alloy 11 24

1.6. Scope of this Research 25

4. Literature Review 28

2.1. Introduction 28

2.2. Morphological Characteristics of the γ′ Precipitate Phase 30

2.2.1. Volume Fraction of the γ′ Precipitate Phase 30

2.2.2. Size and Distribution of the γ′ Precipitate Phase 31
2.3. Structural Characteristics of the γ′ Precipitate Phase 36
2.3.1. Lattice Misfit and Alloy Composition 37
2.3.2. Temperature Dependence of the Lattice Misfit 38
2.3.3. Lattice Misfit and Precipitate Morphology 40
2.4. Compositional Characteristics of the γ′ Precipitate Phase 42
2.4.1. Diffusivity of Solutes 42
2.4.2. Compositional Variations 44
2.5. Carbide and Boride Phases 46
2.5.1. Carbide Phases 47
2.5.2. Boride Phases 48
2.6. Characteristics of Oxide Scale 52
2.7. Effects of Microstructure on Creep Properties 55
2.7.1. Size of Multimodal γ′ Precipitate Populations 56
2.7.2. Lattice Misfit between γ and γ′ 57
2.7.3. Grain Boundary Serrations 58
2.7.4. Carbides and Borides 59
2.7.5. Oxidation Induced Damage 59
2.8. Conclusions 60
5. Experimental Methods 62
3.1. Introduction 62
3.2. Electro-Thermal Mechanical Testing 63
3.2.1. Solution Heat Treatment with Controlled Cooling Rates 63

3.2.2. Macroscopic Thermal Expansion Measurements 64
3.3. Neutron Diffraction 64
3.3.1. Neutron Diffraction Data Analysis 65
3.4. Differential Scanning Calorimetry 69
3.5. Scanning Electron Microscopy 69
3.5.1. Basic Operation Principles 69
3.5.2. Experimental Method 71
3.6. Focused Ion Beam 72
3.7. Transmission Electron Microscopy 73
3.7.1. Basic Operation Principles 73
3.7.2. Scanning Transmission Electron Microscopy 75
3.7.3. Energy Dispersive X-ray and Electron Energy-Loss Spectroscopy Analyses 78
3.7.4. Sample Preparation 81
3.8. Atom Probe Tomography 83
6. *In situ* neutron diffraction study on crystal lattice variations during heating to super-solvus temperature 86
4.1. Introduction 86
4.2. Experimental Method 87
4.3. Temperature Evolution of the γ/γ′ Lattice Misfit 89
4.3.1. Experimental Results by *in situ* Neutron Diffraction 89
4.3.2. Correlation between γ/γ′ Lattice Misfit and CTE of γ and γ′ Phases 91
4.4. Temperature Evolution of Thermal Expansion Coefficient 97
4.4.1. Definitions of Thermal Expansion Coefficient 97
4.4.2. Experimental Results 100

4.4.3. Temperature Evolution of the Lattice Parameters of γ and γ′ 105
4.5. Discussion 107
4.5.1. Thermal Expansion of Ni_3Al 107
4.5.2. Thermal Expansion of Unconstrained γ′ Precipitates 108
4.5.3. Temperature Evolution of the γ/γ′ Lattice Misfit 110
4.6. Conclusions 112
7. On the dependence of γ′ precipitate size on the cooling rate from super-solvus temperature 115
5.1. Introduction 115
5.2. Literature Review 116
5.2.1. Nucleation 116
5.2.2. Growth 118
5.2.3. McLean Model of Growth 121
5.3. Materials and Methods 123
5.4. Experimental Results 124
5.4.1. Derivation of the Correlation 126
5.4.2. Intergranular γ′ Precipitates 130
5.5. Discussion 133
5.5.1. The Effect of Ageing Heat Treatment 133
5.5.2. Comparison with Literature 134
5.6. Conclusions 135
8. Room temperature HR-STEM analysis of the structural and compositional variations between precipitate populations 137
6.1. Introduction 137

6.2. Experimental Method 138
6.3. Experimental Results 139
6.3.1. Quantitative HR-STEM Analysis of γ′ Precipitate Populations 140
6.3.2. Boride Phase Identification 144
6.3.3. Geometric Phase Analysis (GPA) 149
6.4. Discussion 151
6.4.1. Intergranular γ′ Precipitates 151
6.4.2. M_2B-type Boride Phase 153
6.4.3. Grain Boundary Serrations 154
6.5. Conclusions 159
9. *Operando* nanoscale observation of the dissolution of γ′ populations and oxidation sequence during heating 162
7.1. Introduction 162
7.2. Experimental Method 164
7.2.1. Sample Preparation 164
7.3. Experimental Results 166
7.3.1. BSE Images of the Microstructure at Room Temperature 166
7.3.2. Microstructural Evolution during Heating 167
7.3.3. Compositional Analysis during Heating 170
7.3.4. Atom Probe Tomography 182
7.4. Discussion 185
7.4.1. EELS Data Analysis and Quantification 185
7.4.2. Oxidation of Platinum Layer at Room Temperature 186
7.4.3. Preferential Intergranular Oxidation 187

7.4.4. Elemental Vaporisation 189

7.4.5. Dissolution Path for Different γ′ Precipitate Populations 191

7.4.6. Dissolution Sequence of γ′ Precipitate Populations 192

7.5. Conclusions 196

10. Conclusions & Future Work 199

11. Bibliography 206

1

Introduction

1.1. A Brief Historical Overview

Human history and the advancement of civilisation has been shaped by the discovery, development, and application of metals. From pre-historic times, the human evolution has been indissolubly connected to metals, to an extent that the early human history is divided into time periods characterised by the metal that was discovered and prevalent at that time: the Stone Age, the Bronze Age and the Iron Age.

By engineering tools, the pre-historic man hunted, fought and prospered, and driven by his instinctive, inborn curiosity, he gradually achieved to discover more pure metals and develop alloy systems. Metallurgy evolved from the age of copper and iron into complex alloys, with improved mechanical strength and properties. In the beginning of the 20th century, great breakthroughs in the study and knowledge of metallurgy occurred, including the development of stainless steel, with significant corrosion resistance, as well as, the development of nichrome, the forerunner of future superalloys (Nimonics, Inconels) [1].

Patented in 1906 by Albert Marsh [2], Nichrome consists of 80% nickel and 20% chromium by mass, and it is the oldest documented form of resistance heating alloy. In 1929, Bedford and Pilling, and Merica, introduced small additions of titanium and aluminium to the classic Nichrome (Nimonic 80), which resulted in significant creep strengthening – the first nickel-base superalloy [1]. Although still before the invention of the electron microscope

(1931), metallurgists envisioned that the increased strength was attributed to precipitation hardening: in 1937 Bradley and Taylor [3] discovered the existence of an ordered face centred cubic structure (Ni_3Al) in the nickel-aluminium system by performing an X-Ray diffraction analysis. It was only later in 1951–1952 in a British industrial laboratory in Birmingham where phase diagram work was thought essential, when Taylor and Floyd [4] established the foundation to all superalloys: they found that age-hardening in the early superalloys was entirely due to the ordered intermetallic phases Ni_3Al and Ni_3Ti or rather a mixed intermetallic, $Ni_3(Al, Ti)$, a phase they named gamma prime denoted as γ' dispersed in a more nickel-rich, disordered matrix called gamma (γ).

The quest for new and improved formulations of metallic alloys resistant to mechanical loading at high temperatures has been ongoing since the middle of the 20th century, when it became apparent that these materials are crucial for power generation in the air, on land, and at sea.

1.2. The Jet Engine

1.2.1. Invention and Development

Superalloys have been utilised in a wide variety of applications from high-temperature heat exchangers and furnaces to nuclear reactors. Primarily though, it was their application in aerospace and defence that led to their phenomenal growth. Undoubtedly, the development of superalloys is inextricably intertwined with the invention and development of the jet engine. On December 17, 1903, the Wright brothers made the first successful flight of a distance of 120 feet (which last 12 seconds) with their craft, the `Flyer', using a piston engine. Their success intrigued an accelerating interest in aircraft technologies which led to invention of the far superior jet engine. In 1922, a French engineer Maxime Guillaume conceptualised and patented the idea of a simple jet engine. A bit later, during the 1940s, Francis von Ohain in Germany and Frank Whittle in England developed the concept independently into practical engines: the He-178 and W1X respectively [5].

The materials available at the time of the jet engine invention were incapable of withstanding the extreme conditions of elevated temperatures and stresses developed in the turbine sections. Flight added the aspects of risk, reliability, and strength-to-weight-ratio to the performance of the traditional internal combustion engine. The invention of turbojet engines fuelled by both commercial and defence demand eventually led to development of new alloys with extreme temperature resistance and a balance of strength and toughness. High-temperature steels gave way to nickel- and cobalt-base high-temperature alloys that were then improved by advances in processing technology and eventually after the invention of vacuum melting superalloys became a game changer.

1.2.2. Basic Operation Principles

Jet propulsion is a practical application of Newton's third law of motion, where the incoming air is accelerated and thrust arises by its emergence as exhaust gas at a significantly higher velocity [6]. A turbofan design is illustrated in Figure 1.1. The incoming air is first compressed while passing through the compressor blades that are mounted on rotating discs. Then the compressed air enters the combustion chambers where it is mixed with a fine spray of fuel and burnt while the volume of the gas is considerably expanded at a minimum pressure loss. Subsequently, the hot, compressed gases are allowed to expand through a turbine. The incoming hot gas on its discharge to atmosphere from the exhaust section fully expands and provides a propulsive jet to the engine.

Figure 1.1 illustrates the different stages in a commercial turbine engine, along with the temperature and pressure evolution of the air flow through the different stages. The low-pressure sections, including the fan and compressor sections, are produced using titanium alloys due to their low density, in addition to their strength and fatigue resistance. However, nickel-base superalloys have almost exclusively emerged as the materials of choice in the final compression stages where the conditions are more challenging as well as in the combustor and turbine arrangements. The conditions at the turbine entry can be considered to be the most challenging and demanding on the turbomachinery. The turbine entry

temperature (TET) which defines the efficiency of the turbine engine is limited only by the temperature capabilities of materials of choice in the turbine section.

1.2.3. Turbine Discs

Turbine discs are amongst the most critical components in the aeroengine. In service, turbine discs experience significant rotational speeds generating severe mechanical stresses, repeated start-up and shutdown cycles and prolonged application of stress at elevated temperatures (over 650 °C), in addition to highly corrosive hot exhaust gases that threaten the mechanical performance of the components degrading their life. For the optimisation of the composition and geometry of turbine discs, different factors must be considered, including minimisation of weight, dimensional stability, and mechanical integrity [7]. Metallurgical damage due to creep or fatigue during service and its acceleration due to oxidation must be accurately predicted, as a disc failure represents a potentially fatal hazard to the aircraft [7].

Poly-crystalline nickel-base superalloys have been developed and optimised to fulfil the challenging requirements of disc applications and withstand the extreme operational conditions, balancing the competing demands of properties. The mechanical performance of the nickel-base superalloys lies in their microstructure and the precipitation of secondary strengthening phases. An overview of their physical metallurgy is outlined in the next section.

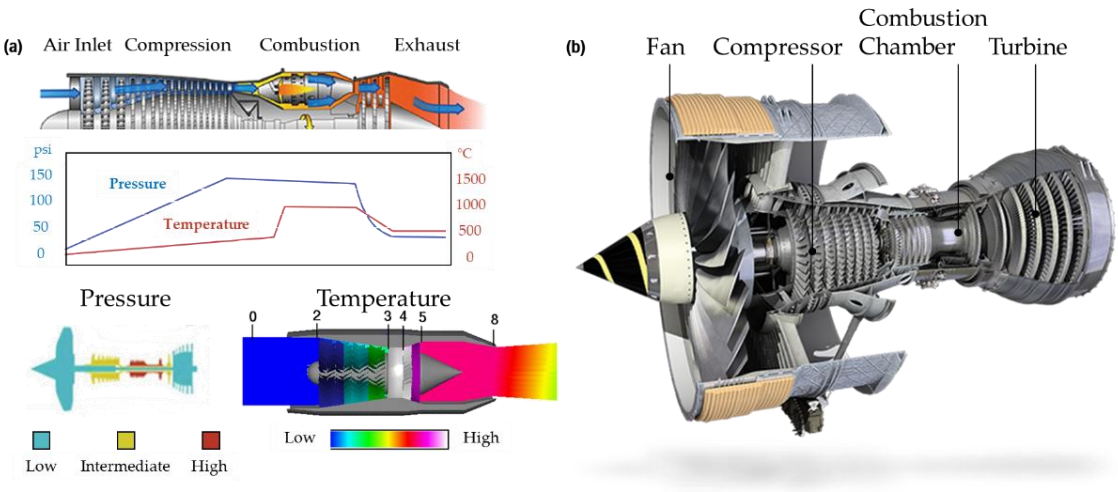


Figure 1.1: **(a)** Different stages in a commercial turbine engine (top) and temperature and pressure evolution of the air flow through the different stages of the turbine engine (bottom). Adapted from [6] ,**(b)** Rolls-Royce Trent 800.

1.3. Physical Metallurgy of Nickel-Base Superalloys

The exceptional high temperature mechanical properties of nickel-base superalloys have resulted in their widespread usage in structural applications at elevated temperatures. Nickel is one of the most suitable solvents for high temperature alloys [7]. Being the fifth more abundant element on earth, it has a moderate cost compared to other metals with the same crystal structure. It displays a face centred cubic (FCC) crystal structure from room temperature up to its melting point (1455°C), which is more ductile compared to BCC, while offers lower diffusion rates than HCP and BCC metals, required for low rates of thermally activated processes. With nickel as a solvent, the essential solutes are aluminium and/or titanium.

Considering the nickel–aluminium binary system in Figure 1.2, which is binary basis for superalloy compositions [8], one can find out that increasing the level of aluminium added to the FCC nickel matrix promotes the formation of a secondary precipitate phase, with a nominal composition of Ni_3Al – the gamma prime phase (γ′). It is the precipitation of γ′ which is largely responsible for the elevated-temperature strength of the material. The γ′ phase has an ordered intermetallic $L1_2$ crystal structure, in which the nickel atoms are at the face centres and the aluminium atoms at the cube corners (Figure 1.2 (b)) [9]. The Ni_3Al phase remains ordered up to the theoretical temperature of 1375°C which is approximately equal to its melting temperature [10].

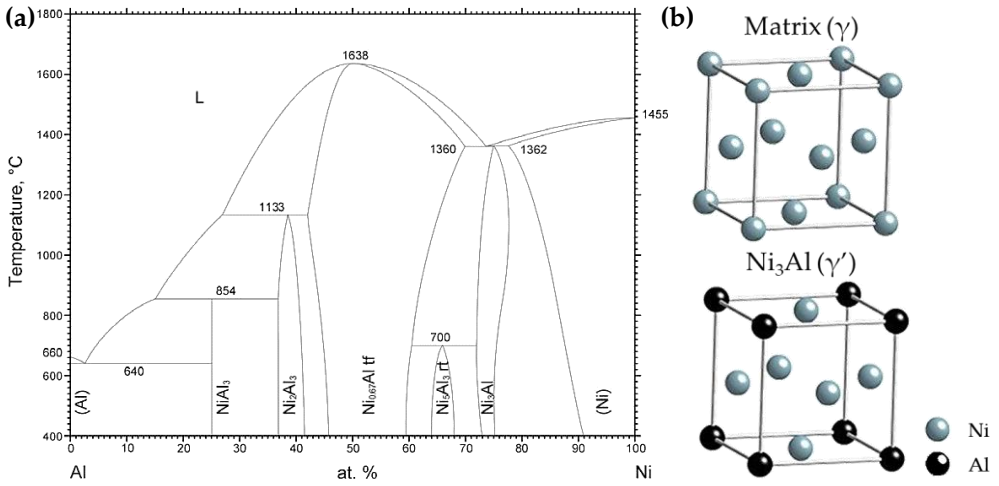


Figure 1.2: (a) Phase diagram of the binary system Ni-Al, **(b)** Crystal structure of matrix (γ) and Ni_3Al (γ′).

1.3.1. Present Phases

Typically, nickel-base superalloys are highly alloyed materials and display complex alloy chemistries to produce the required properties [5]. The alloy design is rigorously optimised, restricting the formation of mechanically deleterious phases, while considering the effect of the various alloying additions not only on the overall strength, but also on the density, and the raw material cost. Although solid-solution strengthening contributes to the high-temperature strength of nickel-base superalloys up to some extent, precipitation hardening is the dominating strengthening mechanism.

A typical polycrystalline nickel-base superalloy consists of an A1 γ matrix with a dispersion of γ′ precipitates that possess an ordered $L1_2$ structure. The matrix γ is the continuous phase, in which the precipitate phases form and reside. It is enriched in elements including cobalt, chromium, molybdenum, and tungsten [7]. These elements have a similar to nickel atomic radii, and thus partition to and stabilise the austenitic γ. Apart from solid solution strengthening of the γ phase, the addition of these alloying elements is multipurpose. For instance, chromium addition largely improves the oxidation resistance, by promoting the formation of chromia (Cr_2O_3), which acts as a protective oxide scale [11].

Superalloys are multiphase materials, which draw their mechanical strength at elevated temperatures from the precipitation of the γ′ phase [5]. In discussing about γ′ precipitates it is common to classify these into different populations depending on their size: primary, secondary, and tertiary γ′, referring to their formation sequence. The size, morphology, and distribution of each population are determined by the heat treatment applied after the manufacturing process. As in many precipitation-hardened systems, the mechanical properties of nickel-base superalloys are strongly influenced by the distribution of the γ′ precipitate phase, as it exerts control over dislocation motion. Exceptional combinations of strength, creep, fatigue, and crack-growth resistance can be achieved in these materials by close control of the characteristics of γ′ precipitates. The presence of a high-volume fraction of the γ′ phase is crucial to maximise high-temperature strength [8]. The volume fraction of

the γ′ phase contained within the γ matrix is primarily dependent upon the content of Al and Ti within the alloy [5]. In addition to aluminium and titanium, niobium, and tantalum partition preferentially into γ′. Nickel-iron and niobium enriched superalloys commonly include gamma double prime (γ′′), instead of γ′ [7].

In addition to the precipitation of γ′, the formation of boride and carbide phases is encouraged in polycrystalline nickel-base superalloys. Traditionally, small amounts of boron and carbon are added to the alloy, considering their so-called grain boundary strengthening effect [7]. Boride and carbide phases reside at the grain boundaries, affecting their morphology. However, the amount of these elements added during the alloy design process is carefully defined as excess additions may lead to the opposite results, adversely affecting the mechanical properties [12]. The same applies to the formation of topologically close packed phases (TCPs) which are brittle phases that can form during heat treatment or service. The alloy design has been developed so that the formation of these phases (μ, σ , Laves, TCP) is inhibited, rather than promoted. TCPs are generally undesirable as they act as crack initiators due to their brittle nature. TCPs capture elements that would partition in γ and γ′ in non-useful form, thus they are observed to downgrade ductility and reducing creep strength [13].

1.4. Thermo-mechanical Processing

The manufacturing process of new heavily alloyed polycrystalline nickel-base superalloys involves various thermo-mechanical processing steps, followed by well-engineered heat treatment, to promote the generation of the characteristic microstructure responsible for its high temperature properties, with optimal distribution of the strengthening γ′ phase. An overview of the common thermo-mechanical processes involved is briefly outlined in the following section.

1.4.1. Processing Routes

During the last decades, remarkable improvements of the processing techniques have been achieved. Starting from equiaxed castings in the 1940s, superalloys were then directionally solidified (DS) during the 1960s, and eventually they were casted as single crystals (SC) in the 1970s. Each casting technique advancement resulted in higher use in temperatures. The advent of vacuum induction melting (VIM) around 1950 benefited forged products and castings, and created a major processing innovation, widely considered as the most important process development made for superalloys in the first 30 years [1]. For polycrystalline nickel-base superalloys for turbine discs, VIM is employed as the standard melting practice for the preparation of the superalloy stock, due to the numerous benefits it provides, including the removal of undesirable alloy impurities and contaminants along with the deoxidisation of the melt [7].

After VIM, there are two different processing routes for polycrystalline nickel-base superalloy components: the conventional ingot metallurgy and powder metallurgy processing. Conventional casting is a cost-efficient technique that enables the production of complex near net-shape part geometries, suitable for a wide range of applications in the aeroengine such as low-pressure turbine blades [5]. However, cast polycrystalline components commonly exhibit a substantially reduced temperature capability. Traditional casting may result in severe macro-segregation within the ingot, and in case of a limited ductility alloy, cracking may be induced due to thermally induced stresses evolving during cooling.

For the production of advanced polycrystalline nickel-base superalloy components, powder processing routes are used, to overcome the limitations introduced by conventional processing routes [5]. Powder metallurgy processing is a more complex technique, associated with a lower concentration of inclusions but higher additional cost, and is mainly preferred for heavily alloyed materials to avoid elemental segregation introduced during melt processing with ingot metallurgy. Powder processing involves gas/vacuum atomisation of a highly alloyed VIM ingot to produce powder followed by rapid solidification to suppresses macro-segregation. To minimise initial defect sizes, the atomised powders are sieved using

standard meshes to improve the cleanliness of the product. To obtain a dense superalloy billet, the powder is then consolidated by hot isostatic pressing (HIP) at a temperature just below the γ′ solvus to promote diffusion bonding and sintering of the powders.

1.4.2. Heat Treatment and Microstructure

After thermo-mechanical processing, powder-processed gas turbine disc alloys are subjected to a carefully designed heat treatment, typically consisting of two stages: sub-solvus or super-solvus solution heat treatment, followed by ageing heat treatment. Solution heat treatment to super-solvus temperature results in the dissolution of the primary γ′ precipitate population, formed during powder consolidation by hot isostatic pressing, whereas in the case of sub-solvus solution heat treatment, primary γ′ is pinned at grain boundaries restricting grain growth. The solution temperature rather than the holding time is the most effective parameter for the dissolution of primary γ′ precipitates, and therefore it exerts a strong effect on the grain size [14].

A super-solvus heat treatment can lead to enhanced properties, as it results to a higher volume fraction of γ′ precipitated in the form of secondary and tertiary γ′ during cooling. Upon cooling from the solution heat treatment, secondary γ′ distributions nucleate and grow. As the temperature decreases, increasing undercooling promotes the nucleation of the secondary γ′ precipitate population. Upon cooling further, the diffusion of solutes into the secondary γ′ becomes increasingly sluggish, and when a critical undercooling is reached, a further nucleation burst of precipitates occurs, tertiary γ′ [15]. Secondary and tertiary γ′ precipitate populations are intragranular distributions and have distinct precipitate size ranges. For a typical commercial disc alloy, the diameter of tertiary γ′ is approximately 5-50 nm, and the diameter of secondary γ′ is approximately 100-400 nm [16]. The cooling rate from solution heat treatment cycles is critical to the development of optimum properties, as it determines to a large extent the beneficial effects of γ′ precipitation. In particular, the

composition, size, morphology, and distribution of γ′, as well as the grain boundary morphology depend highly on the cooling rate applied.

After the solution heat treatment and the subsequent cooling, the superalloys are subjected to ageing heat treatment cycles, during which the desired age-hardening response is observed, as in many precipitation-hardened systems. The ageing heat treatment is conducted at a lower temperature, below the tertiary γ′ solvus, coarsening the secondary and tertiary γ′ distributions to achieve the desired precipitate size distributions. The addition of a high temperature stabilisation heat treatment between the solution treatment and the final ageing treatment is introduced, associated with favourable property balances [17].

1.5. The Alloy 11

The material investigated in this study is a new high γ′ content polycrystalline nickel-base alloy, referred to as Alloy 11 below, which belongs to a family of new alloys that has been introduced recently. Its composition is provided in Table 1. A detailed description of the new family of alloys can be found in European Patent Specification EP2894234B1 [18].

Alloy 11 is one of the new alloy compositions, designed to have higher γ′ content than existing alloys such as RR1000 to provide a higher level of precipitation hardening. It is produced using powder metallurgy to minimise elemental segregation to length scales of a micron (μm), followed by isothermal forging to enable forgings to display a homogeneous coarse grain microstructure, consisting of a uniform average grain size of 20-40 μm [19].

Table 1: Chemical composition of Alloy 11 (wt %) [18].

Ni	Co	Cr	Ta	W	Al	Ti	Mo	Nb	Fe	Mn	Si	Zr	C	Bo
bal	15.0	12.6	4.7	3.2	3.1	2.8	2.1	1.4	0.9	0.4	0.4	0.05	0.02	0.02

1.6. Scope of this Research

Nickel-base superalloys are a unique class of highly alloyed materials with outstanding elevated temperature properties designed to withstand extreme mechanical loads at high temperatures. The exceptional capability of nickel-base superalloys has led to their widespread usage in challenging applications, and thus they have emerged as the material of choice for gas turbine engines. Despite the obvious success of the existing alloy compositions, the quest for improved thermal and mechanical capabilities continues driven by the emerging need to reduce emissions while simultaneously improving performance, and hence the efficiency of aeroengines. To improve turbine efficiency, increasing turbine entry temperature is challenging the operational limits of the superalloys even further. In this context, new and improved formulations are being produced with the potential to replace the existing alloys, that reduce the weight of the components and assemblies, increase the operating temperature, or both. Towards improving strength, new alloy formations have been developed with a higher volume fraction of γ′ precipitates than existing alloys and with a multimodal γ′ distribution.

The overall objective of this study is to shed light on the formation of the different γ′ precipitate populations in a new high γ′ content nickel-base superalloy. The morphology, structure, and composition of γ′ precipitate populations were in depth characterised from micro- to nano- scale. Variations among different populations were detected and quantified, providing useful insights into the underlying physical phenomena that accompany their formation, while differences in terms of their evolution (growth, dissolution) were revealed. To that end, advanced experimental techniques were employed providing complementary information, not only at the overall level, regarding coherency with the γ matrix, but also at local level in terms of local lattice variations between γ′ precipitate populations. A summary of the Thesis is outlined briefly below.

In Chapter 2, a detailed literature review on previously reported studies is provided. Chapter 3 describes the experimental techniques employed in this study, along with the limitations of each technique. In Chapter 4, *in situ* neutron diffraction during heating to solution temperature was employed to investigate the temperature evolution of the γ/γ′ lattice

misfit. Based on the observations and using the Eshelby's eigenstrain formulation a correlation is derived between the temperature evolution of the lattice misfit and the thermal misfit between the γ matrix and the γ′ precipitate phase, with the latter being caused due to their different thermal expansion coefficients. The simple correlation is able to deliver an accurate estimation of the temperature dependence of the lattice γ/γ′ misfit.

In Chapter 5, a power law dependence of the γ′ precipitate size on the cooling rate was first observed experimentally using high-resolution scanning electron microscopy and subsequent image analysis, and then justified on the basis of thermodynamics and diffusion kinetics. McLean's model for precipitate growth [20] is recast to consider the effect of cooling rate, instead of isothermal conditions, and a correlation between the size of γ′ precipitates and the cooling rate is derived.

In Chapter 6, structural and compositional variations between different γ′ precipitate populations were detected. High-resolution scanning transmission electron microscopy imaging (HR-STEM) combined with energy-dispersive X-ray spectroscopy (EDX) analysis revealed local variations in the lattice parameters of the intergranular secondary and intragranular secondary γ′ populations, along with profound compositional variations. Additionally, a boride phase was detected at the grain boundary region, its type was identified and its role on the grain boundary serrations and the formation of secondary intergranular γ′ is discussed.

In situ heating of lamella samples under the electron beam in STEM was performed in Chapter 7 to study the temperature evolution of the microstructure, along with the elemental redistribution during heating, using a synchronous electron energy-loss spectroscopy (EELS) analysis. *Operando* nanoscale observation of the dissolution of γ′ populations was achieved, and the findings provide a direct observation of the Gibbs-Thomson effect in the dissolution behaviour of different γ′ populations. Additionally, the nano-diffusion pathways for preferential intergranular oxidation were studied during heating.

Finally, in Chapter 8, the main results of this Thesis are summarised, along with suggestions for further work.

2

Literature Review

2.1. Introduction

It is widely accepted that the exceptional high temperature mechanical performance of nickel-base superalloys is mainly attributed to the precipitation of the secondary phase with a nominal composition of Ni_3Al, designated as γ′ [5-7]. The FCC lattice of γ′ is stable up to its melting point, which is equal to 1375°C for pure Ni_3Al [10]. In its simplest form, in the FCC unit cell of Ni_3Al, the centres of faces are occupied by Ni atoms (α sites) and Al atoms are located at the corners of the lattice (β sites).

In the modern approach to the design of nickel-base superalloys alloying additions are included to control the mechanical properties such as ductility through solid solution strengthening and other mechanisms. The alloying elements can be classified into two groups, depending on their site preference. Typically, titanium and tantalum are confined to β -sublattice, while chromium, and cobalt are confined to the α -sublattice. Additionally, low quantities of boron and carbon are typically added, due to their well-documented grain boundary strengthening effect. Indeed, in polycrystalline nickel-base superalloys, along with the γ′ precipitate phase, the formation of carbide and boride phases can control the grain boundary morphology and vastly improve the mechanical performance. Carbide and boride particles impede grain boundary sliding during creep, as they would provide a discontinuous path for intergranular cracking [21]. Depending on the application, the different features of

the microstructure can be tailored by the alloy design process and the applied thermo-mechanical processing to optimise the required mechanical properties. For example, the dislocation mobility at elevated temperatures can be controlled by a carefully designed microstructure.

The drive to improve the turbine efficiency by increasing the turbine entry temperature is challenging the operational limits of superalloys even further. The mechanical integrity and thermal stability at elevated temperatures and oxidative environments are among the most crucial operational requirements of new nickel-base superalloys. Under these extreme conditions, several diffusion-mediated degradation mechanisms can occur, driven by the re-distribution of solutes and their partitioning between the γ′ precipitates and γ matrix. First and foremost, elemental partitioning can affect the compositional profile of γ′ precipitate populations and thus their lattice parameter and misfit with the γ matrix, which in turn governs the residual stress and affects the mechanical performance [22]. Additionally, oxidation reactions may be driven by the volume, interfacial and/or intergranular diffusion, while diffusional rearrangements at dislocations influence the rate of creep deformation [23].

This Chapter provides a detailed literature review of the morphological, structural, and compositional characteristics of the γ′ precipitate populations. Studies of the evolution of these characteristics with temperature are also reviewed. First, the morphological characteristics of the γ′ precipitate populations are described, including their size, shape and distribution. A summary of previous studies of the lattice misfit between the γ′ precipitates and the γ matrix is presented. An overview of early studies and recent findings about the elemental profile within γ′ precipitates are also provided, along with the observations of compositional variations between populations. Additionally, a detailed synopsis of the characteristics of the carbide and boride phases is presented. Then, important diffusion-mediated degradation mechanisms are outlined, namely oxidation reactions and creep deformation, together with findings concerning the effect of the characteristics of γ′ and other precipitate phases on these phenomena.

2.2. Morphological Characteristics of the γ′ Precipitate Phase

In precipitation-hardened systems such as nickel-base superalloys the mechanical properties are strongly influenced by the precipitate size distribution (PSD) through exerting control over dislocation motion. The interaction of dislocations with precipitates depends on the interparticle spacing, regulated by the volume fraction and the size of the precipitating phase. Dislocations may either bow around the precipitates or cut through them. In the former case, the stress required is inversely proportional to the interparticle distance, which increases with an increase in particle size in a system with a fixed precipitate volume fraction. In the latter case, the stress required for dislocations to cut a precipitate is proportional to the square root of its size [24].

2.2.1. Volume Fraction of the γ′ Precipitate Phase

The volume fraction of the γ′ phase distributed within the γ matrix is regulated by the composition of the alloy, which is carefully designed to match the requirements of the intended application. The γ′ volume fraction is mostly determined by the content of Al and Ti within the alloy [5]. Alloys with low overall levels of Al and Ti contain low volume fractions of γ′ (~20%). The maximum volume fraction of an alloy is predicted to be approximately equal to 4C*, where C* is the cumulative atomic fraction of γ′ formers in the alloy [25], which typically are aluminium, titanium, niobium and tantalum [24].

It is important to highlight that the γ′ volume fraction is temperature dependent, with the volume fraction decreasing with temperature. The temperature dependence of the volume fraction is commonly assumed to be Arrhenius-type [26], expressed as:

$$V_f^{\gamma'}(T) = V_{f\ RT}^{\gamma'} - m\ exp\left(-\frac{Q^*}{RT}\right) \quad (1)$$

where $V_{f\ RT}^{\gamma'}$ is the volume fraction of γ′ at room temperature, m is a constant, Q^* is the activation energy and T is the temperature. Although the above expression is

phenomenological and Q* has no obvious physical explanation, it can be a useful mathematical expression for modelling the temperature evolution of the γ′ volume fraction. This expression was reported to be of practical use for modelling the observed microstructural changes, particularly for T > 800° C [26].

2.2.2. Size and Distribution of the γ′ Precipitate Phase

The size and distribution of the γ′ precipitate populations are optimised both by the composition of the alloy system and by the applied heat treatment. In particular, the formation of larger γ′ precipitates has been observed in alloys with higher Ni and/or Ti contents [27]. Christofidou et. al. [27] reported a detailed experimental study in which she found out that the composition of the alloy can determine the γ′ solvus temperature, which in turn can be accounted for in terms of the relative γ′ precipitate size. For an alloy system with a defined composition, the PSD is primarily controlled by the applied heat treatment. Most commonly, powder-processed gas turbine disc alloys are subjected to a two-stage heat treatment which consists of a solution heat treatment stage followed by an ageing heat treatment stage [7].

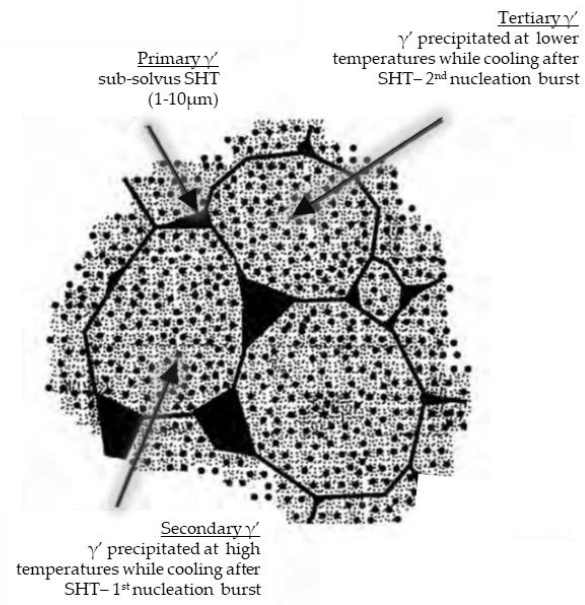


Figure 2.1: Schematic illustration of the distribution of the γ′ precipitate populations in a turbine disc alloy. Adapted from [16].

The temperature of the solution heat treatment governs the multimodal distribution of the precipitate phase. Super-solvus solution heat treatment results in bimodal precipitate distribution as the primary γ′ formed is dissolved, while in the case of sub-solvus solution heat treatment primary γ′ is pinned at grain boundaries and the distribution is trimodal [7] (Figure 2.1). Also, no strong correlation between the solution heat treatment temperature and the resulting γ′ precipitate size has been observed [27].

Upon cooling from the solution temperature, secondary and tertiary γ′ populations nucleate and grow [7, 16]. The cooling rate controls the kinetics of the γ′ precipitation and determines the size and distribution of the secondary and tertiary γ′ precipitates. The average γ′ particle size decreases with increasing cooling rate, and a power law dependence of the mean size of γ′ particles on the cooling rate from super-solvus solution temperature has been reported in previous experimental studies [28-31]. This power law is commonly expressed as:

$$d = Ac^{-n} \tag{2}$$

where d is the diameter of the precipitate, A is a constant and n the power law exponent. Furrer et al. [28] discovered a trend in the dependence of γ′ particle size on the cooling rate, and proposed a formula $d = 442.5c^{-0.4605}$ to fit their experimental results. Vaunois et al. [29] used a power law relation to describe the evolution of size with the cooling rate for both sub- and super-solvus solution heat treatment for cast and wrought Udimet 720Li alloy. For the sub-solvus and super-solvus solution treatments the authors identified the power law parameters A, n as 326.41, 0.2542 and 840.88, 0.3113, respectively. Later studies by Laurence et al. [30] also expressed the γ′ precipitate size evolution as a function of cooling rate from sub-solvus solution treatment for R65 alloy using a power law relationship. The parameters determined here were A = 364.74 and n = 0.3977. Moreover, Masoumi et al. [31] used a power law expression to correlate the average diameter of γ′ precipitates with the cooling rate from super-solvus solution heat treatment in AD730TM nickel-base superalloy. In this case, the power law parameters were A = 521 and n = 0.44. In Chapter 5 (Section 5.4.1), the power law dependence of the mean γ′ precipitate size on the cooling rate is first

observed experimentally, using high-resolution scanning electron microscopy and subsequent image analysis, and then justified on the basis of thermodynamics and diffusion kinetics, by recasting McLean's model for precipitate growth [20].

After the solution heat treatment and the subsequent cooling, nickel-base superalloys are subjected to ageing heat treatment, at a lower temperature below the tertiary γ′ solvus. Ageing heat treatment is carefully designed to achieve a controlled γ′ phase particle size distribution to optimise the mechanical performance of the superalloy components [31]. The average precipitate size is increased with ageing time and temperature, and a critical average size is reached for γ′ particles before the micro-hardness values start to drop [14]. It has been observed that during the ageing heat treatment tertiary γ′ coarsens considerably and thus controls the strength level achieved, whereas the size of the secondary γ′ particles was observed to remain largely unaltered [16]. Zhao et al. [32] studying the age-hardening behaviour of a nickel-base superalloy, showed that coarsening of γ′ precipitates during ageing is a volume diffusion-controlled mechanism. Additionally, they found strong indications that the coarsening of γ′ particles in the alloy was controlled mainly by the volume diffusion of aluminium, titanium, and nickel in the matrix.

Intergranular (Grain Boundary) γ′ Precipitates

Depending on the alloy composition, the applied heat treatment, and particularly on the cooling rate from super-solvus temperature, secondary γ′ particles often precipitate at the grain boundary region, forming the intergranular secondary γ′ precipitate population, also called grain boundary γ′. To avoid any confusion, it should be emphasised that the population of intergranular secondary γ′ precipitates should not be confused with primary γ′ precipitates: the former is formed when the selected solution heat treatment is conducted at super-solvus temperature and the primary γ′ precipitate population is fully dissolved. The formation of intergranular secondary γ′ precipitates is strongly dependent on the cooling rate from super-

solvus solution temperature, which controls the kinetics of the γ′ precipitation. Experimental evidence from numerous studies [33-35] supports the view that the precipitation of the intergranular secondary γ′ population is enhanced with slower cooling rates, which promote heterogeneous nucleation of γ′ precipitates, preferentially along high angle grain boundaries [35].

The intergranular secondary γ′ precipitates differ in size, morphology and composition from the intragranular secondary γ′ precipitates [33]. They are larger in size, while their shape is irregular and deviates from spherical [33-34]. The size of grain boundary γ′ precipitates can be affected by the alloy composition defined during the alloy design process. A recent observation is that the content of cobalt can influence the size of secondary γ′ particles, particularly those in intergranular locations [19,27]. The composition of intergranular precipitates has been observed to be dissimilar to the grain interior γ′. Mitchell et al. [33] performed Energy-dispersive X-ray spectroscopy analysis in a transmission electron microscope (TEM-EDX) on the coarser grain boundary γ′ particles and observed that their composition was consistently enriched in larger sized atoms, and particularly in Al, Ti, Ta, Hf and Zr.

Moreover, intergranular precipitate formation is found to have a significant impact on the grain boundary morphology, and they have been associated with grain boundary serrations [33-36]. As frequently reported in the literature, the grain boundary serrations are affected by the preferential growth of intergranular secondary γ′ precipitates towards the grain boundary, driving it to bow around them [33-34]. It has been claimed that the strong segregation of atoms to the grain boundary region leads to the formation of intergranular particles, triggering grain boundary serrations.

Grain Boundary Serrations

Serrated grain boundaries appear as wave-like formations that force neighbouring grains to interlock with each other, leading to improved mechanical properties. Conclusions

from numerous studies [33-40] suggest that the formation of grain boundary serrations is associated with the cooling rate from super-solvus temperature. An early study by Larson et al. [38] on IN92 alloy showed that slow air cooling through the γ′ solvus temperature can develop highly serrated grain boundaries. Serrated grain boundary morphologies were observed to develop in a wide range of alloy systems. Furrer et al. [39] observed serrations in a powder metallurgy U720LI material, super-solvus solution treated and cooled at different cooling rates. More recently, Mitchel et al. [33] found out that upon cooling from a temperature above the γ′ solvus, the cooling rate determines the grain boundary morphology and the distribution of γ′, regardless of the alloy composition. Slower cooling rates were found to result in more convoluted grain boundaries, whereas as the cooling rate increases the grain boundaries tend to be straight. The amplitude and wavelength of the serrations are inversely proportional to the cooling rate through the solvus temperature of γ′ [33-39].

Numerous research activities have been conducted in order to increase the understanding on the formation of grain boundary serrations and shed light on the underlying physical mechanisms. Since they were first reported, serrations have always been associated with the precipitation of intergranular phases decorating the grain boundaries, and primarily γ′ precipitates and carbide phases the formation of which is assisted by the rapid solute diffusion along the grain boundary. Danflou et al. [41] investigated the growth kinetics of particles producing serrations and found out that the asymmetric growth of γ′ dendrite arms towards grain boundaries perturbs them on both sides and consequently produces grain boundary serrations. This idea was also supported by Henry et al. [42], who claimed that the γ′ dendrites grow preferentially in the direction of the incoherent boundaries. Koul and Gessinger [40] suggested that the driving force for the grain boundary serrations is provided by the net strain energy differential between the matrix side and the boundary side of the γ′ particle/matrix interface.

In the case of alloy systems with low volume fraction of γ′ precipitates, serrations are formed because of the interaction of the grain boundaries with carbide phases, and mainly due to the faceted growth of carbides [36-37]. Tang et al. [36] studied the formation

mechanisms of serrated grain boundaries in Inconel 600. In this alloy system, the γ′ forming elements, such as Al or Ti are present at only trace levels, so the influence of intergranular γ′ phase on grain boundary serrations is limited and only the effect of carbides on the serrations is considered. They suggested that serrations arise when the grain boundary migration is hindered by intergranular particles, which pin to the boundary distorting their morphology.

2.3. Structural Characteristics of the γ′ Precipitate Phase

The γ′ phase displays a primitive cubic $L1_2$ crystal structure, with nickel atoms at the centres of the faces and aluminium atoms at the cube corners of the lattice [9]. It has been demonstrated experimentally that pure stoichiometric Ni_3Al remains ordered up to the theoretical temperature of 1375°C, which is approximately equal to its melting temperature [10]. Using a gamma-ray diffraction technique, it was observed that the intensity of the {100} superlattice reflection shows a sharp decrease just below the melting temperature, implying the onset of disordering. Above this temperature only the fundamental peaks associated with the A1 phase are observed. According to Reed [7], disordering is a possibility which should be taken into consideration, since the contribution of entropy to the total Gibbs energy becomes larger as the temperature is raised. The ordering temperature is strongly dependent on the degree of stoichiometry and the concentrations of any impurities. For instance, addition of Fe has been observed to weaken the ordering and lower the critical ordering temperature [43].

The precipitation of the γ′ structure in a γ matrix gives rise to coherency strains between the two phases, due to the difference in lattice parameters [7]. The γ′ phase precipitates in a cube-cube orientation with the γ matrix, and the mismatch between their lattice parameter results in the deformation of the surrounding lattice. The stress field that arises from the γ/γ′ lattice misfit has a profound effect upon the dislocation mobility, and therefore, the lattice misfit can affect the mechanical performance of nickel-base superalloys.

In nickel-base superalloys, the relative lattice misfit, δ, between the γ and γ′ phases is defined as the ratio of lattice parameter difference to the average value by the following formula:

$$\delta = 2\frac{a_{\gamma'} - a_{\gamma}}{a_{\gamma'} + a_{\gamma}} \quad (3)$$

where $a_{\gamma'}$, a_{γ} are the lattice parameters of γ′ or γ respectively. Therefore, the lattice misfit is positive in case the lattice parameter of γ′ is larger than that of the γ matrix, and then the γ′ precipitates are subjected to isotropic compression. Accordingly, negative lattice misfit corresponds to larger a_{γ} than $a_{\gamma'}$, and therefore the γ′ would be in tension while the matrix in compression. The value and sign of the lattice misfit control the growth and morphology of the γ′ precipitates [44], and therefore the properties of the superalloys are found to depend critically on the lattice misfit δ [22].

2.3.1. Lattice Misfit and Alloy Composition

In order to enhance the stability of γ′ phase and limit coarsening, the composition of the alloy is optimised, such that the γ/ γ′ lattice misfit is small [7] leading to low γ/γ′ interfacial energy. Numerous experimental studies have been devoted to shed light on the effect of alloying additions on the γ/γ′ lattice misfit. MacKay et al. [45] observed that significant Mo addition in high γ′ content single-crystal nickel-base superalloys resulted in a large negative lattice mismatch, which in turn was found to influence the particle size distributions by reducing the coarsening rate of the γ′ cuboids. The same applies to the addition of rhenium, which was also shown to reduce the rate of coarsening, while increasing the γ/ γ′ lattice misfit [46]. Enrichment in the content of W was found to result in the increase of the lattice misfit. Although the addition of W increased the lattice parameters of both γ and γ′, more W tended to partition in γ′ phase, turning the misfit to a positive value [47]. Moreover, the lattice γ/γ′ misfit was observed to increase with higher concentrations of Ti, while it was found to decrease with large Cr contents [27].

The composition of the alloy defined during the alloy design process is an important determinant of the value of the lattice misfit δ. The reason is that the lattice parameter of each phase is controlled by its composition, and thus affected by the partitioning of elements within the alloy. According to Vegard's law, there is a linear correlation between the lattice parameters and the concentrations of the constituent elements of each phase at a constant temperature. The lattice parameters of γ and γ′ phases would then be given by the formulas:

$$a_\gamma = a_\gamma^0 + \sum_i \Gamma_i^\gamma x_i^\gamma, \tag{4}$$

$$a_{\gamma'} = a_{\gamma'}^0 + \sum_i \Gamma_i^{\gamma'} x_i^{\gamma'} \tag{5}$$

where Γ_i^γ and $\Gamma_i^{\gamma'}$ are the Vegard coefficients which are strongly dependent on the position of the solute i in the periodic table [7]. The Vegard's law is an approximate empirical rule, resembling the rule of mixtures. It is can provide a useful estimation of the lattice parameters of γ and γ′ phases at a given temperature, provided the composition of each phase is known. However, it can be challenging to accurately quantify the elemental composition of the phases at elevated temperatures experimentally.

2.3.2. Temperature Dependence of the Lattice Misfit

The γ/γ′ lattice misfit exhibits a strong temperature dependence, considering the distinct thermal expansion coefficients of the γ matrix and the γ′ phase, that arise from the different elemental composition of the two phases. Additionally, the ongoing re-partitioning of elements between γ and γ′ that occur at higher temperatures when the diffusion is activated complicates the prediction of the temperature evolution of the lattice misfit in these complex alloy systems. Extensive research activities have been conducted employing experimental observations [48], analytical techniques, as well as numerical simulations using finite element analysis [49] to study the temperature dependence of the lattice misfit. Typically, the lattice misfit is positive at room temperature and evolves toward negative values as the temperature

increases [48]. Through experimental analysis employing neutron diffraction following a full precipitation sequence it has been observed that the precipitates are fully coherent with the matrix after nucleation. Their growth gives rise to coherency strains, so the lattice misfit increases. The subsequent coarsening during isothermal ageing leads to the relief of the strains due to the incorporation of interfacial dislocations, therefore the value of misfit value is decreased and stabilised [50].

Collins et al. [51] studied the temporal evolution of the lattice misfit of an advanced polycrystalline nickel-base superalloy using *in situ* synchrotron X-ray diffraction during ageing heat treatment. In this study the reduction of the lattice misfit was attributed not only to the to stress relaxation but also to the partitioning and redistribution of solutes between the γ and γ′ phases. This claim was supported by experimental observations performed on phase-extracted γ′ precipitates: the lattice parameter of γ′ was observed to reduce with time in both constrained and unconstrained conditions, indicating that the reduction of misfit could not be assigned solely to stress relaxation. Mitchel et al. [52] also investigated the lattice misfit in both the constrained and unconstrained conditions, by measurements performed on phase-extracted γ′. In this study, the unconstrained lattice misfit was found to increase as the cooling rate decreases. The authors claimed that the change of unconstrained misfit was due to the changes in γ′ precipitate chemistry [52].

Therefore, during heating there are two phenomena contributing to the total misfit: the misfit that arises due to elastic constraints and the thermal misfit produced by the different properties of γ and γ′ phases. To study the temperature evolution of the lattice misfit and distinguish the contribution of each of these phenomena, Eshelby's inclusion method is used to explain the experimental observations obtained with *in situ* neutron diffraction, in Chapter 4. In the pioneering work by J. D. Eshelby [53], an elegant model was developed to determine the elastic field of an ellipsoidal inclusion embedded in a homogeneous linear elastic solid. The Eshelby's solution described the stress, strain and displacement fields, for both the inclusion and the surrounding solid, by introducing the concept of eigenstrain (for more details see Section 4.3.2).

2.3.3. Lattice Misfit and Precipitate Morphology

The growth and morphology of the γ′ precipitates is strongly dependent on the value of δ. Ricks et al. [44] investigated the morphological development of γ′ precipitates during heat treatment, identifying correlations between the morphology and the magnitude and sign of the γ/γ′ misfit. The morphology of γ′ particles though was found to depend not only upon the elastic energy associated with the γ/γ′ lattice misfit, but also upon the nucleation rate. When the nucleation rate is low, the precipitates grow to large sizes in the supersaturated matrix, developing solid-state morphological instability. In this case, the morphological development proceeds in the sequence: spheres, cubes, cuboids, cuboidal arrays and eventually solid-state dendrites, as illustrated in Figure 2.2. The size at which the shape of the γ′ precipitates deviates from sphericity was found to be a sensitive function of the magnitude of the lattice misfit in the alloy [44]. High initial γ′ nucleation density leads to overlapping diffusion fields, as the supersaturation is reduced and γ′ grows in a stable manner. In this condition the precipitates undergoing Ostwald ripening will assume the equilibrium shapes of spheres, cubes, octocubes, aligned cubes, doublets of cubes and plates depending on γ′ size, lattice misfit and thermal processing conditions [54]. Initially, in the early stages of thermal exposure during ageing, the morphology is determined by coherency strains, while at latter stages of precipitate development, the dendritic growth is driven by chemical factors, rather than the magnitude of the lattice misfit [44].

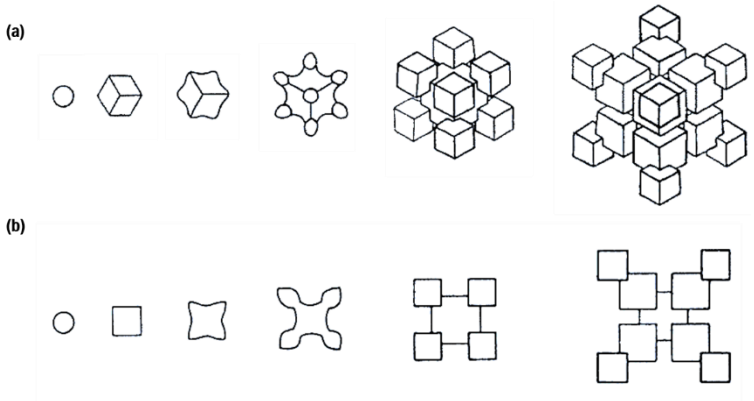


Figure 2.2: Schematic diagrams showing the development of strain induced, faceted γ′ dendrites (a) in <111> and (b) in <001> projections.

Regarding the coarsening process, Khachaturyan et al. [55] developed a theoretical analysis to predict the strain-induced shape changes in cubic precipitates. They considered two distinct stages during coarsening, namely the "interface-controlled" and "strain-controlled". According to their approach, when the size of the particles is small, the contribution of the surface tension dominates their energy, so the coarsening is interface-controlled, and the precipitate shape is spherical. In this case, the classical Lifshitz-Slyozov-Wagner (LSW) theory of coarsening should apply [56]. When the particles become larger, the elastic energy dominates over the interfacial contribution and coarsening becomes strain-controlled. In this case, as their size increases further, precipitates decompose back into smaller particles so that the individual particle size remains nearly the same. This study predicted the critical size to which spherical γ′ precipitates would coarsen before they transform to a cubic shape: the critical size was predicted to be inversely proportional to the square of the lattice misfit.

Grosdidier et al. [57] found out that the dissolution and precipitation processes are also strongly influenced by the γ/γ′ lattice misfit. The local elastic distortions resulting from the lattice mismatch between the two phases determine the local stability of the precipitate phase, so that the more coherent is the particle, the greater is its resistance to dissolution. Another example of the instabilities in the morphology attributed to the γ/γ′ lattice misfit is described in the study by Behrouzghaemi et al. [54], who investigated the effect of cooling rate from a sub-solvus temperature on the morphology of γ′ in a IN738LC nickel-base superalloy. Slow cooling rates would reduce the size of primary γ′, enabling growth to occur in a more stable manner and the precipitates displayed a cubic morphology, while rapid cooling would result in solid state morphological instabilities in the morphology of the particles, which changed from a cubic shape to a flower-like shape. This difference in cooling rate gives rise to large differences in the γ/γ′ lattice misfit and is thought to be a contributing factor to the differences in morphologies observed. Experimental observations indicated that the γ/γ′ misfit between the precipitate and matrix increased with the decrease in cooling rate.

2.4. Compositional Characteristics of the γ′ Precipitate Phase

Modern polycrystalline nickel-base superalloys display complex alloy compositions with high levels of alloying additions. Solid solution strengthening [24], improved ductility [58], oxidation resistance[11], and grain boundary strengthening [12] are only few among the undoubtedly numerous multipurpose contributions of the various alloying constituents. Considering the ongoing demand to improve turbine efficiency, scrupulous alloy design process has been developed to push the operational limits even further and increase the turbine entry temperature. At these elevated temperatures the diffusion process is activated, leading to the partitioning of elements between the matrix and the γ′ precipitate phase. This controls the lattice parameters of the γ′ precipitate populations and the γ matrix and thus the γ/γ′ lattice misfit. The lattice misfit in turn governs the interactions of the γ′ particles with dislocations and therefore the deformation mechanism and the mechanical performance at elevated properties. In the next sections, first a brief outline of the diffusivities of common alloying elements in nickel-base superalloys is provided, and then an overview of recent findings on the compositional variations between the different populations of γ′ precipitates is presented.

2.4.1. Diffusivity of Solutes

The mechanical and thermal stability at elevated temperatures and oxidative environments is one among the most crucial operational requirements of nickel-base superalloys. Under these extreme conditions, several diffusion-mediated degradation mechanisms can occur. First and foremost, oxidation reactions are driven by volume diffusion of elements, as well as interfacial and intergranular diffusion. Diffusional rearrangements at dislocation cores can also influence the rate of creep deformation [23]. Additionally, the diffusion-controlled coarsening of the γ′ precipitates can strongly affect the creep resistance, both in polycrystalline alloys with the dissolution of fine particles [59] and in single crystal superalloys with the so-called rafting effect [7]. What is more, single crystal superalloys can

interdiffuse with thermal barrier coatings (TBCs) used to protect the substrate material. Therefore, to optimise the properties, the diffusional operations should be retarded and the rates of diffusion of the substitutional solutes added to the alloys should be taken into consideration.

The most common diffusion pathways include volumetric diffusion, surface diffusion and short-circuit diffusion along one- and two-dimensional defects, including grain boundaries, interphase interfaces, and dislocations. It is reasonable to assume, while it has also been experimentally verified, that short-circuit diffusion along nanocrystalline GBs has a higher diffusion coefficient than the bulk. This is also clearly demonstrated in the experimental results obtained in this study, where the grain boundaries and the γ/γ′ interfaces serve as paths for fast diffusion, hosting intragranular and intergranular oxides (Chapter 7). There is a commonly accepted model proposed by Fisher [60] that can be used to describe the fast grain boundary diffusion. The reader can find more details and the exact solution of Fisher's model elsewhere [60-61].

Various researchers have tried to shed light on the diffusion rates of the alloying elements in nickel-base superalloys, employing experimental observations [15], first principles calculations [62] and Monte Carlo simulations [63]. Fu et al. [62] studied the diffusion of transition metal solutes in nickel, using quantum-mechanical first principles methods. They observed that diffusion rates are largest for elements at the far west and far east of the 4d and 5d transition metals, which contain Ru and Re respectively, indicating that larger atoms diffuse faster. The authors showed that solute-solvent bonding characteristics and electronic effects dominate, while the solute size has a relatively unimportant effect on diffusion rates. The differences observed in the diffusion coefficient were attributed mainly to variations in the barrier energy for solute-vacancy exchange for elements.

In the ordered γ′ phase most alloying elements display an intra-sublattice vacancy-mediated diffusion behaviour occurring only within the relevant sublattice [15, 64-65]. In the unit cell of the ordered FCC lattice of Ni_3Al, Al atoms are located at the corners (β sites) and centres of faces are occupied by Ni atoms (α sites). The alloying elements can be classified

into two groups depending on their site preference. For example, Ti and Ta are confined to β -sublattice, while the γ formers Cr, Co and Mo are confined to the α -sublattice. As a rule, an element that resides in β sites diffuses more slowly than an element in α sites [15, 65]. It has been shown that in single phase Ni_3Al-X alloys, the greater is the tendency of X to populate the β sites, the lower its diffusion coefficient [65]. The slow diffusion can be attributed to the high activation barrier for diffusion via vacancy–atom exchange.

The diffusion behaviour of most alloying elements in the γ′ phase is well explained by a vacancy-mediated diffusion mechanism, occurring only in the relevant sublattice [15, 64-65]. However, the inter-diffusivity of Al is significantly larger than the diffusivities of other elements at low temperatures [15]. The anomalously fast diffusion of aluminium at low temperatures has recently been explained by inter-sublattice diffusion, i.e. vacancy-mediated antisite-bridging diffusion [15, 64-65]. Aluminium has an enhanced diffusivity in the γ′ precipitates, due to its ability to diffuse preferentially within the β-sublattice via the antisite bridging mechanism. It has been shown using density-functional theory (DFT) that the anomalous diffusion behaviour of Al arises from its lower activation barrier for antisite formation compared to other alloying elements such as Cr, Co, and Ti [64-65]. Chen et al. [15] provided experimental evidence to this claim, as they experimentally observed an anomalous enrichment of aluminium in smaller γ′ precipitates, by performing STEM-EDX on γ′ precipitates electrochemically extracted from the γ matrix. According to the authors, the abnormal diffusion kinetics of aluminium suggests a transition of Al diffusion kinetics from intra-sublattice at high temperature to antisite at low temperature.

2.4.2. Compositional Variations

In recent studies, state-of-the-art characterisation techniques enabled the close examination of the compositional profile of γ′ precipitate populations, probing local compositional variations. First and foremost, experimental observations obtained with advanced characterisation techniques, including atom probe tomography (APT) [66] and

STEM-EDX [15,67], indicate that there is a strong influence of the cooling rate on the composition of different populations of γ′ precipitates, along with the partitioning of elements across the γ/γ′ interface. Using APT, Singh et al. [66] found out that after slower and intermediate cooling rates the composition of secondary γ′ precipitates was closer to equilibrium compared to the monomodal γ′ precipitates after quenching. Likewise, Chen at al. [15] showed that fast-cooled microstructures display negligible compositional variations, while profound variations were detected at slow cooling rates. Secondary γ′ generated at all cooling rates in this study was observed to display near-field equilibrium compositions, that are closer to thermodynamic predictions, than fine-scale tertiary γ′ precipitates, which seem to have far-field compositions.

During slow cooling through the solvus temperature of γ′, the nucleation of secondary γ′ takes place when it is energetically favourable, driven by the increasing undercooling. Secondary γ′ nucleates at relatively high temperatures, when diffusion rates are sufficiently rapid to permit this population to achieve a near-equilibrium composition. Secondary γ′, being the first γ′ precipitate population formed, is expected to have the most thermodynamically stable near-equilibrium composition [15,66]. With continuous cooling, decreasing temperature results in higher undercooling, thus the driving force for nucleation continuously increases. Eventually, a second burst of nucleation occurs, when it leads to the minimisation of Gibbs free energy, forming a very fine distribution of tertiary γ′ precipitates. Smaller precipitates form at lower temperatures and later in the cooling regime. However, the supersaturation of the matrix would be then reduced, with the matrix being depleted of some elements, affecting the composition of the subsequent γ′. An increase in cooling rate results in non-equilibrium compositions of the tertiary γ′ precipitates, due to the limited time available for diffusion [15,66]. In the case of fast quench, the time available for diffusion is extremely short, allowing only very limited partitioning of the alloying elements between the γ′ and γ phases. Consequently, the γ′ precipitates have far-from equilibrium compositions.

What is more very high cooling rates prohibit any further nucleation events, leading to a monomodal γ′ precipitate size distribution [66].

Bagot et al. [68] carried out an in-depth examination of compositional profile of the primary, secondary and tertiary γ′ utilising atom probe tomography (APT) in the commercial poly-crystalline nickel-base superalloy RR1000. They observed the presence of compositional variations between γ′ precipitate populations, with tertiary the most distinct of the three, containing significantly more Mo and Al at the expense of Ti, Ta and Hf. Chen et al. [15,67] also highlighted the noticeable enrichment of aluminium in the fine-scale tertiary γ′ precipitates, with Al exhibiting a different compositional variation behaviour from the other γ′ stabilizers, suggesting the abnormal diffusion kinetics in aluminium. From their experimental analysis coupled with complementary thermodynamic calculations, they explained that the observed compositional trends for secondary and tertiary γ′ result from differences in the diffusivities of the various elements within the γ matrix or within the γ′ precipitates themselves, validating the proposed Al antisite-bridging diffusion mechanism in Ni_3Al at low temperatures.

2.5. Carbide and Boride Phases

Carbon (C) and boron (B) are traditionally added to nickel superalloys in low quantities, promoting the formation of various types of carbides and borides. The precipitation of carbide and boride particles occurs at the grain boundaries, affecting their morphology, which in turn controls the mechanical performance of polycrystalline nickel-base superalloys. Although fine spaced carbides and borides are known to significantly improve the mechanical response of superalloys, in excessive quantities carbon and boron have potentially negative effects, forming continuous carbide/ boride layers between boundaries which reduces strength. The structure and morphology, as well as the effect of the carbide and boride formation on the mechanical properties is an active area of research [7]. In the next sections,

the characteristics of the most common types of carbides and borides in polycrystalline nickel-base superalloys are described, and the findings of key studies are summarised.

2.5.1. Carbide Phases

Traditionally, in polycrystalline superalloys, carbon is added as a grain boundary strengthening element. During solidification, carbon additions result in the formation of primary MC-type carbides [69], where "M" stands for a metal element and "C" represents carbon. They tend to locate in interdendritic regions where heavy refractory elements commonly segregate [70]. The MC carbides precipitate at high temperatures from the liquid phase and they are usually enriched in Ti, Ta and/or Hf, while they exhibit a globular or blocky morphology [7]. Upon the subsequent thermal processing or during prolonged exposure to elevated temperatures in service, the primary MC carbides often decompose into M_6C and $M_{23}C_6$ carbides [71]. It has been shown that the primary MC decomposition occurs by carbon diffusion out of the carbide into the γ matrix, resulting in the formation of $M_{23}C_6$ carbides near the initial interface of the carbide with the matrix [71]. Decomposition of MC carbides may also result in the formation of topologically closed- packed (TCP) phases, such as eta (h), which is often considered detrimental to the mechanical performance of superalloys [13].

The carbides have a cube-on-cube orientation relationship with one of the adjacent grains [69, 72-23], which can be clearly observed for $M_{23}C_6$ in [69]. The $M_{23}C_6$ carbide is a Cr-rich phase with a complex FCC structure, with 116 atoms per unit cell [69]. It contains more metallic elements in addition to Cr, such as Co, Mo and Ni. Hu et al. [72] performed systematic microstructural investigations on $M_{23}C_6$ carbides in a long-term aged nickel-base superalloy and found strong indications of transitional and metastable phases (t- $M_{23}C_6$) in structural and chemical inhomogeneous regions. Contrary to MC carbide, the pristine $M_{23}C_6$ carbide precipitated after standard heat treatment is unstable. Upon thermal exposure, the

morphology of $M_{23}C_6$ has been observed to change from flower-like dendrite to irregular block and finally to regular polyhedron [74].

Among its benefits, carbide formation is used to limit grain growth and control grain size during thermo-mechanical processing [75], as well as to hinder grain boundary sliding during deformation [36-37]. However, there are several cases in which carbides are detrimental to the performance of superalloys. At elevated temperatures rapid oxidation of MC carbides leads to the formation of porous, brittle oxides and soft recrystallised grains in their vicinity, which act as main crack initiation sites [76].

2.5.2. Boride Phases

Boron is a lightweight solid element (with atomic weight approximately equal to 10.81), low quantities of which are also typically added to nickel-base superalloys. Boron resides at the grain boundary region, on account of its different atomic size and electronic properties [79], acting as grain boundary strengthening element [7]. On the grain boundary, depending on the grain size and bulk composition of the alloy, boron can be either in austenitic solid solution form or selectively partitioned into second phase particles [77]. Boron exhibits extremely low solubility in the austenitic matrix, thus it is energetically favourable for boron to partition into intergranular precipitates as M_xB_y (M denotes transitional elements) in multicomponent superalloys [78].

Types of Borides

Generally, three types of borides have been observed in nickel-base superalloys, namely, M_3B_2, M_5B_3 and M_2B borides, where M most commonly refers to Cr, Mo, or W elements [12,24,68,80]. Table 2 summarises basic crystallographic information of binary borides displaying M_5B_3, M_3B_2 and M_2B structures. The structure of these binary borides is then illustrated in Figure 2.3, as derived using the software packages CrystalMaker.

Table 2: Crystallographic information of binary M_5B_3, M_3B_2 and M_2B structures.

Structure	Space Group	Crystal System	a [Å]	c [Å]
Cr_5B_3	I 4/mcm	Tetragonal	5.480	10.01
V_3B_2	P 4/mbm	Tetragonal	5.728	3.026
W_2B	I 4/mcm	Tetragonal	5.568	4.744

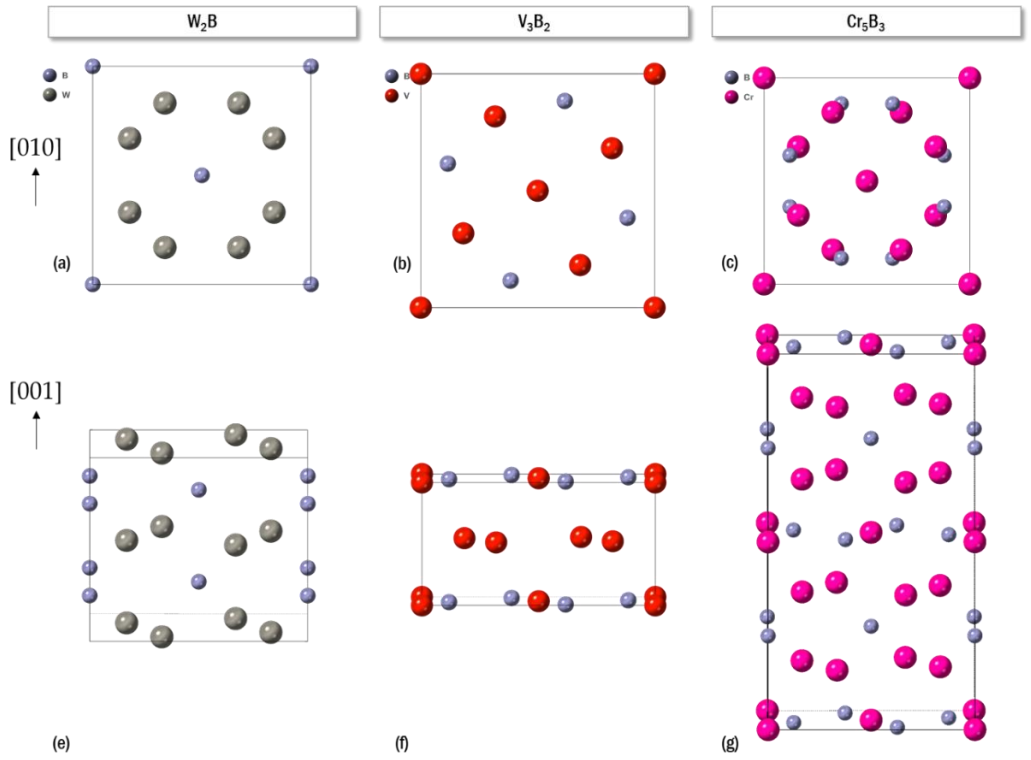


Figure 2.3: **(a), (d)** W_2B boride structure, **(b), (f)** V_3B_2 boride structure, **(c), (g)** Cr_5B_3 boride structures.

Hu et al. [80] investigated extensively the structure and composition of the M_3B_2 and M_5B_3-type borides, using aberration-corrected high angle annular dark field (HAADF) Z-contrast STEM imaging, combined with STEM-EDX analysis for the compositional investigation of the boride phases. The low-energy boron-K edge peak was detected, using the electron energy loss spectrum (EELS). The boride phases M_3B_2 and M_5B_3 were observed to share a similar elemental composition, consisting of B, W, Cr, Mo, Ni, Co. Since the peak height of each element was associated with the content, the authors concluded that the M_5B_3

-type boride is richer in heavy elements with large atomic radius, such as W and Mo, in comparison to the M_3B_2-type boride. In the same study, the structures of M_3B_2 and M_5B_3-type precipitates were revealed by acquiring a series of electron diffraction patterns (EDPs) at different zone-axis. The lattice type of the M_5B_3 phase was found to be body-centered tetragonal with the space group of I4/mcm and lattice parameters of a=0.57 nm and c=1.04 nm.

The M_2B-type borides often possess dual-phase characteristics [81] with highly dense stacking faults, which makes it difficult to identify the true lattice type [82], and consequently, particles of this type may have been misidentified in previous studies [83]. Hu et al. [82] performed a thorough investigation of the crystallographic characteristics in M_2B-type borides in boron containing nickel-base superalloys subjected to long-term ageing treatments. By means of analytical transmission electron microscopy, they found out that M_2B-type precipitations display a number of structural variants: one variant has a body-centred tetragonal structure (Strukturbericht notation C16, space group I4/ mcm), another has face-centred orthorhombic structure (Strukturbericht notation Cb, space group Fddd), while some M_2B-type borides possess dual-phase characteristics. Cadel et al. [84] who detected the existence of M_2B in N18, a P/M polycrystalline nickel-base superalloy, claimed that many orientation variants exist, with respect to the FCC lattice of the parent γ phase.

Orientation with the γ Matrix

Various studies have focused on the analysis of EDPs and HR-TEM to determine the crystallographic relationship between the various boride phases and the γ matrix. The crystallographic relationship of $[001]_{\gamma/\gamma'}//[001]_{M_5B_3}$ is commonly found between M_5B_3 phase and the matrix [21]. More precisely, according to Sheng et al. [85], M_3B_2 was found to grow with an orientation relationship of $(002)_M//(013)_{M_3B_2}$, $[100]_M//[010]_{M_3B_2}$ with the γ/γ′ substrate, while M_5B_3 grew along $(020)_M//(310)_{M_5B_3}$, $[100]_M//[001]_{M_5B_3}$ with the substrate. However, Du

et al. [21] showed that two M_5B_3 borides with the same crystal structure but different orientations could co-exist in a single M_5B_3 particle as an intergrowth of the existing, thus forming special orientation relationship between the two M_5B_3 phases and matrix. Zhang and Ojo [81] found that two M_2B borides with different crystallographic structures could also co-exist in a single M_2B particle in IN738 superalloy. Hu et al. [82] further analysed in detail the crystallographic characteristics of the intergrown M_2B phase.

Benefits of Addition of Boron

The benefits of boron addition in nickel-base superalloys are manifold. An early study on the role of alloying elements in the design of nickel-base superalloys [24] revealed that minor additions of some elements including boron could alleviate embrittlement of internal surfaces like grain boundaries, by segregating solutes and impurities. The addition of boron contributes to the suppression of the rapid agglomeration of Cr-rich $M_{23}C_6$ carbides, possibly due to reduced grain-boundary diffusivity, and promotes the formation of the M_5B_3 borides instead [12,24]. An addition of boron as little as 0.03 at.% promotes the formation of intergranular Cr-rich M_5B_3 borides at the expense of $M_{23}C_6$ carbides [12].

In a recent study, Xia et al. [78] based on the first-principles calculations on the crystallographic structure, elastic and electronic properties of M_2B, M_5B_3, and M_3B_2 showed that the various boride types are thermodynamically and mechanically stable. This claim has also been demonstrated experimentally by Kontis et al. [77]. In this study, the chemical and microstructural evolution during prolonged deformation times at elevated temperatures were investigated. After creep deformation at 850 °C for 3000 h, M_5B_3 borides were found to be microstructurally stable. Regarding their composition, no substantial changes were observed, apart from the Cr content which increased after creep. Also, M_5B_3 particles were coarsened, leading to in γ′ depleted zones in few cases.

2.6. Characteristics of Oxide Scale

Extensive research activities have been performed on the oxidation behaviour of several of nickel-base superalloys for disc applications [11, 86-93], considering its crucial importance on the mechanical performance at elevated temperatures. During operation, the components are subjected to extreme conditions, experiencing high stresses and high temperatures. To improve turbine efficiency, increasing turbine entry temperature is challenging the operational limits of superalloys even further. At these temperatures, environmental degradation such as oxidation may be detrimental to the lifetime of the components and is a factor that must be carefully considered. Although thermal barrier coatings (TBCs) are currently used in turbine engine components, especially in turbine blades, to prevent direct contact between high-temperature gas and protect the substrate material, the oxidation is still inevitable, especially when spallation occurs [86,90].

The formation of oxides in nickel-base superalloys for disc applications is usually twofold, consisting of a surface chromia (Cr_2O_3) layer and a sub-surface internal oxidation zone (IOZ) of alumina (Al_2O_3), often consisting of acicular intergranular penetrations [86-88]. The surface oxide is often protective, acting as an effective barrier against the potentially damaging environment [11]. The external layer of chromia has been reported to contain detectable amounts of titanium, in addition to discrete crystals of rutile (TiO_2) on its outer surface [11, 88-89]. Other surface oxides have been reported, e.g. NiO and CoO, mainly attributed to early-stage transient oxidation [87-88]. Additionally, underlying the chromia scale, a near-continuous layer of Ta-rich oxide has been detected in some Ta containing alloy systems, in specific $(Ti,Ta)O_2$ in RR1000 and $(Ta, Cr)O_2$ ME3, lying at the interface between the external oxide and the alloy [88]. Underneath the surface oxide layers, the internal oxidation zone of alumina is present, often associated with a γ′ denuded zone, caused by Al depletion. The alumina grain boundary penetrations are dominant features that may extend further to great depths into the alloy, using grain boundaries as paths of faster diffusion [11].

Oxidation studies on nickel-base alloys commonly use weight-change measurements to assess the reaction kinetics and have shown that the rate of oxidation in terms of weight

gain can be approximated as a parabolic function of time [11,88]. A parabolic function can also be used to describe the intergranular penetration rates of oxides of Al and Ti [11,88]. Ma et al. [86] studied the effect of loading on the oxidation kinetics of a single crystal superalloy. They showed experimentally that loading stress can result in a higher oxidation rate. Loading results in the increase of the dislocation density, as well as promotes the vacancy and detect formation. The channels formed by dislocations and vacancies are mainly gathered in the interface between the precipitates and the matrix, where the diffusion of Al atoms was observed to be enhanced, leading to an accelerating trend in the growth of oxide scale.

Thermally grown oxides may result in a significant degradation of the mechanical properties as they interact with solutes, removing them from solid solution, while they have been reported to promote the dissolution of strengthening phases in the internal oxidation zone [87-90]. First, a significant depletion of Cr has been reported ahead of and within the IOZ, due to the depletion of Cr to the external oxide [87-88]. In an early study by Molins et al. [87], the first stages of oxidation were investigated in both single- and poly- crystalline nickel-base superalloys, using TEM in association with analytical techniques. In Inconel 718 in addition to the formation of two distinct oxide layers a significant depletion of Cr near the oxidised surface was observed, along with the denudation of γ′ precipitates in that region. The authors claimed that the high chromium content of Inconel 718 would lower the solubility of Al in the matrix, so that it would promote Ni_3Al precipitation. During oxidation, Cr diffuses to the surface to form Cr_2O_3, and thus, the dissolution of the intermetallic phases may be promoted.

On the other hand, the Al-rich internal oxidation zone of alumina, is associated with the intake of specific elements, especially Al, in the oxide scale and thus with decreasing the Al content in the surrounding γ region, promoting the dissolution of γ′. Ding et al. [91] performed *in situ* environmental transmission electron microscopy (ETEM) to study oxidation-induced γ/γ′ microstructure modification in a single crystal nickel-base superalloy. Oxygen existed preferentially in the γ′ phase in their alloy system, due to the strong oxygen affinity of aluminium. Using electron energy-loss spectroscopy (EELS) elemental mapping, they showed

that the oxygen diffusion path is more inclined to be at the γ/γ′ interface rather than matrix channels. At 850 °C, with aluminium oxidised to alumina, it was observed that the Al depletion in γ′ phase induced the phase transformation of ordered γ′ to disordered γ phase. The γ′ denuded zones lead to local mechanical softening, which can cause serious performance degradation. Moreover, within the γ′ particle free region, recrystallisation, or grain growth, have been reported [88].

Although Ni, Cr and Al are considered to be the predominant elements that control the oxidation behaviour of nickel-base superalloys, the addition of other elements as alloy constituents, including Ti and Mn, can affect the oxidation kinetics significantly. Numerous studies have documented the deleterious effect of titanium content on oxidation resistance [11,92]. Besides the formation of Ti-rich oxides, Ti alloying additions can result in large enhancements in chromia growth rates [11,88,92]. A substantial thickening of the chromia scale is associated with the dissolution of titanium in the external oxide layer of chromia and has been observed not only in Ni-Cr-Ti ternary alloy systems [92], but also in more complex, heavily alloyed commercial nickel-base superalloys (RR 1000) [11,88]. According to Cruchley et al. [11], a plausible explanation to this observation is that titanium is incorporated within the chromia layer as the Ti^{4+} ion, since this would introduce the minimal distortion to the chromia lattice spacing, even at high dopant levels. Then, an increase in chromium vacancies would be expected, as a result of the incorporation of this high-valent ion. These excess vacancies will increase oxidation rates through increasing the diffusion rate of the chromium ion across the oxide layer. The enhancement in the growth rate of chromia is described with a sub-parabolic function of time, considering the depletion of titanium in the underlying alloy as the chromia layer thickens [11,88]. Additionally, titanium addition is known to promote the formation of titanium nitrides (TiN). At high temperatures (≤ 850 °C), sub-surface particles of TiN have been detected to form ahead of the internal oxidation zone of alumina, particularly at the alloy grain boundaries ahead of the alumina penetrations [11].

Using high-resolution analytical techniques, Pedrazzini et al. [93] examined potential benefits of Mn on the oxidation behaviour of new generation alloys, by comparing V207J (Mn

1%) and RR1000 (Mn 0%) after 100 hours exposure at 800 °C. They observed the shrinkage of the thickness of the oxide scale, as well as a strong reduction in alumina finger depth, when comparing the V207J alloy with RR1000, oxidised under the same conditions. Using atom probe tomography, they found out that the combined effect of the highly protective $MnCr_2O_4$ and Cr_2O_3 is sufficient to improve oxidation resistance.

2.7. Effects of Microstructure on Creep Properties

The turbine discs are amongst the most critical of components in the gas-turbine engines [7]. In service, the turbine discs experience significant rotational speeds, with higher values for larger diameters, generating severe mechanical stresses, while the temperatures in the rim of the turbine discs exceed 650 °C. Consequently, creep resistance is a crucial operational requirement for nickel-base superalloys.

Creep is a time-dependent, inelastic and irrecoverable deformation, under a certain mechanical loading at elevated temperatures. In pure metals and simple alloys [94], the evolution of creep strain with time normally consists of three stages. First, there is a short transient stage, known as primary creep, when the creep rate decreases with time, due to hardening of the material from the accumulation of dislocations. The primary creep is followed by a regime in which the creep strain rate is approximately constant, referred to as secondary creep. The constant, or steady state, creep rate implies a balance between creep hardening, due to the increase in dislocation density, and creep softening, associated with the thermally driven annihilation of dislocations and recovery. As time increases, creep strain is accumulated, leading to a final short period of sharply increasing creep rate, the tertiary creep stage, when the initiation and growth of damage such as cavities and cracks leads to failure. In many complex engineering alloys like nickel-base superalloys, there is often only a progressively increasing creep rate, after a short primary creep regime, caused by the development of damage processes, while it has been claimed that steady state behaviour may not reflect an intrinsic material property but the inaccuracy of the measurement technique [94].

Creep resistance in polycrystalline nickel base superalloys can be obtained both from solid solution strengthening due to alloying additions, and from precipitation hardening due to formation of secondary phases, and primarily of γ′.

2.7.1. Size of Multimodal γ′ Precipitate Populations

The characteristics of the γ′ precipitate phase, and primarily its volume fraction [95], precipitate size [96] and multimodal distribution [97], have a strong effect on creep resistance. At elevated temperatures and isotheral conditions, the volume fraction remains constant, while the precipitate size increases due to particle coarsening, which in turn affects the interaction with dislocations. Indeed, experimental evidence has demonstrated that particle coarsening, which obeys diffusion-controlled kinetics and is independent of the applied stress [98], can strongly affect the creep life [99]. The reason is that below the solvus temperature of γ′ precipitate size is capable of modifying the rate controlling mechanism of creep and its associated deformation mechanism [96]. In particular, when the precipitate size is below a threshold value, creep deformation is governed by γ′ particle cutting by matrix dislocations, as observed after microstructural examination of crept specimens. As the precipitate size increases, it is generally agreed that interparticle spacing will also increase, promoting bowing of dislocations around particles instead of particle cutting. Therefore, there is a critical size above which Orowan bowing becomes favourable. The critical particle size determines the time at which the rate-controlling mechanism changes from precipitate cutting to dislocation bowing. Beyond this critical size, the strain rate increases rapidly in the tertiary creep regime, as shown in Figure 2.4.

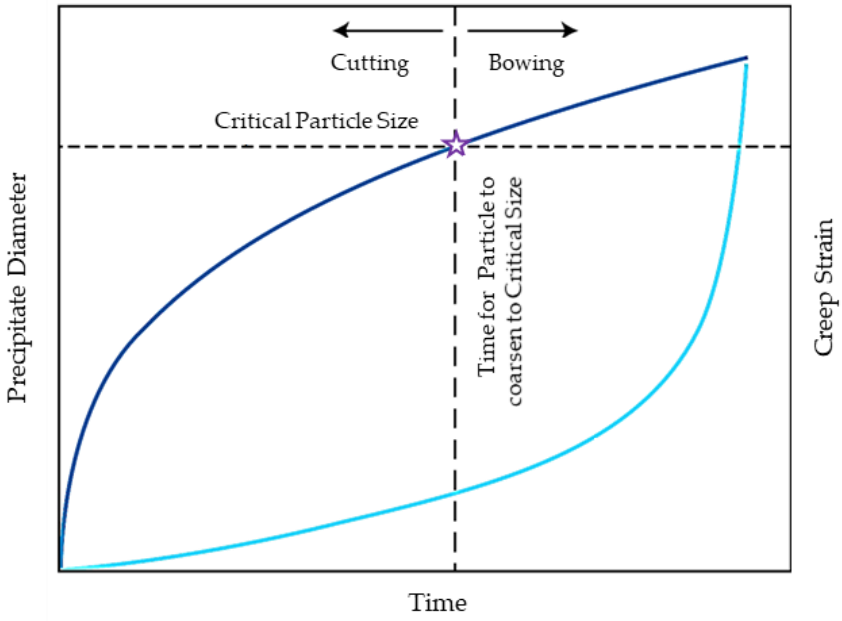


Figure 2.4: Relationship between precipitate size and creep, adapted from [96].

2.7.2. Lattice Misfit between γ and γ′

The sign and magnitude of the lattice misfit between the γ′ precipitates and the γ matrix define the morphological development of γ′ particles in nickel-base superalloys [44], and thus it is an important factor in determining stability of the γ′ precipitate phase. It has been claimed that apart from its well-established effect upon the growth and morphology of the γ′ precipitates, the sign and magnitude of γ/ γ′ lattice misfit has a significant impact on the mechanical performance of nickel superalloys. In particular, in single crystal superalloys, Sugui et al. [100] observed that the γ/ γ′ misfit reduces the rafting rate of γ′ phase during stress, and enhances the stress rupture life of the alloy at high temperatures. What is more, alloys with negative values of lattice mismatch have been reported to exhibit superior temperature capability and creep properties, with deformation being more limited to the γ matrix [22]. Additionally, lattice misfit was found to be strongly correlated to the Vickers hardness values in a Ni–Co–Al–Ti–Cr alloy system, an observation further indicating that the lattice misfit has a crucial role in the strengthening nickel alloys [27].

2.7.3. Grain Boundary Serrations

The morphology of grain boundaries has a large effect on creep life. First and foremost, it has been observed that a coarse-grained is preferable to a fine-grained microstructure to obtain the highest creep resistance [97]. The creep curves of the coarse-grained microstructure were found to display the three usual creep stages, while the creep curves of the fine-grained microstructure showed a transition directly from primary to tertiary creep without any obvious steady state [101]. What is more, the formation of serrated grain boundary morphologies can largely improve the creep resistance of polycrystalline superalloys. Although grain boundary serrations do not affect primary and secondary creep regions, they can hinder the sliding of grain boundaries and prolong the tertiary creep stage to extend the overall creep rupture life. For example, in the study by Yeh et al. [102] creep tests were performed on samples with and without serrated grain boundaries under the creep regime of 650° C/625 MPa. Serrated grain boundaries were shown to lower the creep strain rate in the tertiary creep region, and significantly prolong the creep rupture life. In particular, the creep rupture life of the microstructure with serrated grain boundaries was found to be 30% longer that of the microstructure without serrated grain boundaries.

Both the precipitate size distributions and the morphology of the grain boundaries have been associated with the cooling rate from solution temperature, as it controls the kinetics of γ′ precipitation. Slower cooling although promotes the formation of grain boundary γ′ precipitates that can induce grain boundary serrations, it also results in a coarse distribution of intragranular γ′ particles. In a polycrystalline nickel-base superalloy optimal resistance to high temperature deformation mechanisms could be achieved with a fine dispersion of secondary and tertiary γ′ precipitates in the interior of the grains, combined with a small fraction of intergranular γ′ precipitates that serrate and mechanically interlock the grain boundaries. Alabbad et al. [35] showed that this microstructure can be generated by a two-step or interrupted cooling rate with a slow initial cooling to a transition temperature slightly below the γ′ solvus temperature followed by a faster cooling step.

2.7.4. Carbides and Borides

Carbon and boron additions have been observed to enhance creep performance and prolong creep rupture life, due to the enhancement of grain boundary strength by introducing grain boundary serrations [12,36]. Using high resolution characterisation techniques Kontis et al. [12] performed a thorough investigation of the effect of boron content on the grain boundary character, and in turn on creep resistance. The results of this study demonstrated that boron rather than carbon plays the dominant role in grain boundary strengthening. In the boron containing alloys, a mixed inter- and trans-granular creep failure mode was observed, compared to an intergranular creep failure in the boron-free case. Excessive boron addition though results in the precipitation of a higher volume fraction of borides at grain boundaries, abolishing the beneficial effect of boron on creep properties [12]. Du et al. [21] concluded that M_5B_3 borides would improve the mechanical properties of superalloys not only by dispersing at the grain boundary to impede grain boundary sliding during tertiary creep but also by interrupting an otherwise continuous path for intergranular cracking. It has also been shown that the addition of boron improves the ductility under tensile stress at 750 °C as boron addition, and thus grain boundary serration, retards void formation and cavity propagation promoting ductility [58].

2.7.5. Oxidation Induced Damage

Oxides in general have lower values of thermal expansion than metals and alloy systems, as well as low tensile fracture strains (< 1.0%) and low fracture toughness (0.4-2 MPa $m^{1/2}$) [88]. Additionally, the formation of a layered oxide scale changes the local mechanical properties and stress field by introducing a large compressive residual stress field in the oxide [89]. Therefore, oxidation can pose a serious threat to the overall integrity of the system, mediating various damage mechanisms and downgrading the overall performance of the alloys. Surface or intergranular cracking are among the most common oxidation-induced damage mechanisms [88,103]. Cruchley et al. [88] observed the presence of intergranular

cracking penetrating into the alloy ahead of the oxidation front within a presumably weak zone depleted of γ′ precipitates. Besides cracking, oxide spikes were found to develop at grain boundaries under creep, and grain boundary oxidation was found to be creep strain-assisted [103]. Additionally, creep has been observed to promote cavity formation in the oxide or at oxide–matrix interface, leading to the crack linkup [104], while other creep-oxidation interaction consequences, such as embrittlement, have also been reported in IN738 [105]. Chateau at. [103] identified the major damage mechanisms occurring during tertiary creep and then proposed a model to describe the oxidation-assisted intergranular damage and the oxidation embrittlement of the microstructure, while accounting for precipitate coarsening.

2.8. Conclusions

The detailed literature review provided in this Chapter offers an up-to-date overview of the main characteristics of the γ′ precipitate populations, in terms of morphology, structure, and composition, and describes extensively the current understanding of the effect of the applied heat treatment on the microstructure. Significant findings on the effect of microstructural features on creep resistance are also outlined to demonstrate the vital importance of a rigorous design of the heat treatment to tailor the microstructure. This research aims to extend the current understanding and shed light on the formation of different γ′ precipitate populations in a new high γ′ content nickel-base superalloy. Considering the fundamental role of γ′ precipitation in the high temperature mechanical performance of superalloys, the morphology, structure, and composition of the γ′ precipitate populations were in depth characterised from micro- to nano- and even atomic- scale. Variations among different populations were detected in this study, and differences in terms of their evolution (growth, dissolution) were revealed. To that end, various experimental techniques were employed providing complementary information, not only at the overall level but also at a local level. A brief overview of the experimental methods is provided in the next Chapter (Chapter 3).

3

Experimental Methods

3.1. Introduction

In this Thesis, advanced experimental techniques have been employed to study the characteristics of γ′ precipitate populations in a new high γ′ content polycrystalline nickel-base superalloy. Besides detecting variations between γ′ populations, the main focal point of this study is to shed light on the growth and dissolution paths while monitoring the temperature evolution of the different characteristics of the γ′ precipitate phase, which implies the use of *in situ* experiments to enable *operando* observations. To that end, in Chapter 4 *in situ* neutron diffraction during heating was performed to measure the thermal expansion of the crystal lattice parameter of the matrix γ and the γ′ precipitate phase. The observations were then correlated with the temperature evolution of the γ/ γ′ lattice misfit. Chapter 5 describes the dependence of γ′ precipitate size on the cooling rate from super-solvus temperature investigated employing scanning electron microscopy (SEM) and subsequent image analysis. In Chapter 6, different modes of scanning transmission electron microscopy (STEM) were used to obtain insights into structural and compositional characteristics of γ′ precipitate populations at room temperature and in Chapter 7, *in situ* heating in STEM coupled with electron energy-loss spectroscopy (EELS) was carried out to provide quantitative information for the composition of the γ′ precipitate populations up to their dissolution. The aim of this Chapter is to provide a brief and concise overview of the of the most important aspects of the experimental techniques utilised and to introduce their fundamental principles.

3.2. Electro-Thermal Mechanical Testing

3.2.1. Solution Heat Treatment with Controlled Cooling Rates

Solution heat treatments with controlled cooling rates ranging between 0.7 and 4°C /s were carried out using an Electro-Thermo-Mechanical Testing (ETMT) system (Instron, High Wycombe, UK). Miniature bar specimens with the nominal size of 40 x 2 x 1 mm^3, extracted from the forging by electro-discharge machining were solution treated at the temperature of 1180° C, above the γ′ solvus in this alloy (≈1155° C) in argon atmosphere to minimise oxidation.

In the ETMT system, sample heating is achieved by providing electrical current with a 400 A DC supply. Direct current flows through the sample to generate heat using the Joule effect. While cooling, ETMT heating current is set to a value that maintains the temperature close to the required value regulated by a proportional-integral-derivative controller (PID). The test piece is held in water cooled grips, leading to a non-uniform temperature distribution along the test piece. For a dogbone-shaped specimen with end grip cooling, current heating leads to an approximately parabolic temperature distribution [106]. The middle gauge section of each specimen was used for microstructural analysis, where the temperature was monitored by a K-type thermocouple spot-welded to the centre of the specimen.

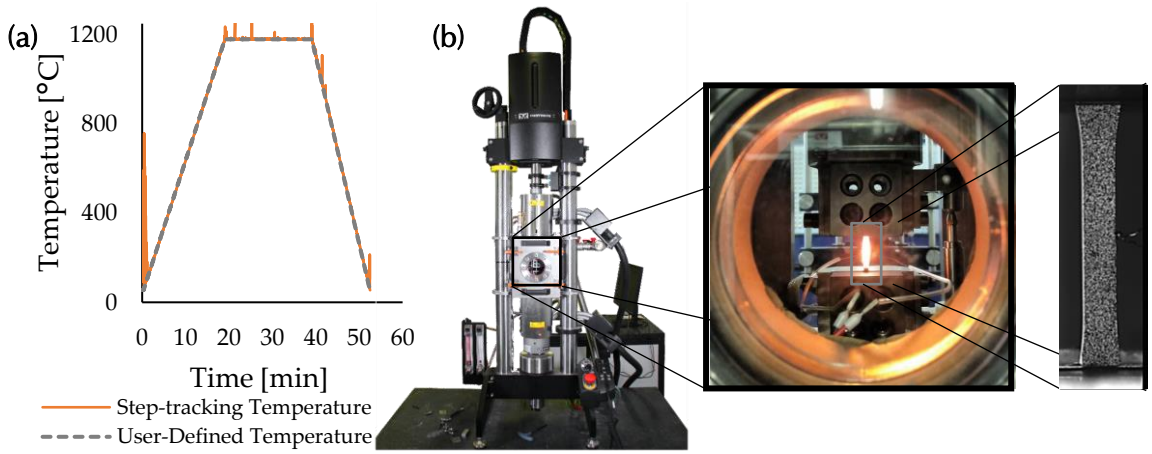


Figure 3.1: (a) Solution heat treatments with controlled cooling rate were carried out using Instron Electro-Thermo-Mechanical Testing (ETMT) system. **(b)** Illustration of the experimental set-up adopted for thermal expansion measurements.

3.2.2. Macroscopic Thermal Expansion Measurements

Macroscopic thermal expansion measurements have been carried out using an Electro-Thermo-Mechanical Testing (ETMT) system (Instron, High Wycombe, UK), in argon atmosphere to minimise oxidation. Figure 3.1 portrays a schematic illustration of the experimental set-up employed. An Imetrum video strain gage system and a digital image correlation (DIC) system were used to capture the macroscopic deformation of the specimen while heating to super-solvus solution temperature. During testing, the specimen was illuminated by a bright, diffuse LED light source positioned behind an Allied Vision Technologies Manta G-146 camera which recorded the test with a frame rate of 10 fps. The frames captured by the camera were analysed by the Imetrum Ltd Video Gauge software tool to detect the displacement of marks/targets on the surface of the specimen in comparison to a reference distance, so that it could be converted into actual metric values. For the accurate tracking of the changes that occur while heating, high-temperature paint was used to generate a fine speckle pattern on the sample surface. Displacement was measured and strain was calculated in the region of interest, which in this case was 3 mm around the centre of the specimen, with a strain resolution of around 20 micro strain.

3.3. Neutron Diffraction

Diffraction exploits the periodic crystal structure of crystalline materials to determine their structural characteristics. The measurement principle of diffraction is based on Bragg's law [107] that was developed to describe the interaction of X-ray beam with a crystal and is given by:

$$n\,\lambda = 2d_{hkl}sin\theta \tag{6}$$

where n is an integer, λ the wavelength of the incident beam, d_{hkl} the interplanar spacing, and θ is the angle of the incidence. X-rays where the first type of source tested with crystals, but neutron diffraction which was later developed can provide complementary information

about both the atomic and the magnetic structure of a material. For time-of-flight (TOF) neutron scattering, the initial position of a pulse of neutrons is fixed, and by timing their travel over a fixed path length L, their velocity v can be determined and related to the wavelength λ of the pulse, using the de Broglie equation:

$$\lambda = h/m\, v = h\, t/m\, L \tag{7}$$

where t is the time of flight, h is Planck's constant (= 6.626×10^{-34} Js) and m is the mass of the neutron (= 1.675×10^{-27} kg). Combining Eq. (7) with Bragg's law in Eq. (6), yields to the key idea of TOF neutron diffraction.

In the study described in Chapter 4, *in situ* time-of-flight neutron diffraction experiments were carried out at the ENGIN-X beamline at ISIS neutron source, UK, to study the variations in the crystal lattice of γ and γ′ phases.

3.3.1. Neutron Diffraction Data Analysis

Nickel-base superalloys consist of an A1 γ matrix with a dispersion of γ′ precipitates that possess an ordered $L1_2$ structure. The diffraction pattern from the disordered FCC γ matrix produces fundamental reflections only from planes with unmixed (all even or all odd) {h k l} indices, whereas the ordered γ′ precipitate phase produces both fundamental and superlattice reflections from planes with mixed {h k l} indices [108]. An example diffraction pattern obtained during this experiment is shown in Figure 3.2, in which the superlattice reflections from γ′ and the fundamental reflections from both γ and γ′ are identified. A section of the diffraction spectrum is magnified, illustrating the superlattice peak {110}, which was used for the analysis described in detail in Chapter 4, due to its higher signal to noise ratio.

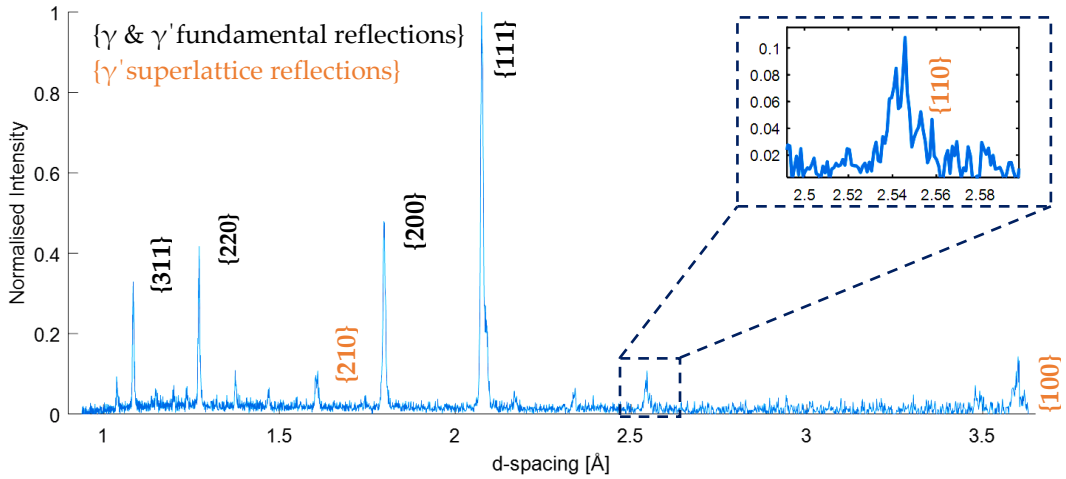


Figure 3.2: Diffraction pattern of Alloy 11 at room temperature.

To obtain the information required for the matrix γ one must separate the fundamental peak by distinguishing the contribution of the γ′ phase using the information obtained from fitting the superlattice peak. The intensity of a superlattice peak is weaker than that of a fundamental peak and it depends strongly on the degree of order present. Regardless of their inherent weakness compared to fundamental reflections, superlattice reflections with sufficient intensity can provide insights into the evolution of the interplanar spacing d_{hkl} of the γ′ phase with temperature and time. For reliable fitting, the {110} superlattice reflection is used in this analysis, due to its highest signal-to-noise ratio in this case. A Gaussian function was used for fitting the superlattice reflection {110}. A Gaussian fit was preferred over a Lorentzian, or pseudo-Voight fit, as the normal distribution fits the experimental measurements best in terms of goodness of fit (R^2) in this case. Throughout this analysis, a single peak was used for fitting the γ′ superlattice reflections. Ideally, multiple peaks would be used to fit the superlattice reflections to distinguish the contribution of intergranular and intragranular secondary and tertiary γ′ populations. The similarity in lattice parameters between these distributions though prohibits fitting them separately.

The crystal structures and lattice parameters of the γ matrix and the γ′ precipitate phase are very similar, leading to overlapping fundamental reflections, which contain information for both phases. The separation of the contribution of each phase is not straight forward.

Collins et al. [109] developed a detailed step-by-step methodology for separating the fundamental peaks to distinguish the contribution of γ and γ′, by inferring the information required from superlattice peaks. According to this study, to correctly fit the superalloy diffraction patterns, the integrated intensity I of a polychromatic incident neutron beam for a single Laue spot is considered as:

$$I \propto \frac{I_0(\lambda_0)\lambda_0{}^4|F_{hkl}^2|^2}{2\,sin^2\theta_0}\frac{\Delta v}{v_\alpha{}^2} \tag{8}$$

where $I_0(\lambda_0)$ is the intensity-wavelength λ_0 distribution, F_{hkl} is the structure factor for reflection {h k l}, Δv is the diffracted volume, v_α is the unit cell volume and θ_0 is the Bragg angle. For the fundamental {h k l} reflections, the measured intensity is the superposition of intensity I_{hkl}^{γ} from the matrix γ and of the intensity $I_{hkl}^{\gamma'}$ from the γ′ phase. The simplified ratio of intensity between the two reflections, after eliminating the parameters equivalent for γ and γ′, can be expressed as:

$$\frac{I_{hkl}^{\gamma'}}{I_{hkl}^{\gamma}} = \frac{|F_{hkl}|_{\gamma}{}^2}{|F_{hkl}|_{\gamma'}{}^2}\frac{\Delta v_{\gamma}}{\Delta v_{\gamma'}} \tag{9}$$

The structure factor F_{hkl} describes how the atom arrangement affects the scattered beam, and it depends on the composition and the scattering length b, which for neutrons varies by element and isotope. Hence, for a fundamental {h k l} reflection, for the γ phase which possesses a disordered FCC structure, one has:

$$|F_{hkl}|_{\gamma} = 4\sum c_{\mathrm{Z}} b_{\mathrm{Z}} \tag{10}$$

where c_{Z} is the composition and b_{Z} is the bound coherent scattering length for each element Z. For the γ′ phase (ordered FCC) one has:

$$|F_{hkl}|_{\gamma'} = 3\sum_{A} c_{\mathrm{Z}_A} b_{\mathrm{Z}} + \sum_{B} c_{\mathrm{Z}_B} b_{\mathrm{Z}} \tag{11}$$

where an element Z may be present on the face ('Ni' site, A) or the corner ('Al' site, B) sites in the unit cell of the ordered $L1_2$ lattice of the γ′ phase, with respective site occupancies c_{Z_A} and c_{Z_B}.

Therefore, in order to determine the contribution of γ′ to the intensity of the superlattice peak, it is necessary to estimate the scattering lengths and hence the phase compositions and the site occupancies for each of the principal elements (Ni, Co, Cr, Ta, W, Ti, Al) for both γ and γ′ phases. This is challenging experimentally, especially at elevated temperatures, when the high diffusion rates lead to strong elemental partitioning affecting the compositional profiles of the matrix and the precipitates, therefore most commonly equilibrium temperature dependent phase compositions are estimated using the thermodynamic calculation tools [109].

For Chapter 4, the evolution of the lattice parameter of the γ matrix and the γ′ precipitate phase, is investigated through monitoring the changes in the interplanar spacing d_{hkl} during heating to solution temperature. The position of the γ′ component of the composite fundamental peak {2h 2k 2l} can be inferred from the corresponding superlattice reflection {h k l}, by assuming that the strain in the γ′, as measured on the superlattice reflection, was the same as that on the fundamental reflection. Therefore, the position of the superlattice peak {220} is inferred from the superlattice reflection {110} position, given as:

$$d^{\gamma}_{220} = \frac{d^{\gamma'}_{110}}{2} \tag{12}$$

This allows the position of the γ reflections to be obtained by fitting the sum of two Gaussian peaks to the data for the composite fundamental reflections. For the data analysis a flat background was assumed. All analysis and fitting functions were written in Matlab, using the methodology described above.

3.4. Differential Scanning Calorimetry

The differential scanning calorimetry (DSC) is a well-established method, used to determine the equilibrium temperatures of phase transitions of materials. For nickel-base superalloys, DSC is widely used to study the dissolution/precipitation kinetics. DSC involves the measurement of the heat released by a sample during a heating or cooling cycle [110]. It is a thermo-analytical technique in which the difference in the amount of heat required to increase the temperature of a sample is measured as a function of temperature. Precise measurements require a proper calibration of the measuring apparatus using standard materials of known heat capacity, e.g. sapphire or platinum, which do not exhibit a phase transformation over the temperature range of interest. The result of a DSC experiment is a curve of heat flux versus temperature or versus time, and a phase transformation will appear as upward (exothermic) or downward (endothermic) peak in the DSC versus temperature curves.

A differential scanning calorimetry (DSC) analysis was performed to measure the specific heat of Alloy 11. Samples were prepared using electrical discharge machining (EDM) into cylindrical discs of 3 mm diameter and grinded until a weight of approximately 82.6 mg was achieved. Two subsequent thermal cycles were performed, while recording the heat flow between reference (sapphire) and sample crucibles during the thermal cycles to interpret phase transformations. A constant heating and cooling rate of 5 ˚C/min was used, with a 15 min isothermal dwell at the temperature of 1450 ˚C between the thermal cycles. In all cases, a flow of Ar gas (20 ml/min) as inert protection was used.

3.5. Scanning Electron Microscopy

3.5.1. Basic Operation Principles

The scanning electron microscope (SEM) is among the most important instruments for the examination and analysis of micro- to nano- scale particles. In SEM, an electron beam is emitted from an electron gun, accelerated in vacuum, and focused by a condenser-lens system

to a spot with diameter about 2–10 nm. The fine electron probe is scanned in a serial manner over the area of interest in the plane of the sample, being deflected in the x and y axes by pairs of scanning coils in the electron column so that it scans in a raster fashion over a rectangular area of the sample surface. Then, the position of the electron beam is combined with the intensity of the detected signal to produce an image.

The interaction between the electrons of the beam with the atoms of the specimen results in either elastic or inelastic scattering of the impinging electrons [111]. The former is caused by the interaction of beam electrons with the positively charged atom nucleuses and results in a deflection of the beam without loss of kinetic energy. The inelastic scattering is caused by the interaction of beam electrons with electrons in the sample and is associated with energy loss. When bulk samples are irradiated with a beam of fast electrons multiple scattering events occur, leading to beam electrons leaving the sample. The energy spectrum of the emitted electrons consists of secondary electrons, backscattered electrons, and Auger electrons. Secondary electrons are generated by inelastic scattering of the beam electrons at low energies while backscattered electrons consist of high-energy electrons generated by elastic scattering. Emerging from greater locations within the sample, BSE can provide superior phase contrast within the material.

The interactions between the electron beam and the specimen produce various signals that contain information about the surface topography and composition of the sample, illustrated schematically in Figure 3.3. The signal intensity depends on various factors, including the topographic contrast, the crystal orientation as well as the compositional contrast [111]. The resolutions of the different modes of operation and types of contrast depend on the information volume that contributes to the signal. In general, high beam energies result in a large diameter of the electron diffusion region, and therefore reduce the resolution of secondary electrons. However, higher energies are necessary for energy-dispersive X-ray spectroscopy, especially if heavy elements are to be detected. Recent developments in Schottky and field emission gun design have increased the gun brightness at low electron energies, leading to low-voltage scanning electron microscopy (LVSEM) in the range 0.5–5 keV, which is recently attracting great interest.

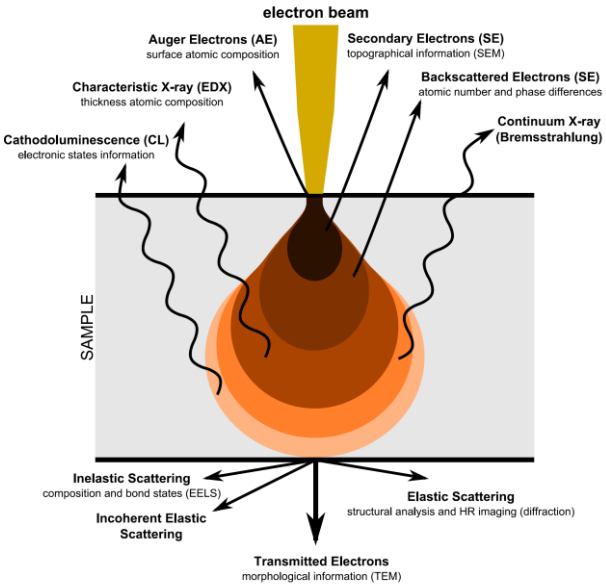


Figure 3.3: Schematic drawing of electron interaction with a thin sample. Adapted from [111].

3.5.2. Experimental Method

The morphological analysis in terms of size of secondary and tertiary γ′ was performed by high-resolution electron microscopy, coupled with subsequent image analysis. The samples were prepared for microstructural examination using standard metallographic mechanical grinding and polishing techniques. A LYRA3 Focused Ion Beam-Scanning Electron Microscope (FIB-SEM) system (Tescan, Brno, Czech Republic), operating at an accelerating voltage of 10 kV, was employed to carry out microstructural examination. A backscattered electron detector was used to obtain good contrast between the precipitates and the matrix, allowing different populations to be distinguished. Subsequent image analysis was carried out on the BSE micrographs using ImageJ software (version 1.50e) to quantify the size of the secondary and tertiary γ′ precipitates. An appropriate number of randomly selected images with magnifications ranging between x20,000 and x290,000 were analysed, covering a total area of 100 μm^2 to ensure that the γ′ size-frequency histograms generated were representative. An example is illustrated in Figure 3.4. To achieve statistical reliability, the diameters of a minimum of 1500 precipitates were measured for each cooling rate. The minimum dimension detected was better than 5 nm.

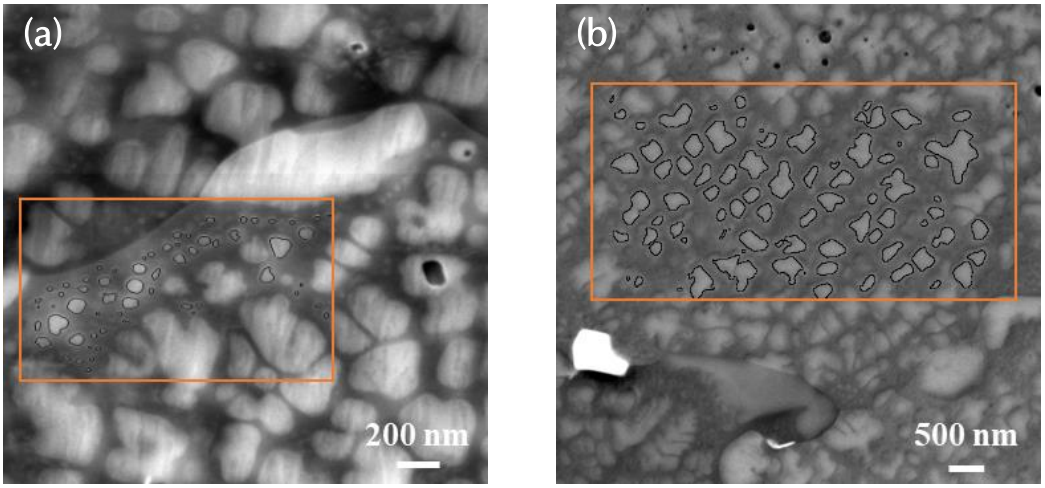


Figure 3.4: Examples of backscattered scanning electron microscopy (BSE) images used for precipitate size analysis in Chapter 5: (a) for tertiary γ′, the magnification was ≈x170,000 and (b) for secondary γ′, the magnification used was ≈x21,000.

3.6. Focused Ion Beam

In modern Dual-Beam systems, apart from the SEM, the microscope is equipped with a focused ion beam (FIB) column, which is inclined at a specific angle in the range of 52° to 55° depending on the manufacturer (Figure 3.5). Dual-Beam FIB-SEM systems offer great flexibility in site-specific TEM sample preparation, following standard preparation techniques that have been developed and optimised over the past years (see Section 3.7.3). Additionally, this system enables the user to perform three-dimensional FIB tomography.

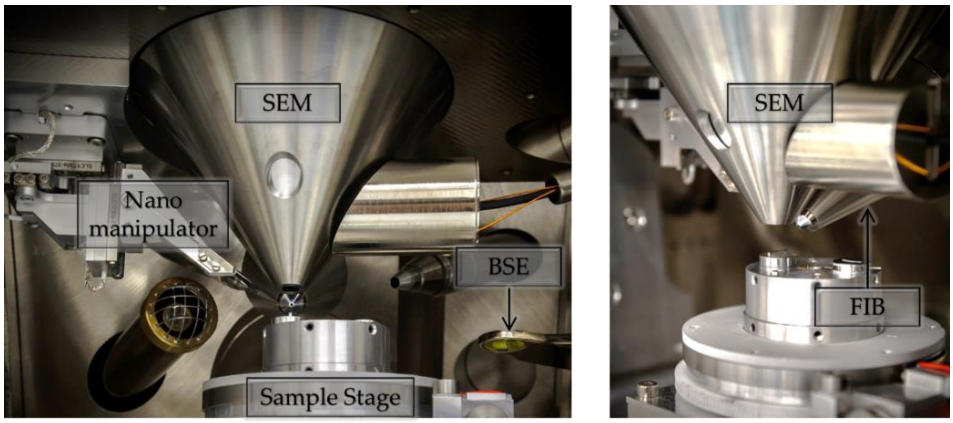


Figure 3.5: Dual-Beam FIB-SEM system in Multi Beam Laboratory for Engineering Microscopy, (MBLEM, Oxford).

In a FIB instrument, a beam of ions is focused using a series of electromagnetic lenses so that it can directly modify or 'mill' the surface of the specimen via the sputtering process. Ions are generated with the field emission process, using a liquid metal ion source (LMIS), most commonly Ga, heated to its melting temperature (~30 °C). Gallium is placed in contact with a small tip of a tungsten needle, and field emission occurs induced by the presence of a large electric field. The Ga^+ ions generated are focused with electromagnetic lenses and used to remove material in a sputter process. The milling process is highly localised allowing for precise preparation, which is very useful for site-specific TEM lamella sample preparation.

3.7. Transmission Electron Microscopy

3.7.1. Basic Operation Principles

Transmission electron microscopy (TEM) is a powerful microscopy technique, widely used in Materials Science for imaging and analysis at high resolution. In a conventional transmission electron microscope (CTEM or TEM), an electron beam of uniform current density is transmitted through a thin specimen. The specimen is irradiated by the electron beam and the interaction of electrons with the atoms of the specimen is used for the formation of images and diffraction patterns, providing significantly increased resolution.

In a TEM, electrons emitted from an electron gun are accelerated to high velocities ($2.3 \cdot 10^8$ m/s at 300 kV) to travel in vacuum along the column of the microscope. The electron beam is controlled by a condenser lens system, which consists of several stages of electromagnetic lenses used to define the illumination aperture and the area of the specimen illuminated. The specimen holder is seated between the upper and lower pole piece of an objective lens. The image generated by the objective lens is afterwards further magnified by projection lenses onto an image formation device, typically consisting of a fluorescent screen or a camera (complementary metal-oxide-semiconductor (CMOS) or charged-coupled device (CCD)).

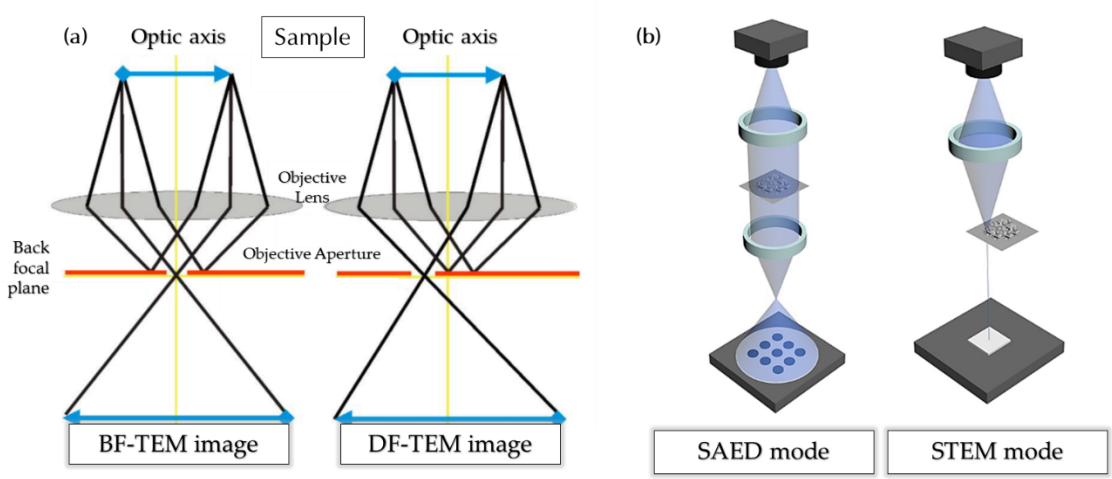


Figure 3.6: (a) TEM imaging modes: scheme of the beam paths from the sample to the first intermediate image. Adapted from [114], **(b)** Scheme of SAED and STEM modes. Adapted from: http://toutestquantique.fr/en/scanning-electron/. Viewed on 17 February 2020.

Conventional imaging is based on the formation of diffraction contrast. In crystalline specimens, the use of the primary beam (bright field) or a Bragg-reflected beam on-axis (dark field) gives rise to diffraction contrast [115]. Electrons form a parallel illumination in the sample plane, interact with the atoms of the specimen and are transmitted through its thickness. Bragg's condition is fulfilled when the scattered electron waves undergo constructive interference, which means if they remain in phase and their path difference is equal to an integral multiple of the wavelength $n\lambda$ (Eq. (6)). The image is formed by placing an aperture in the back focal plane of the objective lens, around the transmitted or diffracted beam resulting in a bright or dark field image respectively, as shown in Figure 3.6 (a). In dark field imaging (DF), only regions which give rise to Bragg diffraction in a specific crystallographic direction appear bright in an otherwise dark background, while in the case of bright field imaging (BF), contrast formation takes place by excluding the diffracted electrons from contributing to the image. With the diffraction contrast being typically the determining factor, there are several other determinants contributing to the contrast of the images in the conventional TEM, including the mass-thickness contrast due to sample areas with different thickness, as well as the intensity reduction due to heavy atom species in the specimen.

Along with the conventional imaging mode, TEM instruments boast an enormous array of operating modes, including the diffraction mode (SAED) and scanning transmission electron microscopy imaging (STEM) mode (Figure 3.6 (b)). Regarding the selected area electron diffraction (SAED) mode, the intermediate lens is focused on the back focal plane of the objective lens such that a diffraction pattern is obtained. The TEM instrument can also operate in the scanning transmission (STEM) mode, by means of a three- or four-stage condenser-lens system enabling the formation of nanometre-sized electron probes. In this study, scanning transmission electron microscopy was performed, using the JEOL ARM200F microscope and the JEOL Centurio Silicon Drift Detector (SDD), housed in the electron Physical Science Imaging Centre (ePSIC) at Harwell Campus. The compositional profile of the different populations of γ′ precipitates was investigated, using STEM combined with energy-dispersive X-ray spectroscopy (STEM-EDX) and electron energy loss spectroscopy (STEM-EELS) analyses, for elemental mapping in the nanoscale. Moreover, high-resolution scanning transmission electron microscopy (HR-STEM) in combination with geometrical phase analysis (GPA) was used to measure the elastic strain field surrounding the γ′ precipitates, caused by the matrix–precipitate lattice mismatch. A brief overview of this techniques is outlined in the next Section (3.7.2).

3.7.2. Scanning Transmission Electron Microscopy

In the scanning transmission mode, the electron beam is focused to a fine electron probe with typical spot size 0.2-5 nm. The specimen is scanned by the incident electron probe in a serial manner point-by-point unlike the conventional transmission mode of TEM in which the whole area of interest of the specimen is illuminated simultaneously. A typical STEM is a conventional transmission electron microscope which apart from condenser and objective lens is equipped with scanning coils for the formation of a convergent nanometre-sized electron probe [115].

In STEM mode, bright and dark field detectors can be used in analogy with conventional TEM depending on the scattering angle. The bright field detector (BF) placed on

the optic axis of the microscope detects the intensity of the direct beam after passing through a point of the specimen. For electrons scattered or diffracted into small angles the annular dark field detector (ADF) detector is used for image formation. The ADF detector is a ring-shaped semiconductor device covering collection angles in the range of 10-50 mrad. For even larger angular ranges (> 50 mrad) the high-angle annular dark field detector (HAADF) is used. The HAADF detector is also a semiconductor disk with a hole but the inner diameter is much larger than in the ADF detector. Thus, it detects electrons that are scattered into high angles arising almost exclusively from incoherent scattering events. The larger the collection angle, the more sensitive the signal is on the atomic number Z: heavy atoms scatter more intensely and at higher angles than light ones. In a BF image, thicker or higher-Z areas of the specimen will scatter more electrons off axis, thus will appear darker in the BF images. Dark field imaging with large collection angles is considered one of the benefits of STEM, since it provides additional, easily interpretable information not only about mass-thickness contrast, but also about the average atomic number [115].

High-Resolution Scanning Transmission Electron Microscopy

In a conventional transmission electron microscope, the electron beam when incident on the specimen produces a Bragg-diffracted beam, inclined at an angle 2θ to the primary beam. The two beams are focused by the objective lens and form a lattice-fringe image in the image plane (reciprocity theorem for a three-beam case [115]). A lattice-fringe image is formed with the interference of the transmitted wave emitted from a crystal and the diffracted wave from a set of lattice planes of the crystal. Then, a series of bright and dark stripes appear corresponding to the lattice spacing reflecting the periodicity of the atomic planes.

High-resolution imaging in STEM (HR-STEM) mode is achieved with a variety of detector configurations including bright-field/dark-field (BF/DF) imaging and high-angle annular dark-field (HAADF) imaging. With the use of post-specimen lenses to expand/compress the whole diffraction pattern, the collection angles of both the BF and the ADF detector can be varied continuously and different detector configurations may be

realised. In the STEM bright-field (BF) mode the primary beam is focused in an electron probe that scans across the specimen, and produces two Bragg-diffracted beams at angles ±2θ to the primary beam, when incident on the specimen. The interference between these three waves produces the lattice image [115]. An alternative way of imaging crystal lattices is the high-angle annular dark-field (HAADF) method. In this case, a fine probe with diameter less than the dimension of a unit cell can produce bright images of atomic rows with the intensity increasing with atomic number Z. The contrast is caused by thermal diffuse electron scattering, and no reversals are seen when the thickness and/or defocus are varied [115]. High resolution scanning transmission electron microscopes require exceptionally stable room environments. In order to obtain atomic resolution images in STEM, the level of vibration, temperature fluctuations, electromagnetic waves, and acoustic waves must be limited in the room housing the microscope.

Geometric Phase Analysis

Geometric phase analysis (GPA) is an image processing technique which is used for the analysis of variations in lattice fringe images with respect to a reference lattice in a quantitative manner [116]. The basis of this technique is that any change of the periodicity of lattice fringes results in a continuously changing phase shift in the direction of the reciprocal lattice vector. The phase change is estimated and related to lattice displacements and in turn to the estimation of the strain filed. By employing this technique, it is possible to study strain fields of various extended defects and has been successfully employed to study strain fields surrounding precipitates in alloys [117]. It has become a widely recognised tool to quantitatively measure the two-dimensional strain state on the basis of HR-TEM images. In this study, the evaluation of the strain field surrounding the microstructural phases and precipitates from high resolution images by GPA was performed utilizing the open source software plug-in from Christof Koch for Digital Micrograph (Gatan) [118].

3.7.3. Energy Dispersive X-ray and Electron Energy-Loss Spectroscopy Analyses

When operating in STEM mode, spectroscopic mapping is enabled by simultaneous acquisition of spatial and compositional information employing energy dispersive X-ray (EDX) spectroscopy or electron energy loss spectroscopy (EELS). In EDX, the characteristic elemental peaks in the X-ray spectrum emitted by a sample bombarded with a focused beam of electrons is used to obtain localised compositional information. High atomic number elements provide broad energy spectra with multiple peaks, allowing for accurate peak identification even in case of overlapping peaks. However, light elements, i.e. Be, B, C, N, O and F, are less efficiently detected by EDX, due to their low photon energy peaks, as they are positioned close to the electronic noise of the detection system (which can be seen at about 0 keV). Additionally, high absorption in the specimen and in the detector may result in peak shifting and consequently in inaccurate and misleading measurements. Quantitative information can also be obtained by EDX with a relatively high accuracy, if the specimen thickness is small ($\leq$ 10 nm). In this case, the Cliff-Lorimer method, also called the thin-film approximation method, can be applied to obtain quantitative measurements of elements [115-119]. On the contrary, if a specimen is thick, corrections for the atomic-number effect, the absorption effect and the fluorescence excitation effect have to be performed for the measured intensities for accurate quantification.

Complementary results can be obtained with the electron energy-loss spectroscopy (EELS) technique. EELS is a technique that involves the measurement of the energy distribution of electrons that pass through a thin sample (< 100 nm) and is able to provide compositional information on the nanometre scale, when coupled with S/TEM [120]. Incident electrons may interact with the specimen elastically (without energy change) or inelastically, causing their energy to be altered. In this process energy is transferred from incident electrons to the atoms in the sample in discrete characteristic quantities. The energy loss can be measured to provide quantitative evaluation of the elemental content of the specimen.

Among its various benefits, EELS provides improved signal to noise ratio compared to EDX, better spatial resolution (down to 1 nm), higher energy resolution (<1 eV for EELS) and increased sensitivity to the lower atomic number elements [120-121]. The main limitation of the technique lies in the sample preparation, as controlling the thickness of the sample is crucial. Since EELS analysis is based on the energy loss of the transmitted electrons, the thickness of the specimen controls the signal to background ratio and edge identification, extraction, and quantification. In Chapter 7, *in situ* heating in STEM coupled with electron energy-loss spectroscopy (EELS) was carried out to provide quantitative information for the composition of the γ′ precipitate populations up to their dissolution. The next Section summarises the basic principles for EELS data analysis and quantification.

EELS: Data Analysis and Quantification

The energy loss spectrum can be divided into the low loss and the high loss region. The low loss region contains the zero-loss peak (ZLP) that corresponds to the electrons which undergo elastic scattering when interacting with the specimen, and the plasmon peak that can provide information about band structure, bandgap, and optical properties [120]. Plasmon is a phenomenon that originates from the collective oscillation of weakly bound electrons. Thick samples may result in convoluted plasmon peaks, and the low intensity of the plasmon signal may be difficult to distinguish from the background. Zero-loss peak can be used to determine the thickness of specimen, using the formula:

$$\frac{t}{\lambda} = \ln\left(\frac{I_t}{I_{ZLP}}\right) \tag{13}$$

where t stands for the thickness, λ is inelastic mean free path (IMFP), I_t stands for the total intensity of the spectrum and I_{ZLP} is the intensity of zero-loss peak. For 200 kV electron, the MFP of most materials is on the order of 80 – 120 nm; however, it strongly varies with Z, sample density, and the TEM accelerating voltage. For reliable elemental composition quantification, the sample thickness needs to be between 0 – 1.2 times the local mean free path.

In the high loss region, characteristic signals termed as `ionisation edges' appear in the spectrum identifying the presence of specific elements in the specimen. The onset of ionisation edges corresponds to the specific energy that is required for the excitation of inner, or core electrons (i.e. K, L, M shells, etc.) of specific atoms in the specimen from the ground state to the lowest unoccupied state. The critical ionisation energy is unique for different shells and elements. The intensity of the ionisation edges can be related directly quantitatively to the content of each element [122], with the following formula:

$$N = \frac{\mathrm{I_k}}{\mathrm{I_0}\,\sigma_\mathrm{k}} \tag{14}$$

where I_k is the integral of the ionisation edge k, I_0 is the zero-loss integral and σ_k is the inelastic cross section. In practice, the cross sections are computed for specific experimental conditions (energy, convergence angle) using available models, with the most common among them being the Hartree-Slater model in which the cross-sections are computed using tabulated atomic wave-function values [122].

In addition to the compositional information, the ionisation edges contain information on the electronic structure (i.e. chemical bonding) of the atoms of the different elements within the specimen. This information can be obtained by the analysis of the energy-loss near-edge structure (ELNES), which corresponds to intensity fluctuations just above the edge onset. The ELNES has been found to be dependent on the details of the local atomic environment, such as coordination, valence and the type of bonding. For transition metals, at the onset of the L2 and L3 absorption edges the so-called white lines are observed that appear as high intensity peaks. The peaks have been called white lines because they were originally observed in overexposed regions on the photographic film used to record x-ray-absorption spectra.

For accurate quantification, the background signal has to be fitted and removed first. The background signal in the core-loss region is caused by plasmon peaks and core-loss edges and can be described by a power law. Moreover, absolute quantification requires considering the effect of multiple scattering. Multiple scattering occurs when a significant fraction of incident electrons that pass through a sample are scattered inelastically more than once.

For this study, the edges of Ni, Co, Cr, Al, Ti and O were detected and quantified for temperatures up to 950 °C (Chapter 7). For the data analysis and the quantification of EELS measurements, a model-based quantification approach was employed using the Gatan Microscopy Suite (GMS) software version 3.4.2. Background was subtracted by fitting a decaying power law curve in the pre-edge region at each ionisation edge. To compute the cross-sections, the Hartree-Slater model was used. Plural scattering effects were incorporated into the analysis to improve accuracy, while the analysis of the electron loss near-edge fine-structure (ELNES) features was excluded, since it is out of scope of the current work.

3.7.4. Sample Preparation

Sample preparation is of critical importance for a successful experimental investigation with transmission electron microscopy. It is essential that the samples not only include the features of interest, but they also have the optimal thickness and orientation, while any possible sources of damage during preparation should be minimised. The sample preparation process can be tricky and more often than not very time-consuming, and therefore it should be carefully designed. Modern Dual-Beam FIB-SEM systems offer great flexibility in TEM sample preparation. A gas-injection system (GIS) when introduced into the microscope chamber, is used for site-specific material deposition, by introducing reactive gases (typically of Pt) in the vicinity of the electron probe during operation. The capabilities for TEM sample preparation are further extended by the addition of micro/nano manipulators, which enable lift-outs, and transfers of microscopic sample parts during preparation.

Prior to FIB preparation, polishing and cleaning of the material surface was carried out to create a homogeneous and clean sample surface to reduce artefacts, such as preferential milling and the so-called ‘curtaining effect’. Next, the grain with the required orientation was located, as described below, and the region of interest was defined. A protective surface layer of platinum with a minimum thickness of 250 nm was deposited on the region of interest using the GIS. Then, staircase-shaped patterns were used to mill rectangular trenches on each side of the lamella, sufficiently deep below the area of interest to avoid any ion beam damage.

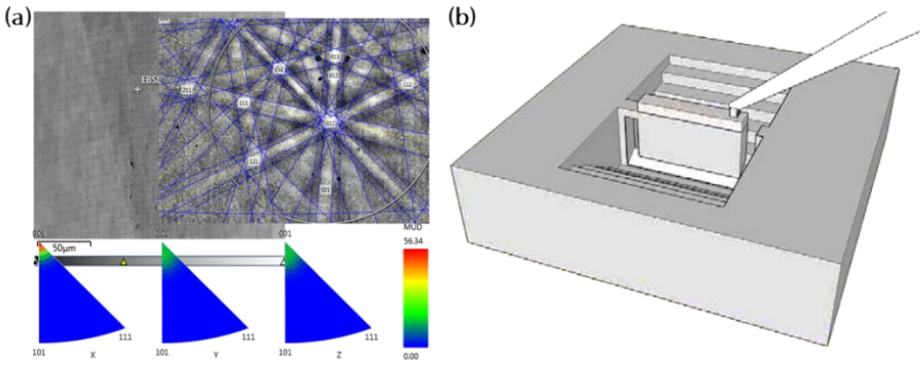


Figure 3.7: (a) EBSD analysis to detect the grains with <001> direction along the rolling, transverse, and normal directions, **(b)** FIB lift-out technique for site specific TEM lamella sample preparation.

This step was followed by milling a U-shaped undercut, consisting of three rectangular parts, to separate the lamella from the bulk. Subsequently, the lamella was attached to the needle of the micromanipulator with material deposition from GIS, and then separated and lifted out of the sample. The lamella was transferred to a TEM grid, attached to it by material deposition, and detached from the needle. Copper grids with four standing bars have been used for the samples in this work. Finally, the mounted lamella was thinned to achieve the desirable thickness, which has to be less than 100nm.

When samples are prepared with focused ion beam milling, amorphization of the surface and redeposition of sputtered material is a general problem. Despite the challenges involved, the FIB lift-out technique is one of the most popular methods for TEM lamella sample preparation. The main advantage of the FIB preparation technique over the other available methods is the ability to create site-specific, cross-sectional samples, so that any particularly interesting features can be identified and investigated. To achieve the required thickness while minimising the FIB induced damage, an optimised thinning technique was employed. Since larger currents give faster milling but less precise milling, during the final steps lower beam-currents offer sharper probes with less tails keeping the top protection layers intact until the end. Low energy milling while adjusting the tilting angles significantly improved the quality of the lamellae. Detailed description of the step-by-step methodology for the sample preparation is presented in [123] by Schaffer et al. Preventing sample damage at the areas of

interest during milling without introducing inhomogeneities is critical. To that end, the energy was progressively lowered during the process down to 2 kV milling at the final stage. Additionally, substantially thicker protection layers than suggested were used to ensure protection during the whole procedure including the final thinning.

Provided successful alignment to the zone axis, atomic resolution of the lattice of the matrix and the precipitate phases can be achieved with the high-resolution transmission electron microscopy (HR-STEM) imaging mode (Section 6.3.1). In nickel-base superalloys, the observation of the superlattice structure of the γ′ precipitate phase is assisted when alignment to the [001] direction is reached. The alignment involves specimen-stage tilting and can be benefited by a sample prepared to be conveniently orientated. To that end, prior to TEM sample preparation an electron backscatter diffraction analysis (EBSD) was performed on the bulk sample to identify the orientation of the grains on its surface. The grains with <001> direction along the rolling, transverse, and normal directions were detected and marked with a reference mark milled using the FIB. The reason is that for the EBSD analysis the sample is mounted on a pre-tilted stage at 70°, so marking the grains is necessary for locating them when the EBSD analysis is completed and the pre-tilted stage is removed. Then, the selected grains were located using the reference marks and the sample was tilted to 55° for the standard TEM lamella sample preparation, using the FIB lift-out technique [123].

3.8. Atom Probe Tomography

Atom Probe Tomography (APT) is a three-dimensional micro- to atom-scale characterisation technique that offers unique insights in the elemental composition and atomic structure of materials due to its extensive capabilities in terms of elemental sensitivity and spatial resolution (around 0.1-0.3 nm in-depth resolution and 0.3-0.5 nm lateral resolution). In APT, a very sharp needle-shaped specimen is cooled and subjected to a high, positive voltage V, and individual atoms are successively removed from the apex of the sharp tip by field evaporation [124]. The formula that gives an estimation of the electric field, F, induced at the surface of the tip is given by:

$$F = \frac{V}{k_f r} \tag{15}$$

where r is radius of curvature of the tip and k_f is the field factor constant with a value between 2 to 5. Therefore, sharper needles cause higher electric field amplification, since F is inversely proportional to r. During atom probe tomography, the ionisation of the surface atoms by field evaporation is induced by the combined effects of a standing (DC) electrostatic field and either a pulsing voltage or a pulsed laser beam transmitted across a counter-electrode (CE) to the sample. The initial stage of field evaporation is a thermally activated ion escape over an activation barrier followed by a second stage of post field ionisation. The pulsed voltage or laser beam applied to the specimen provides the initial "jump start" required by providing the excess activation energy for start of field evaporation [125]. Immediately after their ionisation, the surface atoms are evaporated from the surface and projected onto a Position Sensitive Detector (PSD) with a very high detection efficiency. The detector allows to simultaneously measure the position, the order of arrival and the time of flight of the ions. The time of flight of individual ions is estimated by the time difference between the applied pulse to atom and its arrival at detector recorded by the time-of-flight mass spectrometer. A cross delay line detector is used to record the x and y coordinates of the ion impact position on the detector. The order of arrival of the ions on the PSD allows to reconstruct the original position of the atoms on the tip. Repeating this sequence, the atoms are progressively removed from the apex of the sharp tip, and a three-dimensional reconstruction of the material can be obtained at the atomic scale.

In the current study, APT data was collected using a Cameca LEAP™ 3000X HR instrument housed in the Department of Materials, University of Oxford. The samples were run in voltage mode at a specimen temperature of 50 K, with pulse frequency at 125 kHZ and pulse energy 80 pJ.

4

In situ neutron diffraction study on crystal lattice variations during heating to super-solvus temperature

4.1. Introduction

The mechanical performance of the nickel-base superalloys is sensitive to the sign and magnitude of the γ/γ′ lattice parameter misfit. The precipitation of the γ′ structure in the γ matrix occurs in a cube-cube orientation, giving rise to coherency strains between the two phases, due to the mismatch between their lattice parameters. The deformation of the surrounding lattice and the stress field that arises from the γ/γ′ lattice misfit has a profound effect upon the dislocation mobility, and thus can affect the mechanical performance of nickel-base superalloys [22], particularly at elevated temperatures. A detailed outline of important studies on the γ/γ′ lattice misfit can be provided in Chapter 2 (Sections 2.3 and 2.7.2).

A considerable body of research activities have been conducted, employing both experimental and analytical techniques, to shed light on the temperature evolution of the lattice misfit [48-49,126-127]. Among the contributing factors determining the temperature

dependence of the γ/γ′ lattice misfit, the difference in thermal expansion of the γ and γ′ phases is believed to be dominant, along with elemental redistribution between the γ and γ′ phases that inevitably occurs at high temperatures. In this study, the temperature evolution of the γ/γ′ lattice misfit is correlated with the thermal expansion behaviour of the γ matrix and the γ′ precipitates using the Eshelby's eigenstrain formulation. A simple yet solid correlation is derived able to deliver an accurate prediction of the temperature evolution of the lattice misfit.

For heat resistant gas turbine components, superalloys with controlled low thermal expansion coefficients are preferred [128]. Previous studies have investigated the evolution of the thermal expansion coefficient (CTE) with temperature and composition in nickel-base superalloys employing experimental observations, thermodynamic modelling or both [129-135]. Attention has been placed on the overall thermal expansion response of nickel-base superalloys comprising of γ and γ′ phases, whereas the local behaviour of the γ and γ′ phases is still less well characterised and understood. In this study, a brief synopsis of available empirical models on the thermal expansion coefficient is presented. The empirical models are critically evaluated and compared with estimations made using macroscopic and mesoscopic experimental measurements obtained by Electro-Thermo-Mechanical Testing (ETMT) and neutron diffraction, respectively. Local variations that occur in the lattice of the γ matrix and the γ′ precipitates during heating to solution temperature were investigated through monitoring the changes in the interplanar spacing d_{hkl} of the matrix and the precipitates with temperature using *in situ* neutron diffraction while heating.

4.2. Experimental Method

Macroscopic thermal expansion measurements have been carried out using an Electro-Thermo-Mechanical Testing (ETMT) system (Instron, High Wycombe, UK), in argon atmosphere. In the ETMT system, heating was provided by passing current directly through a miniaturised specimen (with cross-sectional area of 1 mm^2), and the temperature was monitored with a thermocouple spot-welded to the centre of the specimen, while the

specimen ends were held in water cooled grips. An Imetrum video strain gage system and a digital image correlation (DIC) system were used to capture the macroscopic deformation of the specimen while heating to super-solvus solution temperature (see Section 3.2.2). This set-up has been successfully employed for CTE measurements by previous researchers [136].

A differential scanning calorimetry (DSC) analysis was performed to measure the specific heat of Alloy 11 (see Section 3.43.2.2). EDM machined cylindrical samples of 3 mm diameter and of approximately 82.6 mg weight were subjected to two subsequent thermal cycles while recording the heat flow between reference (sapphire) and sample crucibles with constant heating and cooling rate of 5 °C/min.

In situ time-of-flight neutron diffraction experiments were carried out at the ENGIN-X beamline at ISIS neutron source, UK. The experimental setup adopted during the acquisition of neutron diffraction data is illustrated in Figure 4.1(a). The neutron signal was obtained from a probed volume measuring 8 x 4 x 4 mm^3, controlled by the incident beam cross section and the collimator size. Samples were mounted in a vanadium can and heated in a vacuum furnace while the temperature was measured with a K-type thermocouple. The heat treatment applied to the sample is shown in Figure 4.1 (b).

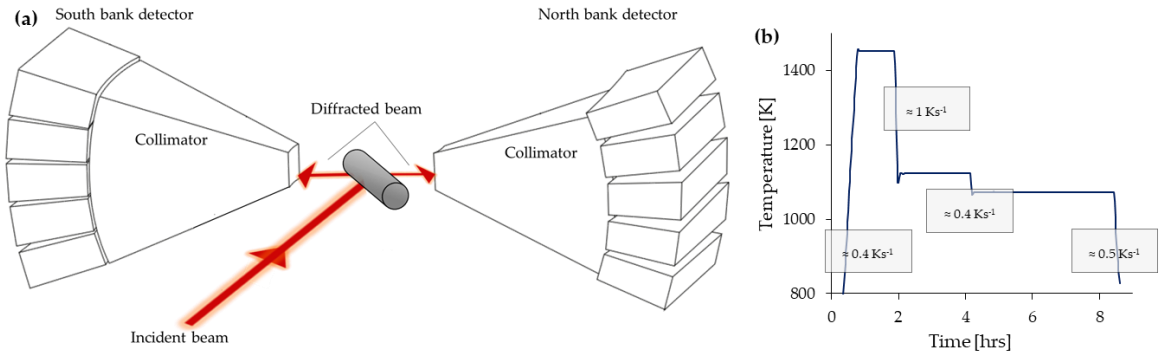


Figure 4.1: **(a)** Experimental setup for *in situ* neutron diffraction measurements, **(b)** Heat treatment profile for *in situ* neutron diffraction, including the heating and cooling rates.

4.3. Temperature Evolution of the γ/γ′ Lattice Misfit

4.3.1. Experimental Results by *in situ* Neutron Diffraction

To obtain the information needed for the temperature evolution of the lattice parameter of the matrix γ the contributions of γ and γ′ phases to the fundamental reflection {220} were separated using the corresponding superlattice peak {110} that contains solely information about the γ′ phase. Following this procedure (described in detail in Section 3.3.1), the variation of the lattice misfit during heating to solution temperature was measured employing *in situ* neutron diffraction, depicted in Figure 4.2. During heating, the lattice misfit decreases gradually from positive values, then when the temperature is in the vicinity of 1100 K the misfit is equal to zero and eventually at elevated temperatures it turns to negative values until γ′ is fully dissolved.

In Figure 4.2, the markers refer to the measurements obtained by neutron diffraction and the continuous lines correspond to Gornostyrev's model [126]. Gornostyrev et al. investigated the temperature dependence of the lattice misfit for Ni–Al alloys, using ab initio electronic calculations. In their study, two contributing factors were considered: (i) the difference in thermal expansion between γ and γ′, and (ii) the compositional variations due to redistribution of the alloying elements between γ and γ′ at elevated temperatures. The authors expressed the temperature dependence of the lattice misfit using the following expression:

$$\delta(T) = \delta^{(0)} + \frac{1}{3}\int_0^T (\alpha_{\gamma'}(T') - \alpha_{\gamma}(T'))dT' + \left(\varepsilon_{\gamma'}^{C} - \varepsilon_{\gamma}^{C}\right) + \left(\varepsilon_{\gamma'}^{V} - \varepsilon_{\gamma}^{V}\right) \qquad (16)$$

where $\delta^{(0)}$ is the lattice misfit at T = 0 K, $\alpha_{\gamma}, \alpha_{\gamma'}$ the coefficients of thermal expansion of γ and γ′ phases respectively, ε^{C} the lattice dilatations due to compositional changes and ε^{V} the lattice dilatations due to vacancy formation. The contribution of the vacancy formation, ε^{V}, to the overall lattice dilatation is considered to be insignificant [126] and can therefore be neglected in Eq.(16). On the contrary, as the lattice parameter of the γ and γ′ phases can change by up to several per cent due to their thermal expansion while heating, the difference

between their coefficients of thermal expansion is critical. Therefore, the temperature dependence of the lattice misfit could be described by the simplified formula:

$$\delta(T) = C + \frac{1}{3}\,(\alpha_{\gamma'}(T) - \alpha_{\gamma}(T))T \qquad (17)$$

The term C contains information about the lattice misfit at $T = 0$, $\delta^{(0)}$, as well as about the contribution of compositional variations to the lattice dilatation.

The coefficients of thermal expansion (CTE) of γ and γ′ phases were calculated from the *in situ* neutron diffraction measurements and used to estimate the temperature evolution of the γ/γ′ lattice misfit (see more details in 4.4.3). For $C = 0 \div 0.001$, the simplified formula in Eq. (17) can follow the trend of the evolution of misfit with temperature adequately for lower temperatures (Figure 4.2). At elevated temperatures though, the simplified version of Gornostyrev's model, fails to capture the trend of the experimental observations. At high temperatures, the solute diffusion is activated, and the high diffusion rates lead to strong elemental partitioning between the γ and the γ′ phases. Since the compositional profiles of the matrix and the precipitates vary with temperature, the term C would be temperature dependent and its exact determination would require an accurate estimation of the phase chemistry of the precipitates and the matrix.

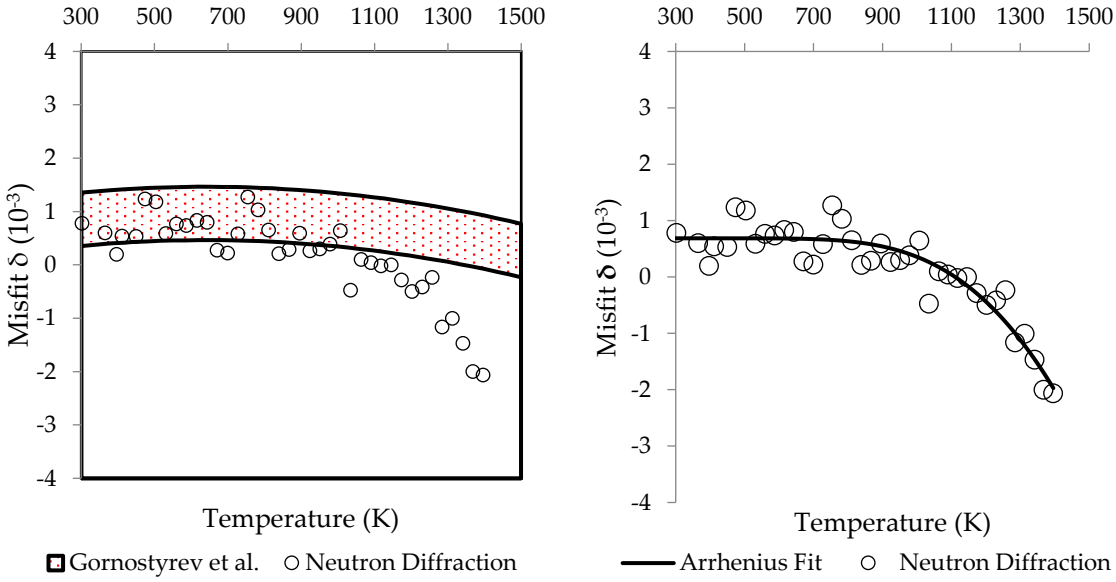


Figure 4.2: Evolution of the lattice misfit while heating. The markers correspond to the *in situ* neutron diffraction measurements, the dotted area (left) to Eq. (17) for $C = 0 \div 0.001$ and the solid line (right) to Arrhenius fit Eq. (18).

Another convenient assumption for the temperature evolution of the γ /γ′ lattice misfit, is that it follows an Arrhenius type temperature dependence with:

$$\delta(\mathrm{T}) = \delta_{RT} - k \exp\left(-\frac{Q}{RT}\right) \tag{18}$$

where δ_{RT} is the lattice misfit at room temperature, k is a constant, Q is the activation energy and T is the temperature. A good fit to the experimental data was obtained with values of 76.8 kJ mole^{-1} for Q, 2.24 for k, and δ_{RT} = 0.78 10^{-3} (Figure 4.2). Although the above expression is phenomenological and Q does not have a physical explanation, it can be a useful mathematical expression for modelling the temperature evolution of the lattice misfit.

4.3.2. Correlation between γ/γ′ Lattice Misfit and CTE of γ and γ′

At room temperature the mismatch between the lattice parameters of the matrix and precipitates results in the deformation of the lattice surrounding the precipitates. When the temperature is raised the different thermal expansion coefficients of the two phases results in the modification of the deformation field of the lattice. Therefore, during heating, there are two phenomena contributing to the total lattice misfit: the misfit that arises due to elastic constraints to maintain coherency between the two phases and the thermal misfit generated by the different properties of γ and γ′. To study the temperature evolution of the lattice misfit, and distinguish the contribution of each of these phenomena, Eshelby's inclusion method is used. J. D. Eshelby [53] developed an elegant approach to determine the elastic field of an ellipsoidal inclusion embedded in a homogeneous linear elastic solid. In his pioneering work, the two phases are treated as continuous materials obeying the macroscopic laws of linear theory of elasticity, and the interface between them is treated as a geometrical surface (i.e. its thickness is ignored). In the following sections, a brief overview of Eshelby's inclusion method is summarised and then applied to develop a correlation between the temperature evolution of the lattice misfit and the difference between the coefficients of thermal expansion of γ and γ′ phases.

Eshelby's Inclusion Method

In its simplest form, Eshelby's method considers an ellipsoid region with volume V_0 within an isotropic elastic solid with volume V resembling the inclusion and the matrix, respectively. It is supposed that the inclusion undergoes a spontaneous change such as a phase transformation, which would cause a prescribed deformation if the inclusion was free from the constraining matrix. Because of the presence of the surrounding material though, stresses will be present both in the inclusion and in the matrix. Assuming that within the ellipsoid inclusion the stress is uniform Eshelby approached the problem 'by visualising a sequence of imaginary cutting, straining and welding operations', and he developed analytical solutions for the stress and strain fields both in the inclusion and the matrix.

The inclusion is first cut and removed from its surrounding matrix (1) and is then imagined undergoing a transformation accompanied with a shape change (2). A uniform transformation strain ε^T, is developed within the inclusion, while it will experience zero stress since it is free from the constraining matrix. The transformation strain is often called *eigenstrain*, meaning the strain under zero stress. To be placed back to the hole from where it was cut, the inclusion has to return to its original shape before removal, so an appropriate surface traction is applied to restore its initial shape (3). Once back in position the two regions are welded together (4) and the surface traction is removed from the inclusion. Equilibrium is then reached between the matrix and the inclusion at a constrained strain ε^C of the inclusion relative to its initial shape before removal (5). The stages described above are illustrated in Figure 4.3.

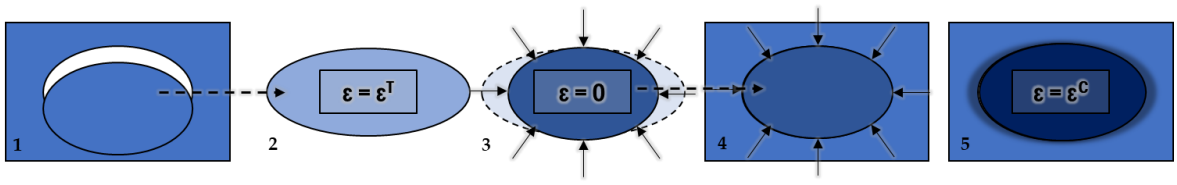


Figure 4.3: Schematic illustration of Eshelby's cutting and welding processes.

Therefore, the final constrained strain ε^C, apart from the contribution of the transformation strain ε^T, includes the elastic strain ε^{el}, that arises when the inclusion is placed back in position embedded in the matrix. Since the inclusion is strained uniformly, the stress within it can be calculated using Hooke's Law in terms of the elastic strain and the stiffness tensor of the material:

$$\sigma_I = C_M \varepsilon^{el} = C_M(\varepsilon^C - \varepsilon^T) \tag{19}$$

Since transformed ellipsoids always give rise to constrained shapes that are also ellipsoidal [137], Eshelby showed that the constrained strain ε^C can be estimated from the transformation strain ε^T, using the formula:

$$\varepsilon^C = S\varepsilon^T \tag{20}$$

where S is a tensor, termed the Eshelby tensor, which can be calculated in terms of the aspect ratio of the ellipsoidal inclusion and the Poisson's ratio of the material. The S tensor expresses the relationship between the final constrained inclusion shape and the unconstrained shape[137]. Now, the uniform inclusion stress can be described by combining Eq. (19) and (20):

$$\sigma_I = C_M(S - I)\varepsilon^{\mathrm{T}} \tag{21}$$

where I is the identity matrix. The S tensor for common inclusion shapes is described in the book of Clyne & Withers [137]. In this study, the morphology of γ' precipitates is assumed to be spherical. In the case of spheres, the tensor S has the following form:

$$S = \begin{bmatrix} S_{1111} & S_{1122} & S_{1133} & 0 & 0 & 0 \\ S_{2211} & S_{2222} & S_{2233} & 0 & 0 & 0 \\ S_{3311} & S_{3322} & S_{3333} & 0 & 0 & 0 \\ 0 & 0 & 0 & S_{2323} & 0 & 0 \\ 0 & 0 & 0 & 0 & S_{1313} & 0 \\ 0 & 0 & 0 & 0 & 0 & S_{1212} \end{bmatrix}$$

where:

$$S_{1111} = S_{2222} = S_{3333} = \frac{7 - 5\nu}{15(1 - \nu)} \tag{22}$$

$$S_{1122} = S_{2211} = S_{1133} = S_{2233} = S_{3311} = S_{3322} = \frac{-1 + 5\nu}{15(1 - \nu)} \tag{23}$$

$$S_{1212} = S_{1313} = S_{2323} = \frac{4 - 5\nu}{15(1 - \nu)} \tag{24}$$

The discussion so far refers to a single inclusion embedded within an infinite matrix, and the results are therefore applicable only to systems in which the volume fraction of the precipitates is low. To extend the scope of the model to systems containing more than one inclusion, Eshelby's solution can be modified by introducing the concept of average or *background stress* σ^b [137]. The background stress, commonly called average, image stress or mean field stress, partitions between the phases as if it was externally applied to maintain the balance of stress. Therefore, to incorporate into the model the effect of the volume fraction of inclusions, f, one can define macroscopic average stresses $\langle\sigma\rangle_M$ and $\langle\sigma\rangle_I$ applied to the matrix and the inclusions respectively. The balance of stress then becomes:

$$(1 - f)\langle\sigma\rangle_M + f\langle\sigma\rangle_I = 0 \tag{25}$$

This procedure models a random spatial distribution of reinforcing particles, and the average effect of all the inclusions is considered, rather than individual inclusion/inclusion interactions.

Derivation of the Correlation

Using Eshelby's model a reliable description of the temperature evolution of the total lattice misfit can be achieved developed for high γ′ content nickel base superalloys, but with broad applicability. The total lattice misfit between γ′ precipitates and the γ matrix is defined as the total disturbance introduced to the surrounding lattice as a result of their difference both in terms of size and properties. At any temperature, the total lattice misfit is the difference between the total strain within the precipitates and the total strain within the matrix, given by:

$$\delta(T) = \varepsilon_I^{TOT} - \varepsilon_M^{TOT} \tag{26}$$

Changes in temperature can cause internal stresses to arise as a result of different thermal expansion coefficients between the phases [137]. Assuming the material to be stress-free at a temperature T_1 the stress state at a lower temperature can be envisaged as arising from fitting an oversized inclusion (precipitate) into an undersized hole in the matrix. Thus, a temperature change ΔT will generate a thermal misfit strain ε^{T^*}, given by:

$$\varepsilon^{T^*} = (\alpha_I - \alpha_M)\Delta T \tag{27}$$

where α_I, α_M are the coefficients of thermal expansion of the precipitate and the matrix respectively and $\Delta T = T - T_0$, with T_0 the room temperature. The thermal misfit strain can be considered as a transformation strain similar to that used in the discussion above. Assuming that the stress field in the precipitate is uniform, by Eq. (21) one could describe the stress in the precipitate as:

$$\sigma_I = C_I(\varepsilon^C - \varepsilon^T) = C_I(S - I)\varepsilon^{T^*} \tag{28}$$

where ε^C is the constrained strain when the precipitate is embedded in the matrix and ε^{T^*} is the unconstrained thermal misfit strain referring to the state when the precipitate is removed and free from the surrounding matrix. It is assumed that the particle has the same elastic constants as the matrix, $C_I = C_M = C$, which is not far from reality for a γ/γ′ system [127].

To examine the total deformation of the system the effect of the volume fraction of γ′ precipitates should be included. As discussed, in a system with volume fraction of inclusions f, the balance of stresses can be expressed by Eq. (25), by introducing the concept of background stress σ^{b}. In Eq. (25), the average stress of the matrix $\langle\sigma\rangle_M$ includes the total effect of the volume fraction of inclusions as an average background stress σ^{b}, and the average stress of the precipitates $\langle\sigma\rangle_I$ incorporates not only the average background stress σ^{b} but also the uniform stress field developed within the inclusions. Therefore, $\langle\sigma\rangle_M$ and $\langle\sigma\rangle_I$ are given by:

$$\langle\sigma\rangle_M = \sigma^b \tag{29}$$

$$\langle\sigma\rangle_I = \sigma_I + \sigma^b \tag{30}$$

Substituting Eq. (29) and Eq. (30) in Eq. (25) gives:

$$\langle\sigma\rangle_M = \sigma^{\mathrm{b}} = -f\sigma_I \tag{31}$$

where σ_I refers to the stress field in the precipitates given by Eq. (28). The average deformation field of the matrix is then given by:

$$\langle\varepsilon\rangle_M^{el} = -f(S-I)\varepsilon^{T^*} \tag{32}$$

Regarding the precipitates using Eq. (31) the average stress is expressed as:

$$\langle\sigma\rangle_I = \sigma_I + \sigma^b = \sigma_I - f\sigma_I = (1-f)\sigma_I \tag{33}$$

The average deformation of the inclusions would then be:

$$\langle\varepsilon\rangle_I^{el} = (1-f)(S-I)\varepsilon^{T^*} \tag{34}$$

Therefore, for the total lattice misfit estimation, the total deformation of the matrix and the inclusions is required given by:

$$\varepsilon_M^{TOT} = \langle\varepsilon\rangle_M^{el} \tag{35}$$

$$\varepsilon_{\mathrm{I}}^{\mathrm{TOT}} = \langle\varepsilon\rangle_{\mathrm{I}}^{el} + \varepsilon^{\mathrm{T}^*} \tag{36}$$

Therefore, by substituting and simplifying Eq. (26) the temperature dependence of the total lattice misfit is described by:

$$\delta(T) = S\varepsilon^{T^*} \tag{37}$$

This outcome suggests that the temperature evolution of the lattice misfit is controlled exclusively by differences in thermal expansion of the matrix and the precipitates other than by elastic constraints. The lattice misfit is independent of the volume fraction of particles and is dominated purely by physical rather than mechanical factors. This simple formula that can be used to provide a guideline for the design of new alloy formulations.

The thermal misfit strain ε^{T^*} defined by Eq. (27) depends solely on the coefficients of thermal expansion of the precipitate and the matrix. As discussed in the next section (Section 4.4), at high temperatures the thermal expansion coefficient of each phase increases linearly

with temperature. Therefore, the expression for the evolution of the total lattice misfit with temperature is:

$$\delta(T) = S(\alpha_{\gamma'}(T) - \alpha_{\gamma}(T))\Delta T \quad (38)$$

It should be noted that the term ε^{T^*}, refers to the thermal misfit strain when the particles are in the unconstrained condition, free from the surrounding matrix. As it will be extensively discussed in the next sections (Section 4.5), the coefficient of thermal expansion of the γ′ precipitates in constrained state differs from that in the unconstrained state.

4.4. Temperature Evolution of Thermal Expansion Coefficient

4.4.1. Definitions of Thermal Expansion Coefficient

In response to temperature variations metals and alloys undergo dimensional changes, a phenomenon that has profound implications for their high temperature applications. The expansion of any material with temperature can be quantified in terms of the associated change in a characteristic dimension. The coefficient of thermal expansion (CTE) is a material property indicative of the extent to which a characteristic dimension of a material expands upon heating. The coefficient of thermal expansion is a temperature-dependent property, which gradually increases with temperature for most metals and alloys.

To avoid any confusion, it is first important to examine the alternative definitions of the thermal expansion coefficient. In its simplest form, the coefficient of linear thermal expansion of any material can be defined as the fractional increase in a linear dimension (e.g. length) per temperature increment over a particular temperature range. The most general definition of CTE, also referred to as the 'mean' or 'average' coefficient of thermal expansion α [136], is given by:

$$\alpha = \frac{1}{l_R}\frac{\Delta l}{\Delta T} = \frac{l - l_R}{l_R(T - T_R)} \quad (39)$$

where l is the expanded dimension at temperature T and l_R is the reference dimension at temperature T_R that is generally considered to be equal to the room temperature of 25 ° C.

A more fundamental definition, also referred to as the *true* coefficient of linear thermal expansion, linear thermal expansivity or *physical expansion coefficient* (PEC) [136] is given by:

$$\alpha_t = \frac{1}{l_R}\frac{\mathrm{d}l}{\mathrm{d}T} \tag{40}$$

For the rest of the discussion α will be referred to as CTE and α_t as PEC.

For pure metals, there are available sources including scientific publications and electronic databases with reliable data for the coefficient of thermal expansion up to their melting temperatures. Xie et al. [138] while studying the properties of pure Ni observed that the CTE increases exponentially with temperature at low temperatures and gradually approaches a linear increase at high temperatures. For engineering alloys though, the available data is often limited particularly at high temperatures. Considering its vital importance, several techniques have been improved and optimised to provide accurate measurements of the coefficient of thermal expansion of any metal and alloy including the complex heavily alloyed nickel-base superalloys. Among the different experimental approaches that have been employed, the most common include mechanical dilatometry, optical imaging and diffraction techniques [136]. Each of these techniques provides different accuracies, has distinct limitations and a defined temperature range over which they can be used. A detailed review of the experimental techniques and empirical methods that can be employed to obtain accurate measurements of thermal expansion coefficient is provided by James et al. [136].

Empirical Models

Among the empirical models derived for superalloys consisting mainly of γ/γ′ mixtures, the model developed by Sung and Poirier [130] includes the widest range of alloy compositions and temperatures. In their study, the authors derived a temperature and concentration dependent CTE model determined up to 1300 K, by fitting experimental data

for several nickel-base superalloys. In brief, in their model simple multilinear regression was used to estimate the CTE:

$$\alpha = d_0 + d_1 C_{Ti} + d_2 C_{Al} + d_3 C_{Cr} + d_4 C_{\Sigma} \tag{41}$$

where C_{Ti}, C_{Cr} are the concentrations (wt.%) of Ti and Cr respectively, C_{Al} is the concentration (wt.%) of Al plus V and C_{Σ} is the sum of the concentrations of Ta, Nb, Mo and W. The constants d_0, d_1 d_2, $d_3$and $d_4$were estimated as a function of temperature, and are given by:

$$d_0 = (b_0 + b_1 T^n + b_2 T^{2n} + b_3 T^{3n})\ 10^{-5} \tag{42}$$

$$d_i = (p_i + q_i T)\ 10^{-5} \tag{43}$$

where b_0, b_1, b_2, b_3, q_i and p_i are constants, summarised in Table 3. The n was selected as 1/3 to give a linear behaviour at high temperatures, guided by the theory of Pollock [131] that predicts that for temperatures above the Debye temperature, the CTE displays a linear behaviour, expressed as:

$$\alpha = k\,T \tag{44}$$

where k is a constant. Using the empirical model described above, the temperature evolution of the coefficient of linear thermal expansion of Alloy 11 was estimated and compared with estimations made for two other commercial nickel-base superalloys alloys for turbine disc applications, as shown in Figure 4.4.

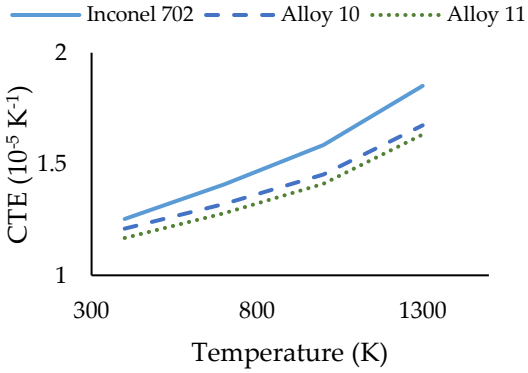


Table 3: Coefficients for Eq. (42) and Eq. (43).

	T < 1300 K	T ≥ 1300 K		p_i	q_i
b_0	-5.9431	6.94E-02	1	-3.24E-03	-6.83E-06
b_1	2.5805	0.50692	2	-1.30E-02	1.47E-05
b_2	-0.30383	-6.50E-02	3	-1.57E-02	1.07E-05
b_3	1.22E-02	3.08E-03	4	-4.54E-03	-9.49E-06

Figure 4.4: Temperature evolution of coefficients of thermal expansion of Alloy 11, Alloy 10, and IN702, estimated by Sung's model [130].

In another study by Mills et al. [132], the authors delivered empirical estimations of various thermo-physical properties of nickel-base superalloys including the thermal expansion coefficient from the composition of the alloys. The linear thermal expansion coefficient, α, at 298 K and its temperature dependence were found to be linear functions of the Al content, described briefly below:

$$\alpha\,(T) = \alpha_{298} + A(T - 298) + B(T - 298)^2 \tag{45}$$

where α_{298}:

$$\alpha_{\,298} = 11.6 - 0.29(mass\%Al) \tag{46}$$

$$A = \alpha_0^* + \alpha_1^*(mass\%Al), B = \beta_0^* + \beta_1^*(mass\%Al) \tag{47}$$

with $\alpha_0^* = 8.32\ 10^{-3}, \alpha_1^* = -1.90\ 10^{-6}, \beta_0^* = -1.34\ 10^{-6}, \beta_1^* = 1.32\ 10^{-7}$.

Previous studies [133-135] have also detected a linear correlation between the specific heat and the thermal expansion coefficient of metals and alloys. In particular, Mel'nikova and co-workers [134] developed the following relationship to describe the correlation between specific heat and linear thermal expansion coefficient:

$$a\ =\ C_p\ (A + BT) \tag{48}$$

where A and B are constants and T is temperature. The above relationship is reported to give a reasonable correlation down to about 150 K.

In the next section, the abovementioned empirical models are critically evaluated and compared with macroscopic and mesoscopic experimental measurements on the coefficient of thermal expansion.

4.4.2. Experimental Results

Macroscopic Thermal Expansion Measurements

Macroscopic experimental measurements of the CTE were obtained employing ETMT – Imetrum system following the methodology described in Section 3.2.2. The experimental measurements were used to evaluate the estimations from the empirical models described

previously and a direct comparison between them is portrayed in Figure 4.6 (a). To estimate the thermal expansion coefficient according to the model proposed by Mel'nikova et al. [134] the specific heat of Alloy 11 was measured employing a DSC analysis (Figure 4.5)

Additionally, Figure 4.5 demonstrates the dissolution sequence of the alloy under consideration. First, the dissolution of the γ′ precipitate phase occurs with $T_{\gamma',Solvus} \approx 1425$ K, followed by the dissolution of the γ + γ′ eutectic. Finally, the large endothermic peak corresponds to the melting of the γ matrix, with $T_{Solidus} = 1463$ K and $T_{Liquidus} = 1590$ K.

Concerning Mills et al. [132], it seems that their model overestimates the values of the coefficient of thermal expansion, particularly at high temperatures. On the contrary, Sung's predictions [130] are closer to the ETMT measurements, particularly for temperatures above 900 K. It is apparent though that the model developed by Mel'nikova et al. captures best the gradient of the slope of the CTE curve, which increases significantly at high temperatures, and particularly when the temperature exceeds 1200 K. Indeed, as illustrated in Figure 4.6 (a), the empirical formula in Eq. (48) is in good agreement with the experimental observations obtained by ETMT. The parameters used for fitting are $A = 2.3\ 10^{-5}$ and $B = 10^{-9}$.

The observed trend could be attributed to the reduction of the volume fraction of the precipitates with increasing temperature, until they are fully dissolved at $T_{\gamma',solvus}$. Therefore, at high temperatures when the volume fraction of γ′ is diminished, the contribution of the γ matrix is dominant. The temperature evolution of γ′ volume fraction can be obtained from the thermodynamic calculation software ThermoCalc, employing the Thermotech Ni-base Superalloys Database (TTNI8) [139]. As shown in Figure 4.7, the temperature evolution of the γ′ volume fraction reduces gradually with temperature, following an Arrhenius-type temperature dependence given by Eq. (1). This expression has been reported to be a practical configuration for modelling the observed changes, particularly for T > 800° C [26]. Indeed, a good fit (R^2=0.993) of the ThermoCalc predictions to Eq. (1) was achieved with values of 96.76 kJ mole-1 for Q^*, 2361 for m, and $V_{f\ RT}^{\gamma'} = 0.5601$.

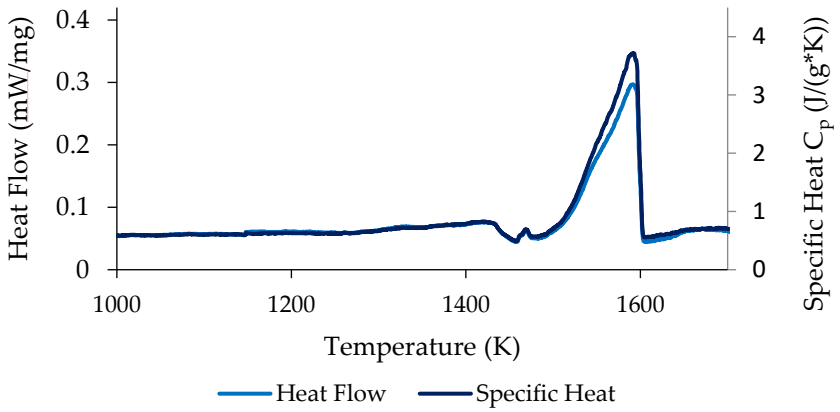


Figure 4.5: DSC thermogram for Alloy 11 cycled at 5 °C/s.

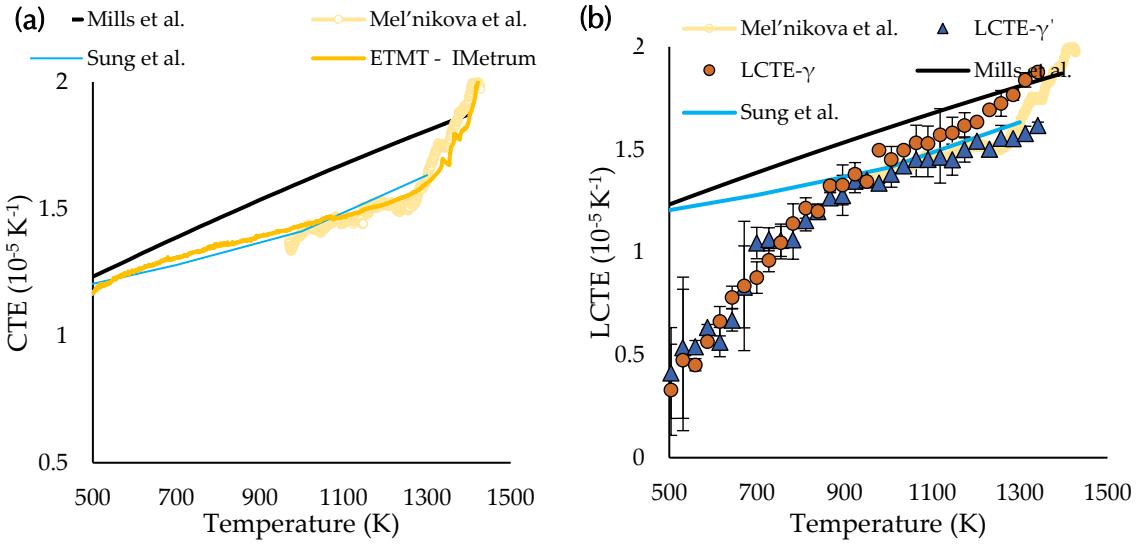


Figure 4.6: **(a)** Comparison between measurements of the macroscopic thermal expansion coefficient obtained employing the ETMT - Imetrum video system and estimations from the available empirical models. **(b)** Comparison between measurements of the mesoscopic thermal expansion coefficient of γ and γ′ calculated by neutron diffraction measurements and estimations from the available empirical models.

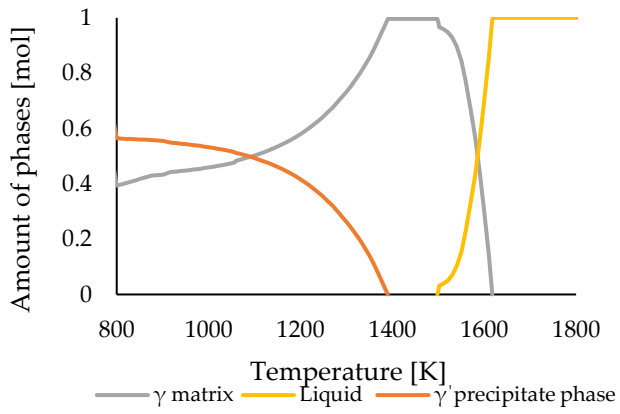


Figure 4.7: ThermoCalc predictions of the amount of phases present in Alloy 11 as a function of temperature.

Mesoscopic Thermal Expansion Measurements

Apart from the macroscopic CTE measurements obtained with ETMT-Imetrum, reflecting the overall behaviour of the alloy system, neutron diffraction was employed to measure the temperature evolution of the thermal expansion of the lattice of the γ matrix and the γ′ precipitate phase separately. This was achieved by measuring the increase in atomic spacing between crystal lattice planes in each phase during heating to solution temperature. For each temperature, the interplanar spacing d_{hkl} of γ and γ′ phases was estimated by fitting the fundamental peak {220}, which contains information for both γ and γ′ phases. Distinguishing the contribution of the γ′ phase and separating the fundamental peak, was achieved using information obtained by fitting the superlattice peak {110} (Figure 4.9). More details on the step-by-step procedure for the data analysis is described in Chapter 3 (Section 3.3.1). The diffraction pattern of Alloy 11 at room temperature is displayed in Figure 4.8. For each phase, the coefficient of thermal expansion is estimated as follows:

$$\alpha = \frac{d_{hkl} - d_{hkl_R}}{d_{hkl_R}(T - T_R)} \tag{49}$$

where d_{hkl} is the interplanar spacing, T is the temperature and d_{hkl_R} is the reference interplanar spacing measured at temperature $T_R = 298.7$ K.

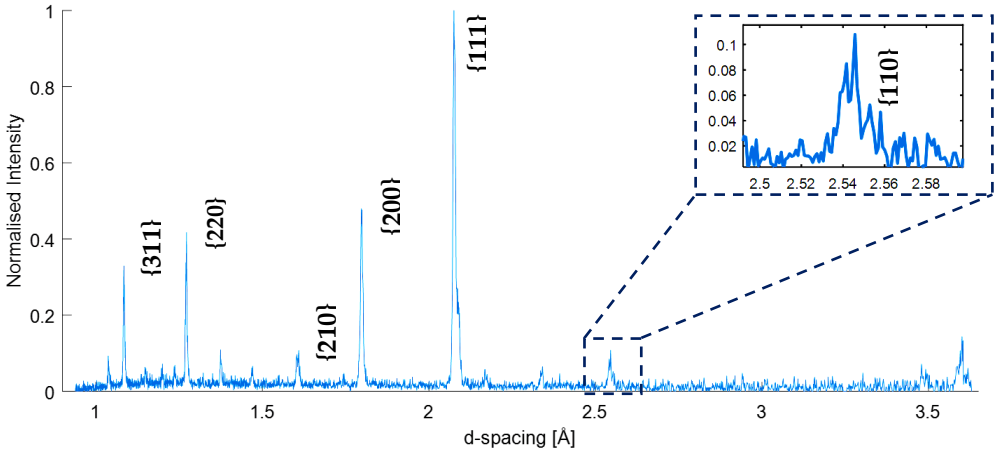


Figure 4.8: Diffraction pattern of Alloy 11 at room temperature.

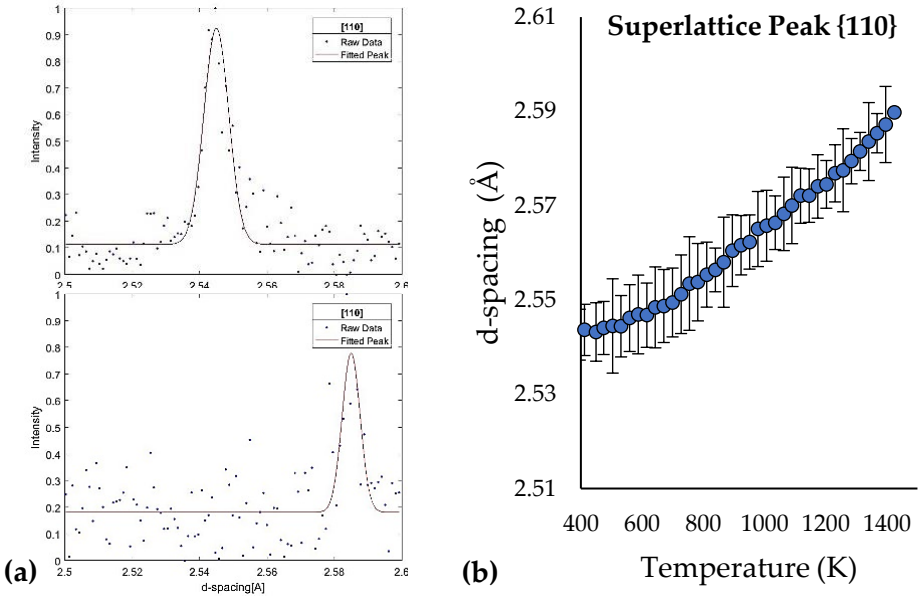


Figure 4.9: (a) Fitting of the superlattice peak {110} to get the evolution of the interplanar spacing with temperature $d_{110}^{\gamma'}$, shown in **(b)**.

Figure 4.6 (b) illustrates estimations of the CTE of γ and γ′ obtained from neutron diffraction measurements using Eq. (49), compared to the empirical estimations suggested by Sung et al. [130], Mills et al. [132] and Mel'nikova et al. [134]. The continuous black line corresponds to Mill's model, the continuous blue line corresponds to Sung' s model, and the thicker line refers to estimations based on the DSC measurements, according to Mel'nikova et al. The markers represent the CTE estimations based on the neutron diffraction measurements for γ and γ′.

First and foremost, it should be highlighted, that a potential drawback of applying neutron diffraction on the measurement of CTE is the error propagation, as the estimations rely on the subtraction of two separate measurements of the interplanar spacing. Considering that these two values will be very close, the percentage error involved in the thermal expansion coefficient estimation could be significant [136], which seems to be the case for low temperatures in Figure 4.6 (b). Undoubtedly though, for low temperatures, the empirical models examined in this study deviate from the values estimated from the measurements, regardless of the possible error introduced (see the error bars in Figure 4.6 (b)). For higher temperatures (T > 900K), when the temperature dependence of the CTE is expected to be

linear, Sung's model is in good agreement with the experimental observations. A closer examination of the graph in Figure 4.6 (b) reveals that Sung's model mainly follows the behaviour of γ', the volume fraction of which diminishes with temperature until its dissolution when the temperature equals to $T_{\gamma',solvus}$. Then, for even higher temperatures, the model developed from Mel'nikova et al. that relates the CTE to the specific heat measured by DSC, seems to capture more accurately the thermal expansion behaviour, including the rising trend of the CTE of the γ phase.

Therefore, the available empirical models can give an indication of the temperature evolution of the CTE of the overall alloy system but cannot be used to describe accurately the thermal expansion of the crystal lattice of each phase. This is not unexpected since measurements of the expansion of the lattice parameter do not necessarily correspond to the macroscopic expansion of the bulk material [136]. The macroscopic expansion will be affected by various factors, including the temperature variation of the volume fraction of the various phases present besides γ and γ', as well as the increase of the vacancy concentration [136-140].

4.4.3. Temperature Evolution of the Lattice Parameters of γ and γ'

An accurate description of thermal expansion of the crystal lattice of γ and γ' is delivered based on the definition of physical expansion coefficient given in Eq. (40). One could define the thermal expansion coefficient as the differential increase in interplanar spacing per temperature increment, given by:

$$\alpha_t = \frac{1}{d_{hkl}} \frac{\mathrm{d}d_{hkl}}{\mathrm{d}T} \tag{50}$$

This formula could be rephrased in the following way:

$$\alpha_t = \frac{1}{d_{hkl}} \frac{\mathrm{d}d_{hkl}}{\mathrm{d}T} = \frac{\mathrm{d}(\ln d_{hkl})}{\mathrm{d}T} \tag{51}$$

For convenience, the polynomial approximation of the $\ln d_{hkl}$ versus T curve is used so that:

$$\ln d_{hkl} = p_0 + p_1 T + p_2 T^2 \tag{52}$$

Consequently, the evolution of d_{hkl} as a function of temperature could be expressed by:

$$d_{hkl} = d_{hkl_{0K}} \exp(p_1 T + p_2 T^2) \tag{53}$$

with $p_0 = \ln d_{hkl_{0K}}$, $p_1 = \alpha_{OK}$ and $p_2 = \frac{1}{2}\mathrm{d}\alpha/\mathrm{d}T$.

For a cubic unit cell the lattice parameter, a, is linearly related to the interplanar spacing, d_{hkl}, with:

$$d_{hkl} = \frac{\mathrm{a}}{\sqrt{h^2 + k^2 + l^2}} \tag{54}$$

Therefore, the temperature dependence of the lattice parameter of each phase is given by:

$$\mathrm{a} = \mathrm{a}_{0K} \exp(\alpha_{0K} T + \frac{1}{2}\frac{\mathrm{d}\alpha}{\mathrm{d}T} T^2) \tag{55}$$

From Eq.(51)-(52), it is apparent that the fitting parameters (Table 4) can also be used to describe the temperature evolution of the thermal expansion coefficient of the lattice parameters of γ and γ′ phases, $\alpha_{\gamma'}(T)$ and $\alpha_{\gamma}(T)$ respectively, by substituting to the expression:

$$\alpha(T) = \alpha_{OK} + \frac{\mathrm{d}\alpha}{\mathrm{d}T} T \tag{56}$$

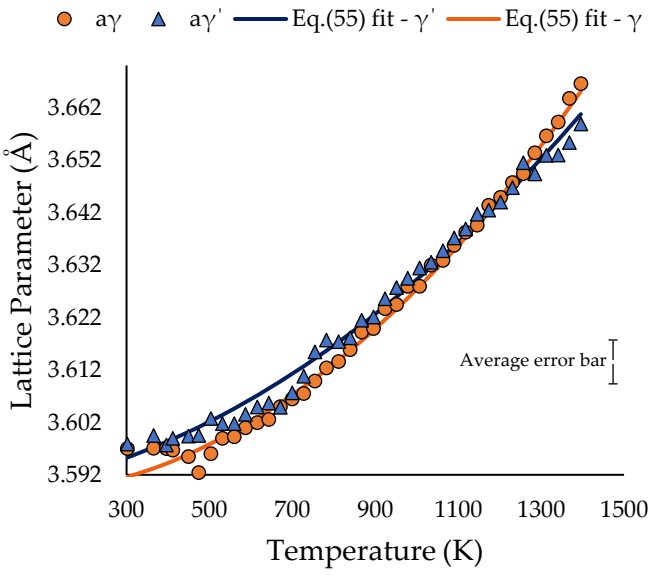


Table 4: Fitting parameters for Eq. (55).

	γ′	γ
a_{0K}	3.589	3.588
α_{0K}	3.47E-06	2.22E-14
$\frac{1}{2}\mathrm{d}\alpha/\mathrm{d}T$	7.67E-09	1.09E-08
R^2	0.9883	0.994

Figure 4.10: Comparison of the derived model (Eq. (55)) to the experimental results obtained with neutron diffraction.

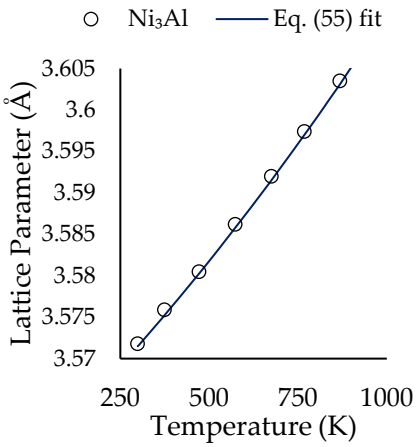
Indeed, the simple correlation derived from the definition of the α_t can capture the trend of the thermal evolution of the lattice parameters of γ and γ′ phases with accuracy. In Figure 4.10, the markers represent the results obtained from the *in situ* neutron diffraction experiment, while the continuous lines denote a fit of the experimental data for the lattice parameter of the matrix γ and the γ′ precipitates to the formula (55). The parameters used for fitting are given in Table 4. The derived correlation is in good agreement with the experimental observations ($R^2 > 0.988$).

4.5. Discussion

4.5.1. Thermal Expansion of Ni_3Al

Rao et al. [140] investigated the temperature dependence of the thermal expansion of pure γ′ (Ni_3Al) employing X-ray diffraction and dilation methods. They found out that the evolution of the lattice parameter with temperature is exponential, while its thermal expansion was observed to vary linearly with temperature. This is a strong validation for the model derived in this study. Indeed, as illustrated in Figure 4.11, the experimental measurements on the evolution of the lattice parameter of Ni_3Al with temperature reported in [140], follow the observed trend and agree exactly (R^2= 0.9987) with the derived model given by Eq. (55).

The parameters used for fitting are: $a_{0K} = 3.558$, $\alpha_{0K} = 1.17\ 10^{-5}$, and $\frac{1}{2}d\alpha/dT = 3.26\ 10^{-9}$. What is more, according to the measurements obtained by dilation and reported in the same study, the slope of the linear temperature evolution curve of the CTE of Ni_3Al is approximately equal to $6.5\ 10^{-9}$. This is validating the reliability and relative accuracy of the derived correlation (the fitting parameter obtained from this approach is equal to $\frac{1}{2}d\alpha/dT = 3.26\ 10^{-9}$).



Temperature (K)	Lattice Parameter (Å)
298	3.5718
374	3.5759
471	3.5805
573	3.5862
675	3.592
767	3.5974
867	3.6035

Figure 4.11: The variation of lattice parameter of Ni_3Al with temperature as reposted in ref. [140] follows the proposed correlation.

4.5.2. Thermal Expansion of Unconstrained γ′ Precipitates

It should be noted that in this study the measurements of the thermal expansion of the lattice parameter of γ and γ′ refer to the constrained condition when the γ′ precipitates are surrounded and constrained by the γ matrix. Undoubtedly, in modern nickel-base superalloys, the phase chemistry and the high temperature behaviour of γ′ particles in the unconstrained condition is much more complicated than that of Ni_3Al. A number of recent studies [51-52,141-142] has successfully attempted to measure the unconstrained lattice parameter of the γ′ precipitates from phase-extracted samples at elevated temperatures. In these studies, γ′ powder was obtained using a powder extraction technique. Most commonly, the extraction electrolyte is a water solution containing 1% ammonium sulphate ($(NH_4)_2SO_4$) and 1% citric acid ($C_6H_8O_7$). Detailed description of the extraction process can be found in [143].

Figure 4.12 summarises the experimental measurements of the constrained (bulk) and unconstrained (powder) lattice parameters of γ′ for common nickel-base superalloys for turbine disc applications reported in the literature [51-52,141-142]. For convenience, the values are also plotted in Figure 4.12 (b). As expected, there are profound differences between Ni_3Al and γ′ phase extracted from modern alloys, with the latter being mainly expanded after the alloying additions. For RR1000, at room temperature, the lattice parameters of γ′ in the

powder and in the bulk conditions are very similar, with the latter being 0.027% larger. In the same alloy at higher temperatures, γ'_{bulk} is 0.075% smaller than γ'_{powder}.

By fitting the available experimental measurements to the derived model which has been validated on Ni_3Al the temperature dependence of the lattice parameter of the constrained and the unconstrained γ′ for RR1000 can be predicted using Eq. (55). Then, assuming that it is linear the temperature evolution of the coefficient of thermal expansion of phase-extracted γ′ can be obtained by substituting the fitting parameters in Eq. (56). Figure 4.13 can be used to obtain useful insights into the coefficient of thermal expansion of γ′ in the unconstrained condition. The continuous lines in this graph refer to the CTE of γ'_{bulk} for Alloy 11 and RR1000, while the dotted lines correspond to Ni_3Al and phase-extracted γ′ from RR1000. First, the behaviour of the alloy under consideration, Alloy 11 appears to be directly analogous to RR1000 in the constrained condition. Interestingly, the curves for the CTE of γ'_{powder} and Ni_3Al display a very similar slope. Therefore, it is sensible to assume that the general formulation of the observed trend of the temperature evolution of the lattice parameters and the coefficient of thermal expansion of γ and γ′ phase is expected to be valid both for the constrained and for the unconstrained condition. This assumption which is also supported by previous studies [140,144].

			Lattice Parameter [Å]	
Ref.	Alloy	Temp. [K]	γ′ Powder	γ′ Bulk
[51]	RR1000	298	3.597	3.598
		1033		3.632
[141]	RR1000	1073	3.618	3.615
[52]	Alloy	293	3.595	3.593
	UC01	1073	3.625	3.627
[142]	Rene88DT	1033	3.595	3.592

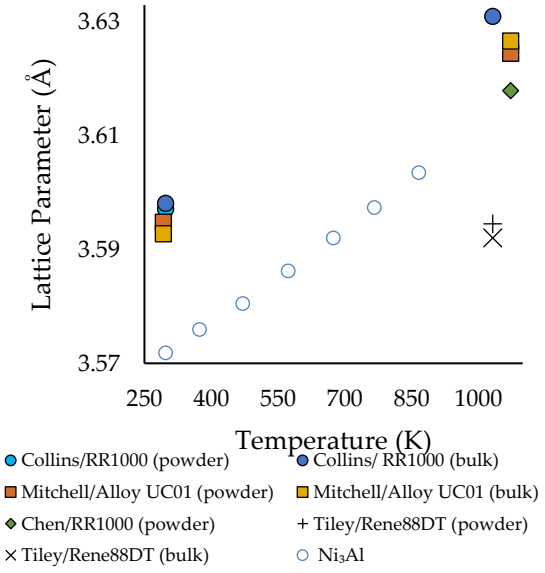


Figure 4.12: (a) Table of measurements of the constrained (bulk) and unconstrained (powder) lattice parameter of γ′ for disc nickel- based superalloys reported in the literature, **(b)** Graphical representation of (a).

	RR1000 γ′ (powder)	RR1000 γ′ (bulk)	Ni_3Al
a_{0K}	3.593	3.593	3.558
α_{0K}	2.778E-06	2.560E-06	1.17E-05
$\frac{1}{2}d\alpha/dT$	3.412E-09	7.381E-09	3.26E-09

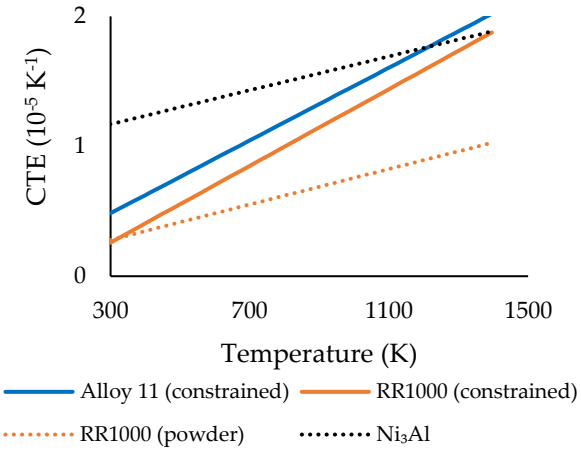


Figure 4.13: **(a)** Table of the fitting parameters for Eq. (55), **(b)** Temperature evolution of coefficient of thermal expansion of γ′ of Alloy 11 (constrained), and RR1000 (constrained and unconstrained), compared to Ni_3Al.

4.5.3. Temperature Evolution of the γ/γ′ Lattice Misfit

Due to its considerable significance, numerous studies have been carried out to investigate the temperature evolution of the lattice misfit of precipitate phases in nickel-base superalloys, but only few of them have utilised Eshelby's inclusion method to rationalise the experimental observations and derive accurate predictions. First, Ma et al. [127] performed *in situ* neutron diffraction to monitor elastic micro-strains in a high volume fraction (≈65%) nickel-base superalloy CM247 LC in the case of cuboidal inclusions. A simple formula was derived to relate the misfit strain to the thermal mismatch between the precipitates and the matrix up to 900 °C using the eigenstrain formulation of Eshelby. The result was found to be independent of the volume fraction of particles which is in total agreement with the proposed correlation. In a recent study by Zhang et al. [145], misfit stresses in the γ′′ strengthened Inconel 718 were calculated from the measured constrained misfit strain using Eshelby's inclusion method. The constrained misfit strain of the γ′′ precipitates was measured using neutron diffraction at various temperatures. Then, after reasonable assumptions for the temperature dependence of the Young's modulus Eshelby's tensor was calculated and used to estimate the stresses developed. Additionally, the linear coefficient of thermal expansion

(CTE) of the γ and γ'' phases in the constrained state was obtained by the deviation of polynomial plots, assuming that it is linear.

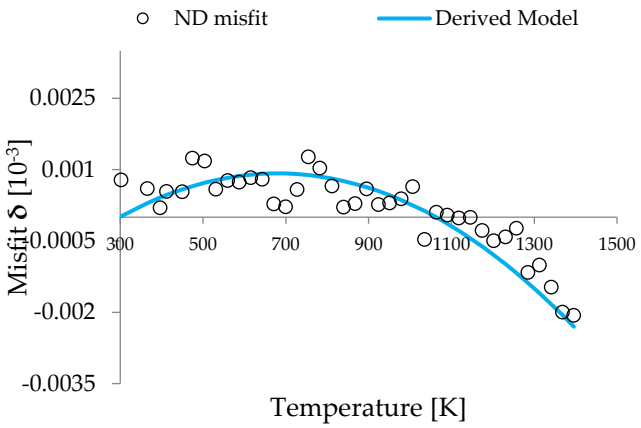
In this study, the focus is placed mainly on understanding the mechanism that controls the lattice misfit evolution with temperature till the dissolution of the precipitate phase. It is concluded that during heating the total lattice misfit arises due to the thermal misfit generated by the different physical properties of γ and γ′ and particularly their (unconstrained) thermal expansion coefficients.

To validate the reliability of the derived correlation an approximate estimation of the unconstrained thermal misfit is attempted. To estimate the temperature evolution of the lattice misfit one needs to specify four variables in Eq. (57) for the coefficients of thermal expansion of the γ′ precipitates and the γ matrix:

$$\delta(T) = S\left[\left(\alpha_{OK_{\gamma'}} - \alpha_{OK_{\gamma}}\right) + \left(\frac{\mathrm{d}\alpha}{\mathrm{d}T_{\gamma'}} - \frac{\mathrm{d}\alpha}{\mathrm{d}T_{\gamma}}\right)T\right]\Delta T \tag{57}$$

For defining the thermal expansion coefficient of the γ matrix, $\alpha_{\gamma}(T)$, the high temperature macroscopic thermal expansion measurements (Section 4.4.3) are fitted to Eq. (56). At high temperatures the volume fraction of γ′ is diminished and the contribution of the γ matrix to macroscopic thermal expansion measurements is dominant. Regarding $\alpha_{\gamma'}(T)$, available measurements from various studies in the literature are collected (Figure 4.11 and Figure 4.12) and used to obtain an estimate of the coefficients of thermal expansion of Ni_3Al, and of phase-extracted γ′ particles from RR1000 (Figure 4.13) assuming that they are linear functions of temperature. It can be seen that the curves of the Ni_3Al and of the phase-extracted γ′ from RR1000 have a very similar gradient so it would be sensible to assume that the term $\frac{\mathrm{d}\alpha}{\mathrm{d}T_{\gamma'}}$ for Alloy 11 will also be in the close proximity of that value. For the fitting parameter $\alpha_{OK_{\gamma'}}$, it was assumed to be equal to the one estimated for the constrained condition by fitting the neutron diffraction measurements. For the estimation of the Eshelby's tensor the Poisson's ratio was assumed to be equal to 0.3 so $S = 0.619$ by Eq. (22) – Eq. (23).

The fitting parameters are summarised in Table 5. As illustrated in Figure 4.14, the results obtained by this estimation although not rigorous are in good agreement with the experimental observations and provide strong validation to support the derived correlation.



	γ'	γ
α_{OK}	4.82E-06	-6.00E-06
$\frac{d\alpha}{dT}$	6.83E-09	1.70E-08

Table 5: Fitting parameters for Eq. (57).

Figure 4.14: Validation of the derived estimation on the temperature dependence of the γ/ γ′ lattice misfit. Neutron diffraction measurements are compared with predictions obtained using Eq.(57) and the fitting parameters in Table 5.

4.6. Conclusions

In this study, through monitoring the changes in the interplanar spacing d_{hkl} of the matrix and the precipitates with temperature useful insights on the temperature evolution of the γ/γ′ lattice misfit were obtained and rationalised using the Eshelby's eigenstrain formulation. It was shown that the temperature evolution of the lattice misfit is independent of the volume fraction of particles and is dominated exclusively by the difference between the thermal expansion coefficients of the matrix and the precipitates, other than by elastic constraints imposed by their different lattice parameter to maintain coherency.

Macroscopic and mesocopic experimental measurements on the coefficient of thermal expansion were collected and compared with available empirical models derived for superalloys consisting mainly of γ/γ′ mixtures. The macroscopic thermal expansion behaviour was measured utilising an ETMT-Imetrum system recording the overall behaviour of the alloy system, and local variations that occur in the lattice of the γ matrix and the γ′ precipitates

during heating to solution temperature were investigated employing neutron diffraction. It was shown that some of the available empirical models can give an adequate estimation of the temperature evolution of the CTE of the overall alloy system but cannot be used to describe accurately the thermal expansion of the crystal lattice of each phase. Using the experimental observations, a simple model was derived based on the definition of the thermal expansion coefficient able to describe the thermal evolution of the lattice parameters of γ and γ′ phases with accuracy. The correlations described in this study offer a useful guideline reliably validated on available experimental results.

5

On the dependence of γ′ precipitate size on the cooling rate from super-solvus temperature

5.1. Introduction

The cooling rate from super-solvus solution heat treatment controls the kinetics of the secondary and tertiary γ′ precipitation, hence it determines to a large extent the morphology, size, and distribution of the precipitates. Primarily, as shown by previous experimental studies [28-31] the size of the precipitated γ′ is largely controlled by the cooling rate after the super-solvus temperature with the average γ′ particle size decreasing with increasing cooling rates. As in many precipitation-hardened systems, the mechanical properties of nickel-base superalloys are strongly influenced by the precipitate size distribution (PSD) as it exerts control over dislocation motion. The effect of the size of the secondary and tertiary γ′ precipitates on the mechanical properties has been extensively studied (see Section 2.7.1), and it has become apparent that the optimum combination of desired mechanical properties for specific applications can be achieved by close control of the size of γ′ precipitates.

By controlling the cooling rate from solution heat treatment temperature, the γ′ precipitate size can be tailored to obtain the optimum properties required. To achieve this, it is of crucial importance to quantify the dependence of the average particle size on the cooling rate. This allows developing heat treatment schedules to obtain the desired precipitate size for optimum properties. In this study, a power law dependence of the secondary and tertiary γ′ precipitate size on the cooling rate is first observed experimentally, and then justified on the basis of thermodynamics and diffusion kinetics analysis. McLean's model for precipitate growth is recast to consider the effect of cooling rate instead of isothermal conditions and a simple correlation between the size of γ′ precipitates and the cooling rate is derived.

5.2. Literature Review

To support the experimental work described later, a review of the relevant literature is first provided. This review fist provides an overview on the basic thermodynamic principles for the nucleation and the growth of a new precipitate phase, and then the model developed by McLean [20] to predict γ′ growth in nickel-base superalloys is described.

5.2.1. Nucleation

The driving force for spontaneous phase transformations is the minimisation of Gibbs free energy G, which increases in magnitude with decreasing temperature. Considering a binary system consisting of phases α and β, phase β would become thermodynamically stable at temperatures below the equilibrium temperature T_c, only if it results in the reduction of Gibbs free energy. When the temperature is equal to the equilibrium temperature T_c, both phases are equally stable, so they have the same free energy, given by:

$$\Delta G = 0 \Leftrightarrow \Delta H - T_c \Delta S = 0 \Leftrightarrow \Delta H = T_c \Delta S \tag{58}$$

So, the temperature dependence of the ΔG could be expressed as:

$$\Delta G(T) = \Delta H - T\Delta S = T_c\Delta S - T\Delta S \Rightarrow \Delta G(T) = (T_c - T)\Delta S \quad (59)$$

Defining $\Delta T = T_c - T$, as the degree of undercooling, it is well established that as the temperature decreases below the equilibrium transformation temperature T_c, the thermodynamic driving force for nucleation of the new phase β increases.

There are three contributions to the total free energy change that accompany the nucleation of the new phase β. The first is the reduction of the volume free energy ΔG_V, and its contribution is the product of ΔG_V and the volume of the nucleus. The second energy contribution results from the increase of surface energy γ due to the formation of the interphase boundary during the phase transformation. Finally, the lattice distortion due to the formation of the new phase leads to misfit strain energy increase equal to $V\Delta G_S$. The total free energy change is equal to the sum of these contributions, that is:

$$\Delta G = V\Delta G_V + A\gamma + V\Delta G_S \quad (60)$$

Assuming that the nucleus is spherical (Figure 5.1(a)):

$$\Delta G = 4\pi r^2\gamma + \frac{4}{3}\pi r^3(\Delta G_V + \Delta G_S) \quad (61)$$

Consequently, in Figure 5.1 (b) the curve associated with ΔG first increases, then reaches a maximum, and finally decreases. Differentiating the above expression for ΔG gives the following expression for the nucleus critical radius r^*:

$$r^* = \frac{2\gamma}{\Delta G_V + \Delta G_S} \quad (62)$$

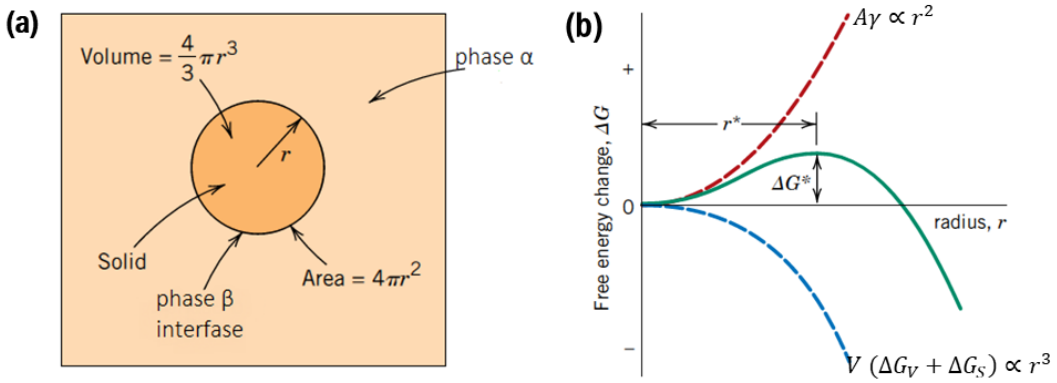


Figure 5.1: Schematic diagram showing the nucleation of a spherical particle. Adapted from [146].

A subcritical particle, with radius less than the critical radius r*, also termed as embryo, will shrink and redissolve. Whereas, if the particle reaches a size corresponding to the critical radius r^*, then growth will continue with the decrease in free energy. Nucleation in solids is almost always heterogeneous, as the formation of new phase usually takes place at special favourable nucleation sites. The reason being that the activation energy for nucleation ΔG is lowered when nuclei form on pre-existing surfaces or interfaces, since the surface free energy is reduced. Sites which are suitable for nucleation are non-equilibrium defects, such as dislocations and grain boundaries.

5.2.2. Growth

The growth begins once an embryo has exceeded the critical size, r^*, and becomes a stable nucleus. Once a nucleus of super-critical size is formed, the thermodynamic driving force promotes its growth, since the free energy decreases further (Figure 5.1(b)). The growth of the new phase reaches completion when equilibrium is attained.

The growth of the nucleated particles involves the diffusion of solutes across the particle/matrix interface. According to first Fick's Law, the diffusion flux J across a plane (moles/m^{2}s) is proportional to the gradient of concentration:

$$J = D\frac{\mathrm{d}C}{\mathrm{d}x} \tag{63}$$

where D is the diffusion coefficient.

A classic example is briefly outlined which refers to the growth of a planar slab of a solute-rich precipitate phase behind a planar incoherent interface with instantaneous speed of advancement v. The concentration of solute in the precipitate phase C_β is higher than the bulk concentration C_0 in the matrix. At the interface, local equilibrium is assumed, so that the concentration within the matrix directly adjacent to the interface is the equilibrium concentration C_e. The growth speed v, being a diffusion-controlled process, depends solely on the concentration gradient at the interface.

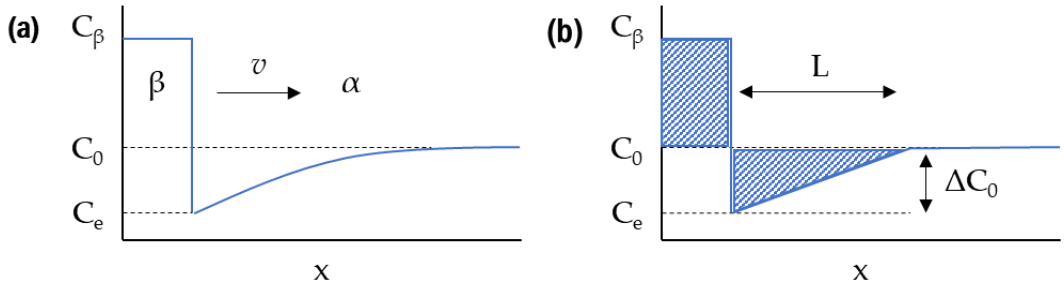


Figure 5.2: (a) Concentration profile at the interface during diffusion-controlled growth (b) Zener simplified model.

Zener introduced a simplified approach, approximating the concentration profile as linear over a diffusion zone with width L, shown in Figure 5.2 (b). This approximation is expressed as by:

$$\frac{\mathrm{d}C}{\mathrm{d}x} = \frac{C_0 - C_e}{L} = \frac{\Delta C_0}{L} \tag{64}$$

where $\Delta C_0 = C_0 - C_\mathrm{e}$ denotes the supersaturation prior to precipitation. Consequently, using Fick's first Law and the requirement of solute conservation at the interface, the growth could be described by:

$$x = \frac{\Delta C_0}{\sqrt{C_\beta - C_e}}\sqrt{Dt}\,, v = \frac{\Delta C_0}{2(C_\beta - C_e)}\sqrt{\frac{D}{t}} \tag{65}$$

This proves that the thickening of the particle is related to the square root of time also known as the parabolic growth law. The above results demonstrate the parabolic kinetics of precipitate growth: precipitate thickness varies proportionally to the square root of time, while the growth rate decays as the inverse square root of time. Although for the above derivation, a planar interface was assumed, the conclusions are broadly applicable for other instances of incoherent interface migration.

Growth is accompanied by the diffusion of solute atoms across the interface into the precipitate phase, where the concentration of solute must be higher. When diffusion through the bulk to the interface is the rate-limiting process, the growth is diffusion-controlled. The interface composition therefore is assumed to be the equilibrium one. In processes that do not involve a composition change but only interface motion, the boundary migration kinetics involve local atomic rearrangements as atoms jump from one grain to its neighbour. Such a

process is considered interface controlled. A combination of the two previous rate-controlling processes is termed as mixed-controlled growth. It is generally assumed that most precipitation phenomena occur at relatively high-temperature are diffusion-controlled and display a strong dependence on temperature. The diffusion rate follows an Arrhenius type of temperature behaviour given by:

$$D(\mathrm{T}) = D_0 \exp\left(-\frac{Q}{RT}\right) \tag{66}$$

Therefore, the diffusion rate increases with increasing temperature. However, the precipitate growth rate is also strongly affected by the undercooling: the higher the temperature, the lower the supersaturation ΔC_0. Considering the above, the temperature dependence of the rate of the overall transformation could be expressed by the following form:

$$R \propto (T_c - T)\exp\left(-\frac{Q}{RT}\right) \tag{67}$$

A schematic illustration of the temperature dependence of the overall transformation rate is shown in Figure 5.3. When the temperature is equal to the equilibrium temperature T_c, the new phase becomes thermodynamically stable as it results in the reduction of Gibbs free energy. As the temperature decreases below the T_c, the degree of undercooling increases and so does the thermodynamic driving force for nucleation of the new phase. Once an embryo has exceeded the critical size, *r**, and becomes a stable nucleus, its growth rate is enhanced by increasing the temperature considering that diffusion is activated.

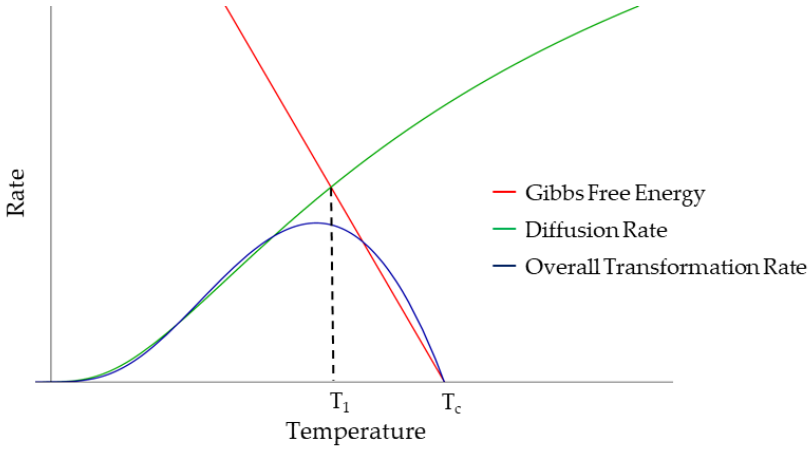


Figure 5.3: Schematic representation of the overall transformation rate as a function of temperature.

Therefore, the transformation rate is maximised at an intermediate temperature T_1, when the temperature is sufficiently low to promote nucleation and at the same time adequately high to activate the diffusion of solutes.

5.2.3. McLean Model of Growth

To predict the γ′ particle coarsening over service lifetimes in the case of relatively Al-rich nickel-base superalloys, McLean [20] considered two possible mechanisms, namely, diffusion-controlled growth (Eq. (68)) and interface-controlled reaction (Eq. (69)) corresponding to the following formulations:

$$r = [k(\, t - t_0)]^{1/3} \tag{68}$$

$$r = [k'(\, t' - t_0')]^{1/2} \tag{69}$$

where r is half the mean particle size, t is time and k is the growth rate, which was shown to follow an Arrhenius type of temperature behaviour:

$$k = \frac{2.3 \times 10^{15}}{\mathrm{T}} c \exp(-32520/\mathrm{T}) \tag{70}$$

Here c is the solute concentration in the matrix in wt%, i.e. the solid solubility of the diffusing element in equilibrium with a γ′ particle of infinite radius. McLean attempted to achieve an unambiguous discrimination between the growth laws to determine which theory describes best the long-term γ′ particle growth. By combining several experimental studies to cover a wide range of conditions, he managed to disprove the validity of one of the laws in the long term.

McLean's approach was developed to study the steady long-term particle growth, rather than the initial stages of nucleation and growth from supersaturated solid solution. The constant terms t_0 and t_0' in the above equations are used for time-zero adjustment. When fitting the plot of the experimental values of particle size versus time, t_0 is the intercept with the t axis and k the slope of the fitting curve. For large values of time the term t_0 becomes insignificant and may be reasonably omitted.

McLean's approach is in accordance to Herring [147] who showed by an elegant dimensional analysis that experimental studies can prove valuable in identifying the predominant mechanism responsible for the kinetics of a transformation. According to Herring, a linear dimension d characterizing the scale of a microstructural feature is given by the expression:

$$d^n = {d_0}^n + pGt \Leftrightarrow d = ({d_0}^n + aGt)^{1/n} \quad (71)$$

where d_0 is the value of d when $t = 0$, t is time, G is a parameter characterizing the kinetics of the appropriate mass transport mode, p is a dimensionless constant which depends on the geometry of the unstable phase, and the exponent n takes the following integral values depending on the mechanism controlling the kinetics of the process: $n = 1$ for viscous or plastic flow, $n = 2$ for interface reaction, $n = 3$ for volume diffusion in one or both phases, and $n = 4$ for interface diffusion.

The study performed by McLean showed that long term coarsening behaviour in several binary and ternary nickel-base superalloys largely follows diffusion-controlled growth behaviour. Figure 5.4 illustrates the experimental data investigated in McLean's study plotted according to the Eq. (68) (a) and Eq. (69) (b) corresponding to diffusion-controlled growth and interface-controlled reaction, respectively. For the latter, the curve is not linear, indicating that when Eq. (69) is tested over a wide range it does not hold in the case of nickel-base superalloys alloys containing γ' precipitate particles. However, for the initial stages of growth, scatter in experimental data generally makes it impossible to distinguish diffusion-controlled from interface-controlled growth, since data often fit $t^{1/3}$ and $t^{1/2}$ approximately equally well. When experimental data fail to follow one of the scaling laws of Herring, it is ascribed to more than one of the above mechanisms being operative over the range of sizes covered by the experiment. Therefore, in the initial stages of growth both the diffusion-controlled and the interface-controlled growth mechanisms are believed to be active, and the time exponent lies between the two extremes $1/3$ for the former and $1/2$ for the latter.

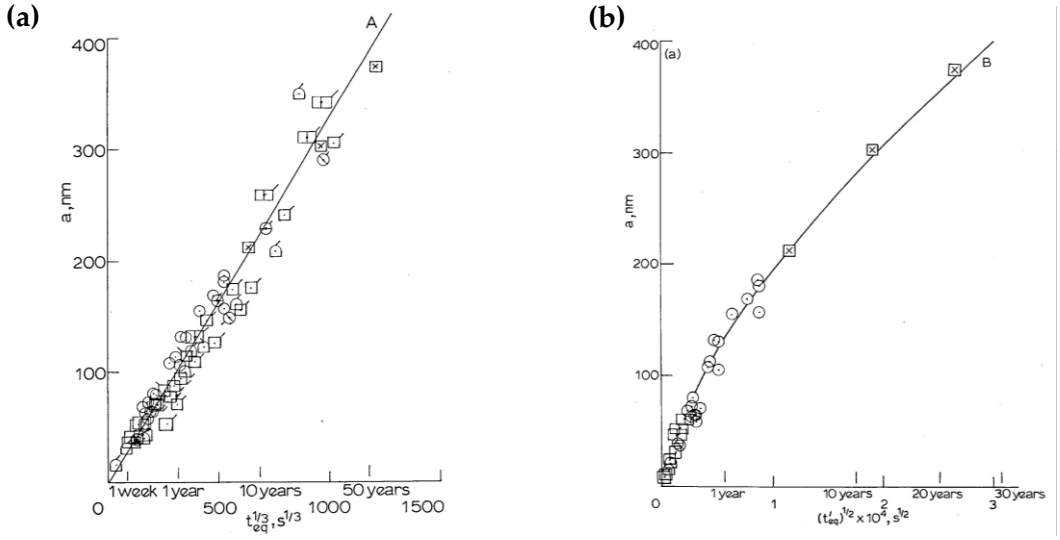


Figure 5.4: McLean's model fitted on experimental data (a) Diffusion-controlled growth, Eq.(68), (b) Interface-controlled growth, Eq.(69). Adapted from [20].

5.3. Materials and Methods

In this study, the effect of the cooling rate after solution heat treatment on the precipitate size distribution is investigated. The material analysed was obtained from a pancake forging of Alloy 11, produced by isothermally forging a powder isostatic pressed cylindrical compact. A detailed description of the alloy under consideration is provided in Chapter 1 (1.5). Miniature bar specimens with the nominal size of 40 x 2 x 1 mm^3, extracted from the forging by electro-discharge machining, were solution treated for 1 hour at 1180 °C, above the γ′ solvus of this alloy (≈1155 °C), and cooled at various rates ranging from 0.2 to 4 °C/s. Solution heat treatments with controlled cooling rates were carried out using an Electro-Thermo-Mechanical Testing (ETMT) system (Instron, High Wycombe, UK), in an argon atmosphere to minimise oxidation (Section 3.2.1).

In the ETMT system, sample heating was provided by passing current directly through it, and the temperature was monitored with a thermocouple spot-welded to the centre of the specimen, which was held in water cooled grips. The middle gauge section of each specimen was used for microstructural analysis, where the temperature was monitored by the thermocouple. The solution heat treatment was followed by ageing heat treatments, for 2 h at 850 °C and then for 4 h at 800 °C.

5.4. Experimental Results

Figure 5.5 illustrates the changes that occurred in the microstructure as a function of cooling rate. The size and distribution of precipitates as well as the morphology of grain boundaries were observed to be strongly dependent on the cooling rate from the super-solvus solution heat treatment. First and foremost, for slower cooling rates grain boundaries appear to be heavily serrated bowing around intergranular secondary γ′ particles and the degree of serration seems to drop with faster cooling. Apart from intergranular secondary γ′, carbides appear as the bright phases in the grain boundary region as well as in the grain interior. What is more interesting though is the strong refinement of secondary and tertiary γ′ precipitates with faster cooling rates.

Subsequent image analysis was carried out on the backscattered scanning electron (BSE) micrographs using ImageJ software (version 1.50e) to quantify the size of the secondary and tertiary γ′ precipitates. A detailed description of the procedure is described in Chapter 3 (Section 3.5.2).The results of quantitative image analysis are shown in Figure 5.6 which presents histograms of the probability distribution of the size of the γ′ precipitates for each cooling rate assessed. The precipitate populations appeared to conform to a bimodal size distribution indicating the presence of secondary and tertiary γ′ particles. The continuous lines denote a fit to the data where the left peak corresponds to the size distribution of tertiary γ′ and the right peak to that of secondary γ′ precipitates. The size distribution was fitted to a double-Gaussian function:

$$y = a_1\, e^{-\frac{1}{2}\left(\frac{d-\bar{d}_1}{\beta_1}\right)^2} + a_2\, e^{-\frac{1}{2}\left(\frac{d-\bar{d}_2}{\beta_2}\right)^2} \tag{72}$$

where $\bar{d}_1$, $\bar{d}_2$ are the mean diameters for tertiary and secondary γ′ precipitates in nm, respectively, β_1, β_2 are the standard deviations, and α_1, α_2 are the area ratios of the precipitates observed (Table 6).

Table 6: Parameters for the double-Gaussian fit for each cooling rate.

Cooling rate (°C/s)	$\bar{d}_1$	$\bar{d}_2$	β_1	β_2	α_1	α_2	R^2
0.2	66.98	362.8	12.79	175.5	414.2	50.94	0.9757
0.7	36.5	216.4	10.72	90.26	381.7	119.6	0.989
2	27.34	175.8	9.224	82.34	236.7	97.95	0.9854
4	13.37	96.83	1.806	52.17	116.8	116.1	0.8986

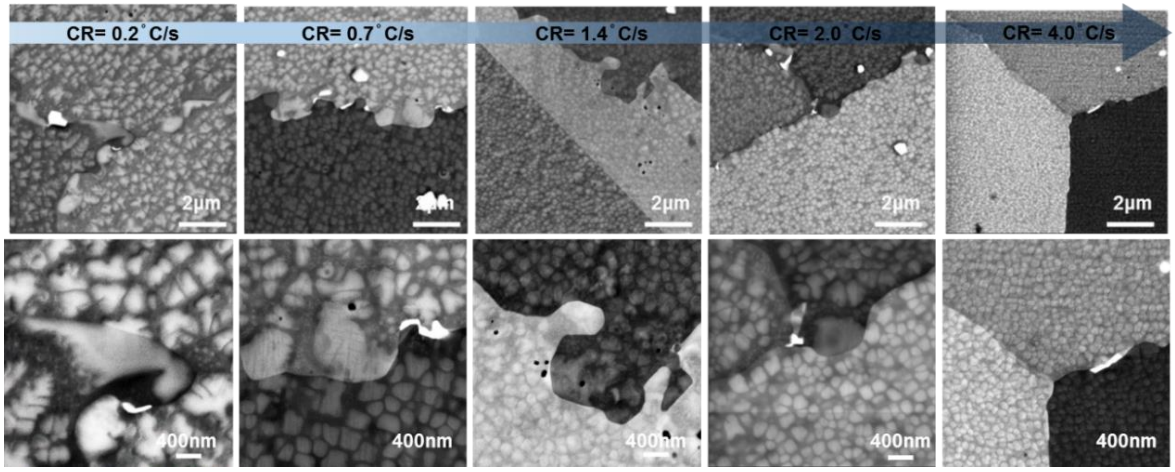


Figure 5.5: BSE images of the microstructures generated by different cooling rates.

The mean precipitate size is clearly highly sensitive to the cooling rate applied. Increasing the cooling rate from the super-solvus solution heat treatment temperature resulted in significant refinement of both the secondary and tertiary γ′ particles. The variation in the average size of the γ′ particles with the cooling rate is illustrated in Figure 5.6 (b), where the dotted curves represent a power law fit to the experimental data, given by:

$$d = A\,c^{-n} \tag{73}$$

where d is the average precipitate diameter (nm), c is the cooling rate from super-solvus solution temperature (°C/s), A is a constant that is different between the secondary ($A = 205.58$) and tertiary ($A = 31.183$) γ′ populations. The exponent n also differs between the secondary ($n = 0.437$) and the tertiary ($n = 0.498$) γ′ precipitates. The measured mean precipitate size data fitted very well with the power law curve, displaying a high correlation coefficient (R^2) value of ~0.95 over the cooling rate range.

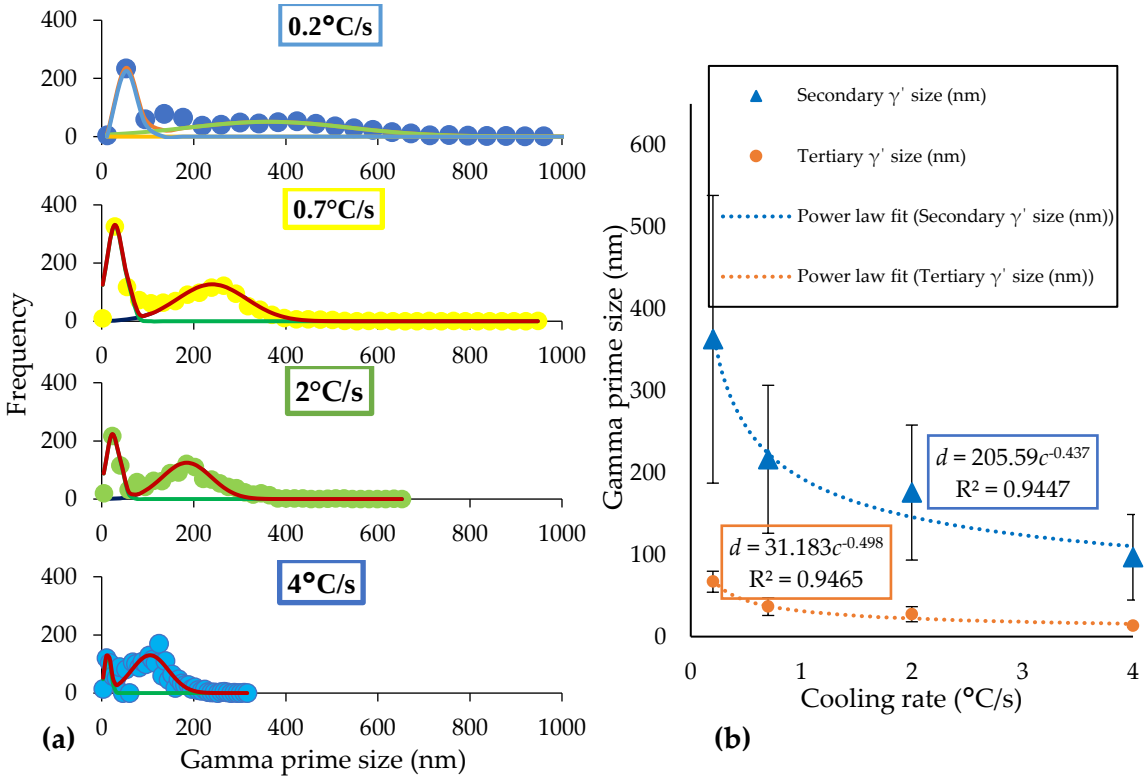


Figure 5.6: The variation in secondary and tertiary γ′ mean precipitate size with the cooling rate.

5.4.1. Derivation of the Correlation

The precipitation of the γ′ phase during cooling is driven by the local concentration gradients and involves redistribution of elements at the γ/γ′ interface, with the cooling rate determining the kinetics of the transformation. Indeed, the partitioning of elements between γ and γ′ precipitates and therefore the composition of each phase, is strongly affected by the cooling rate following solution heat treatment [15,52]. The composition of γ and γ′ phases determines their lattice parameters and thus the lattice misfit between the two faces, which in turn controls the morphology and size of precipitates [44], and thus the mechanical properties (Section 2.7.2). Previous studies have analytically and experimentally investigated the complex interactions between chemistry, process history, and γ′ morphology (e.g. [31,51-52]) and incorporated these factors into complex modelling [148]. In this approach, I deliberately did not focus my attention on the fine details of the chemical and mechanical processes that accompany the precipitate formation and population evolution, to eliminate the need to

calibrate for a large number of temperature-dependent material properties. By recasting McLean's theory to consider the effect of cooling rate rather than isothermal conditions, a simple correlation is derived, able to rationalise the experimental observations and explain the power law dependence of secondary and tertiary γ′ particle size on the cooling rate, based on well-established thermodynamic and kinetic principles. The derived model provides a useful expression that captures the correlation correctly despite its simplicity and can provide valuable predictions.

The peak temperature for precipitation T_1 corresponds to the maximum overall transformation rate K resulting from the competition between two opposing factors: (1) the thermodynamic driving force for nucleation determined by the degree of undercooling $\Delta T = T_c - T$, with T_c the equilibrium transformation temperature, so it decreases for higher temperatures; and (2) the diffusivity of the precipitating elements for the growth of the nucleus formed, which follows an Arrhenius-type temperature dependence, so it increases at higher temperatures. As discussed, K can be expressed in the following form:

$$K \propto (T_c - T)\exp\left(-\frac{Q}{RT}\right) \tag{74}$$

Thus, the maximum of the overall transformation rate occurs at an intermediate critical temperature T_1. For the purposes of simplified analysis, a convenient approximation of the temperature dependence of the overall transformation rate could be used in the form of a parabolic function, which reaches a maximum when $T = T_1$ (dashed line in Figure 5.7). The normalised temperature θ is introduced as:

$$\theta = \frac{T_c - T}{\Delta T} \tag{75}$$

where $\Delta T = T_c - T_1$. Following the parabolic approximation, the overall transformation rate can be then written in the form:

$$K(\theta) = 1 - (1-\theta)^2 \Rightarrow K(\theta) = \theta(2-\theta) \tag{76}$$

Assuming the cooling rate from the solution temperature to be constant, it holds that:

$$c = \frac{\mathrm{d}\theta}{\mathrm{d}t} \Rightarrow \theta = ct \tag{77}$$

Therefore, the overall transformation rate can be expressed as:

$$K(t) = ct(2 - ct) \tag{78}$$

In order to obtain predictions that can be compared to observations and justify the power law dependence of the precipitate size on the cooling rate, a re-derivation of McLean's theory for mean γ′ size [20] as a function of cooling rate was used. As described in the previous section (Section 5.2.3), the model developed by McLean can be used to predict the γ′ particle coarsening for nickel-base superalloys over service lifetimes, by considering two possible mechanisms for growth: diffusion-controlled growth and interface-controlled reaction. If the time-zero adjustment term t_0 is ignored, McLean's model for growth can be re-cast in the following form:

$$r = (k\ t)^{1/3} \Rightarrow r^3 = k\ t \tag{79}$$

$$r = (k'\ t)^{1/2} \Rightarrow r^2 = k'\ t' \tag{80}$$

So, the combination of Eq. (79) and (80) produces:

$$r^{\beta} = Kt, \beta \in [2,3] \tag{81}$$

$$\Leftrightarrow \dot{r} = \frac{1}{\beta} K r^{-(\beta-1)} \tag{82}$$

where the value of β typically lies between the two bounds, and the proximity to one of the extreme values reflects the dominance of a particular growth mode. The rate of the overall transformation, K, is temperature dependent as explained above. Substituting K from Eq. (78) into (82) gives:

$$\dot{r} = \frac{1}{\beta} ct(2 - ct)\ r^{-(\beta-1)} \tag{83}$$

Separating variables and integrating the above equation gives:

$$\int_0^R r^{(\beta-1)} dr = \int_0^{t_{max}} \frac{1}{\beta} ct(2 - ct)\ dt \Rightarrow \frac{R^{\beta}}{\beta} = \frac{4}{3\beta c} \Rightarrow R \propto c^{-1/\beta} \tag{84}$$

where $t_{max}$is the time when precipitate growth terminates (in the simplified description adopted here), i.e., when temperature reaches T_{min}, or $\theta = 2$. This allows the maximum

precipitate size R achieved after time t_{max} to be expressed as a function of β and c. Considering that $\beta \in [2,3]$, it can be concluded that the mean particle size exhibits a power law dependence on the cooling rate that can be expressed in the following form:

$$R = A\,c^{-n}, n \in [\frac{1}{3}, \frac{1}{2}] \begin{cases} n = \frac{1}{2} \rightarrow \text{interface controlled growth} \\ n = \frac{1}{3} \rightarrow \text{diffusion controlled growth} \end{cases} \quad (85)$$

It is apparent that the trend observed in the mean size of the secondary and tertiary γ′ precipitates measured by quantitative image analysis (Figure 5.6) is in good agreement with the predictions of the model described above. Additionally, as indicated in Eq. (85) the power law exponent n indicates the mechanism for growth. The growth of secondary γ′ appears to be controlled by a combination of diffusion-controlled and the interface-controlled mechanisms, with $n = 0.437$. However, in the case of tertiary γ′ precipitates $n = 0.498$ suggesting that the interface-controlled growth mechanism is predominant. For tertiary γ′ precipitates, the surface over volume ratio is high, promoting the growth to be interface controlled. Regarding the parameter A in Equation (85), it is probably an alloy-dependent constant with different values for the secondary and tertiary γ′ populations.

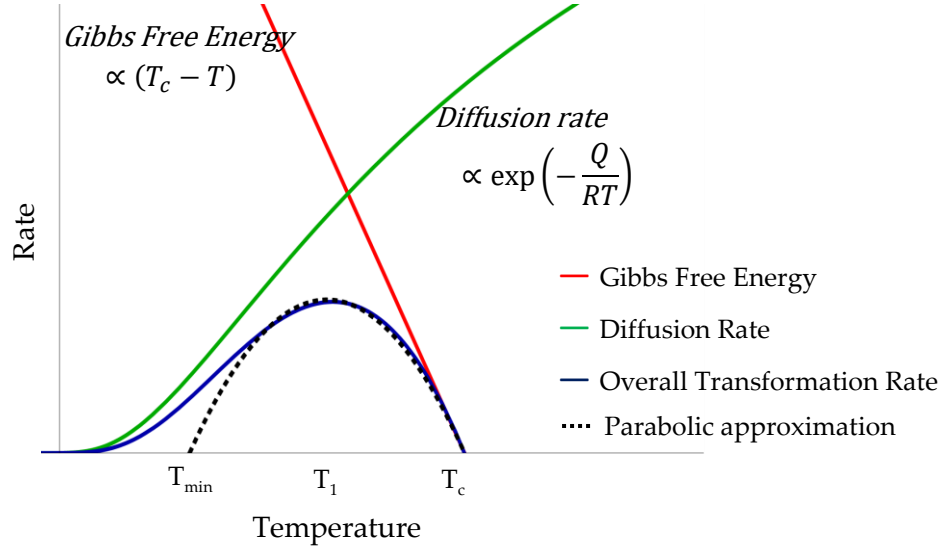


Figure 5.7: Illustration of the overall transformation rate as a function of temperature. The dashed line illustrates the parabolic approximation for the temperature dependence of the rate of the overall transformation. T_{min}: Assumed to be the minimum temperature below which the diffusivity is too slow for the transformation. T_1: Critical temperature for maximum overall transformation rate. T_c: Equilibrium transformation temperature for nucleation.

5.4.2. Intergranular γ′ Precipitates

As described in Section 2.2.2, slow cooling rate from super-solvus temperature has been associated with the precipitation of the intergranular γ′ precipitate population. Indeed, when slower cooling rates from the super-solvus solution temperature were applied the formation of secondary γ′ precipitates at the grain boundary region was observed (Figure 5.8) distorting the grain boundary morphology and introducing serrations. In this section, observations on the morphology of intergranular γ′ particles are presented, and an attempt is made to correlate the size of this population with the applied cooling rate from super-solvus temperature.

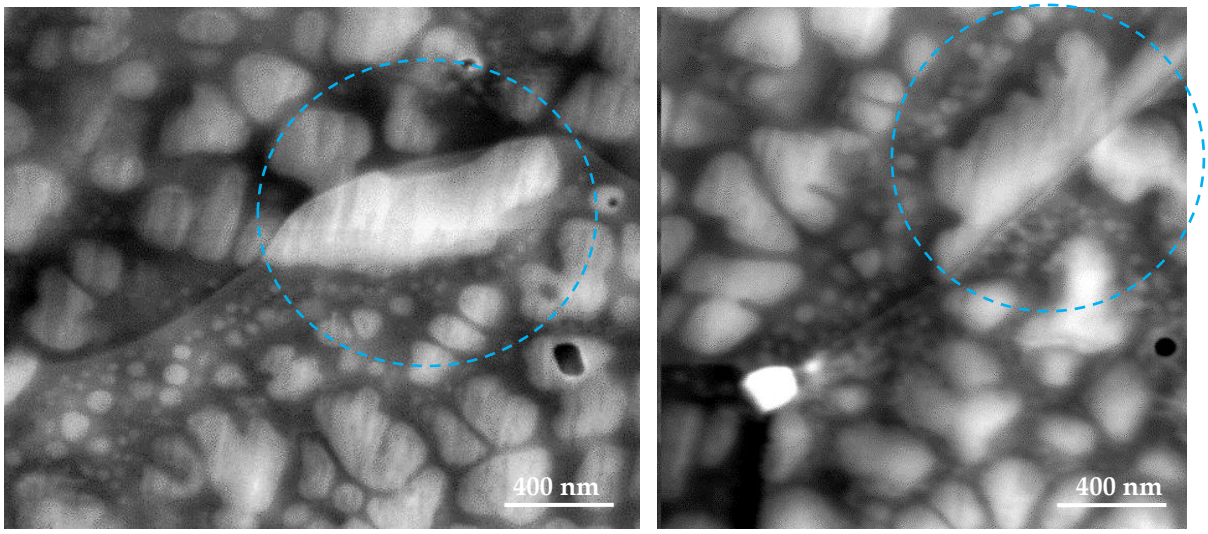


Figure 5.8: BSE images of the intergranular secondary γ′ particles formed during slow cooling (0.7 °C/s).

Dependence of the Intergranular Precipitate Size on the Cooling Rate

Following the procedure explained in Section 3.5.2, quantitative image analysis was performed to quantify the variation in the intergranular secondary γ′ precipitate size with cooling rate. In this analysis only the population of the grain boundary γ′ precipitates which differs significantly in terms of size and shape from the intragranular secondary γ′ was considered (circled in Figure 5.8) produced after slow and intermediate cooling rates. The quantitative image analysis showed that the mean precipitate size of this population has also

a power law dependence on the cooling rate from super-solvus solution temperature (Figure 5.9). It should be noted that the volume fraction of intergranular secondary γ′ precipitates is lower than that of secondary and tertiary γ′ precipitates distributed in the grain interior. To reduce the uncertainty and make the results more statistically significant, a population of 100 intergranular precipitates was measured for each cooling rate compared to 1500 precipitates for each of the intragranular populations. Although the error in terms of the quantitative values could be higher for the intergranular γ′ precipitates, the observed trend is believed to be valid.

The derived model outlined in the previous section (5.4.1) can explain the power law dependence of the size of secondary and tertiary γ′ particles on the cooling rate from solution temperature in a simple yet accurate way. To extend the proposed model to include the case of grain boundary γ′ precipitates the coarsening behaviour of intergranular precipitates is first examined. Svoboda et al. [150] proposed a model for the coarsening behaviour of intergranular precipitates in multicomponent systems using evolution equations for individual precipitates within a mean-field approach. The growth low derived in this study supports that the size of intergranular precipitates is proportional to $t^{1/4}$ (t is time). As discussed, according to the scaling laws developed by Herring et al. [147] a linear dimension d of a microstructural feature is proportional to $t^{1/n}$ and the value of the exponent n indicates the mechanism controlling the kinetics of the process; when $n = 4$, the growth process is dominated by interface diffusion. Accordingly, the model proposed in this study could be extended, if in Eq. (85) $\beta = 4$ and therefore:

$$R = A\, c^{-n} \begin{cases} n = 1/2 \rightarrow \text{interface controlled growth} \\ n = 1/3 \rightarrow \text{diffusion controlled growth} \\ n = 1/4 \rightarrow \text{interface diffusion growth} \end{cases} \tag{86}$$

By fitting the experimental observations, the value of the power law n for intergranular γ′ particles was found to be $n = 0.306$ (Figure 5.9). Only the slow and intermediate cooling rates were considered when the intergranular secondary γ′ population was formed.

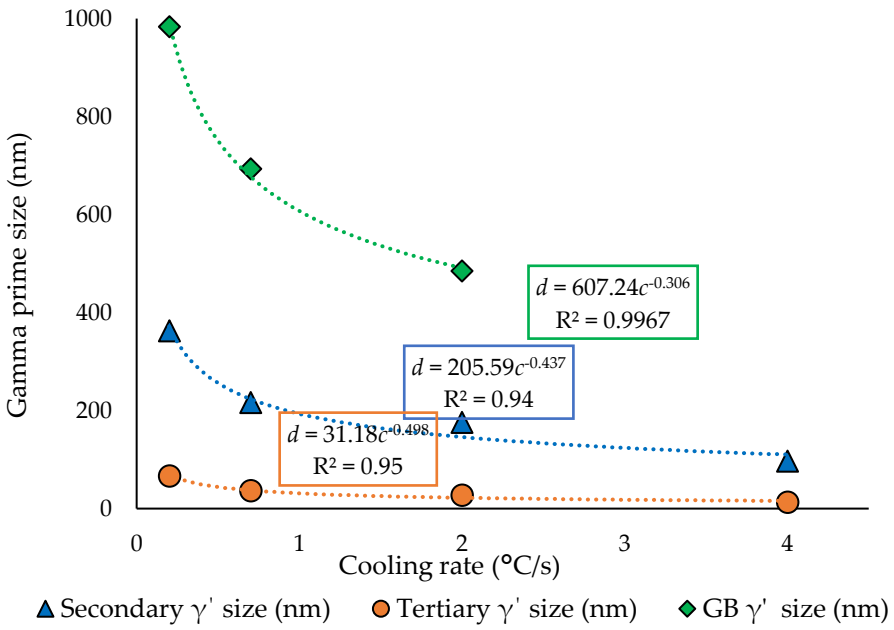


Figure 5.9: The variation in the intergranular precipitate size with cooling rate compared to secondary and tertiary γ′ mean precipitate size.

This observation indicates that the growth of intergranular γ′ precipitates follows a different mechanism than that of intragranular particles. For tertiary γ′ precipitates $n = 0.498$ suggesting that the interface-controlled growth mechanism is predominant. Regarding the secondary γ′, the growth is controlled by a combination of diffusion-controlled and interface-controlled mechanisms, as the value of n lies between the two bounds. It appears that the same applies to intergranular γ′ particles with the value of n lying between two bounds. In this case, the growth of intergranular γ′ precipitates is a result of the combination of diffusion controlled growth and interface diffusion growth, being assisted by the presence of the grain boundary that serves as a path for faster diffusion.

5.5. Discussion

5.5.1. The Effect of Ageing Heat Treatment

In the present study, the samples were exposed to consistent ageing heat treatment after cooling from solution temperature at different rates. Various theories have been developed to describe the effect of ageing and long-term isothermal exposure to the precipitate distribution function. The Lifshitz-Slyozof-Wagner (LSW) theory [56] was developed to model the kinetics of growth in a supersaturated solid solution and has been applied to model the diffusion-controlled Ostwald ripening of the γ′ precipitate particles in nickel-base superalloys [149]. According to the classical LSW theory, the average precipitate radius r is predicted to increase with time, such that $r^3 \propto t$, whereas the precipitate distribution function is declared to be time independent: the particle radius distribution was found to be self-similar under the scaling of the average particle size. Hopgood et al. [151] compared the experimentally determined values for the precipitate size and the theoretical distributions predicted by LSW theory. They found that after short ageing times there was good connection between the shapes of the experimental distributions and those predicted.

McLean [20] examined literature data on the precipitate size distributions after isothermal exposure for binary, ternary, and commercial nickel-base superalloys. The literature data was analysed on the basis of equivalent time (t_{eq}) calculated for a chosen equivalent temperature (T_{eq}). By plotting the precipitate size distributions at the beginning of the process, after considerable growth and at the end of t_{eq}, the error introduced by regarding the precipitate size distribution as steady state was minor, as the change in distribution was very sluggish compared to the growth of the average precipitate size.

From the aforementioned studies [20,56,151], it can be inferred that after the ageing heat treatment, the size distribution of the γ′ precipitates would shift towards a larger mean size, but the overall pattern would remain unaltered. The effect of ageing heat treatment on this pattern may be minor compared to the effect of the cooling rate, and thus the observed pattern is fully attributed to the cooling rate from the super-solvus solution heat treatment.

5.5.2. Comparison with Literature

The power law dependence of the size of γ′ particles on the cooling rate from solution temperature has been observed and reported previously. In this study, the experimentally observed trend was justified and explained by the derived model outlined in the previous section (5.4.1). Table 7 summarizes the formulas suggested by previous researchers mainly focused on the variation of the size of secondary γ′ precipitates. First, regarding the value of the power law exponent n it appears to lie in the range predicted from the derived model. This provides a strong validation for the generic correlation given in Eq. (85). The value of the parameter A in Eq. (85) is a constant that was observed to differ for secondary and tertiary γ′ populations, and apparently is different for different alloy systems.

Table 7: Power law dependence of the size of γ′ particles on the cooling rate from the literature.

Authors [Ref]	Material	A	n
Furrer et al. [28]	U720Li	442.5	0.4605
Vaunois et al. [29]	U720Li	840.88	0.3113
Laurence et al. [30]	R65	364.74	0.3977
Masoumi et al. [31]	AD730TM	521	0.44

In order to provide a further verification, the derived model is used to estimate the size of secondary γ′ precipitates of the nickel-base superalloy RR1000 for different cooling rates and the estimations are compared to available experimental observations reported in the literature. This specific alloy system is chosen as it has been extensively studied by previous researchers. Mitchel et al. [52] investigated the influence of cooling rate after super-solvus heat treatment on the microstructure of RR1000. The size of secondary γ′ precipitates produced under furnace cooling (0.1 °C/s) and intermediate cooling (≈1 °C/s) corresponds to approximately 460 nm and 185 nm respectively. Using the ab Eq. (85) one can estimate the values for the parameters A and n for RR1000 which are approximately $A = 185$ and n= 0.4. Therefore, for the air cooling (≈15 °C/s) the size of the secondary γ′ precipitates estimated to be equal to approximately 63 nm, which is in the vicinity of the value measured and reported

in the same paper (≈55 nm). Of course, this is a rough estimation which could be further refined and optimised for each alloy system, but it could still be used as an indication for the size range.

5.6. Conclusions

To summarise, in this study, changes in terms of size of γ′ precipitates in a polycrystalline nickel-base superalloy, Alloy 11, were investigated after super-solvus heat treatment with various controlled cooling rates. Through quantitative image analysis, I observed that the variation in secondary and tertiary γ′ precipitate size had a power law dependence on the cooling rate from super-solvus solution temperature. This trend was interpreted by a simplified model based on the McLean theory of growth of γ′ in nickel alloys. During cooling from the solution temperature, the growth of secondary γ′ is controlled by a combination of diffusion-controlled and interface-controlled mechanisms, and the growth of tertiary γ′ is primarily controlled by the interface-controlled mechanism. The case of intergranular secondary γ′ precipitates was also examined, for which there is a combination of diffusion-controlled growth and interface diffusion growth. The primary contribution of this model is the identification of a simple correlation between the γ′ precipitate size and the cooling rate, with which useful insights and predictions can be obtained, even without knowing the large number of temperature-dependent material properties required for complex modelling.

6

Room temperature HR-STEM analysis of the structural and compositional variations between precipitate populations

6.1. Introduction

In new high γ′ content nickel-base superalloys, during slow cooling from super-solvus solution heat treatment, secondary γ′ often precipitates at the grain boundary region forming the intergranular γ′ precipitate population, or grain boundary γ′ (GB γ′). The formation of this population has been associated with grain boundary serrations, and thus it is believed to be beneficial prolonging the creep life (see Section 2.2.2 and 2.7.3).

Intergranular secondary γ′ precipitates differ in size and morphology from the precipitates in the grain interior. However, their structure, in terms of lattice misfit with the matrix and elemental composition is still not well characterised. To increase the understanding on the mechanism behind the formation of serrations and the role of the intergranular γ′ precipitate population, a detailed local characterisation at the grain boundary region is required.

In this Chapter, the structural and compositional variations between different γ′ precipitate populations are investigated using scanning transmission electron microscopy

(STEM). In the first part of this study, variations in the lattice parameters of the two populations are detected and related to compositional variations unveiled by high-resolution scanning transmission electron microscopy imaging (HR-STEM) combined with energy-dispersive X-ray spectroscopy (STEM-EDX) analysis. Additionally, a boride phase is detected at the grain boundary region, its type is identified and its role on the grain boundary serrations and the formation of intergranular γ′ is discussed.

6.2. Experimental Method

The material in this study was obtained from a pancake forging of Alloy 11, produced by isothermally forging a powder isostatic pressed cylindrical compact. A detailed description of the alloy under consideration is provided in Chapter 1 (1.5). Miniature specimens extracted from the forging by electro-discharge machining, were solution treated for 1 hour at 1180 °C, above the γ′ solvus of this alloy (≈1155 °C), and furnace cooled. The cooling rate from solution temperature (1180 °C) to 1000 °C (below the γ′ solvus) was approximately linear and equal to 0.6 °C/s, as the temperature was monitored by a thermocouple attached on the specimen. The solution heat treatment was followed by ageing heat treatments, for 2 h at 850 °C and then for 4 h at 800 °C.

High-resolution scanning transmission electron microscopy was performed using the JEOL ARM200F microscope and the JEOL Centurio Silicon Drift Detector (SDD) housed in the electron Physical Science Imaging Centre (ePSIC) at Harwell Campus. Site-specific TEM lamellae samples of thickness less than 100 nm were prepared with the standard FIB lift-out technique in Multi Beam Laboratory for Engineering Microscopy (MBLEM, Oxford). To facilitate the observation of the superlattice structure of the γ′ precipitates the lamella samples were prepared oriented in the [001] zone axis along the normal direction. To that end, the grain from which the lamellae were lifted was first carefully selected after an electron backscatter diffraction (EBSD) analysis on the surface of the specimen. The step-by-step process is described in detail in Chapter 3 (Section 3.7.3).

For imaging, the bright field (BF), annular dark-field (ADF) and high-angle annular dark-field (HAADF) detectors were utilised using a condenser lens aperture size of 30 µm while the camera length was set to 3 cm. Simultaneous STEM-EDX analysis was performed for elemental mapping to obtain synchronous compositional information. For the data analysis of the EDX spectrums, the HyperSpy toolbox was utilised. HyperSpy is an open-source Python library which provides tools to facilitate the interactive data analysis of multi-dimensional datasets [152]. Additionally, HyperSpy provides easy access to several 'machine learning' algorithms that can be useful when analysing multi-dimensional data, such as STEM-EDX spectrum images. In this study, non-negative matrix factorisation (NMF) algorithm was used for mapping the measured STEM-EDX spectrum which is a popular decomposition method that forces the components to be strictly non-negative to aid the physical interpretation of components.

6.3. Experimental Results

The STEM images in Figure 6.1 present low magnification images of the microstructure of the specimen investigated in BF (Figure 6.1(a)) and HAADF (Figure 6.1(b)) modes. Despite the FIB induced damage and the so-called curtaining effect introduced during the site-specific sample preparation, a close examination of the images can provide valuable information on the microstructural features included. Various neighbouring grains are depicted with secondary γ′ precipitates distributed in the grain interior and a large intergranular secondary γ′ precipitate formed at the grain boundary. The grain boundaries exhibit a serrated morphology, and their distortion seems to follow a phase that appears dark in the bright-field STEM and bright in HAADF indicating a strong difference in its atomic number (Z). This intergranular phase which is most probably one of the typical carbide or boride phases preferably resides at the grain boundary triple junctions. It is also interesting to note that this grain boundary phase neighbours with large intergranular secondary γ′ precipitates. In fact,

both of the intergranular secondary γ′ particles detected in the region of interest are adjacent to the grain boundary phase.

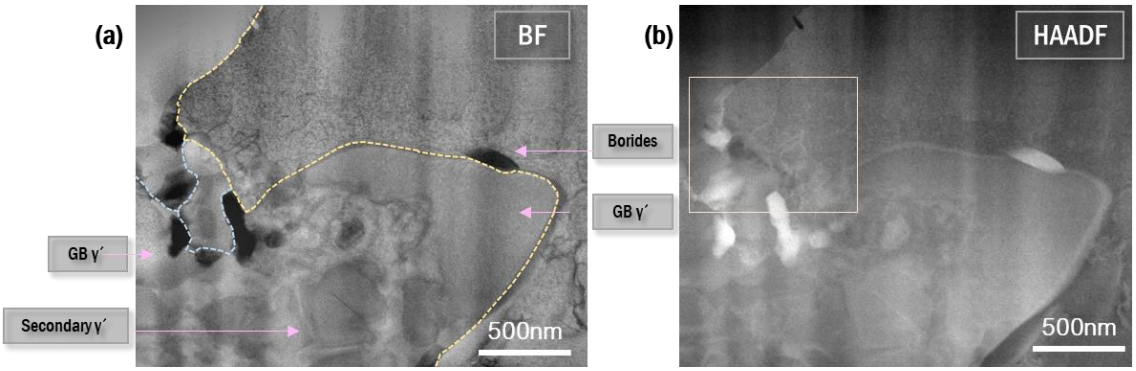


Figure 6.1: (a) BF-STEM image and **(b)** HAADF-STEM image of the region of interest.

6.3.1. Quantitative HR-STEM Analysis of γ′ Precipitate Populations

The lattice fringes in HR-STEM images were used to perform interplanar spacing measurements to detect any variations among the lattice parameters of the different populations of γ′ precipitates. A commonly used method was employed for measuring lattice spacing with high precision involving the Fast Fourier Transform (FFT) of the HR-STEM images. In this practical method, an aperture is placed on selected points of the power spectrum in the FFT of the input HR-STEM image and then the inverse FFT is calculated and used for the interplanar spacing measurements. This method is straightforward and provides various advantages, along with its accessibility and fast estimations [153]. Nonetheless, the results must be interpreted with caution and a number of limitations should be borne in mind. It has been reported that in the case of small nanoparticles (with diameter ≤3 nm), artifacts arising from edge effects and particle tilt may result in inaccurate measurements, with errors even up to 10% [154]. In that case, to obtain accurate and reliable measurements a large number of particles should be analysed which for picometer precision should be in the range of ~100 particles [155]. Since the particles investigated in this study are considerably larger (see Figure 6.1), I assume that the error involved from tiling or edge effects is insignificant.

First and foremost, to study the features of interest accurately, the major internal structure and the exact viewing direction have to be determined [155]. The γ′ phase displays a cubic, ordered $L1_2$ crystal structure with nickel atoms at the centres of the faces and aluminium atoms at the cube corners of the lattice [9]. The simulated structure of Ni_3Al derived using the software packages CrystalMaker and SingleCrystal is illustrated in Figure 6.2 (a) and its reciprocal lattice is shown in (b). A careful examination of the FFT of the HR-STEM image in Figure 6.2 unveils some weak diffraction spots which correspond to the superlattice structure of the γ′ precipitate phase. As shown in Figure 6.2 (e), the simulation of the Ni_3Al structure matches the FFT of the HR-STEM image for the viewing direction (002).

The interplanar spacing of intergranular and intragranular secondary γ′ precipitates can be determined. The steps involved in the procedure outlined briefly above, are explained in detail in Figure 6.3. The first two steps involve the acquisition of the HR-STEM image and the calculation of its FFT. In Step 3, an aperture is placed on the strong diffraction spots indexed as $(0\bar{2}2)$ and (022) in the FFT, to exclude any other periodicity other than the interplanar spacing of the cubic lattice. In Step 4, the inverse FFT produces an image which is intermediate between direct and reciprocal space and contains localised information about periodicities. This image is then used in Step 5 to measure the lattice spacings for the different populations of γ′ precipitates.

In Table 8, the measurements obtained using the methodology described above are summarised, comparing the interplanar d_{002} spacing and the lattice parameter of intergranular secondary γ′ formed at the grain boundary region and the intragranular secondary γ′ located in the grain interior. In the analysis, the interplanar spacings of three (3) γ′ particles were measured and averaged for each population, from more than twenty (20) HR-STEM images with magnification ranging between x60,000-x100,000 in each case. The measurements displayed a noticeable consistency for each population.

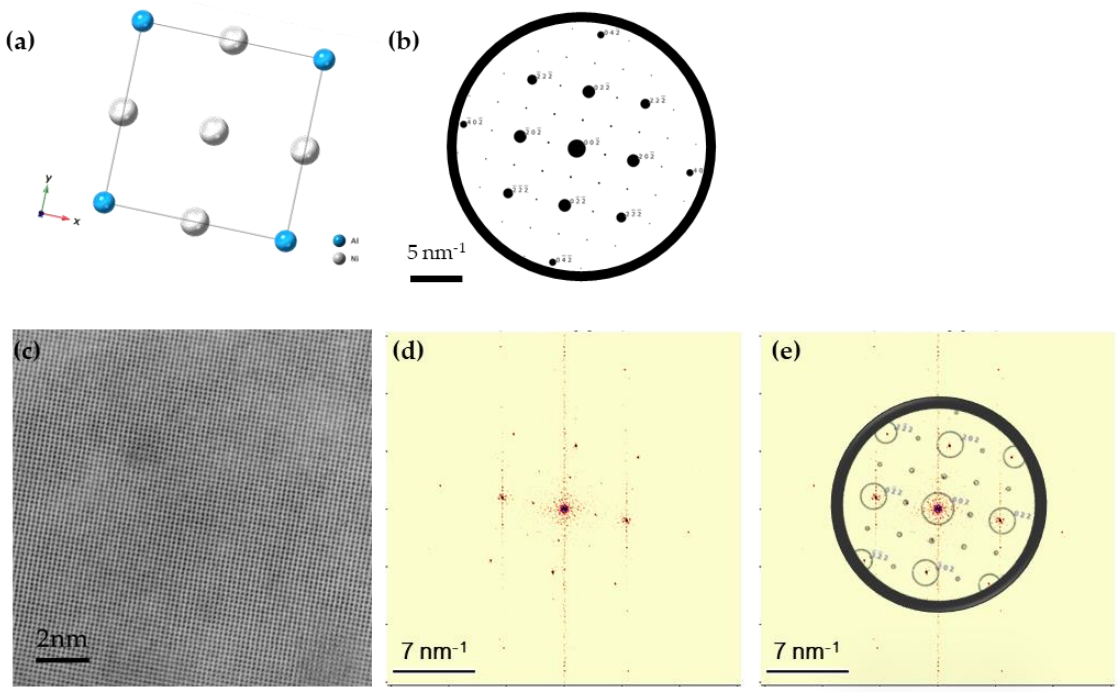


Figure 6.2: (a) Simulated structure of Ni_3Al, **(b)** Weighted reciprocal lattice of (a) in the viewing direction (002), **(c)** HR-STEM image of a secondary γ′ precipitate, **(d)** FFT of the HR-STEM image in (c), **(e)** Superimposed (b) on (d).

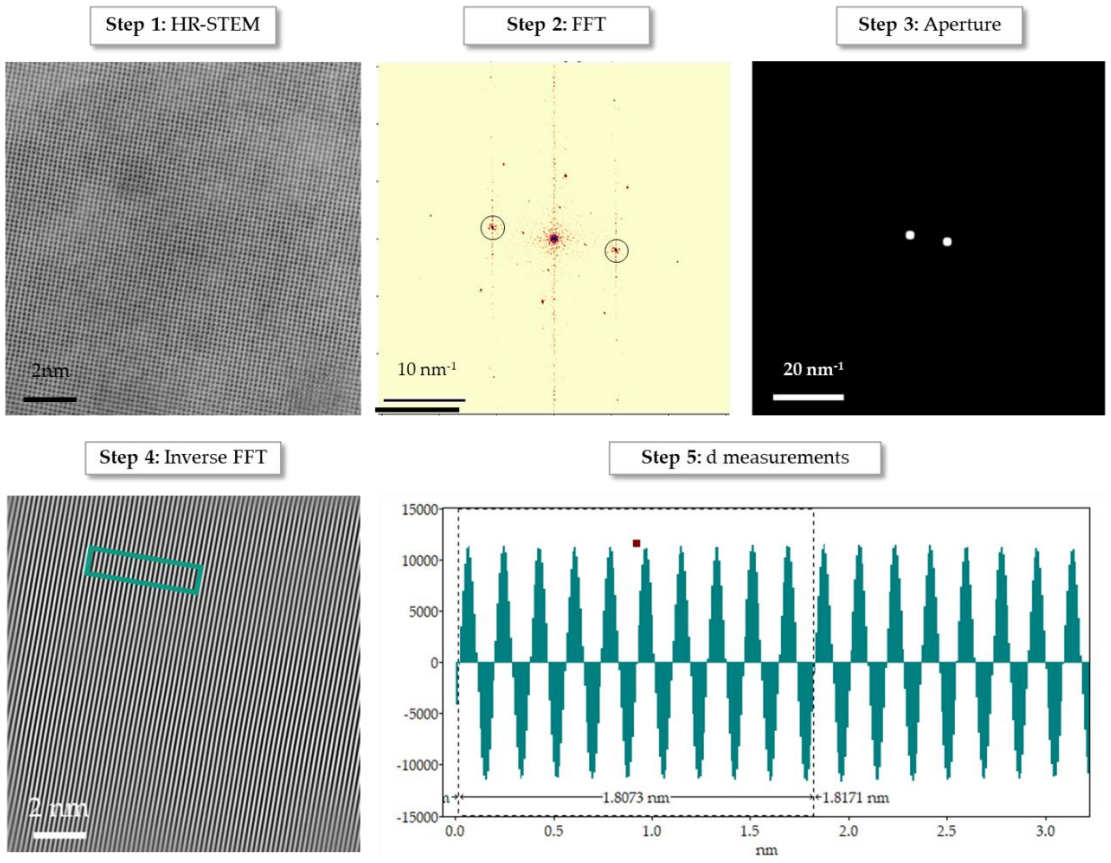


Figure 6.3: Steps involved in the procedure of determining the interplanar spacing of intergranular and intragranular secondary γ′ precipitates.

Table 8: Measurements of the interplanar spacing obtained by quantitative analysis of HR-STEM images.

	d Interplanar Spacing [Å]	Lattice Parameter {002} [Å]	Misfit (%)
GB γ′	1.831	3.662	0.88
Secondary γ′	1.813	3.625	-0.14
Matrix γ	1.815	3.630	

The obtained observations provide a strong indication that the lattice parameter of the intergranular secondary γ′ differs from that of intragranular with the former being larger than the latter. To further increase the accuracy of the measurements and make a confident claim for the quantitative value of γ/γ′ lattice misfit additional measurements are needed considering the error propagation introduced for the lattice misfit estimation.

The observed variation in the lattice spacings between intergranular and intragranular secondary γ′ could originate by elemental variations between the two populations affecting their lattice parameters. To that end, a STEM-EDX analysis was performed to detect any compositional variations between grain boundary γ′ and secondary γ′ in grain interior. For the analysis of the EDX spectrum, the HyperSpy toolbox was used.

Figure 6.4 (a) displays the region of interest that contains part of a large intergranular γ′ particle pinned at the grain boundary as well as some secondary γ′ precipitates distributed in the grain interior. The compositional map in Figure 6.4 (b) corresponds to the Ni-Ka peak and the colour contrast represents the relative difference in nickel content between the two populations. It is apparent that there are profound variations in the nickel content between the populations with intergranular γ′ precipitate being enriched in nickel compared to the intragranular secondary γ′. In Figure 6.4 (c), the line profile of the rectangular region shown in Figure 6.4 (b) is displayed. Apart from nickel, the GB γ′ seems to be enriched in Ta, Ti, and Al, compared to intragranular secondary γ′. Additionally, the content of Fe and W is observed to be slightly higher in intergranular γ′. These experimental observations provide valuable information on the compositional variations between the intergranular and intragranular γ′

populations. The diffusion of larger sized atoms (such as Ti, W and Ni) into the grain boundary γ′, could explain the variation in their lattice parameter.

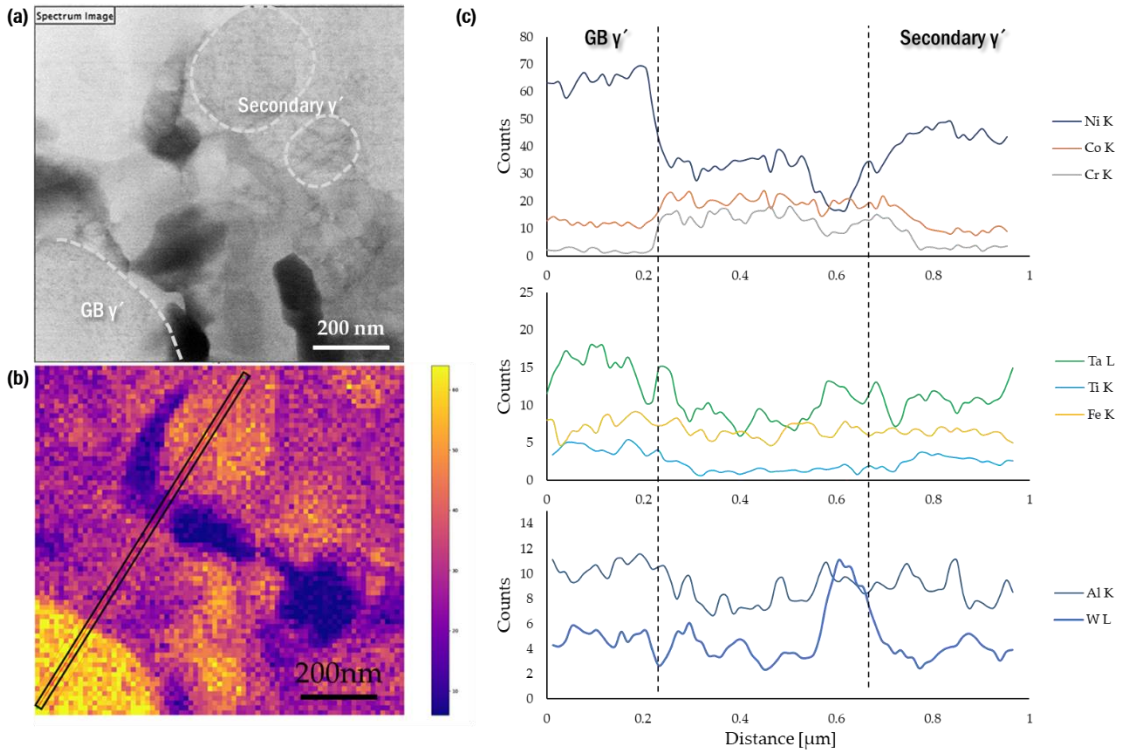


Figure 6.4: (a) BF image of the region of interest. **(b)** Compositional map of the Ni-Ka peak of the EDX spectrum. **(c)** Line profiles of the region highlighted in image b.

6.3.2. Boride Phase Identification

Apart from the intergranular γ′ precipitates, the grain boundary region is decorated by various microstructural features that appear dark in the bright-field STEM, and bright in HAADF. In the alloy under consideration, the boron content is 0.12 at. % and the carbide content is 0.13 at.% so the precipitation of boride and carbide phases is promoted. Small amounts of carbon and boron are traditionally added in nickel-base superalloys to promote the formation of fine spaced carbide and boride phases at the grain boundaries due to their beneficial effect on mechanical properties (Section 2.7.4).

The bright contrast of the grain boundary phase in the HAADF image in Figure 6.1 (b) indicates its relatively higher average atomic number (Z) compared with the matrix [156]. To

identify the elemental composition of the grain boundary phases a STEM-EDX analysis was performed (the region is highlighted with a rectangle in Figure 6.1). Figure 6.5 portrays the spectrum obtained by the STEM-EDX analysis, decomposed into three components: the matrix, the γ′ precipitates and the grain boundary phase using the NMF decomposition algorithm in HyperSpy. Regarding the matrix and the precipitate phases, they demonstrate their known elemental distribution enhanced in Co, Cr and Al, Ti respectively. Additionally, artificial Cu signals have been induced to the spectrum due to the copper grid on which the TEM lamellae samples were mounted. Regarding the intergranular phase, it is enriched in Cr, Mo, and W. The elemental distributions of Cr, Mo, and W are depicted in the compositional maps in Figure 6.6. Undoubtedly, the content of these elements is enhanced in the intergranular phase. Interestingly though, there are profound variations between the intergranular particles, particularly in terms of their chromium and molybdenum content.

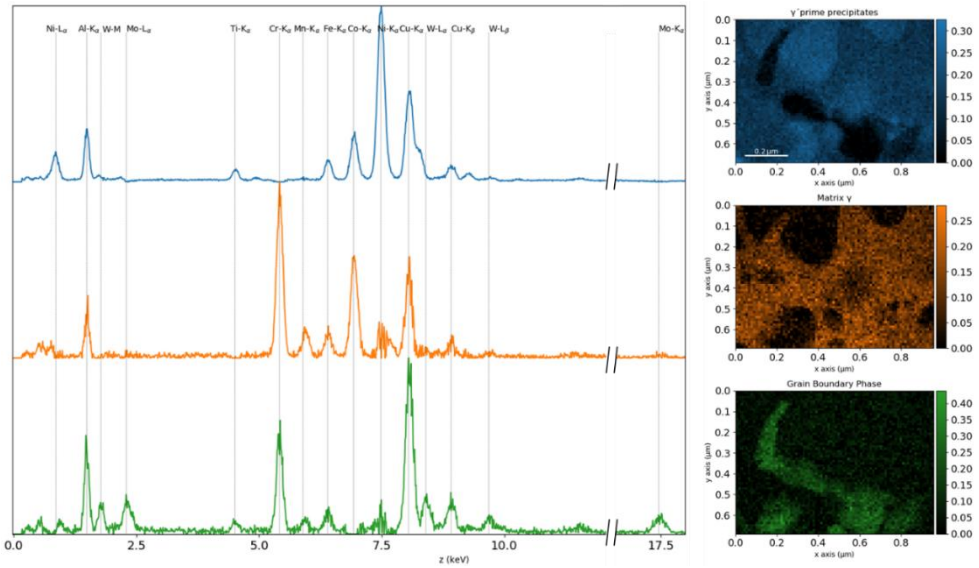


Figure 6.5: STEM-EDX spectrum decomposed into three components: the matrix, the γ′ precipitates and the grain boundary phase.

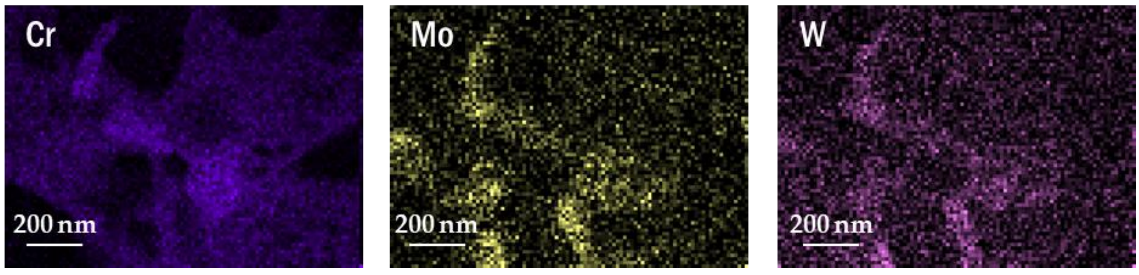


Figure 6.6: Compositional maps of the Cr-K, Mo-K and W-L peaks of the EDX spectrum.

However, this information is not adequate to characterise and identify the observed phase. The detection and analysis of the boron and carbon peaks was not achieved because of the inherent limitation of the EDX to obtain information of light elements due to their low photon energy peaks. Among the commonly observed phases in nickel-base superalloys, there are various carbide and boride types with different structure and stoichiometry. Boron can combine with elements such as molybdenum, titanium, chromium, and nickel to form borides, and the most common boride types in nickel-base superalloys include M_5B_3, M_3B_2 and M_2B, where M denotes metal atoms [80]. Regarding carbides, primary MC carbides precipitate at high temperatures from the liquid phase and they are usually enriched in Ti, Ta and/or Hf [7]. Upon the subsequent thermal exposure, the primary carbides often decompose into M_6C and $M_{23}C_6$ carbides. The $M_{23}C_6$ carbide is a Cr-rich phase with a complex FCC structure, which contains metallic elements, such as Co, Mo and Ni (Section 2.5).

Therefore, since it is not straightforward to chemically discriminate between possible carbide and boride phases with EDX, the structure of the observed phase was investigated with the analysis of HR-STEM images. The structure of the intergranular phase observed experimentally (Figure 6.8 (a), (b)) is compared with the simulated structure of binary carbide and boride structures, derived using the software packages CrystalMaker and SingleCrystal. Table 9 summarises basic crystallographic information of binary borides and carbides, displaying M_5B_3, M_3B_2 and M_2B and $M_{23}C_6$ structures illustrated in Figure 6.7 in the (002) projection.

Table 9: Crystallographic information of binary M_5B_3, M_3B_2 and M_2B and $M_{23}C_6$ structures.

Structure	Space Group	Crystal System	a[Å]	c [Å]
Cr_5B_3	I 4/mcm	Tetragonal	5.480	10.01
V_3B_2	P 4/mbm	Tetragonal	5.728	3.026
W_2B	I 4/mcm	Tetragonal	5.568	4.744
Cr_2B	I 4/mcm	Tetragonal	5.185	4.316
$Cr_{23}C_6$	$Fm\bar{3}m$	Cubic	10.64	10.64

The interplanar spacing of the observed intergranular phase was determined using a series of HR-STEM images and their corresponding FFT patterns. According to the measurements obtained following the methodology described in Figure 6.3 the lattice parameter of the grain boundary phase detected was measured to be equal to 5.64 Å approximately. Therefore, assuming that the measured value should be in the vicinity of the lattice parameter of the binary systems obtained by the simulation, the intergranular phase cannot be a carbide, considering the deviation between the values. Hence, the intergranular phase is believed to be a boride.

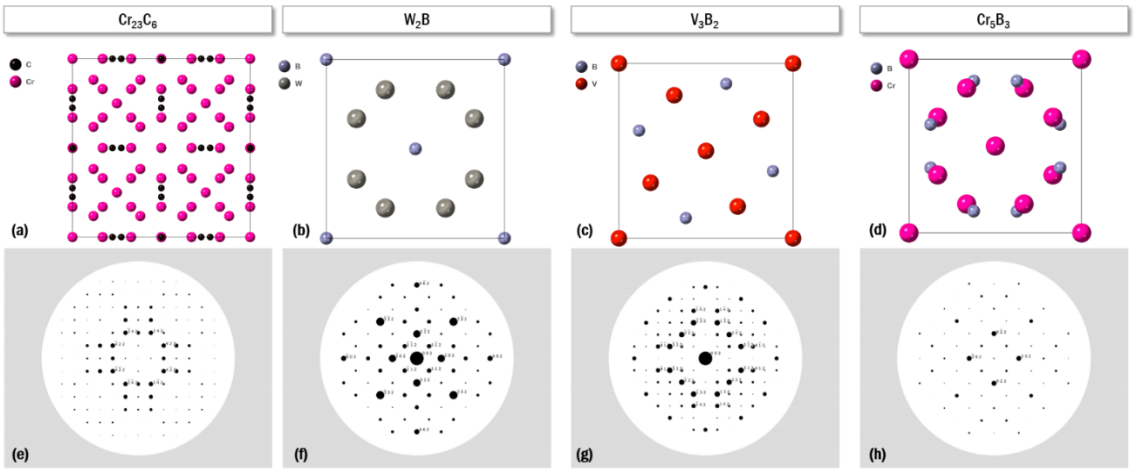


Figure 6.7: **(a)** $Cr_{23}C_6$ carbide structure, **(b)** W_2B boride structure, **(c)** V_3B_2 boride structure, **(d)** Cr_5B_3 boride structure, all of the structures are displayed in (002) projection. **(e-h)** Weighted reciprocal lattice of images (a-d).

To determine the exact type of the boride phase, the FFT of HR-STEM images is compared with the simulated reciprocal lattice of binary boride structures, both in terms of the symmetry and of d-spacings. Using the method of exclusion, the other possible candidates are eliminated (e.g. Figure 6.8) and the grain boundary boride was identified as M_2B as shown in Figure 6.9.

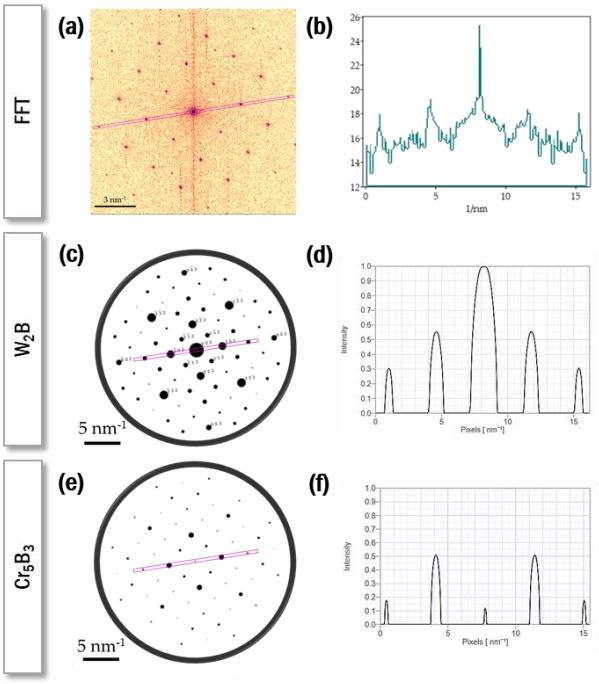


Figure 6.8: (a) FFT of HR-STEM image of the intergranular boride phase, **(b)** Line profile of the highlighted region in image (a), **(c)** Weighted reciprocal lattice of simulated structure of W_2B in the viewing direction (002), **(d)** Line profile of the highlighted region in image (c), **(e)** Weighted reciprocal lattice of simulated structure of Cr_5B_6 in the viewing direction (002), **(f)** Line profile of the highlighted region in image (e).

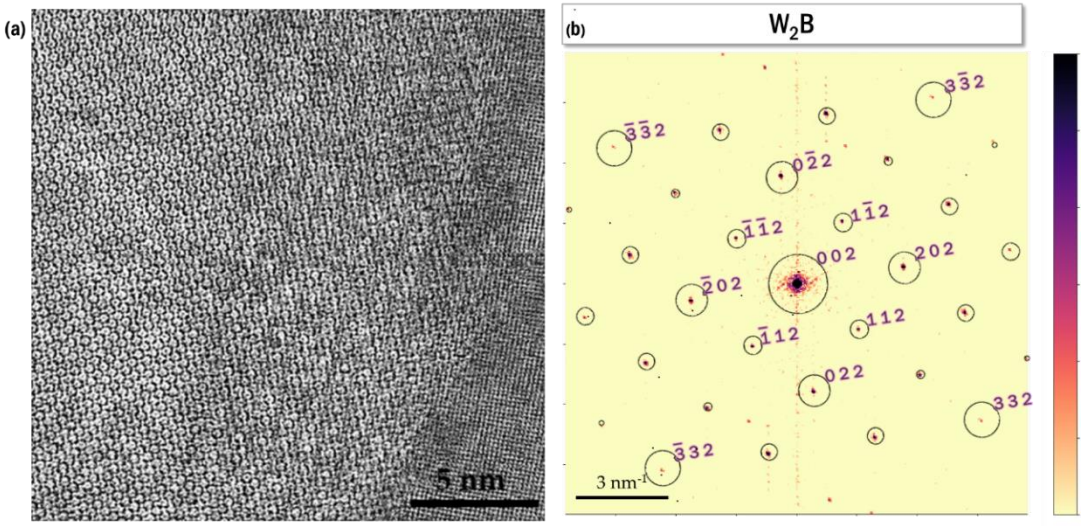


Figure 6.9: (a) HR-STEM image of the boride phase, **(b)** Simulation of the binary M_2B overlayed on the FFT of (a).

6.3.3. Geometric Phase Analysis (GPA)

The precipitation of the boride phase may result in the deformation of the surrounding lattice. The deformation introduced to the lattice depends on the coherency of the boride particle with the host grain. When particles remain coherent or semi-coherent the surrounding matrix will be strained to accommodate the lattice mismatch. In the case of incoherent particles their lattice planes are not continuous with the planes of the host lattice. In that case strain may be introduced due to the different cell volume of the precipitated particle.

Using geometric phase analysis (GPA), an estimation of the strain distribution surrounding the M_2B-type boride phase in the proximity of the grain boundary can be obtained. The region of interest for the GPA is shown in Figure 6.10 (c), highlighted with a rectangle in the lower magnification BF image in Figure 6.10 (b). As observed in Figure 6.10 (a), the chromium distribution suggests that the boride phase borders with a secondary γ′ precipitate. Tis can also be better realised by the periodic FFT of the γ′ in Figure 6.10 (c.ii), in which the superlattice reflections are visible (highlighted in circles). The speckle contrast on the surface of the γ′ phase in the BF images is caused by preparation artifacts introduced during FIB milling. An area free of contamination was used for the geometric phase analysis.

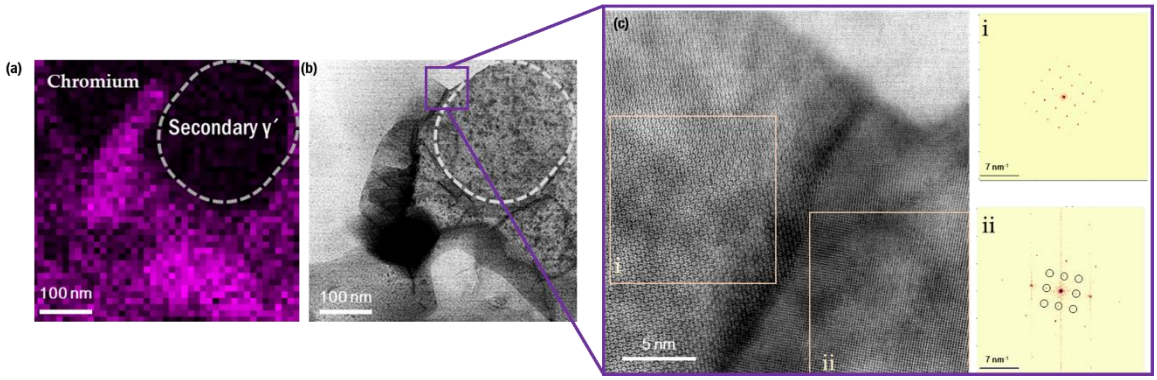


Figure 6.10: (a) Compositional maps of the Cr-K peak of the EDX spectrum, **(b)** BF image of the region of interest, **(c)** Higher magnification BF image of the region of interest, including the FFT of the present phases: (i) M_2B-type boride and (ii) secondary γ′ precipitate phase.

From the HR-STEM image in Figure 6.11 (a), the associate FFT pattern and phase map have been created. In the FFT in Figure 6.11 (b), two diffraction patterns are superimposed together, one from the cubic lattice of the γ′ precipitate and one from the lattice of M_2B-type boride. Using geometric phase analysis on the lattice of the γ′ precipitate the local strain distributions of ε_{xx} and ε_{yy} were calculated within the secondary γ′ precipitate. A description of this technique is provided in detail Chapter 3 (3.7.2). The aperture size used in the Fourier transform was set to r = 5 nm^{-1}. Higher lateral resolution stain maps could have been obtained by decreasing the size of the aperture, but the local variations would have been significantly stronger complicating the averaging. However, regardless of the size of the aperture and the lateral resolution, the measured strain value was not affected.

The estimations of the local strain distribution of ε_{xx} and ε_{yy}, obtained by applying GPA to HR-STEM images, are illustrated in Figure 6.11 (d) and (e). The colour scalebar indicates compressive and tensile strains ranging from -0.05 to +0.05, respectively. As a reference lattice, the undeformed lattice of γ′ precipitate away from the grain boundary was used (shown with a dashed square in Figure 6.11 (c)), hence it appears to be unstrained in Figure 6.11 (d-g). The evaluation of ε_{xx} strain map in Figure 6.11 (d) revealed that it increases gradually from γ′ particle to the grain boundary. Similarly, an increase in the ε_{yy} strain is observed across the grain boundary region on which the boride resides.

Undoubtedly, the GPA technique has various limitations, as it depends strongly on image quality and can be directly affected by artifacts, hence the results should be interpreted with caution. However, regardless of the accuracy of the estimated values, from the local strain variations it can be inferred that the precipitation of the M_2B-type boride phase influences strongly the spatial distribution of lattice strain at the grain boundary region.

Kontis et al. [58] claimed that the presence of boron and the formation of M_5B_3 borides in their study heavily affected the lattice strain. Based on experimental evidence obtained employing HR-EBSD, they also found that higher lattice strain was concentrated at the grain boundary, around and within the borides and grain boundary γ′ precipitate layers. The lattice strains could be induced by the misfit in their lattice parameters and by the mismatch in the

coefficient of thermal expansion between the two phases. Changes in temperature during cooling from the heat treatment stages can cause internal stresses to arise, as a result of different thermal expansion coefficients between the phases.

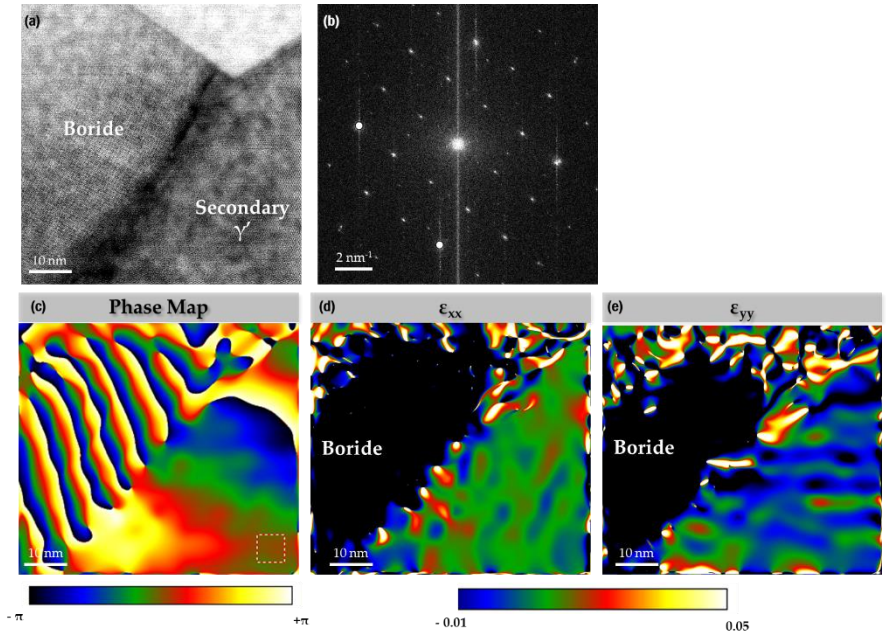


Figure 6.11: **(a)** HR-STEM image of the grain boundary region, **(b)** FFT of HR-STEM image in (a), **(c)** Phase map of the geometric phase analysis on the lattice of the γ′ precipitate, **(d)** Distribution of ε_{xx} strain, **(e)** Distribution of ε_{yy} strain.

6.4. Discussion

6.4.1. Intergranular γ′ Precipitates

It is interesting to put into perspective the information collected by HR-STEM and compare it with the overall measurements obtained by *in situ* neutron diffraction during heat treatment of Alloy 11 (Chapter 4). From the analysis of the superlattice reflection (001), the lattice parameter of the γ′ precipitate phase was measured to be in the vicinity of 3.62 [Å] (3.6185 Å) at room temperature. However, the similarity in lattice parameters between the different populations of γ′ prohibits fitting them separately, so it is not possible to obtain local information on the different γ′ populations with neutron diffraction. Therefore, to shed light on the local variations between intergranular and intragranular secondary γ′ precipitates HR-

STEM imaging combined with EDX analysis is a valuable tool. From the obtained measurements, since the lattice parameter of secondary γ′ is approximately 3.625 Å while that of GB γ′ is 3.662 Å, it can be inferred that the contribution of grain interior secondary γ′ dominates, since its volume fraction is much larger than that of intergranular γ′.

Regarding the misfit between the γ′ precipitate phase and the matrix γ, form neutron diffraction it was measured to be approximately equal to – 0.05% at 500 °C with an increasing trend for lower temperatures. Considering the variations detected among the lattice parameter of different γ′ populations, each population is expected to have a distinct lattice misfit with the matrix. Its estimation involves the uncertainties of the measurements of the lattice parameter of intergranular or intragranular secondary γ′ and of the matrix γ along with the combination of those uncertainties. The error propagation will therefore inevitably downgrade the accuracy of the value of lattice misfit, so it could be considered as a rough estimation that could be further refined with additional measurements.

The results obtained about the elemental variations between intergranular and intragranular secondary γ′ precipitates are in good agreement with previously reported observations. Mitchel et al. [33] performed TEM-EDX spot analyses on grain boundary γ′ in RR1000, a popular disc alloy which displays similar composition with Alloy 11. They found that the grain boundary γ′ particles are enriched in Ni, Al, Ti, Ta, Hf and Zr, compared to grain interior γ′. Sufficient diffusion of larger sized atoms into the grain boundary γ′ was associated with the coarsening of intergranular γ′ particles at the grain boundary region. This is also consistent with Vegard's law that resembles the rule of mixtures and holds that at constant temperature a linear relation exists between the lattice parameters and the mole fractions of added solutes (Section 2.3.1). Different elements have a different impact on the crystal lattice parameter determined by the so-called Vegard coefficients which are strongly dependent on the position of the solutes in the periodic table [157]. Among the other constituent elements, intragranular γ′ is found to be enriched in W and Ta, for which the Vegard coefficients are relatively large.

6.4.2. M_2B-type Boride Phase

The identification of the observed intergranular phase in this case is not possible based solely on EDX compositional analysis. In boron-containing nickel-base superalloys, it is not uncommon for intergranular boride particles to coexist with carbides (e.g. [58,158]). The detection of the low energy carbon and boron peaks though is not always successful with EDX, while the carbide and boride particles usually exhibit comparable metallic compositions. Thus, it is not easy to chemically discriminate between possible carbide and boride types with EDX analysis alone since there is high risk to misidentify the phases. The EELS technique is more sensitive to light elements with higher energy resolution and has been successfully used to identify chemically carbide and boride particles. In [158] careful EELS analysis in IN738 detected both nanosized M_5B_3 boride particles and $M_{23}C_6$-type carbides, with sizes typically above 100 nm.

In this study, the identification is based on the structural characteristics of the observed phase and is supported by the simulations obtained from CrystalMaker and SingleCrystal. The crystallographic characteristics in M_2B-type borides has been thoroughly investigated in a study by Hu et al. [82] in boron-containing nickel-base superalloys subjected to long-term ageing treatments. By means of analytical transmission electron microscopy, they found out that M_2B-type precipitations display a number of structural variants: one variant has a body-centred tetragonal structure, another has face-centred orthorhombic structure, while some M_2B-type borides possess dual-phase characteristics. Regarding its orientation with respect to the FCC lattice of the parent γ phase, Cadel et al. [84] who detected the existence of M_2B in N18, a P/M polycrystalline nickel-base superalloy, showed that many orientation variants exist. Because of the dual-phase characteristics and the high density of stacking faults [82] the identification of M_2B-type borides is often challenging, and it has been claimed that particles of this type may have been misidentified in previous studies [83].

6.4.3. Grain Boundary Serrations

In the alloy under consideration, the formation of grain boundary serrations is promoted after slow cooling from super-solvus solution temperature, while rapid cooling produces straight grain boundaries. This observation is illustrated in the backscattered scanning electron (BSE) images in Figure 6.12, which display the morphology of grain boundaries for various cooling rates ranging from 0.2 to 4 °C/s. It should be noted that the scale bar in each micrograph is the same to facilitate direct comparisons between them. Slow cooling rates (0.2- 0.7 °C/s) were found to result in convoluted, wave-like grain boundaries. For intermediate cooling rates (2.0 °C/s) the grain boundaries appear less serrated, while with faster cooling (4.0 °C/s) they seem fairly straight.

A closer look at the grain boundary regions in Figure 6.12 reveals that serrations are typically decorated with intergranular γ′ precipitates often surrounded by a γ′ denuded zone. Less often grain boundary serrations are occupied by carbide particles which are also distributed in the grain interior. The regions of triple junctions where three grains and grain boundaries meet are heavily populated by both GB γ′ precipitates and carbide particles for slow and intermediate cooling rates. It is interesting to notice that regardless of the cooling rate the grain boundaries appear slightly darker, almost like a thin black line is pulled between the neighbouring grains. This could originate from the precipitation of thin boride nanoparticles at the grain boundary region. This claim is supported by the BF and HAADF images in Figure 6.13, displaying the microstructure of a slow cooled sample (0.6 °C/s). The grain boundary serrations seem to follow a phase that appears dark in the bright-field STEM, and bright in HAADF, indicating a strong difference in its atomic number (Z). As discussed in detail in the abovementioned sections, this phase has been identified as a boride, and in this case its type is M_2B. However, this does not exclude the presence of different types of boride phases considering the local perspective of this approach and the variations detected in terms of Cr and Mo content (Figure 6.6).

Although the beneficial effect of grain boundary serrations on the mechanical properties of nickel-base superalloys has been well-established, the mechanism that promotes

their formation is still not fully understood yet. On the one hand, grain boundary serrations have been frequently associated with the precipitation of intergranular γ′ [33-35]. It has been claimed that during slow cooling the preferential growth of intergranular γ′ precipitates towards the grain boundary drives the grain boundary to bow around them [80]. As the cooling rate controls the kinetics of the γ′ precipitation slower cooling promotes heterogeneous nucleation of intergranular γ′ precipitates preferentially along high angle grain boundaries [35]. Strong segregation of atoms to grain boundaries leads to the formation of intergranular particles claimed to trigger grain boundary serrations.

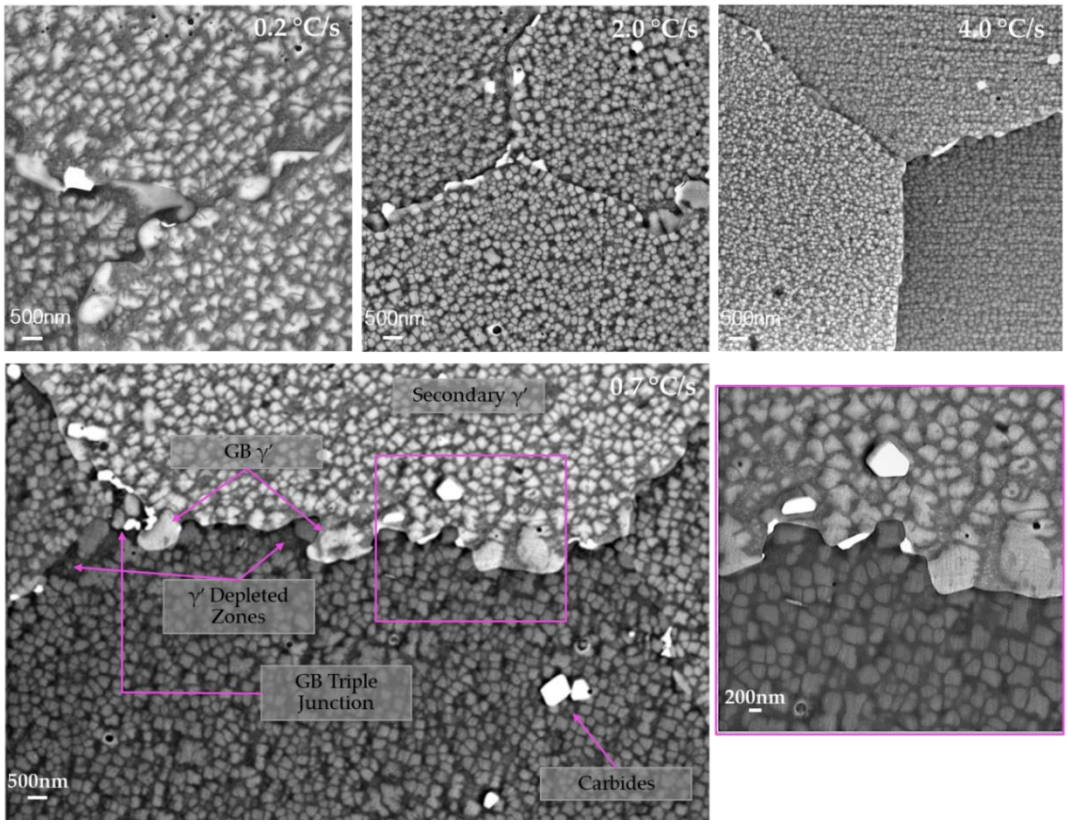


Figure 6.12: BSE images of the morphology of grain boundaries for various cooling rates ranging from 0.2-4 °C/s.

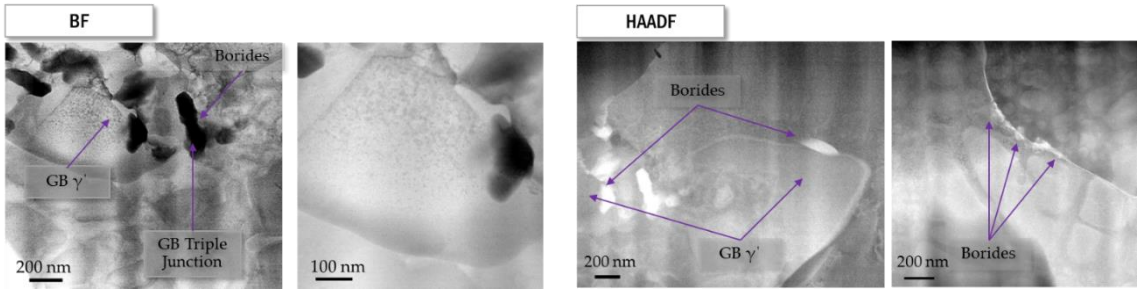


Figure 6.13: BF and HAADF images of the morphology of grain boundaries after slow cooling rate (0.6 °C/s).

On the other hand, in the case of alloy systems with low volume fraction of γ′ precipitates, the formation of serrations may arise because of the interaction of grain boundaries with other intergranular particles. Tang et al. [36-37] found out that serrations in an alloy system with low content of γ′ forming elements arose when the grain boundary migration was hindered by carbide phases which pin to the boundary distorting their morphology. The formation of borides has been also related to serrated grain boundaries. Boron addition has been observed to prolong creep rupture life, due to the enhancement of grain boundary strength by introducing grain boundary serrations. Kontis et.al [58] claimed that the grain boundary morphology and the γ′ particles decorating the grain boundaries is a result of the addition of boron.

In principle, the formation of grain boundary serrations is believed to be energetically driven from lowering the interfacial free energy of grain boundaries per unit area, and thus being energetically favourable. Hong et al. [159] investigated the mechanism for the formation of serrated grain boundaries in the case of low γ′ volume fraction nickel-base superalloys. They showed that discontinuous solute segregation at the GBs may trigger serrations for relieving excessive elastic strain energy. In particular, they inspected the onset of GB serrations at an early stage of the slow cooling process by conducting an EELS study on random or high-angle serrated GBs ($\Sigma > 29$) before $M_{23}C_6$ precipitation. The discontinuous GB segregation of C and Cr atoms was observed, and excess C and Cr atoms were alleged to generate lattice distortional strain energy near GBs. Therefore, it was inferred that a stress due to the uneven distortional lattice strain may develop near GBs and promote the onset of GB serrations.

Furthermore, in the same study, the authors demonstrated the effect of the lattice distortional energy due to the atomic size difference on the serration behaviours of binary nickel alloy model systems, in which GB serrations were observed even without the precipitation of intergranular secondary phase particles. In a Ni-Zr binary system, the formation of serrated GBs initiated when the content of Zr was higher than 0.05%, in the

absence of any secondary phase particles. The atomic size of Zr is large which might have led to a sufficient development of stress exerting a force on GBs.

A classical model on grain boundary segregation was proposed in an early study by McLean [160]. McLean's model is based on the relief of lattice strain energy upon segregation and can be used to provide a simplified description of segregation. In binary systems, since solute atoms that differ is size from the solvent atoms create a strain in the lattice, misfitting impurity atoms may be benefitted energetically from sitting on a disordered grain boundary plane, as opposed to residing in the grain. Atoms diffuse under this driving force towards the boundary and the kinetics are controlled by the diffusion of impurity atoms in the matrix. McLean proposed the following formula for the lattice distortion energy, W, generated by a solute atom in the bulk by using elastic continuum theory:

$$W = \frac{24\,\pi\,K\,\mu\,\mathrm{N}\,r_0(r_1 - r_0)^2}{3K + 4\mu(r_0/r_1)} \tag{87}$$

where K is the bulk modulus of the solute, μ is the shear modulus of the solvent, N is Avogadro's number and r_0, r_1 are the atomic radii of the solvent and the solute respectively. Values estimated by this practical approach are generally correct within a factor of two [161]. Although this early study had to rely on various approximations, it is a practical model for estimating interfacial energy changes due to solute segregation.

Using McLean's model, the lattice distortion energy introduced by atoms of common alloying elements in nickel-base superalloys is estimated, for binary alloy systems with nickel as a solvent. The estimations are shown in detail in Table 10. Although various more recent studies, have worked systematically to improve and extend McLean's model to provide a more complete analytical description of segregation, accurate modelling of the phenomena involved is out of the scope of this work. Instead, McLean's lattice distortion energy is used as an index, to explore any correlation between borides and serrations. Since, the size of the boron atom is larger than that of other interstitial atoms and smaller than that of substitutional atoms in nickel-base superalloys, the lattice distortion introduced by boron addition seems to be the largest, compared to the alloying elements contained in Alloy 11.

Table 10: Lattice distortion energy introduced by solute atoms of common alloying elements in binary alloy systems with nickel as a solvent, estimated using McLean's model in Eq. (87).

	Shear modulus of solvent μ [GPa]		Radius of solvent atom r_0 [nm]
Ni	76		0.121
	Bulk modulus of solute K [GPa]	Radius of solute atom r_1 [nm]	Lattice distortion energy W [kJ/mol]
Co	180	0.126	2.26
Cr	160	0.127	3.125
Al	76	0.118	0.53
Ti	110	0.136	17.21
Ta	200	0.138	27.85
W	310	0.146	68.45
Mo	230	0.145	58.62
Nb	170	0.137	23.34
Fe	170	0.125	1.41
Mn	120	0.139	25.99
Zr	96.7	0.148	54.65
C	33	0.076	47.86
B	185	0.082	**117.07**

Using the experimental results, the detailed discussion on previous observations in the literature and McLean's model as an index, one could infer that the energy minimisation is the main determinant of the grain boundary morphology. The precipitation of boride phases influences the spatial distribution of lattice strain at the grain boundary region. At thermal processing boron tends to segregate to the grain boundaries where B would interact with Cr, Mo and W to form borides. Using McLean's model in Eq. (87) as an index the lattice distortion energy introduced by B, Mo and W is expected to be significant. The boride formation is assisted by the solute diffusion along the grain boundary facilitated by the slow cooling rates.

Strong discontinuous segregation of atoms to grain boundaries leads to the formation of intergranular particles, including intergranular γ′ in high γ′ volume-fraction nickel-base superalloys. The discontinuous segregation of solute atoms at the grain boundary region strongly affects the lattice strain distribution and is believed to trigger serrations for relieving excessive elastic strain energy.

6.5. Conclusions

In this Chapter, the structural and compositional variations between different γ′ precipitate populations were investigated, using high resolution scanning transmission electron microscopy. A commonly used method was employed for measuring the interplanar spacings of intergranular and intragranular secondary γ′ precipitates, involving the Fast Fourier Transform of HR-STEM images. The lattice parameter of intergranular secondary γ′ was found to be larger than that of intragranular secondary γ′. The observed variations in the lattice parameters of the two populations were attributed to compositional variations detected by STEM-EDX analysis. The intergranular secondary γ′ precipitate population is enriched in Ni, Ta, Ti, and Al, compared to intragranular secondary γ′. Also, the content of Fe and W was observed to be slightly higher in intergranular γ′.

Additionally, a boride phase was detected at the grain boundary region and its exact type was determined by comparing the FFT of HR-STEM images to simulated reciprocal lattice of binary boride structures commonly precipitated in nickel-base superalloys. The grain boundary boride was identified as M_2B. This does not exclude the precense of more types of boride phases considering the observed variations between the chromium and molybdenum content among the boride particles. The estimations of the local strain distribution of ε_{xx} and ε_{yy}, obtained by applying geometric phase analysis of the HR-STEM images, revealed that the precipitation of the M_2B-type boride phase affected the spatial distribution of lattice strain at the grain boundary region. Based on the experimental results, and supported by literature studies, the effect of boron addition on the lattice strain distribution at the grain boundary

region is believed to trigger the grain boundary serrations for relieving excessive elastic strain energy and also promote the formation of intergranular γ′ due to discontinuous solute segregation at the grain boundaries.

7

Operando nanoscale observation of the dissolution of γ′ populations and oxidation sequence during heating

7.1. Introduction

During operation, gas turbine components are subjected to extreme conditions combining significant mechanical stresses with high temperatures. To improve the overall efficiency, increasing turbine entry temperature is required that represents a challenge of expanding the operational limits of superalloys outside the current envelope. The mechanical and thermal stability at elevated temperatures and oxidative environments is one among the most crucial operational requirements for nickel-base superalloys. However, at these elevated temperatures diffusion-controlled phenomena are inevitably activated, mediating several degradation mechanisms to occur.

First and foremost, the diffusion-controlled coarsening of the γ′ precipitates that can occur strongly affects the creep resistance both in polycrystalline superalloys accompanied by the dissolution of fine particles [59], and in single crystals in which the so-called rafting effect is observed [7]. Diffusional rearrangements at dislocation cores can also influence the rate of creep deformation [23]. What is more, oxidation reactions are driven by volume diffusion of elements, as well as interfacial and intergranular diffusion. When exposed to

oxidative environments at operating temperatures, in the range of 750 - 900°C, nickel-base superalloys can experience microstructural modifications induced by oxidation, including inhibition of coarsening or even local γ′ precipitate dissolution by the adsorption of solutes into oxides [91]. After oxidation, γ′ denuded layers have been reported by numerous previous studies [87,90] leading to local mechanical softening and thus inhibiting the mechanical integrity of the system.

Environmental degradation due to oxidation may be detrimental to the lifetime of the components. Even before operation, while manufacturing, oxygen contamination inevitably occurs during severe plastic deformation of metallic powders by exposure to air [162]. For alloys produced by powder metallurgy, during premixing and consolidation of powders, oxygen contamination seems to be inescapable, with oxygen being incorporated into the material, generating discrepant morphologies, mechanical properties, and thermal stabilities.

Oxidation may pose a serious threat to the overall integrity of the system, by introducing either surface or intergranular cracking [88,103]. Although thermal barrier coatings (TBCs) are currently used in turbine engine components such as turbine blades to prevent direct contact between high-temperature gas and protect the substrate material, a certain degree of degree of oxidation is still inevitable [90]. To quantify and control the oxidation-induced damage, there is a need for detailed information about the rate of oxidation and dissolution of γ′ during heating in nanocrystalline alloys, and competition between these processes. *In situ* heating experiments within a scanning transmission electron microscope (STEM) combined with electron energy loss spectroscopy (EELS) technique enables probing the mechanisms underlying these complex physicochemical processes at the nanometric scale as they unfold.

In this study, the microstructural evolution during heating of a new polycrystalline nickel-base superalloy is explored by performing *in situ* heating of thin lamella samples under the electron beam in STEM. Along with the microstructure, the elemental distribution and the compositional profile of γ′ precipitate populations is investigated using a synchronous EELS analysis. *Operando* nanoscale observation of the dissolution of γ′ populations was achieved,

and the findings provide a direct observation of the Gibbs-Thomson effect in the dissolution behaviour of different γ′ populations. Additionally, the nano-diffusion pathways for preferential intergranular oxidation were studied during heating. The diffusional phenomena that take place when heating TEM lamella specimens with local thickness less than 100 nm can provide quantitative input data for validating accurate numerical simulations. It should be noted that the diffusional phenomena observed may appear accelerated due to the small interaction volume and reduced diffusion paths within thin specimens [163]. The dwell time at each temperature level was chosen accordingly.

7.2. Experimental Method

STEM studies were carried out using the probe corrected JEOL ARM200CF scanning transmission electron microscope, operated at 200 kV, at the electron Physical Science Imaging Centre (ePSIC) at Harwell Campus. For imaging of the variations of the microstructure with temperature, the bright field (BF), annular dark field (ADF) and high-angle annular dark field (HAADF) detectors were utilised. A condenser lens aperture size of 30 μm was used, while the camera length was set to 3cm. *In situ* heating of the sample was performed using the single tilt DENSsolutions heating holder. The analysis was coupled with simultaneous EELS analysis for synchronous compositional information and elemental mapping at the nanometre scale at elevated temperatures. STEM-EELS was carried out using a Gatan Quantum Dual EELS spectrometer, with collection semi-angle equal to 55.56 mrad. For the data analysis of the EELS spectrums, the Gatan GMS version 3.4.2 software was utilised.

7.2.1. Sample Preparation

The material in this study was obtained from a pancake forging of Alloy 11, produced by isothermally forging a powder isostatic pressed cylindrical compact. A detailed description of the alloy under consideration is provided in Chapter 1 (1.5). Thin TEM lamellae samples of the material in the as-forged condition prior to any heat treatment were prepared with the site-specific FIB lift-out technique using a LYRA3 Focused Ion Beam-Scanning Electron

Microscope (FIB-SEM) system (Tescan, Brno, Czech Republic) equipped with a nanomanipulator and a gas injection system housed in the Multi Beam Laboratory for Engineering Microscopy (MBLEM, Oxford). The lifted lamella was positioned on the single tilt DENS Solutions heating chip (Figure 7.1) with careful adjustment of the angle and position of the sample stage with a 45° pre-tilted support.

DENSsolutions Nano-Chip is a functional consumable sample carrier that is used instead of the traditional TEM copper grids offering a micro-scale hotplate for heating. The micro-hotplate is based on the Joule heating principle of a metal spiral. The heating chip consists of a metal heater embedded in silicon nitride of thickness roughly equal to 20 nm. Silicon nitride Si_3N_4 offers the advantages of being chemically inert and mechanically robust [164]. Holes have been carefully designed in the Si_3N_4 supporting film, allowing TEM imaging of the sample mounted on top of them. The control method used is four-point resistive feedback providing temperature accuracy < 5% [164]. The initial calibration was done by the manufacturer and calibration values are provided to be introduced in the control software, which is also used to record the temperature during the experiment. Uniform temperature distribution in the region shown in (b) has been verified previously by simulations in the software COMSOL Multiphysics® [165].

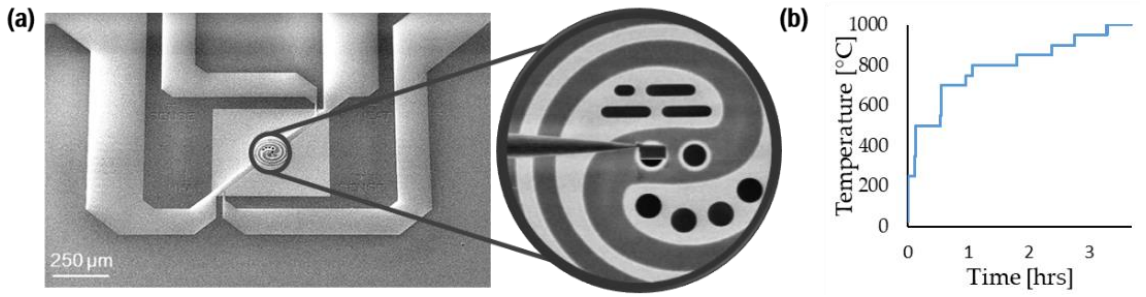


Figure 7.1: **(a)** SEM image of the DENSsolutions Nano-Chip used for is situ heating, **(b)** Higher magnification image of the metal spiral on the micro-hotplate of the heating chip with windows for FIB samples, **(c)** *In situ* heating profile, as measured by the heater.

7.3. Experimental Results

7.3.1. BSE Images of the Microstructure at Room Temperature

Figure 7.2 depicts the microstructure of the sample at room temperature, right after isothermal forging of the isostatically pressed powder cylindrical compact, prior to any subsequent heat treatment. The micrographs depict a trimodal γ′ precipitate distribution with the volume fraction of the γ′ precipitate phase being above 50%. The isothermal forging is conducted at sub-solvus temperature, therefore the primary γ′ precipitate population is not dissolved. Instead, it resides at the grain boundary regions, restricting grain growth. This results in significantly smaller grain size (Figure 7.2 (a)) compared to the full heat-treated condition, as discussed in detail in the previous Chapters. Large primary γ′ precipitates are observed to be located at the grain boundaries, and fine secondary and tertiary γ′ precipitates are distributed in the grain interior (Figure 7.2 (b), (c)). Additionally, carbide phases are detected at the grain boundaries, enveloped in between the large primary γ′ precipitates.

To obtain an estimation of the size distribution of each of the populations of the γ′ precipitates, the software package ImageJ was utilised to perform quantitative image analysis. The average size of each γ′ precipitate population was estimated from the square root of the measured precipitate area. Figure 7.3 presents histograms of the size distribution of γ′ precipitate populations. The precipitate populations appeared to conform to a trimodal size distribution, validating the presence of primary, secondary and tertiary γ′ particles. In Figure 7.3 (a), the left peak corresponds to the size distribution of tertiary γ′, and the right peak to that of secondary γ′ precipitates, while Figure 7.3 (a) illustrates the size distribution of primary γ′. In Figure 7.3 (a) and (b), the markers correspond to the measurements and the continuous lines denote a fit to the data. Table 11 summarises the mean diameters and standard deviations for each population, obtained by the gaussian fit of the measurements on the γ′ precipitate size.

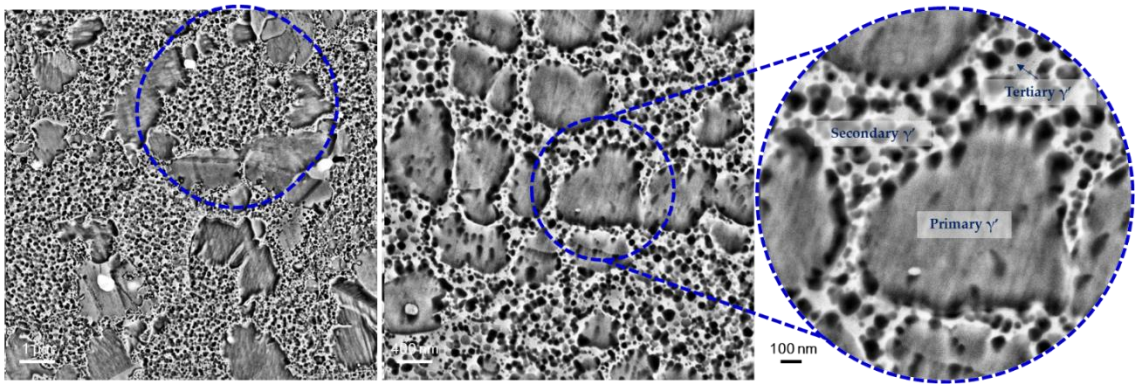


Figure 7.2: Backscattered SEM images of the microstructure at room temperature.

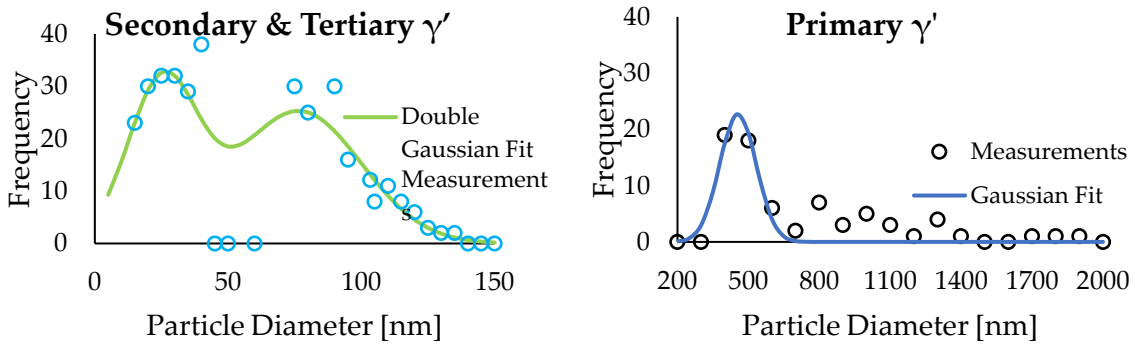


Figure 7.3: Histograms of γ′ precipitate size distribution corresponding to **(a)** secondary and tertiary and **(b)** primary γ′ precipitates.

Table 11: Mean size and standard deviation of each γ′ precipitate population.

	Primary γ′	Secondary γ′	Tertiary γ′
Mean Size [nm]	429.99	76.44	25.32
Standard Deviation [nm]	125.17	23.52	13.06

7.3.2. Microstructural Evolution during Heating

In situ heating of the samples in the as forged condition was performed, aiming to track the microstructural changes until the dissolution of the γ′ precipitate populations. The thin TEM samples were *in situ* annealed for approximately 20 minutes at different temperatures in steps of 50 °C from room temperature to a maximum temperature of 1150 °C. A close examination of the BF and ADF images can reveal useful information on the gradual dissolution of the γ′ precipitate populations, and the concurrent diffusional phenomena and oxidation reactions.

For Sample 1, the region of interest illustrated in Figure 7.4 (b) contains a small grain which contains a few large secondary γ′ precipitates and neighbours a coarse primary γ′ precipitate. The microstructural features appear clearer in the Energy Dispersive X-ray Spectroscopy (EDX) elemental maps shown in Figure 7.4 (b). A series of low magnification BF images of the region of interest obtained after consecutive temperature increments are shown in Figure 7.4 (a). For temperatures below 500 °C, no visible changes appear to occur. The dissolution of secondary γ′ precipitates appears to be initiated in the vicinity of 850 °C, as the particles contained in the region of interest appear to fade. At 1100 °C, when the secondary γ′ precipitates seem to be almost completely dissolved, the gradual dissolution of primary γ′ takes place, along with the migration of the adjacent grain boundary. However, the speckle contrast on the surface of the sample prohibits close examination of the microstructural evolution. These dark features are caused by oxidation introduced to the sample while heating, which results in obstructing the observation of the dissolution of the fine γ′ precipitates.

For Sample 2, an ADF image of the region of interest at room temperature is illustrated in Figure 7.5 (a). A clearer visualisation of the microstructural features contained in the region of interest can be realised by the EDX compositional maps in Figure 7.5 (b). The region of interest includes a small grain that contains a large primary γ′ precipitate, surrounded by some secondary and a crowd of fine tertiary γ′ precipitates. ADF images of the region of interest obtained after consecutive temperature increments are shown in Figure 7.5 (a), and the heating profile corresponds to that plotted in Figure 7.1 (c). For temperatures below 750 °C, the microstructure appears to be unaltered. The dissolution of secondary and tertiary γ′ precipitates seems to be initiated at temperatures ranging from 850 to 950 °C, as also observed in Sample 1. At the same time at this temperature range preferential intergranular oxidation is detected, with the dark features that decorate the GBs corresponding to oxides. Regarding the bright spots at the grain interior, they are also associated with oxidation, but they appear to differ from the intergranular oxides in terms of composition.

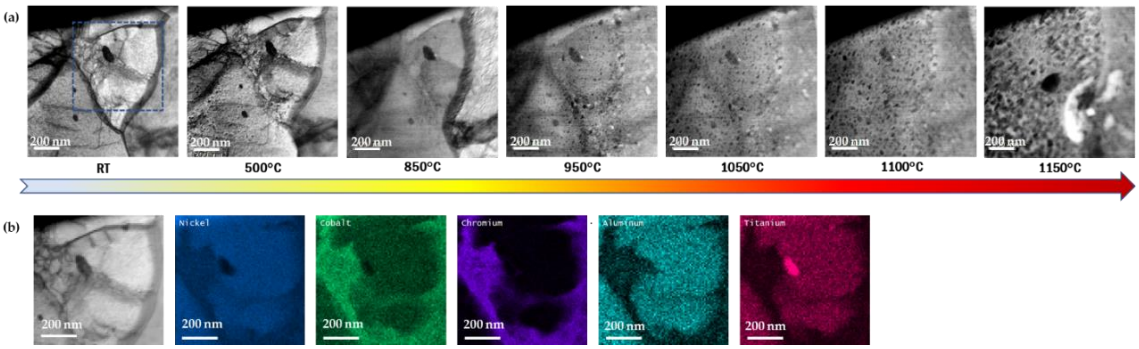


Figure 7.4: **(a)** Low magnification BF images of the region of interest of Sample 1 after consecutive temperature increments. **(b)** Elemental maps of the square region in (a) at room temperature, corresponding to the Ni K, Co K, Cr K, Al K and Ti K lines in the EDX spectrum.

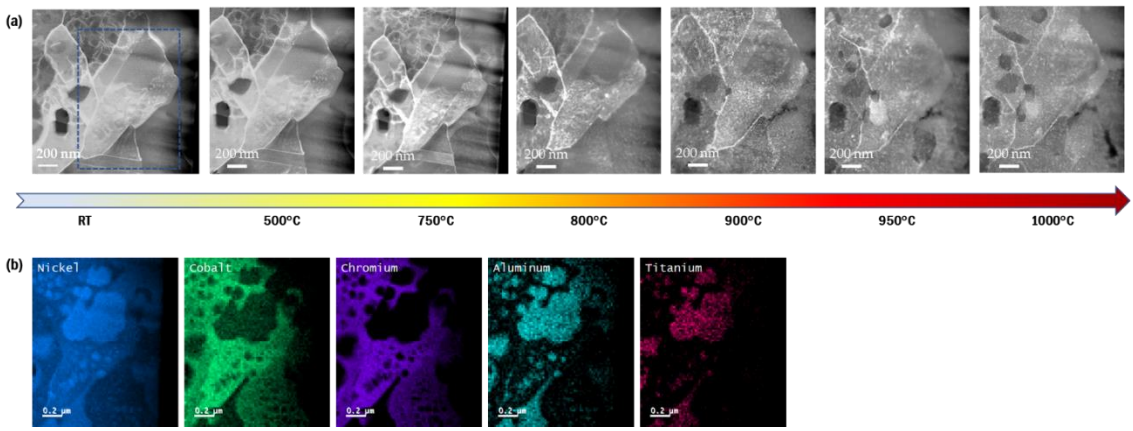


Figure 7.5: (a) Low magnification ADF images of the region of interest of Sample 2 after consecutive temperature increments. **(b)** Elemental maps of the square region in (a) at room temperature, corresponding to the Ni K, Co K, Cr K, Al K and Ti K lines in the EDX spectrum.

From the microstructural examination of the two samples, it becomes apparent that in the temperature range from 800 to 950 °C, the diffusion of solutes is activated, triggering several diffusion-mediated phenomena. In particular, the dissolution of secondary and tertiary γ′ precipitates is promoted, while at the same time oxidation reactions are apparent, particularly at the grain boundary region. Therefore, the evolution of the distribution of solutes at elevated temperatures is crucial and needs to be further investigated. Fortunately, in situ heating under the electron beam in STEM combined with EELS enables probing the mechanisms behind these complicated physicochemical processes at the nanometric scale.

7.3.3. Compositional Analysis during Heating

For Sample 2, for every temperature increment, elemental information of the region of interest was collected by performing simultaneous EELS analysis. At elevated temperatures, EELS compositional maps can provide a sharper depiction of the microstructural features compared to the ADF images, with the latter being strongly affected by the inevitable oxidation of the sample, hindering the observation of fine γ′ precipitate populations. Apart from the qualitative examination of the microstructural features, the quantification of their elemental concentrations was performed to capture accurately the distribution of solutes and the compositional profile of the γ′ precipitate populations at high temperatures.

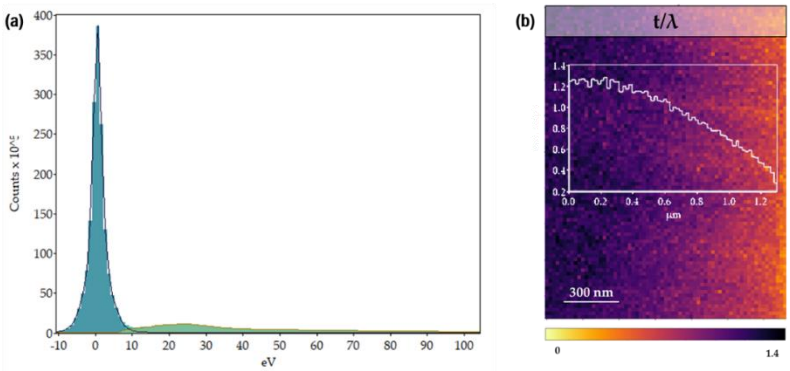


Figure 7.6: (a) Low-loss EELS spectrum at room temperature, **(b)** Map of relative thickness t/λ estimated by Eq.(13).

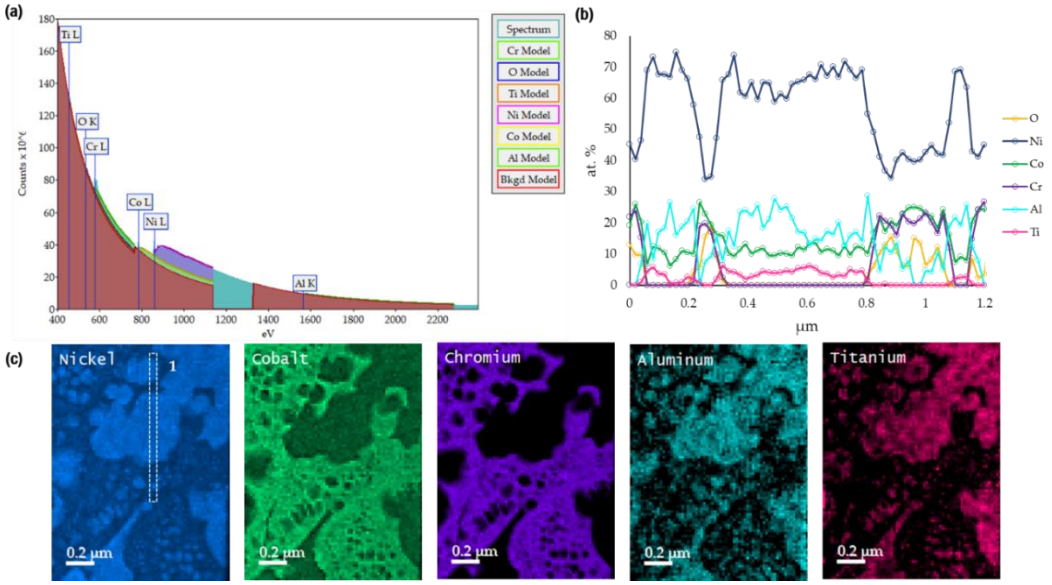


Figure 7.7: (a) High-loss EELS spectrum at room temperature, **(b)** Line profile of the elemental distribution in Region 1 highlighted in (c) at room temperature, **(c)** EELS elemental maps at room temperature, corresponding to the Ni L, Co L, Cr L, Al K and Ti L ionisation edges in the EELS spectrum.

Absolute quantification can be performed only if the relative thickness t/λ of the sample is appropriate. As described previously, the ratio of the intensity of the zero-loss electrons to the total transmitted intensity can provide a relative measure of the thickness of the specimen in units of the local inelastic mean free path λ (see Eq. (13), Section 3.7.3). In Figure 7.6 (a), the low-loss EELS spectrum at room temperature is shown, including the zero-loss and plasmon peaks. In the specimen under examination, the relative thickness is less than 1.2 times the inelastic mean free path, therefore the thickness is considered acceptable for quantification. However, the thickness of the sample is not uniform, as it includes a decreasing gradient towards the edge. To avoid any errors and artifacts introduced due to the varying thickness the analysis is focused on the central region with uniform relative thickness ($t/\lambda \approx 1$).

Figure 7.7 (a) displays the high-loss EELS spectrum at room temperature, in which the ionisation edges of the elements detected are labelled. The edges of Ti, O, Cr, Co, Ni and Al were selected for elemental quantification for temperatures up to 950°C. For edges Cr -L, Co-L and Ni-L, a strong peak was detected compared to the weak Al-K edge, for which the poor signal-to-noise ratio may introduce errors, and thus should be interpreted with caution. To obtain quantitative information, the cross-sections were computed using the Hartree-Slater model, which yields a good fit to the experimental data as shown in Figure 7.7 (a). It should be highlighted though that the main objective of the quantification in this work is to detect relative differences in the elemental concentrations while heating. However, although not rigorous, the measurements in terms of atomic percent (at. %) provide valuable estimations for the evolution of the elemental distributions while heating.

The results of the elemental quantification are illustrated in the EELS compositional maps in Figure 7.7 (b). First and foremost, the direct comparison of the EELS to the EDX (qualitative) maps in Figure 7.5 (d) can demonstrate the improved spatial resolution of the former method compared to the latter. The effect of thickness is limited in the EELS quantitative maps, while in the EDX maps no signal was detected from the thinner region of the specimen. Additionally, the EELS detector is usable under a wider temperature range compared to EDX.

The line graph in Figure 7.7 (b) corresponds to Region 1 shown in the map of Nickel in Figure 7.7 (c). Region 1 corresponds to a region of uniform thickness that contains two primary γ′ precipitates with considerably different diameters, and one secondary γ′ precipitate, as well as all the relevant interfaces between the respective particles and the matrix. The γ′ precipitate populations display a typical compositional profile, being enriched in Ni, Al and Ti compared to the γ matrix, which has the expected higher Co and Cr content. It is interesting to note though that the content of nickel in both of the primary γ′ particles contained in this region display an irregular profile, with higher Ni content concentrated at the edges of the particles, while their interior has a lower Ni concentration. Secondary γ′ particle seem to have a slightly enhanced Al atomic concentration compared to primary γ′, an observation which further supports previous reports of size-dependent elemental concentrations in γ′ precipitates [67].

Regarding tertiary γ′ precipitates, the particles of this population are enveloped on all sides by the surrounding γ matrix, since the thickness of the sample is larger than the mean diameter of tertiary γ′ (≈ 25 nm). This complicates the distinction between the composition of the precipitates from that of the surrounding matrix. For the accurate quantification of tertiary γ′, an electrochemical method for TEM sample preparation should be employed in order to extract individual γ′ precipitates by dissolving the surrounding γ matrix, as demonstrated in previous studies, such as in [15]. However, these approaches require careful development and lie outside the scope of the current work deliberately focused on the compositional evolution while heating rather that the compositional contrast between single particles.

Dissolution of γ′ precipitate populations

The compositional information obtained by EELS measurements at each temperature during *in situ* heating is illustrated in the elemental maps shown in Figure 7.8. The arrow shown at the top of the figure denotes the temperature to which each elemental map refers, and the range of the atomic concentration (at. %) for each element is shown in the colour bar

displayed next to the corresponding elemental maps. The region of interest indicated with a dashed square in the elemental maps at room temperature contains representative precipitates corresponding to all different γ′ precipitate populations, namely primary, secondary and tertiary γ′, as well as a grain boundary, located at its bottom right corner. The analysis of the same location enables direct observation of the compositional modifications during *in situ* heating and variations between the populations with temperature and exposure time.

At temperatures below 500 °C and even up to 700 °C (not included in Figure 7.8), no apparent changes in the elemental distributions seem to occur. At 800 °C, two successive maps were obtained, with a dwell of 20 minutes. During thermal exposure at 800 °C there is evident diffusion of chromium solutes towards the grain boundary seen in the depiction of grain boundaries in the Ni and Co maps. It is interesting to note that at this temperature the crowd of fine tertiary γ′ precipitates at the top corner of the region of interest begins to fade, especially in terms of its Ni content, indicating the initiation of the dissolution of this population. This is not observed for primary and secondary γ′ precipitates.

At 850 °C, the enrichment of chromium in the grain boundary region continues, as well as Ni and Co depletion in the same region. The diffusional phenomena that occur at this high temperature trigger the gradual dissolution of secondary γ′ precipitates that escalates at 900 °C. As shown by the arrows in the elemental maps of nickel and aluminium, the secondary γ′ precipitates located in the proximity of the grain boundaries have vanished at 900 °C, while the tertiary γ′ precipitate population appears to be completely dissolved. At even higher temperatures, at 950 °C, the large primary γ′ particle at the top right corner still remains not dissolved, while the fine secondary and tertiary γ′ populations have disappeared.

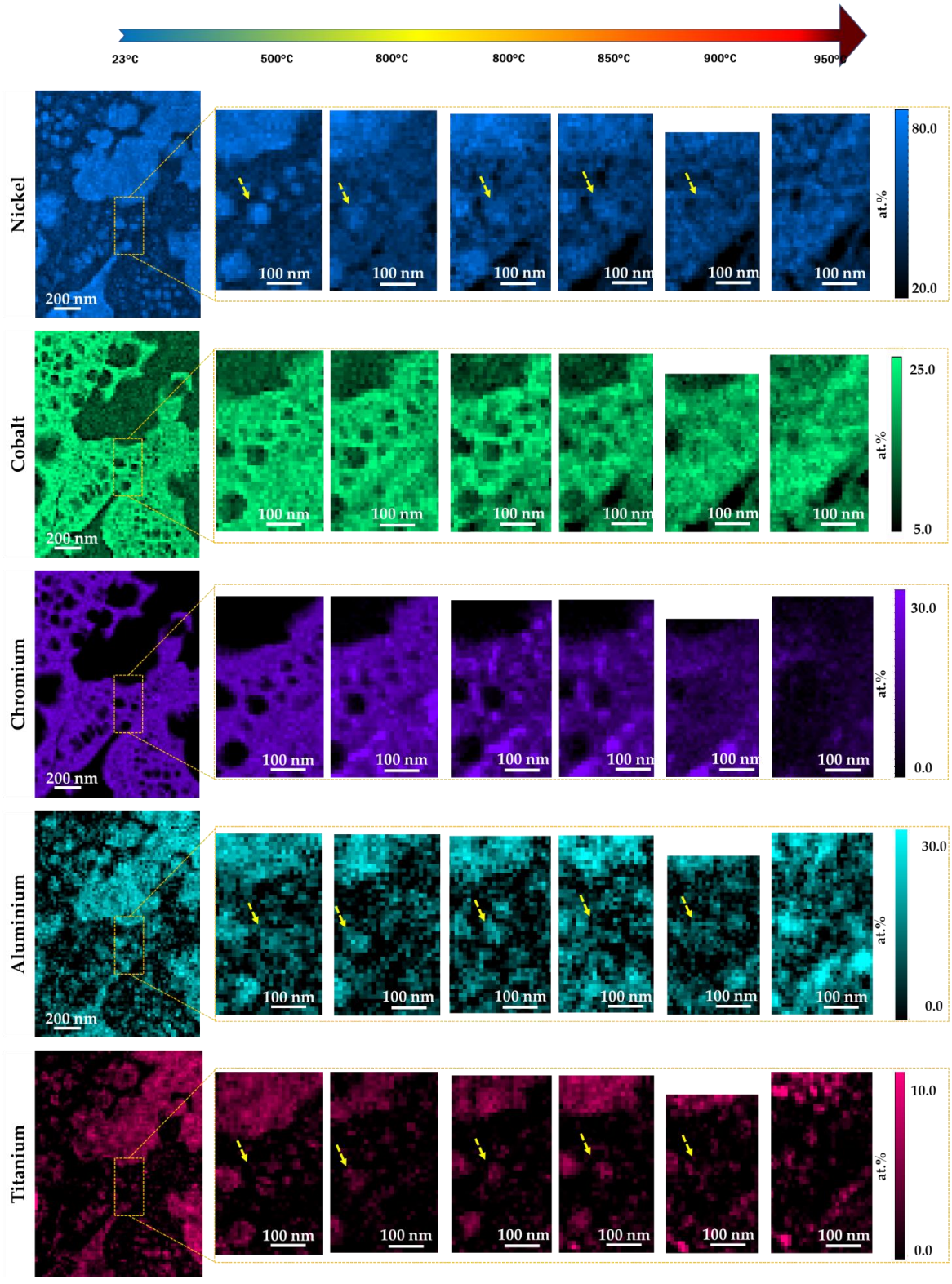


Figure 7.8: EELS elemental maps while *in situ* STEM heating, corresponding to the Ni L, Co L, Cr L, Al K and Ti L ionisation edges in the EELS spectrum.

Oxidation sequence during heating

During *in situ* heating, the diffusion of solutes is activated, stimulating not only the dissolution of γ′ populations, but also oxidation mechanisms. The HAADF images in Figure 7.9 depict the region of interest at three different temperatures, demonstrating the gradual formation of intragranular and intergranular oxides. The region of interest includes a grain boundary that runs along its diagonal, as well as a grain boundary that runs diagonally through its bottom right corner. The grain enclosed by the GBs contains various secondary γ′ precipitates. Analysis of the same location allows direct comparison of the compositional variations and re-distribution of elements with temperature and exposure time.

First and foremost, it can be clearly observed that when the temperature increases above 800 °C, localised oxidation reactions start to occur in the grain boundary region, which escalate around 900 °C. The intergranular oxides correspond to the dark features decorating the grain boundaries. Below 700 °, no oxidation reactions seem to occur. It has been reported though that even at medium temperatures (650 °C), nickel-base superalloys are prone to oxidation, driven by volume diffusion of elements, as well as interfacial and intergranular diffusion [87]. Along with the preferential intergranular oxidation, the formation of intragranular oxides can be seen in Figure 7.9. Fine bright features start to develop around 700 °C, and further coarsen at higher temperatures.

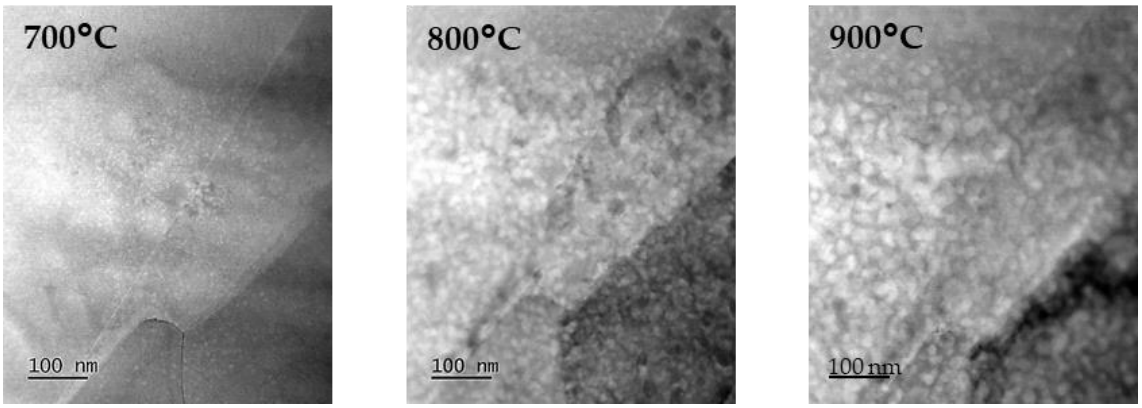


Figure 7.9: Low magnification STEM-HAADF images showing the gradual formation of intergranular and intragranular oxides while heating.

It is apparent that the intragranular oxides display different composition than the intergranular oxides, therefore they appear bright and dark respectively in the HAADF images. STEM-EELS mapping was employed to characterise the elemental distributions in the proximity of the GBs, as well as to detect any compositional modification of the γ' precipitate populations induced by oxidation. The initial stages of preferential intergranular oxidation, the sequential evolution and the gradual formation of intergranular and intragranular oxides are displayed in the elemental maps in Figure 7.10, which correspond to the O K ionisation edge. The line profiles in Figure 7.11 refer to the square region highlighted in Figure 7.10, and can describe in detail the distribution of each element in the proximity of the GBs at different temperatures while heating, providing quantitative information. The colours of the line profiles (from yellow to dark red) refer to the temperature range from 800 °C to 950 °C.

Figure 7.10 (a) and (b) portray the spatial distribution of oxygen in the region of interest at 800 °C. After 20 minutes of exposure time at this temperature, a noticeable increase in the concentration of oxygen can be observed at the grain boundary located at the bottom right corner. At this time, an increase of the Cr content in the same region had already occurred as also seen in Figure 7.8, and is followed by the subsequent increase in the O content. Apart from Cr, the oxidised region contains small quantities of Al and Ti, particularly within the intergranular penetrations, which are still mild. Regarding the other alloy constituents, the content of Ni and Co is significantly lowered in the oxidised area.

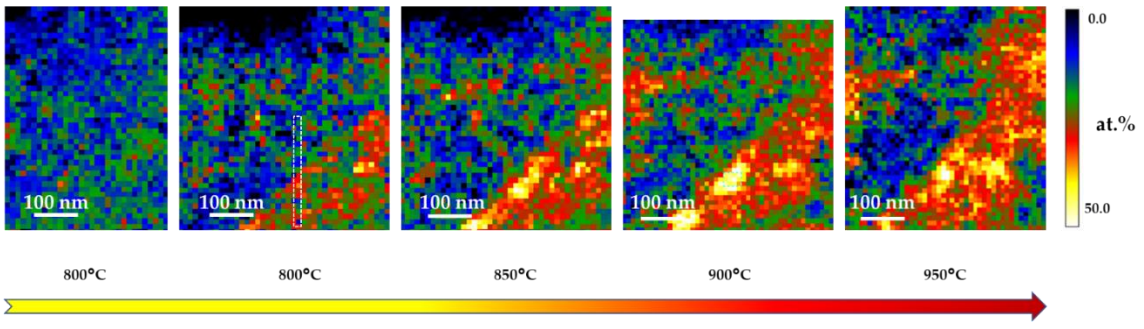


Figure 7.10: EELS maps of oxygen distribution while *in situ* STEM heating, corresponding to the O K ionisation edge in the EELS spectrum.

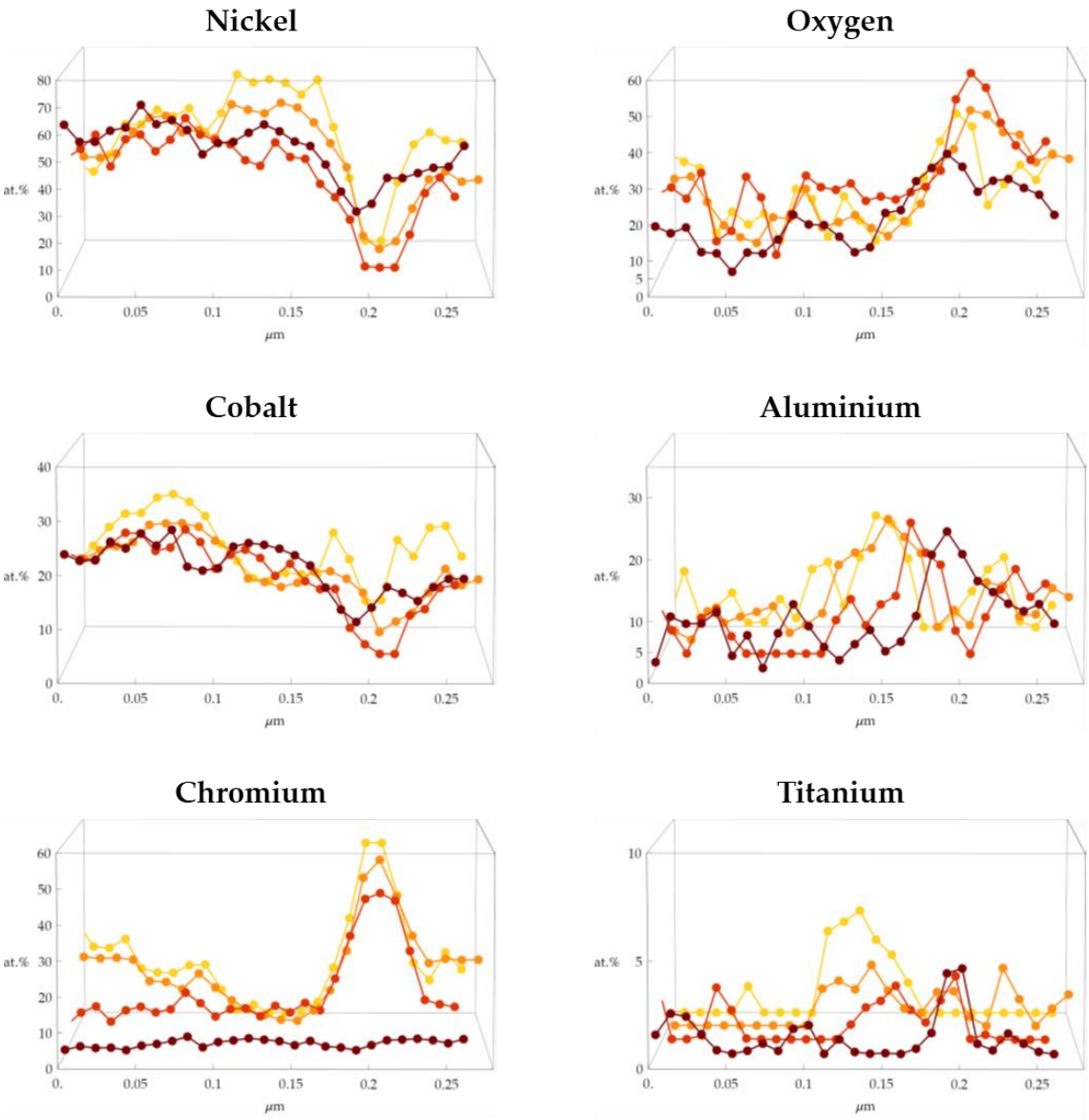


Figure 7.11: Line profiles of the evolution of the distribution of solutes while heating of the square region highlighted in Figure 7.10.

When the temperature is raised to 850 °C, a near-continuous Cr-rich oxide layer seems to develop at the GBs. The preferential intergranular oxidation results in the gradual depletion of chromium from the region adjacent to the grain boundaries, demonstrated in the line graphs in Figure 7.11. What is more, as clearly seen in the line profile of titanium, the Ti content of the secondary γ' particle adjacent to the GB is noticeably lowered, compared to that at 800 °C. At the same time, the Ti content of the intergranular oxide is significantly increased.

Therefore, it is apparent that the diffusion of Ti solutes from the γ′ particle to the oxides has taken place.

A close examination of Figure 7.12 reveals that the formation of oxides occurs not only along the grain boundary, but also within the grain, along the γ/γ′ interface. The dashed lines in Figure 7.12 correspond to grain boundaries, along which intergranular Cr-rich oxides have developed. At this temperature (850 °C), the elemental profile of γ′ populations is slightly modified, although the content of oxygen in the particles is considerably low. As clearly depicted in Figure 7.12, a secondary γ′ particle is surrounded by an Al-rich oxide that also contains quantities of Cr and Ti. What is more, Al is being depleted next to the oxide-particle interface.

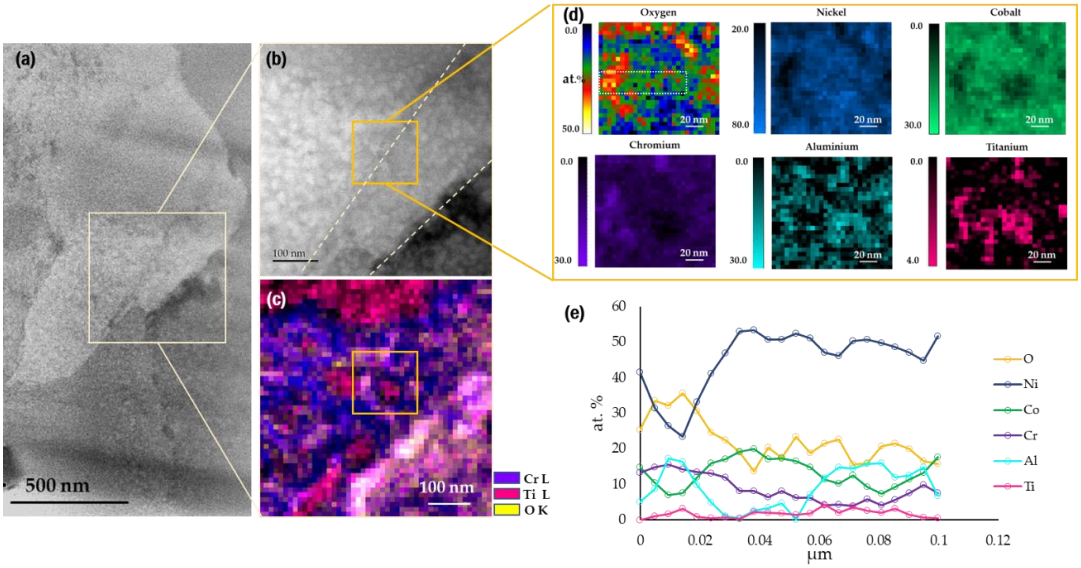


Figure 7.12: **(a)** Low magnification STEM-HAADF image of the region of interest at 850 °C, **(b)** Higher magnification STEM-HAADF image of the intergranular and intragranular oxides, **(c)** Qualitative compositional map showing the distribution of Cr, Ti and O in (b), **(d)** EELS elemental maps of the square region in (b), **(e)** Line profile of the distribution of solutes in the square region in (d).

After each temperature increment, the morphology of the intergranular oxides becomes more complex, developing protuberances within the neighbouring grains. At 900 °C, the nanoscale grain boundary penetrations sharpen considerably (Figure 7.10). At this temperature, the secondary γ′ particles adjacent to the grain boundaries have been partially or even fully dissolved (Figure 7.8), as the solutes that they contained have been, at least to

some extent, captured by the intergranular oxides. In particular, from the line profile of Al in Figure 7.11 it is evident that the peak in the aluminium content is gradually transferred from the particle to the intergranular oxide. This evolution of aluminium distribution represents a clear and direct evidence of the diffusion of aluminium solutes from the secondary γ′ particle to the grain boundary, where they become involved in the ongoing oxidation reaction. The distribution of titanium displays a similar behaviour, as Ti solutes diffuse from the γ′ particle to intergranular and intragranular oxides. It is interesting to note that only the γ′ particles located in the close proximity of the grain boundaries seem to be gradually dissolved at 900 °C, while the particles distributed in the grain interior do not display similar behaviour (Figure 7.8). The diffusion of solutes towards the boundary promotes the re-distribution of nickel and cobalt, clearly demonstrated in the line profile of cobalt in Figure 7.11 at 900 °C. The dissolution of the γ′ particle and the diffusion of γ′ forming solutes (Al, Ti, Ni) to the grain boundary is accompanied by the gradual Co enrichment of the region where the γ′ particle was located. As for oxygen, it appears to diffuse and distribute further in the grain interior.

At 950 °C, the secondary γ′ particle adjacent to the grain boundary is now fully dissolved and transformed to matrix γ. The region previously occupied by the γ′ particle is now depleted of aluminium and titanium and enriched in cobalt, as seen in the line profiles in Figure 7.11. At this temperature one can observe the dissolution not only of the particles in the vicinity of the GBs, but also of the entire secondary and tertiary γ′ precipitate populations. On the contrary, the large primary γ′ particle is still not dissolved at 950 °C.

Interestingly, at 950 °C the depletion of chromium as well as the reduction in the O content in the region of interest can be clearly observed in the line profiles in Figure 7.11 . This could be attributed to the spread of chromium and oxygen from the region of interest to different locations across the sample along grain boundaries as paths of faster diffusion, as well as to the evaporation of Cr, discussed in more detail in next sections (Section 7.4.4). The HAADF images in Figure 7.12 display the same region of the sample, before and after 23 minutes of thermal exposure at 950 °C. It is apparent that various oxides have been formed, particularly along the grain boundaries. They appear as the dark features in the HAADF images

in Figure 7.12, while their compositional profile is also shown in the same picture. The oxides contain a high chromium content, while they are depleted of Ni and Co. It should be highlighted though that the compositional information in the graph is mainly qualitative, considering the high relative thickness of the sample in that region (≈2.5) (Figure 7.12 (c)).

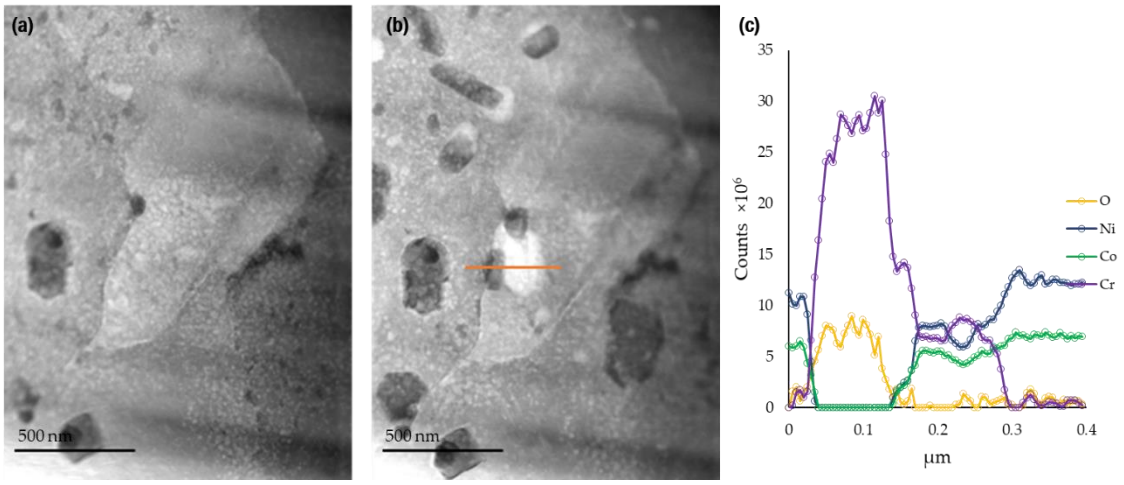


Figure 7.13: (a) Low magnification STEM-HAADF image of the region of interest at 950 °C, **(b)** Low magnification STEM-HAADF image of the same region after 23 minutes exposure at 950 °C, **(c)** Qualitative line profile of the region shown in (b).

From the close examination of the results obtained and described in detail in this section it becomes apparent that diffusional phenomena are progressively activated during heating promoting asymmetric solute redistribution and oxide formation. The results obtained provide a direct observation of the diffusion of solutes towards and across the grain boundaries and at the interphase interfaces, both of which are serving as paths of faster diffusion. With the main elements contributing to the oxide formation being chromium and aluminium, it is worth examining the temperature evolution of the content of each of these elements within the oxides. A qualitative illustration of the distributions of Al and Cr at each temperature is provided in Figure 7.14(a). It is apparent that the intergranular oxides are Cr-rich, while the intragranular oxide penetrations contain a higher Al content, especially at higher temperatures. The graphs in Figure 7.14 (b) and (c) provide quantitative information of the Al and Cr content of the oxides formed along the grain boundaries and within the grains, from the quantification of the Al K and Cr L ionisation edges in the high-loss EELS spectrum. They

correspond to the average value of 4 measurements for each temperature. The results can accurately describe the oxidation sequence in this complex alloy at the temperature range 800 – 950 °C. First, at 800 °C the redistribution of chromium solutes is observed leading to preferential concentration across the grain boundaries (Figure 7.8). EELS analysis confirmed the absence of any pre-existing Cr-enriched regions at the GB. At the same time, the concentration of oxygen gradually increases in the grain boundary region, stimulating intergranular oxidation reactions. At this temperature, preferential intergranular oxidation is encouraged, while limited intragranular oxidation is observed, so the values reported in the graph (c) correspond to 2 measurements.

At 850 °C, the concentration of oxygen increases, promoting the formation of a Cr-rich oxide particularly in the grain boundary regions, and sporadically at the γ/ γ' interfaces. At 900 °C, a near-continuous layer of chromia (Cr_2O_3) has occupied the grain boundaries. Additionally, the aluminium content of the intragranular and intergranular oxides seems to be strongly enhanced at 900 °C. In particular, the O/Al ratio of the intragranular oxides is equal to 1.54, which is very close to the elemental ratio of alumina (Al_2O_3). This coincides with the dissolution of the fine γ' precipitate populations, fuelling the oxides with γ' forming solutes, including Al and Ti. Indeed, not only the aluminium, but also the titanium content of the oxides is increased at high temperatures. At even higher temperatures at 950 °C, the intergranular Cr_2O_3 seems to decompose to form an oxide close to CrO_3 [166], while the depletion of chromium of the region of interest is observed. The diffusional phase transformations that control the kinetics of the oxidation mechanisms are accelerated at this high temperature, and thus numerous intergranular oxides are formed across the sample. It is also worth mentioning that the primary particle γ' located in the top-left corner of the qualitative maps in Figure 7.14 (a), is still not dissolved at this temperature (950 °C), while its compositional profile is not modified due to oxidation. Oxidation has occurred solely at the grain boundaries surrounding the particle, and occasionally at its interface with the γ matrix, while oxides have not been formed within the particle.

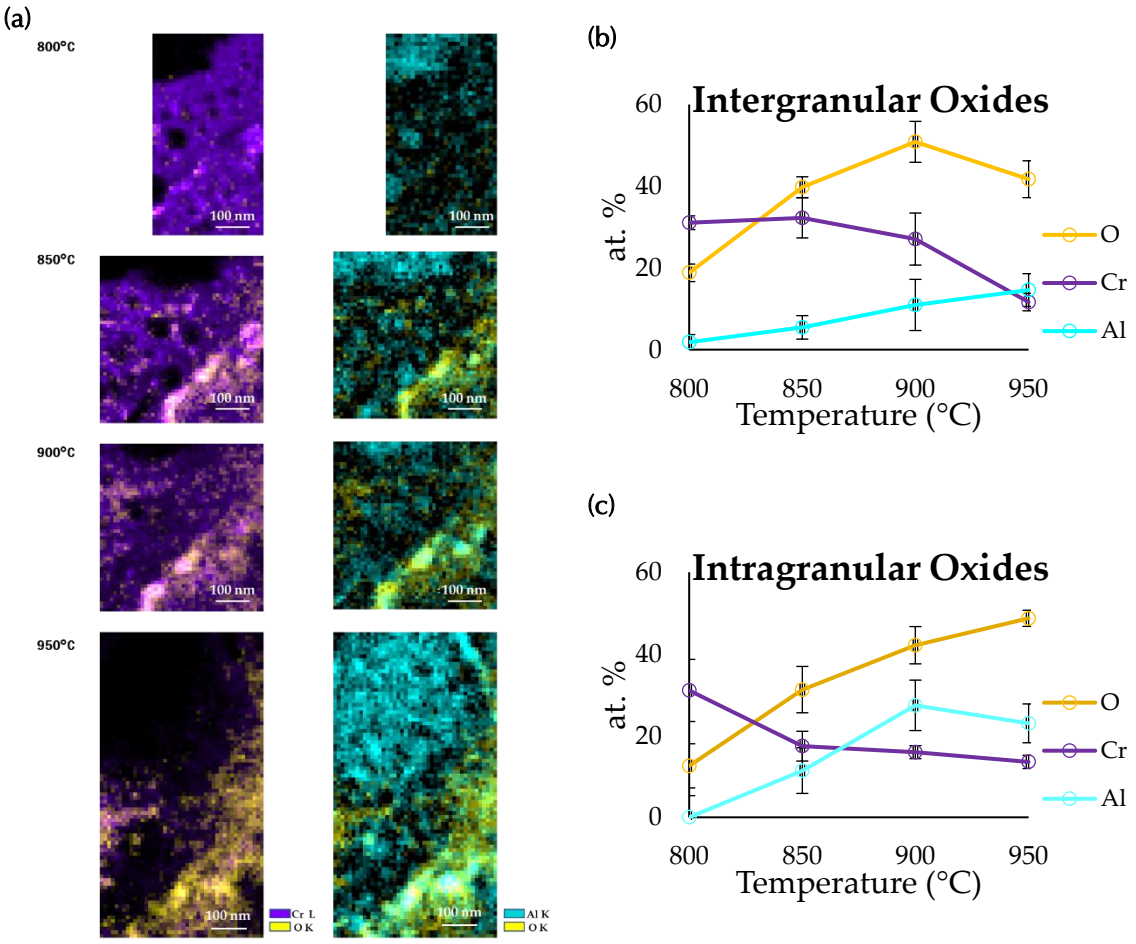


Figure 7.14: **(a)** Qualitative illustration of the distributions of O, Cr and Al at different temperatures, **(b)** Evolution of O, Cr and Al content of intergranular oxides while heating, **(c)** Evolution of O, Cr and Al content of intragranular oxides while heating.

7.3.4. Atom Probe Tomography

To complete the in-depth characterisation of the elemental distribution of the γ′ populations at room temperature and map the local elemental variations between them, experiments using atom probe tomography (APT) were carried out. APT measurements were utilised to provide a reliable reference point to validate the accuracy of the EELS quantitative measurements obtained during *in situ* heating in STEM.

Atom probe measurements were carried out on a fully heat-treated sample that was solution treated for 1 hour at a super solvus-temperature (1180 °C), furnace cooled with a cooling rate of 0.6 °C/s, and then annealed for 2 h at 850 °C and then for 4 h at 800 °C. For

APT analysis, matchsticks (0.5 x 0.5 x 15 mm) cut from the alloy forging after heat treatment were initially electropolished in a 10 vol% perchloric acid/ acetic acid solution, then finished with a solution of 2 vol% perchloric acid in butoxyethanol to obtain suitably sharp needle-shaped samples. APT data was collected using a Cameca LEAP™ 3000X HR instrument housed in the Department of Materials, University of Oxford. The samples were run in voltage mode at a specimen temperature of 50 K, with pulse frequency at 125 kHZ and pulse energy 80 pJ.

First and foremost, the results obtained by the quantification of the EELS spectrum at room temperature in Figure 7.7 are compared with the atom probe measurements in Figure 7.15, to get an idea of the reliability of the results. It is noted that the elemental concentration of Ni, Co and Cr are quantified very efficiently, capturing the overall distributions. However, the EELS quantification seems to overestimate significantly the content of aluminium, that may be understood considering the poor signal-to-noise ratio of the Al K edge. Additionally, the distribution of titanium is mapped adequately, while the quantitative values are also slightly overestimated. It should be mentioned that the results are not directly comparable, considering that APT was performed on a fully heat-treated sample, while *in situ* STEM coupled with EELS was performed on as forged sample. However, an estimate of the measurement quality can be obtained using the APT measurements as a reference.

One of the main focal points of this study is to quantify the local compositional variations between different γ' populations, for which APT is a valuable tool. In the atom probe reconstructions in Figure 7.15, both secondary and tertiary γ' particles are included, allowing direct comparisons to be made between them. To obtain accurate and reliable composition measurements, evaluations were conducted in different locations. Iso-concentration regions were used to isolate the different regions of the microstructure and allow accurate measurement of the composition of each feature. In particular, for tertiary γ', considering the small surface area of each single precipitate, the compositional data in Table 12 was averaged over several precipitates, in order to improve statistical analysis.

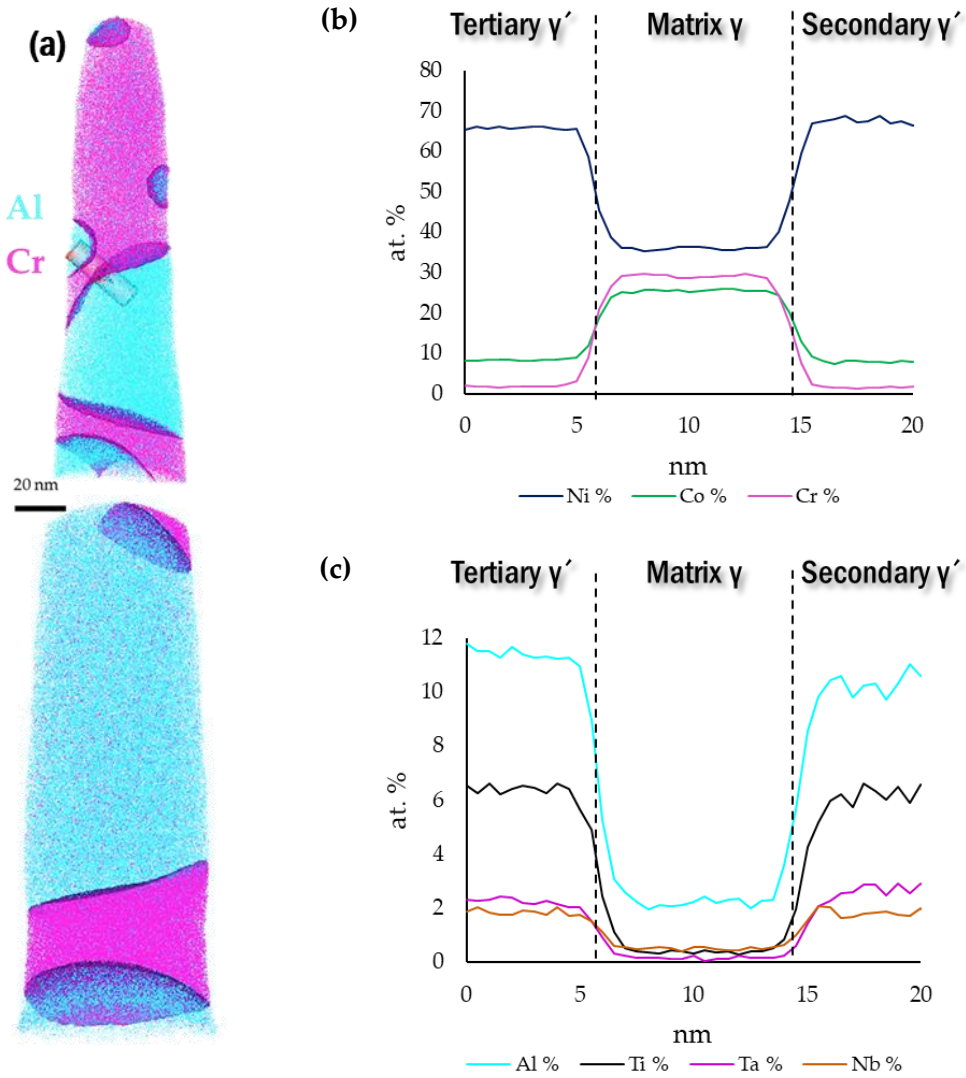


Figure 7.15: **(a)** Atom probe reconstructions showing distribution of Al and Cr, along with secondary and tertiary γ′ precipitates, **(b),(c)** Compositional profile of selected species, corresponding to the analysis cylinder marked in (a).

Figure 7.15 illustrates the compositional profiles across the precipitate-matrix interfaces, both for tertiary and for secondary γ′. For all the alloying elements, the transition zone widths in the γ /γ′ interfaces are around 2 nm, similar to previously reported measurements on superalloys [68]. What is more interesting though, is the enrichment of tertiary γ′ in Al, along with its higher W content. On the other hand, secondary γ′ contains a considerably higher amount of nickel, while it is also enriched in Ta and Ti. Similar observations on size-dependent compositional variations have also been detected in RR1000

[15]. The Al-enrichment of fine tertiary precipitates was attributed to the anomalous diffusion behaviour of aluminium, which follows an antisite-bridging diffusion mechanism [15, 64-65].

Table 12: Composition of γ′ precipitate populations as measured by atom probe tomography (at.%).

	Secondary γ′		Tertiary γ′	
	at.%	σ	at.%	σ
Ni	66.3549231	0.01596	65.2291599	0.177842
Co	8.0515681	0.00893	8.1892329	0.084476
Cr	1.61016301	0.00394	1.38276531	0.044782
Al	10.9264903	0.01097	11.6356236	0.096176
Ti	6.80623722	0.00911	6.59560628	0.083696
Ta	2.71026868	0.0058	2.53364058	0.055604
Nb	1.40118945	0.00367	1.74297433	0.039952
W	0.56518312	0.00401	0.9332142	0.04948
Si	0.63165848	0.00293	0.682561963	0.028148
Mn	0.35572206	0.00195	0.374114944	0.02161
Mo	0.33971276	0.00207	0.376930291	0.022334
Fe	0.26038627	0.00193	0.299561401	0.031906
B	0.01545982	0.00068	0.024372726	0.007285
C	0.00156872	0.00041	0.000241633	0.002488

7.4. Discussion

7.4.1. EELS Data Analysis and Quantification

For the data analysis and quantification of the EELS measurements, a model-based quantification approach was employed using the Gatan Microscopy Suite (GMS) software version 3.4.2 in which model-based quantification has been simplified and vastly improved (e.g., [167]). Among its main advantages one notes improved tolerance to the thickness of the

sample compared to conventional quantification the results of which are heavily influenced by thickness [168]. When mapping low concentration elements in specimens of varying thickness, the shape of the energy-loss spectrum varies with specimen thickness due to plural inelastic scattering events. Plural scattering effects were incorporated into the analysis to improve accuracy, while the analysis of the electron loss near-edge fine-structure (ELNES) features was excluded.

It has been shown that this approach offers a reasonably robust way of performing compositional quantification [167-168]. The principal challenge concerns achieving good accuracy, since artefacts and errors are may be introduced e.g due to incorrect determination of background for subtraction, of signal sum width, etc. Several modifications and extensions of this approach have been suggested to obtain a more accurate quantification [168]. However, this would solely affect the absolute values of the compositional measurements and not alter the elemental distributions and the overall trends in terms of evolution with temperature for the different elements. Therefore, the results obtained are undoubtedly reliable in terms of compositional variations and elemental distributions, while the absolute values should be treated as rough estimations of the actual atomic composition and not as precise measurements.

7.4.2. Oxidation of Platinum Layer at Room Temperature

The oxidation of the platinum layer on the edge of the sample is demonstrated in the elemental maps in Figure 7.16 (b), which refer to room temperature prior to *in situ* STEM heating. The oxide formed within the FIB-deposited Pt layer is also enriched in tungsten, while bands of aluminium, titanium and tantalum are also present (Figure 7.16 (a)). The deposition of a protective layer, typically of platinum, during sample preparation is essential for the preparation of very thin high-quality TEM lamellas and is the first step in the standard FIB lift-out technique. The exposure of the specimen to air after fabrication promotes the formation of an oxide on the platinum layer. At room temperature, PtO_2 is most probably invariably present on platinum surfaces, while PtO may also be formed [169]. It should be noted that

the oxidation is localised solely on the platinum layer, while the concentration of oxygen in the main sample seems to be insignificant. In particular, as observed in the elemental maps in Figure 7.16, at room temperature the Al-rich γ′ precipitate populations are free of oxygen, while the matrix contains a very mild O content.

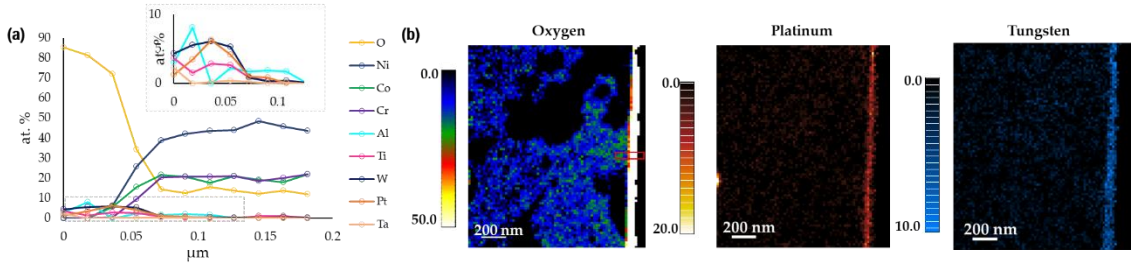


Figure 7.16: (a) Line profile of the elemental distribution at room temperature in the region highlighted with red in (b), **(b)** EELS elemental maps at room temperature, corresponding to the O K, Pt M, and W M ionisation edges in the EELS spectrum.

7.4.3. Preferential Intergranular Oxidation

It is well documented that surface oxidation in nickel-base superalloys usually leads to the formation of distinct layers consisting of a surface chromia (Cr_2O_3) film and a sub-surface internal oxidation zone (IOZ) of alumina (Al_2O_3) [88].The external layer of chromia often acts as a protective barrier against the potentially damaging environment [11]. It has been reported to contain detectable amounts of titania, and even discrete crystals of rutile (TiO_2) on its outer surface [11,88]. Underneath the surface oxide layers the internal oxidation zone of alumina is present forming acicular intergranular penetrations that may extend further to great depths into the alloy [88] along grain boundary as path of faster diffusion [11].

The rate of oxidation in terms of weight gain can be approximated as a parabolic function of time, while a parabolic function can also be used to describe the intergranular penetration rates of oxides of Al and Ti [11,88]. Chromium and aluminium are considered to be the predominant elements controlling the oxidation behaviour of nickel-base superalloys. However, other alloying elements, including Ti and Mn, can strongly affect the oxidation kinetics [11,92-93]. Numerous studies have documented the deleterious effect of titanium on

oxidation resistance [11,92]. Along with the formation of Ti-rich oxides, Ti alloying additions can enhance the growth rates of chromia. Additionally, titanium addition is known to promote the formation of titanium nitrides (TiN). At high temperatures (≤ 850 °C), sub-surface particles of TiN have been detected to form ahead of the internal oxidation zone of alumina, particularly at the alloy grain boundaries ahead of the alumina penetrations [11].

Thermally grown oxides may result in a significant degradation of the mechanical properties as they react with solutes, removing them from the solid solution. In particular, significant depletion of Cr has been reported ahead of and within the IOZ, due to the migration of Cr to the external oxide [88]. Moreover, the Al-rich internal oxidation zone of alumina causes consumption of Al, thus promoting the dissolution of γ′ particles [91]. Various studies [88-93] report as a consequence the formation of a zone depleted of γ′ precipitates ahead of the oxidation front that is also associated with a reduction of strength. The γ′ denuded zones can lead to local mechanical softening, which can cause serious performance degradation, with further strength reduction caused by oxidation-induced damage appearing as intergranular cracking penetrating into the alloy.

Ding et al. [91] performed *in situ* environmental transmission electron microscopy (ETEM) to study the γ/γ′ microstructural modifications induced by oxidation in a single crystal nickel-base superalloy. In this study, oxygen was observed to be present preferentially within the γ′ phase, and it was shown that after thermal exposure at 850 °C when aluminium oxidised to alumina, Al depletion in the γ′ phase induced the phase transformation of ordered γ′ to disordered γ phase. Additionally, using elemental EELS mapping, they observed that the diffusion path of oxygen was more likely to be associated with the γ/γ′ interface rather than matrix channels.

The oxidation reactions occurring in this study are thought to arise partially from the diffusion of low quantities of oxygen contained in or adsorbed on the sample, from the inevitable oxidation of the protective platinum layer and side surfaces of the lamella after FIB fabrication of the sample. Additionally, low oxygen partial pressure persisting under the vacuum conditions of the TEM chamber can be sufficient to oxidise certain metals [170].

Indeed, Kojima et al. [170] observed the growth of tungsten oxide nanowires forming via vapor–solid–solid growth mechanism when using a thin resistively heated tungsten wire. This observation strongly indicates that the vacuum conditions in the TEM retain sufficient partial pressure of oxygen to oxidise tungsten upon heating. For *in situ* heating, the sample was mounted on a micro-hotplate, which would normally consist of tantalum, tungsten or platinum. This could explain why the oxide detected at sample edge at room temperature contains significant amount of tungsten alongside platinum (Figure 7.16).

Despite the low quantities of oxygen involved, preferential intergranular oxidation reactions were found to take place while heating, likely to be triggered by the strong diffusional driving forces at elevated temperatures. In the alloy system under consideration, regardless of the widely accepted strong oxygen affinity of aluminium, the oxygen content in the γ′ populations was observed to be remarkably low, even at very high temperatures, as can be clearly discerned from Figure 7.12 and Figure 7.14. Instead, oxygen is mainly concentrated at grain boundaries and at interphase interfaces, both of which are serving as paths for faster diffusion. This observation suggests that in this study the oxidation reactions do not introduce any microstructural modifications and cannot be attributed for the dissolution of the γ′ precipitate populations. Instead, their sequential evolution seems to be strongly affected by the dissolution path of the particles, reacting with γ′-forming solutes after precipitate dissolution. Besides, the Al content of this alloy (3.16 wt.%) is lower compared to its Cr content (12.69 wt.%), which could be an additional factor promoting the formation of chromia and hindering the formation of alumina, which would introduce Al depletion and possibly γ/γ′ microstructural modifications.

7.4.4. Elemental Vaporisation

Under vacuum conditions metals tend to become volatile at temperatures well below their melting points. When performing any type of vacuum heat treatment, evaporation and/or sublimation of material and specific elemental components may occur and should be

carefully considered. Elemental vaporisation often occurs during solution heat treatment of nickel-base superalloys leading to changes in composition, concentration gradients, microstructural instabilities and superficial defect formation [171].

The vapour pressure of any substance increases non-linearly with temperature according to the Clausius-Clapeyron relation [172-173]. Dong et al. [171] accurately determined the partial vapour pressures of Ni, Al and Cr at high temperatures using the Knudsen effusion mass spectrometry (KEMS) both for pure substances and in Ni-Al-Cr alloys of varying compositions. They experimentally observed that the partial vapour pressure of Ni and Cr was approximately two orders of magnitude higher than that of Al. Additionally, although the partial pressure of Ni plays a dominant role due to nickel being the major element in the alloy, the partial vapour pressure of Cr increases significantly with the amount of this solute in the alloy. Based on their observations, the authors concluded that the sublimation of different alloys is driven by the entropy of Cr in the Ni-Al-Cr system.

Since the rate of evaporation is greatest in high vacuum conditions, elemental evaporation almost inevitably occurs during *in situ* heating in STEM at elevated temperatures. This provides a probable reason for the observed sharp Cr content decrease at 950 °C, while the quantities of the other alloying constituents do not display similar behaviour. At even higher temperatures up to 1000 °C further sample degradation is clearly observed, with Cr depletion indicating its continuing vaporisation.

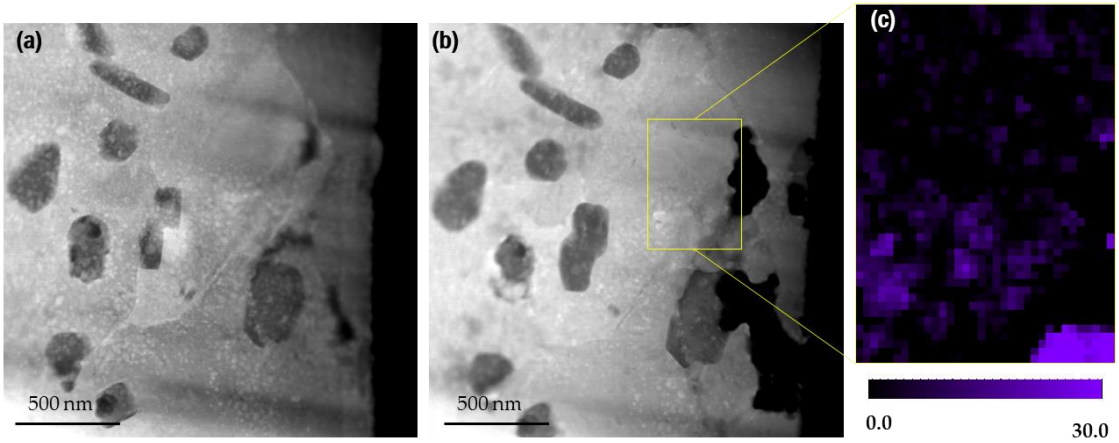


Figure 7.17: **(a)** Low magnification STEM-HAADF image of the region of interest at 1000 °C, **(b)** Low magnification STEM-HAADF image of the same region after 15 minutes exposure at 1000 °C, **(c)** EELS elemental map of Cr distribution in the square region in (b).

7.4.5. Dissolution Path for Different γ′ Precipitate Populations

STEM mapping yields spatially resolved information from nano- down to atomic-scale, and with the help of elemental concentration quantification using EDX or EELS can reveal the evolution of diffusional phenomena and oxidation mechanisms. Although local observation data provides poor statistics and may not be representative of bulk behaviour, significant qualitative or semi-quantitative information can be extracted. Various experimental approaches such as thermoanalysis techniques and neutron diffraction have been employed to study the evolution of the γ′ precipitate populations while heating in terms of structure and misfit strain with the γ matrix in this alloy system. The similarity in lattice parameters between the secondary and tertiary γ′ populations though leads to tightly overlapping diffraction peaks which prevent reliable fitting of them separately. Therefore, *in situ* heating under the electron beam in STEM provides a valuable methodology for the observation of each population that enables direct comparisons between them.

Using this technique, it has been possible to obtain experimental evidence of the difference in the solvus temperature between different γ′ precipitate populations. This variation has also been observed and reported previously. Masoumi et al. [31] studied the mechanisms and kinetics of the reprecipitation of γ′ particles during cooling from super- and sub-solvus temperatures in alloy AD730™, a nickel-base superalloy for turbine disc applications. Using Differential Thermal Analysis (DTA) they detected two distinct endothermal peaks while heating corresponding to the dissolution of secondary and primary γ′ precipitate populations. In particular, depending on the heating rate, the dissolution of secondary γ′ particles occurred in the range between 800 to 825 °C for heating rates equal to 65 °C/min and 120 °C/min respectively. The dissolution of primary γ′ happened around 1080 °C for the 10 °C/min heating rate and 1120 °C for the 120 °C/min heating rate. These observations are in good agreement with my approach, considering the larger size of primary compared to secondary γ′ particles.

7.4.6. Dissolution Sequence of γ′ Precipitate Populations

The dissolution of second phase particles in precipitation-hardened alloy systems is a diffusion-controlled transformation process dominated by the diffusion of solute atoms across the interface between the particles and the matrix [174]. For an isolated particle in an infinite matrix, the concentration field $C(r,t)$ of an element in solid solution can be described using Fick's second law of diffusion given by:

$$D\,\nabla^2 C = \frac{\partial C}{\partial t} \tag{88}$$

where D is the volume diffusion coefficient of solute in the matrix. Eq. (88) must conform to the boundary conditions [175-176], with respect to the solute concentrations in the matrix, C_M, and at the precipitate/matrix interface, C_I, expressed as:

$$\begin{aligned} C(r=\infty,t) &= C_M \quad t \geq 0 \\ C(r,t=0) &= C_M \quad r \geq R_0 \\ C(r=R_0,t) &= C_I \quad t > 0 \end{aligned} \tag{89}$$

A critical parameter describing the kinetics of the diffusional phase transformations of growth and dissolution is the supersaturation parameter k, given by:

$$k = 2\frac{C_I - C_M}{C_P - C_I} \tag{90}$$

In the case of dissolution, one more initial condition should be considered, which is the initial, finite, nonzero precipitate radius R_0:

$$r(t=0) = R_0,\, R_0 > 0 \tag{91}$$

What is more, the flux balance condition should be satisfied as follows:

$$(C_P - C_I)\frac{\mathrm{d}r}{\mathrm{d}t} = D\left.\frac{\partial C}{\partial r}\right|_{r=R_0} \tag{92}$$

where C_P, the solute concentration in the precipitate, is taken to be constant and independent of r and t.

Exact analytical solutions for the kinetics of the diffusion-controlled phase transformations are often difficult to obtain, but several mathematical approximations have

been developed. Aaron and Kotler [176] performed a detailed theoretical study in which they reviewed several widely used mathematical approximations for modelling the growth and dissolution of spherical and planar precipitates. Namely, in their study, they compare and evaluate the reversed-growth, the invariant-field ($\partial C/\partial t = 0$) and the invariant-size ($\mathrm{d}r/\mathrm{d}t = 0$) analyses. The invariant field approximation, for which $\partial C/\partial t = 0$, is generally made in terms of morphological stability calculations. In this case, the dissolution or growth problem may be approached with reasonable accuracy by considering R to be constant and solving the time-independent (Laplace) diffusion problem in the matrix. The invariant size approximation, also known as stationary interface approach, imposes the requirement for $\mathrm{d}r/\mathrm{d}t = 0$, based on the concentration inequality $(C_P - C_M) \gg (C_I - C_M)$ that ensures that $r(t)$ is a slowly varying function of time. In their study, Aaron and Kotler showed that the invariant size approximation is valid for both growth and dissolution of spherical and planar precipitates. Particularly, for the case of dissolution, the stationary interface analysis appears to be the most accurate approximation since it alone satisfies all the boundary conditions without any further assumptions. On the other hand, the invariant field and the reversed-growth analyses ignore the boundary condition $C(r \geq R_0, t = 0) = C_M$, as there is a finite gradient surrounding the precipitate at $t = 0$ resulting from the fact that $R_0 \neq 0$. Between these, the one which most closely approaches the stationary-interface approximation for dissolving spherical precipitates is the reversed-growth approximation in the limit of small $|k|$. Considering its relevant simplicity, this approach will be used in the context of this discussion.

In the limit of small k, the reversed-growth solution can provide an accurate approximation of the dissolution of spherical particles [175-176]. In accordance with this approach, the time evolution of the radius of the spheroidal particles $r(t)$ under isothermal conditions is given by:

$$r(t) = \left[{R_0}^2 - kDt\right]^{-1/2} \tag{93}$$

where R_0 is the initial, nonzero radius, D is the volume diffusion coefficient in the matrix and k is the supersaturation parameter. It is worth pointing out that for most alloy systems of interest $|k| < 0.3$ and in fact $|k| < 0.1$ is quite typical [175-176].

For a spherical particle precipitated in a dilute binary solid solution matrix, according to the well-known Gibbs–Thomson effect, the interfacial concentration C_I is related to the curvature of particle/matrix interface, as follows:

$$C_I = C_e \exp\left[\frac{2\gamma\Omega}{R_B T}\frac{1}{r}\right] \tag{94}$$

where C_e is equilibrium interfacial concentration, γ is the specific interfacial energy of the matrix with the precipitate, Ω is the mean atomic (or molar) volume of the particle, R_B is the Universal gas constant [8.314x10^3 J /(K. kmol)], T is the absolute temperature and r is the current radius of a spherical particle.

For spherical particles, the Gibbs–Thomson relation in Eq. (94) could be written as:

$$C_I = C_e \exp\left[\frac{2}{3}\frac{\gamma\Omega}{R_B T}S\right] \tag{95}$$

where S is the surface-to-volume ratio. Since the surface-to-volume ratio of tertiary γ′ precipitates is larger compared to secondary γ′, the concentration at the interface of the former, C_{I_t} , is higher than that of the latter, C_{I_s}. This, in turn means that the value of the supersaturation parameter of tertiary γ′, k_t, given by Eq. (90), exceeds that of secondary γ′ precipitates k_s, assuming that both populations have the same concentration C_P (C_M is the same for both):

$$C_{I_t} > C_{I_s} \Rightarrow k_t > k_s \tag{96}$$

Therefore, since $k_t > k_s$ and $R_{0_t} < R_{0_s}$, it can be concluded that under isothermal conditions less time is required for the dissolution of smaller tertiary γ′ precipitates than for larger secondary γ′ particles, according to the reverse growth approximation (Eq. (93)).

The Gibbs–Thomson effect alters the interfacial concentration at particle boundary depending on their radii in accordance with the Gibbs energy minimisation principle. There

are three contributions to the total free energy change that govern the formation or dissolution of second phase particles. The first is the reduction of the volume free energy ΔG_V, with its contribution to the overall energy being the product of ΔG_V by the volume of the nucleus. The second energy contribution arises from the interfacial energy per unit area γ. Finally, the lattice distortion of the matrix due to the presence of the second phase particle leads to energy contribution equal to $V\Delta G_S$. The total free energy change is equal to the sum of these contributions, that is:

$$\Delta G = V\Delta G_V + A\gamma + V\Delta G_S \tag{97}$$

The driving force for spontaneous phase transformations is the reduction of Gibbs free energy G. Considering a binary system consisting of phases α and β under increasing temperature, progression towards equilibrium is accomplished by a decrease in the interfacial energy term achieved by particle dissolution when the temperature exceeds the solvus temperature T_s . When the temperature is equal to T_s, both phases are thermodynamically stable and they have the same free energy, so:

$$\Delta G = 0 \Leftrightarrow \Delta H - T_s\Delta S = 0 \Leftrightarrow \Delta H = T_s\Delta S \tag{98}$$

Since the difference between specific phase entropies vary slowly around the solvus temperature, it is often assumed to be constant and equal to its value ΔS at T_s. Then the temperature dependence of ΔG can be expressed as:

$$\Delta G(T) = \Delta H - T\Delta S = T_s\Delta S - T\Delta S \Rightarrow \Delta G(T) = (T_s - T)\Delta S \tag{99}$$

Defining $\Delta T = T - T_s$ as the degree of overheating (or undercooling if negative), one concludes that as the temperature increases over the value of the solvus temperature T_s, the thermodynamic driving force for the dissolution of the phase β increases. Additionally, the diffusion rate increases with increasing temperature following an Arrhenius type of temperature dependence that leads to variation over several orders of magnitude, but over large range of temperatures. Considering the above, in the vicinity of the solvus temperature, T_s, the temperature dependence of the rate of dissolution could be assumed to be linearly

related to the degree of overheating. For the kinetics of dissolution, k is a critical parameter strongly related to the rate of dissolution in the reverse growth approximation given by Eq. (93). This could be expressed by the following form in terms of k:

$$k \propto (T - T_s) \tag{100}$$

Therefore, during heating the dissolution of tertiary γ′ should occur at lower temperatures than for secondary γ′ particles due to the different supersaturation parameters:

$$k_t > k_s \Rightarrow T - T_{s_t} > T - T_{s_s} \Rightarrow T_{s_t} < T_{s_s} \tag{101}$$

This conclusion is in accordance with the experimental observations described in this study. The dissolution of finer particles (tertiary γ′) was observed to initiate at lower temperatures than larger sized particles (secondary γ′). This observation has been explained using basic thermodynamic principles and diffusion kinetics. Conforming to the Gibbs-Thomson relation, the difference between C_{I_t} and C_{I_s} induces a diffusive flux of solute atoms from smaller to larger particles. Solutes diffuse through the concentration gradients across the surface of the smaller sized particles through the matrix to the surface of larger sized particles. Likewise, in diffusion-driven coarsening the average particle radius increases, and the total number of particles decreases with time, as does the total free surface energy of the system resulting in the reduction of Gibbs free energy [31].

7.5. Conclusions

In this study, *operando* nanoscale observation of the dissolution of γ′ populations in a new polycrystalline nickel-base superalloy was achieved by performing *in situ* heating of thin lamella samples under the electron beam in STEM. The dissolution of finer particles (tertiary γ′) was observed to initiate at lower temperatures than larger sized particles (secondary γ′). To explain this observation, basic thermodynamic principles and diffusion kinetics were used. The surface-to-volume ratio of tertiary γ′ precipitates is larger than that of secondary γ′ thus according to the Gibbs-Thomson relation the concentration at the interface of the former, C_{I_t},

is higher than that of the latter, C_{I_s}. The difference between C_{I_t} and C_{I_s} induces a difference in the supersaturation parameter of the two populations, with larger supersaturation for tertiary γ′ particles. Therefore, their different supersaturation parameter defines the kinetics of the dissolution and explains the experimentally observed dissolution of tertiary γ′ at lower temperatures than secondary γ′ particles while heating.

In situ STEM heating, combined with electron energy loss spectroscopy (EELS) technique, enables probing diffusion-mediated phenomena, including the preferential intergranular oxidation. The oxidation reactions occurring in this study arise partially from the diffusion of low quantities of oxygen contained in the sample, and from low oxygen partial pressure existing under the high vacuum conditions of the TEM column. Low quantities of oxygen induced the preferential intergranular formation of chromia followed by the formation of alumina at the γ/γ′ interface. The oxygen content in the γ′ populations was observed to be remarkably low, even at very high temperatures. This observation suggests that in this study the oxidation reactions do not introduce any microstructural modifications to the γ′ precipitate populations. Instead, their sequential evolution seems to be strongly affected by the dissolution of the particles reacting with γ′ forming solutes after the precipitate dissolution.

To validate the accuracy of the EELS quantitative measurements and complete the in-depth characterisation of the elemental distribution of the γ′ populations at room temperature, additional measurements with atom probe tomography (APT) were performed. Local elemental variations between the secondary and tertiary γ′ populations were detected, in agreement with previously detected elemental differences. The elemental concentration of Ni, Co and Cr were quantified very efficiently by the EELS quantification while the content of aluminium seems to be overestimated, while mapping of its distribution was still valid.

8

Conclusions & Future Work

Towards improving the overall gas turbine efficiency, scientists and engineers have to face the challenge of expanding the operational limits of superalloys outside the current envelope. In this context, new and improved alloy formulations are constantly designed and produced aiming to reduce the weight of the components and assemblies, increase the operating temperature, or both. Higher γ′ volume fraction alloys have been developed among the new alloy formations, with a multimodal distribution of γ′ that is tailored with careful consideration of the applied heat treatment. Considering the fundamental role of γ′ precipitation in the high temperature mechanical performance of nickel-base superalloys, the overall objective of this study has been to investigate the multimodal distribution of the γ′ precipitate populations in a new high γ′ content nickel-base superalloy. The results obtained contribute to improving the understanding on the mechanism behind the formation of different γ′ precipitate populations and the findings have a broad applicability to precipitation-hardened alloy systems.

During cooling from the solution temperature, multiple nucleation bursts occur at different temperatures when leading to the minimisation of Gibbs free energy. The cooling rate defines the precipitation kinetics and controls the size of the particles formed. In this study, a simple yet accurate correlation between the size of γ′ precipitates and the cooling rate was derived able to provide accurate predictions of the precipitate size distribution. The analysis in this work also provides evidence that the formation of each of the γ′ precipitate populations is dominated by different growth mechanism towards energy minimisation

depending on the surface-to-volume ratio. Consequently, differences in terms of morphology, structure, and composition among the different populations of γ′ precipitates are produced. In this study, local variations in the lattice parameter of different precipitate populations were detected, quantified, and related to local compositional variations. Moreover, in this work the dissolution of each of the γ′ populations was experimentally observed to occur at different temperatures while heating to solution temperature. The findings in this study provide first direct evidence of the Gibbs-Thomson effect: the dissolution of finer particles was observed to initiate at lower temperatures than larger sized particles. This fundamental result is of particular importance and can provide useful insights into the precipitation of secondary phases in alloy systems. Additionally, the *operando* measurements obtained provide a clear observation of the diffusion of solutes towards and across the grain boundaries and at the interphase interfaces and can provide quantitative input data for validating future numerical simulations.

The results of this study can be used to provide useful design guidelines to optimise the applied heat treatment to tailor the characteristics of γ′ precipitate populations for the optimum combination of the desired properties. In polycrystalline nickel-base superalloys, optimal resistance to high temperature deformation is achieved by a fine distribution of secondary and tertiary γ′ precipitates within the grains, coupled with a small fraction of intergranular γ′ precipitates to induce grain boundary serrations. This microstructure can be generated by a two-step cooling with a slow initial cooling to slightly below the primary γ′ solvus temperature followed by fast cooling [35]. Using the findings of this work accurate predictions of the particle size distribution can be obtained, even without knowing the large number of temperature-dependent material properties required for complex modelling.

Below, a more detailed overview of the most important findings of this study is provided:

In Chapter 4, *in situ* neutron diffraction was employed to monitor the changes in the interplanar spacing of the matrix and the γ′ precipitate phase while heating to super-solvus temperature. Based on Eshelby's inclusion method, the temperature evolution of the γ/γ′

lattice parameter misfit was correlated to the thermal mismatch between the matrix γ and the γ′ precipitate phase introduced due to their different thermal expansion coefficients. A straightforward reliably validated correlation was derived demonstrating that the temperature evolution of the lattice misfit is dominated solely by the difference between the thermal expansion coefficients of the matrix and the precipitates, while the volume fraction of particles does not contribute to the temperature evolution of γ/γ′ lattice misfit. Moreover, using the experimental measurements, a simple model was formulated based on the definition of the thermal expansion coefficient able to describe the thermal evolution of the lattice parameters of γ and γ′ phases with accuracy.

In Chapter 5, through quantitative image analysis on BSE images, a power law dependence of secondary and tertiary γ′ precipitate size on the cooling rate from super-solvus temperature was observed and quantified. McLean′ s theory of growth of γ′ in nickel alloys was recast to include the effect of cooling rate rather than isothermal conditions and a model was built able to rationalise the experimentally observed trend providing useful insights into the growth mechanism of each γ′ precipitate population. The growth of secondary γ′ during cooling from the solution temperature is controlled by a combination of diffusion-controlled and interface-controlled mechanisms, and the growth of tertiary γ′ is dominated by the interface-controlled mechanism. The case of intergranular secondary γ′ precipitates was also examined, for which there is a combination of diffusion-controlled growth and interface diffusion growth.

In Chapter 6, the structural and compositional variations between different γ′ precipitate populations were investigated at room temperature using HR-STEM coupled with STEM-EDX. Using HR-STEM imaging the interplanar spacings of intergranular and intragranular secondary γ′ precipitates were measured, and their lattice parameters were determined. The lattice parameter of intergranular secondary γ′ was found to be larger than that of intragranular secondary γ′. STEM-EDX analysis unveiled compositional variations between the two populations that explain their different lattice parameters. The intergranular secondary γ′ precipitate population is enriched in Ni, Ta, Ti, and Al, compared to

intragranular secondary γ′. Also, the content of Fe and W was observed to be slightly higher in intergranular γ′. Moreover, a boride phase detected at the grain boundary region was identified as M_2B by comparing HR-STEM images to simulations of binary boride structures commonly precipitated in nickel-base superalloys. Based on the experimental results on the local strain distribution and on previous studies in the literature, the effect of boron addition on the lattice strain distribution at the grain boundary region and the formation of intergranular γ′ is discussed.

In Chapter 7, *operando* nanoscale observation of the dissolution of γ′ populations was achieved by performing *in situ* heating of thin lamella samples in STEM. The dissolution of finer particles (tertiary γ′) was observed to initiate at lower temperatures than larger sized particles (secondary γ′). Fundamental thermodynamic principles and diffusion kinetics were used to explain this observation: due to the larger surface-to-volume ratio of tertiary γ′ compared to secondary γ′, the concentration at the interface of the former is higher than that of the latter according to the Gibbs-Thomson relation. The difference between the concentration at the interface of tertiary and secondary γ′ induces a difference in the supersaturation parameter of the two populations, with larger supersaturation for tertiary γ′ particles. Therefore, considering that the kinetics of dissolution is defined by the supersaturation parameter, dissolution occurs at the different temperatures for the two populations. The results of this study provide a direct observation of the Gibbs-Thomson effect in terms of the dissolution behaviour of different γ′ populations. Interestingly, the typical heat treatment of the alloy examined in this study, Alloy 11, consists of super-solvus solution heat treatment followed by ageing heat treatments, for 2 hours at 850 °C and then for 4 hours at 800 °C. Although the diffusional phenomena may appear accelerated in nanoscale samples than in the bulk, the findings provide a rational explanation for ageing heat treatment temperatures and could be used to modify and optimise them.

Moreover, *in situ* STEM heating coupled with EELS enabled probing the nano-diffusion pathways for preferential intergranular oxidation during heating. Low quantities of oxygen induced oxidation reactions and in particular intergranular formation of chromia followed by

the formation of alumina at the γ/γ′ interface. The oxidation reactions did not introduce any microstructural modifications to the γ′ precipitate populations, as the oxygen concentration in the γ′ particles was observed to be remarkably low.

Atom probe tomography was performed to complete the in-depth characterisation of the elemental distribution of the γ′ populations at room temperature. Local elemental variations between the secondary and tertiary γ′ populations were detected, in agreement with previously reported elemental differences.

Although this research has increased the understanding over the complex phenomena that accompany the γ′ precipitation, there are still and always will be more questions to be answered. I believe that further investigations should be addressed at the following specific areas:

1. The derived correlation on the temperature evolution of the γ/γ′ lattice misfit could be further validated by measuring the thermal expansion of the lattice parameter of γ and γ′ in the unconstrained condition. By dissolving the surrounding matrix to extract the precipitate phase, the thermal expansion coefficient of γ′ could be determined using *in situ* neutron diffraction while heating. Also, it would be interesting to apply the derived model to a wide range of alloying systems with varying volume fraction of γ′ to confirm its reliability.
2. The correlation between the formation of intergranular secondary γ′ particles and energy minimisation by the reduction of lattice distortion should be further investigated. Lattice strain is introduced to the host matrix by the precipitation of coherent and semi-coherent particles with larger lattice parameters to maintain coherency. In the case of incoherent particles, their different cell volume as well as their different thermal expansion coefficients may also introduce lattice distortion to the surrounding region. The observations obtained in this study along with relevant literature demonstrate that the formation of borides can increase the strain distribution at the grain boundaries. However, it is not straightforward to isolate the effect of boron addition form the various phenomena that occur in this complex alloy. Therefore, a

way to approach this would be to study a simple alloy formulation without any refractory elements but containing a high volume fraction of γ′. When slow cooled from super-solvus solution heat treatment, intergranular secondary γ′ particles may not be formed in this case, if there is no requirement for strain reduction.

3. *In situ* high temperature STEM-EELS of fully heat-treated samples should be performed at isothermal conditions at the critical temperatures identified in this study (850°C and 900°C). Besides the validation of my original observations, this experiment could be used to quantify important parameters defining the diffusion kinetics, by monitoring the changes that occur to the size of the particles with time and the time required for the dissolution of different populations. Additionally, this experiment would provide insights into the optimal design of the applied ageing heat treatment cycles of similar alloy formulations.

Bibliography

[1]Sims, C.T. A History of Superalloy Metallurgy for Superalloy Metallurgists. *Superalloys.* **1984**, 399–419.

[2]Marsh, A.L. US Patent 811859A. **1906**.

[3]Bradley, A.J.; Taylor, A.; A, P.R.S.L. An X-ray analysis of the nickel-aluminium system. *Proc. R. Soc. London. Ser. A - Math. Phys. Sci.* **1937**, *159*, 56–72.

[4]Taylor, A.; R. W. Floyd. The constitution of nickel-rich alloys of the nickel chromium aluminium system *J. Inst. Metals.* **1953,** 81.

[5]Tin, S. *The Deformation and Processing of Structural Materials*; Woodhead Publishing, **2005**.

[6]Rolls Royce Company. *The Jet Engine*. St Ives Westerham Ltd, 5th edition, **2001**.

[7]Reed, R.C. *The superalloys: Fundamentals and applications*; Cambridge University Press, **2006**.

[8]Pollock, T. M.; Tin, S. Nickel-Based Superalloys for Advanced Turbine Engines: Chemistry, Microstructure and Properties. *Journal of Propulsion and Power.* **2006**, *22*(2), 361-374.

[9]Sims, C. T.; Stoloff, N. S.; Hagel, W. C. *Superalloys II.* New York: Wiley,**1987**.

[10]Bremer, F.J.; Beyss, M.; Wenzl, H. The order–disorder transition of the intermetallic phase Ni3Al. *Phys. Status Solidi* **1988**, *110*, 77–82.

[11]Cruchley, S.; Evans, H.E.; Taylor, M.P.; Hardy, M.C.; Stekovic, S. Chromia layer growth on a Ni-based superalloy: Sub-parabolic kinetics and the role of titanium. *Corros. Sci.* **2013**, *75*, 58–66.

[12]Kontis, P.; Yusof, H.A.M.; Pedrazzini, S.; Danaie, M.; Moore, K.L.; Bagot, P.A.J.; Moody, M.P.; Grovenor, C.R.M.; Reed, R.C. On the effect of boron on grain boundary character in a new polycrystalline superalloy. *Acta Mater.* **2016**, *103*, 688–699.

[13]Long, F.; Yoo, Y.S.; Jo, C.Y.; Seo, S.M.; Song, Y.S.; Jin, T.; Hu, Z.Q. Formation of η and σ phase in three polycrystalline superalloys and their impact on tensile properties. *Mater. Sci. Eng. A* **2009**, *527*, 361–369.

[14]Monajati, H.; Jahazi, M.; Bahrami, R.; Yue, S. The influence of heat treatment conditions on γ′ characteristics in Udimet® 720. *Mater. Sci. Eng. A* **2004**, *373*, 286–293.

[15]Chen, Y.Q.; Francis, E.; Robson, J.; Preuss, M.; Haigh, S.J. Compositional variations for small-scale gamma prime (γ′) precipitates formed at different cooling rates in an advanced Ni-based superalloy. *Acta Mater.* **2015**, *85*, 199–206.

[16]Jackson, M.P.; Reed, R.C. Heat treatment of UDIMET 720Li: The effect of microstructure on properties. *Mater. Sci. Eng. A* **1999**, *259*, 85–97.

[17]Gabb, T.P.; Gayda, J.; Telesman, J.; Garg, A. The effects of heat treatment and microstructure variations on disk superalloy properties at high temperature. *Proc. Int. Symp. Superalloys 2008,* **2008**, 121–130.

[18]Reed, R., Crudden, D., Raeisinia, B., Hardy, M. European Patent Specification. Patent EP2894234B1, 19 October **2016**.

[19]Hardy, M.C.; Argyrakis, C.; Kitaguchi, H.S.; Wilson, A.S.; Buckingham, R.C.; Severs, K.; Yu, S.; Jackson, C.; Pickering, E.J.; Llewelyn, S.C.H.; et al. Developing Alloy Compositions for Future High Temperature Disk Rotors. *Proc. Int. Symp. Superalloys 2020,* **2020**.

[20]McLean, D. Predicting growth of γ′ in nickel alloys. *Met. Sci.* **1984**, *18*, 249–256.

[21]Du, B.; Shi, Z.; Yang, J.; Chu, Z.; Cui, C.; Sun, X.; Sheng, L.; Zheng, Y. M_5B_3 Boride at the Grain Boundary of a Nickel-based Superalloy. *J. Mater. Sci. Technol.* **2016**, *32*, 265–270.

[22]Harada, H.; Murakami, H. Design of Ni-Base Superalloys. In *Computational Materials Design*; Springer Berlin Heidelberg, **1999**; pp. 39–70.

[23]Pollock, T.M.; Argon, A.S. Creep resistance of CMSX-3 nickel base superalloy single crystals. *Acta Metall. Mater.* **1992**, *40*, 1–30.

[24]Jena, A.K.; Chaturvedi, M.C. The role of alloying elements in the design of nickel-base superalloys. *J. Mater. Sci.* **1984**, *19*, 3121–3139.

[25]Semiatin, S.L.; Zhang, F.; Larsen, R.; Chapman, L.A.; Furrer, D.U. Precipitation in powder-metallurgy, nickel-base superalloys: review of modeling approach and formulation of engineering methods to determine input data. *Integr. Mater. Manuf. Innov.* **2016**, *5*, 41–60.

[26]Roebuck, B.; Cox, D.; Reed, R. The Temperature Dependence Of γ′ Volume Fraction In A Ni-Based Single Crystal Superalloy from Resistivity Measurements. *Scr. Mater.* **2001**, *44*, 917–921.

[27]Christofidou, K.A.; Jones, N.G.; Pickering, E.J.; Flacau, R.; Hardy, M.C.; Stone, H.J. The microstructure and hardness of Ni-Co-Al-Ti-Cr quinary alloys. *J. Alloys Compd.* **2016**, *688*, 542–552.

[28]Furrer, D.U.; Fecht, H.J. γ′ Formation in superalloy U720LI. *Scr. Mater.* **1999**, *40*.

[29]Vaunois, J.-R.; Cormier, J.; Villechaise, P.; Devaux, A.; Flageolet, B. Influence of both γ′ distribution and grain size on the tensile properties of UDIMET 720Li at room temperature. In Proceedings of the *7th International Symposiumon Superalloy 718 & Derivatives*, **2010**.

[30]Laurence, A.; Cormier, J.; Villechaise, P.; Billot, T.; Petinari-sturmel, F.; Hantcherli, M.; Mompiou, F. Impact of the solution cooling rate and of thermal aging on the creep properties of the new cast & wrought René 65 TM Ni-based superalloy. In *Proceedings of the 8th International Symposium on Superalloy 718 and Derivatives*, **2014**.

[31]Masoumi, F.; Shahriari, D.; Jahazi, M.; Cormier, J.; Devaux, A. Kinetics and mechanisms of γ′ reprecipitation in a Ni-based superalloy. *Sci. Rep.* **2016**, *6*, 28650,

[32]Zhao, S.; Xie, X.; Smith, G.D.; Patel, S.J. Gamma prime coarsening and age-hardening behaviors in a new nickel base superalloy. *Mater. Lett.* **2004**, *58*, 1784–1787.

[33]Mitchell, R.J.; Li, H.Y.; Huang, Z.W. On the formation of serrated grain boundaries and fan type structures in an advanced polycrystalline nickel-base superalloy. *J. Mater. Process. Technol.* **2009**, *209*, 1011–1017.

[34]Qiu, C.L.; Andrews, P. On the formation of irregular-shaped γ′ and serrated grain boundaries in a nickel-based superalloy during continuous cooling. *Mater. Charact.* **2013**, *76*, 28–34

[35]Alabbad, B.; Li, L.; Tin, S. Controlling the grain boundary morphology and secondary γ′ precipitate size distribution in Ni-base superalloys. *J. Alloys Compd.* **2019**, *775*, 931–941.

[36]Tang, Y.T.; Karamched, P.; Liu, J.; Haley, J.C.; Reed, R.C.; Wilkinson, A.J. Grain boundary serration in nickel alloy inconel 600: Quantification and mechanisms. *Acta Mater.* **2019**, *181*, 352–366.

[37]Tang, Y.T.; Wilkinson, A.J.; Reed, R.C. Grain Boundary Serration in Nickel-Based Superalloy Inconel 600: Generation and Effects on Mechanical Behavior. *Metall. Mater. Trans. A Phys. Metall. Mater. Sci.* **2018**, *49*, 4324–4342.

[38]Larson, J. M. Carbide morphology in p/m IN-792. *Metallurgical Transactions A*. **1976**, 7(10), 1497-1502.

[39]Furrer, D.; Fecht, H. Ni-based superalloys for turbine discs. *JOM.* **1999** *51*(1), 14-17.

[40]Koul, A.K.; Gessinger, G.H. On the mechanism of serrated grain boundary formation in Ni-based superalloys. *Acta Metall.* **1983**, *31*, 1061–1069.

[41]Danflou, H.; Macia, M.; Sanders, T.; Khan, T. Mechanisms of Formation of Serrated Grain Boundaries in Nickel Base Superalloys. *Proc. Int. Symp. Superalloys 1996,* **1996.**

[42]M.F. Henry , Y.S. Yoo , D.Y. Yoon , J. Choi , The dendritic growth of γ′ precipitates and grain boundary serration in a model nickel-Base superalloy, *Metall. Mater. Trans. A* **1993**, 24 (8), 1733–1743.

[43]Cahn, R.W.; Siemers, P.A.; Geiger, J.E.; Bardhan, P. The order-disorder transformation in Ni_3Al and Ni_3AlFe alloys-I. Determination of the transition temperatures and their relation to ductility. *Acta Metall.* **1987**, *35*, 2737–2751.

[44]Ricks, R.A.; Porter, A.J.; Ecob, R.C. The Growth of γ′ Precipitates in Ni-base Superalloys. *Acta Metall.* **1983**, *31*, 43–53.

[45]MacKay, R.A.; Nathal, M. V. γ′ Coarsening in High Volume Fraction Nickel-Base Alloys. *Acta Metall. Mater.* **1990**, *38*, 993–1005.

[46]Hardy, M.; Reed. R.; Crudden, D. European Patent Specification EP 3 112 485 B1, 15 August 2018.

[47]Tian, S. G.; Xia, D.; Li, T.; Meng, F. L.; Wang, M. G.; Yu, X. F. Influence of element W and microstructure evolution on lattice parameters and misfits of nickel-base superalloys. *Journal of Aeronautical Materials.* **2008**, *28*(4), 12-16.

[48]Bruno, G.; Schumacher, G.; Pinto, H.C.; Schulze, C. Measurement of the lattice misfit of the nickel-base superalloy SC16 by high-energy synchrotron radiation. *Metall. Mater. Trans. A Phys. Metall. Mater. Sci.* **2003**, *34*, 193–197.

[49]Muller, L.; Glatzel, U.; Feller-Kniepmeier, M. Modelling thermal misfit stresses in nickel-base superalloys containing high volume fraction of γ′ phase. *Acta Metall. Mater.* **1992**, *40*, 1321–1327.

[50]Bruno, G.; Pinto, H.C. The Kinetics of the Gamma-Prime Phase and Its Strain in the Nickel Base Superalloy SC16 Studied by In-Situ Neutron and Synchrotron Radiation Diffraction. *Proc. Int. Symp. Superalloys* 2004, **2004**, 837–848.

[51]Collins, D.M.; Yan, L.; Marquis, E.A.; Connor, L.D.; Ciardiello, J.J.; Evans, A.D.; Stone, H.J. Lattice misfit during ageing of a polycrystalline nickel-base superalloy. *Acta Mater.* **2013**, *61*, 7791–7804.

[52]Mitchell, R.J.; Preuss, M.; Hardy, M.C.; Tin, S. Influence of composition and cooling rate on constrained and unconstrained lattice parameters in advanced polycrystalline nickel-base superalloys. *Mater. Sci. Eng. A* **2006**, *423*, 282–291.

[53]Eshelby, J.D. *The Determination Of The Elastic Field Of An Ellipsoidal Inclusion, And Related Problems*; **1957**.

[54]Behrouzghaemi, S.; Mitchell, R.J. Morphological changes of γ′ precipitates in superalloy IN738LC at various cooling rates. *Mater. Sci. Eng. A* **2008**, *498*, 266–271.

[55]Khachaturyan, A.G.; Semenovskaya, S. V.; Morris, J.W. Theoretical analysis of strain-induced shape changes in cubic precipitates during coarsening. *Acta Metall.* **1988**, *36*, 1563–1572.

[56]Lifshitz, I.M.; Slyozov, V. V. The kinetics of precipitation from supersaturated solid solutions. *J. Phys. Chem. Solids* **1961**, *19*, 35–50.

[57]Grosdidier, T.; Hazotte, A.; Simon, A. Precipitation and dissolution processes in γ/γ′ single crystal nickel-based superalloys. *Mater. Sci. Eng. A* **1998**, *256*, 183-196.

[58]Kontis, P.; Alabort, E.; Barba, D.; Collins, D.M.; Wilkinson, A.J.; Reed, R.C. On the role of boron on improving ductility in a new polycrystalline superalloy. *Acta Mater.* **2017**, *124*, 489–500.

[59]Masoumi, F.; Jahazi, M.; Shahriari, D.; Cormier, J. Coarsening and dissolution of γ′ precipitates during solution treatment of AD730™ Ni-based superalloy: Mechanisms and kinetics models. *J. Alloys Compd.* **2016**, *658*, 981–995.

[60]Fisher, J.C. Calculation of diffusion penetration curves for surface and grain boundary diffusion. *J. Appl. Phys.* **1951**, *22*, 74–77.

[61]Paul, A.; Laurila, T.; Vuorinen, V.; Divinski, S. V Short-Circuit Diffusion. In *Thermodynamics, Diffusion and the Kirkendall Effect in Solids*; Springer International Publishing: Cham, **2014**; pp. 429–491.

[62]Fu, C.L.; Janotti, A.; Krcmar, M. On the Diffusion of Alloying Elements in the Nickel-Base Superalloys. *Proc. Int. Symp. Superalloys 2004,*. **2004**, 867–876.

[63]Sun, M.; Li, Z.; Zhu, G.; Liu, W.; Liu, S.; Wang, C. Diffusion in Ni-Based Single Crystal Superalloys with Density Functional Theory and Kinetic Monte Carlo Method 1 Introduction 2 Construction of calculation model with relevant experiments. **2016**, *20*, 603–618.

[64]Cermak, J.; Rothova, V. Concentration dependence of ternary interdiffusion coefficients in Ni 3 Al/Ni 3 Al–X couples with X = Cr, Fe, Nb and Ti. **2003**, *51*, 4411–4421.

[65]Cermak, J.; Gazda, A.; Rothova, V. Interdiffusion in ternary Ni 3 Al / Ni 3 Al-X diffusion couples with X = Cr , Fe , Nb and Ti. **2003**, *11*, 939–946.

[66]Singh, A.R.P.; Nag, S.; Hwang, J.Y.; Viswanathan, G.B.; Tiley, J.; Srinivasan, R.; Fraser, H.L.; Banerjee, R. Influence of cooling rate on the development of multiple generations of γ′ precipitates in a commercial nickel base superalloy. *Mater. Charact.* **2011**, *62*, 878–886.

[67]Chen, Y.Q.; Slater, T.J.A.; Lewis, E.A.; Francis, E.M.; Burke, M.G.; Preuss, M.; Haigh, S.J. Measurement of size-dependent composition variations for gamma prime (γ′) precipitates in an advanced nickel-based superalloy. *Ultramicroscopy* **2014**, *144*, 1–8.

[68]Bagot, P.A.J.; Silk, O.B.W.; Douglas, J.O.; Pedrazzini, S.; Crudden, D.J.; Martin, T.L.; Hardy, M.C.; Moody, M.P.; Reed, R.C. An Atom Probe Tomography study of site preference and partitioning in a nickel-based superalloy. *Acta Mater.* **2017**, *125*, 156–165.

[69]Xiang, S.; Mao, S.; Shen, Z.; Long, H.; Wei, H.; Ma, S.; Zhang, J.X.; Chen, Y.; Zhang, J.; Zhang, B.; et al. Site preference of metallic elements in $M_{23}C_6$ carbide in a Ni-based single crystal superalloy. *Mater. Des.* **2017**, *129*, 9–14.

[70]Tin, S.; Pollock, T.M.; King, W.T. Carbon Additions and Grain Defect Formation in High Refractory Nickel-Base Single Crystal Superalloys. **2012**, 201–210.

[71]Lvov, G.; Levit, V.I.; Kaufman, M.J. Mechanism of primary MC carbide decomposition in Ni-base superalloys. *Metall. Mater. Trans. A Phys. Metall. Mater. Sci.* **2004**, *35 A*, 1669–1679.

[72]Hu, X.B.; Qin, X.Z.; Hou, J.S.; Zhou, L.Z.; Ma, X.L. Microstructural characterization of the $M_{23}C_6$ carbide in a long-term aged Ni-based superalloy. *Philos. Mag. Lett.* **2017**, *97*, 43–49.

[73]Thuvander, M.; Stiller, K. Microstructure of a boron containing high purity nickel-based alloy 690. *Mater. Sci. Eng. A* **2000**, *281*, 96–103.

[74]Qin, X.Z.; Guo, J.T.; Yuan, C.; Hou, J.S.; Ye, H.Q. Precipitation and thermal instability of $M_{23}C_6$ carbide in cast Ni-base superalloy K452. *Mater. Lett.* **2008**, *62*, 258–261.

[75]Collins, D.M.; Conduit, B.D.; Stone, H.J.; Hardy, M.C.; Conduit, G.J.; Mitchell, R.J. Grain growth behaviour during near-γ′ solvus thermal exposures in a polycrystalline nickel-base superalloy. *Acta Mater.* **2013**, *61*, 3378–3391.

[76]Kontis, P.; Li, Z.; SegersΔll, M.; Moverare, J.J.; Reed, R.C.; Raabe, D.; Gault, B. The Role of Oxidized Carbides on Thermal-Mechanical Performance of Polycrystalline Superalloys. *Metall. Mater. Trans. A Phys. Metall. Mater. Sci.* **2018**, *49*, 4236–4245.

[77]Kontis, P.; Kostka, A.; Raabe, D.; Gault, B. Influence of composition and precipitation evolution on damage at grain boundaries in a crept polycrystalline Ni-based superalloy. *Acta Mater.* **2019**, *166*, 158–167.

[78]Xia, F.; Sangid, M.D.; Xiao, Y.; Gong, X.; Gang, T.; Chen, L.; Xu, W.W. Theoretical investigation of the crystallographic structure, anisotropic elastic response, and electronic properties of the major borides in Ni-based superalloys. *Philos. Mag.* **2020**, *100*, 998–1014.

[79]Sanyal, S.; Waghmare, U. V; Subramanian, P.R.; Gigliotti, M.F.X. Effect of dopants on grain boundary decohesion of Ni: a first-principles study. *Appl. Phys. Lett.* **2008**, *93*, 223113.

[80]Hu, X.B.; Zhu, Y.L.; Sheng, N.C.; Ma, X.L. The Wyckoff positional order and polyhedral intergrowth in the M_3B_2- and M_5B_3-type boride precipitated in the Ni-based superalloys. *Sci. Rep.* **2015**, *4*, 7367.

[81]Zhang, H.R.; Ojo, O.A. Cr-rich nanosize precipitates in a standard heat-treated Inconel 738 superalloy. *Philos. Mag.* **2010**, *90*, 765–782.

[82]Hu, X.B.; Zhu, Y.L.; Ma, X.L. Crystallographic account of nano-scaled intergrowth of M_2B-type borides in nickel-based superalloys. *Acta Mater.* **2014**, *68*, 70–81.

[83]Kaufman, M.J.; Levit, V.I. Characterization of chromium boride precipitates in the commercial superalloy GTD 111 after long-term exposure. *Philos. Mag. Lett.* **2008**, *88*, 259–267.

[84]Cadel, E.; Lemarchand, D.; Chambreland, S.; Blavette, D. Atom probe tomography investigation of the microstructure of superalloys N18. *Acta Mater.* **2002**, *50*, 957–966.

[85]Sheng, N.; Liu, J.; Jin, T.; Sun, X.; Hu, Z. Precipitation Behaviors in the Diffusion Affected Zone of TLP Bonded Single Crystal Superalloy Joint. *J. Mater. Sci. Technol.* **2015**, *31*, 129–134.

[86]Ma, J.; Jiang, W.; Wang, J.; Zhang, Y.; Zhang, Z. Initial oxidation behavior of a single crystal superalloy during stress at 1150 °C. *Sci. Rep.* **2020**, *10*, 1–9.

[87]Molins, R.; Andrieu, E. Analytical TEM study of the oxidation of nickel based superalloys. *Le J. Phys. IV* **1993**, *03*, C9-469-C9-475.

[88]Cruchley, S.; Evans, H.; Taylor, M. An overview of the oxidation of Ni-based superalloys for turbine disc applications: surface condition, applied load and mechanical performance. *Mater. High Temp.* **2016**, *33*, 465–475.

[89]Everaerts, J.; Salvati, E.; Li, H.; Li, W.; Korsunsky, A.M. Mechanical properties of thermally grown submicron oxide layers on a nickel-based superalloy. *Corros. Sci.* **2020**, *165*, 108388.

[90]Chen, Y.; Reed, R.C.; Marquis, E.A. As-coated thermal barrier coating: Structure and chemistry. *Scr. Mater.* **2012**, *67*, 779–782.

[91]Ding, Q.; Shen, Z.; Xiang, S.; Tian, H.; Li, J.; Zhang, Z. In-situ environmental TEM study of γ′-γ Phase transformation induced by oxidation in a nickel-based single crystal superalloy. *J. Alloys Compd.* **2015**, *651*, 255–258.

[92]Nagai, H.; Okabayashi, M. Deleterious effect of ti addition on the oxidation resistance of Ni-20Cr alloy. *Trans. Japan Inst. Met.* **1981**, *22*, 691–698.

[93]Pedrazzini, S.; Child, D.J.; West, G.; Doak, S.S.; Hardy, M.C.; Moody, M.P.; Bagot, P.A.J. Oxidation behaviour of a next generation polycrystalline Mn containing Ni-based superalloy. *Scr. Mater.* **2016**, *113*, 51–54.

[94]Dyson, B.F.; McLean, M. Creep Deformation of Engineering Alloys: Developments from Physical Modeling. *ISIJ Int.* **1990**, *30*, 802–811.

[95]Murakumo, T.; Kobayashi, T.; Koizumi, Y.; Harada, H. Creep behaviour of Ni-base single-crystal superalloys with various γ′ volume fraction. *Acta Mater.* **2004**, *52*, 3737–3744.

[96]Manonukul, A.; Dunne, F.P.E.; Knowles, D. Physically-based model for creep in nickel-base superalloy C263 both above and below the gamma solvus. *Acta Mater.* **2002**, *50*, 2917–2931.

[97]Locq, D.; Caron, P.; Raujol, S.; Pettinari-Sturmel, F.; Coujou, A.; Clément, N. On the Role of Tertiary γ′ Precipitates in the Creep Behaviour At 700 °C of a PM Disk Superalloy. *Proc. Int. Symp. Superalloys 2004,* **2004**, 179–187.

[98]Stevens, R.A.; Flewitt, P.E.J. The effects of γ′ precipitate coarsening during isothermal aging and creep of the nickel-base superalloy IN-738. *Mater. Sci. Eng.* **1979**, *37*, 237–247.

[99]Dyson, B.F.; McLean, M. Particle-coarsening, σ_0 and tertiary creep. *Acta Metall.* **1983**, *31*, 17–27.

[100]Sugui, T.; Minggang, W.; Huichen, Y.; Xingfu, Y.; Tang, L.; Benjiang, Q. Influence of element Re on lattice misfits and stress rupture properties of single crystal nickel-based superalloys. *Mater. Sci. Eng. A* **2010**, *527*, 4458–4465.

[101]Goff, S.; Couturier, R.; Guйtaz, L.; Burlet, H. Effect of the microstructure on the creep behavior of PM Udimet 720 superalloy - Experiments and modeling. *Mater. Sci. Eng. A* **2004**, *387–389*, 599–603.

[102]Yeh, A.C.; Lu, K.W.; Kuo, C.M.; Bor, H.Y.; Wei, C.N. Effect of serrated grain boundaries on the creep property of Inconel 718 superalloy. *Mater. Sci. Eng. A* **2011**, *530*, 525–529.

[103]Chateau, E.; Rémy, L. Oxidation-assisted creep damage in a wrought nickel-based superalloy: Experiments and modelling. *Mater. Sci. Eng. A* **2010**, *527*, 1655–1664.

[104]Leo Prakash, D.G.; Walsh, M.J.; Maclachlan, D.; Korsunsky, A.M. Crack growth micro-mechanisms in the IN718 alloy under the combined influence of fatigue, creep and oxidation. *Int. J. Fatigue* **2009**, *31*, 1966–1977.

[105]Woodford, D.A. Environmental damage of a cast nickel base superalloy. *Metall. Trans. A* **1981**, *12*, 299–308.

[106]Roebuck, B.; Brooks, M.; Pearce, A. *Good Practice Guide for Miniature ETMT Tests*; NPL Good Practice Guide, **2016**.

[107]Bragg, W.H.; Bragg, W.L. The reflection of X-rays by crystals. *Proc. R. Soc. London. Ser. A, Contain. Pap. a Math. Phys. Character* **1913**, *88*, 428–438.

[108]Cullity, B.D.; Stock, S.R. *Elements of X-ray diffraction, 3rd edition*; **2001**.

[109]Collins, D.M.; Souza, N.D.; Panwisawas, C. In-situ neutron diffraction during stress relaxation of a single crystal nickel-base superalloy. *Scr. Mater.* **2017**, *131*, 103–107.

[110]Jackson, M.P.; Starink, M.J.; Reed, R.C. Determination of the precipitation kinetics of Ni 3 Al in the Ni – Al system using differential scanning calorimetry. **1999**, *264*, 26–38.

[111]Erdman, N.; Bell, D.C.; Reichelt, R. Scanning Electron Microscopy. In *Springer Handbook of Microscopy*; Hawkes, P.W., Spence, J.C.H., Eds.; Springer International Publishing: Cham, **2019**; pp. 229–318.

[112]Holzer, L.; Cantoni, M. Review of FIB-tomography. In *Nanofabrication Using Focused Ion and Electron Beams: Principles and Applications*; Oxford University Press: New York, USA, **2014**; pp. 410–435.

[113]Levin, B.D.A.; Padgett, E.; Chen, C.C.; Scott, M.C.; Xu, R.; Theis, W.; Jiang, Y.; Yang, Y.; Ophus, C.; Zhang, H.; et al. Nanomaterial datasets to advance tomography in scanning transmission electron microscopy. *Sci. Data* **2016**, *3*, 1–11.

[114]Kogure, T. Chapter 2.9 - Electron Microscopy. In *Handbook of Clay Science*; Bergaya, F., Lagaly, G.B.T.-D. in C.S., Eds.; Elsevier, **2013**; Vol. 5, pp. 275–317.

[115]Reimer, L.; Kohl, H. *Transmission Electron Microscopy*; **2012**; Vol. 53.

[116]Müller, J. A Study on Microstructures and Extended Defects in Ni- and Co-Base Superalloys - Development and Application of Advanced TEM Techniques. [Dr. Diss. Friedrich-Alexander-Universitɑt Erlangen-nünb], **2016**.

[117]Tirry, W.; Schryvers, D. Linking a completely three-dimensional nanostrain to a structural transformation eigenstrain. *Nat. Mater.* **2009**, *8*, 752–757.

[118]Rusner, H.; Koch, C. T.; Wilde G. Strain mapping along Al-Pb interfaces. *Acta Mater.* **2010,** 58, 162–172.

[119]University of California Riverside. Introduction to Energy Dispersive X-ray Spectrometry (EDS). **2013**, 1–11.

[120]Hofer, F.; Schmidt, F.P.; Grogger, W.; Kothleitner, G. Fundamentals of electron energy-loss spectroscopy. *IOP Conf. Ser. Mater. Sci. Eng.* **2016**, *109,* 012007.

[121]Müllejans, H.; Bruley, J. Electron energy-loss spectroscopy (EELS); comparison with X-ray analysis. *J. Phys. IV Colloq.* **1993**, 2083–2092.

[122]Hofer, F. Determination of inner-shell cross-sections for EELS- quantification. *Microsc. Microanal. Microstruct.* **1991**, 215–230.

[123]Schaffer, M.; Schaffer, B.; Ramasse, Q. Sample preparation for atomic-resolution STEM at low voltages by FIB. *Ultramicroscopy* **2012**, *114*, 62–71.

[124]Gault, B.; Moody, M.P.; Cairney, J.M.; Ringer, S.P. *Atom Probe Microscopy*; Springer Series, **2009**.

[125]Miller, M.K.; Forbes, R.G. Atom probe tomography. *Mater. Charact.* **2009**, *60*, 461–469.

[126]Gornostyrev, Y.N.; Kontsevoi, O.Y.; Khromov, K.Y.; Katsnelson, M.I.; Freeman, A.J. The role of thermal expansion and composition changes in the temperature dependence of the lattice misfit in two-phase γ/γ′ superalloys. *Scr. Mater.* **2007**, *56*, 81–84.

[127]Ma, S.; Brown, D.; Bourke, M.A.M.; Daymond, M.R.; Majumdar, B.S. Microstrain evolution during creep of a high volume fraction superalloy. *Mater. Sci. Eng. A* **2005**, *399*, 141–153.

[128]Sato, K.; Ohno, T. Development of low thermal expansion superalloy. *J. Mater. Eng. Perform.* **1993**, *2*, 511–516.

[129]Quested, P.N.; Brooks, R.F.; Chapman, L.; Morrell, R.; Youssef, Y.; Mills, K.C. Measurement and estimation of thermophysical properties of nickel based superalloys. *Mater. Sci. Technol.* **2009**, *25*, 154–162.

[130]Sung, P.K.; Poirier, D.R. Estimation of densities and coefficients of thermal expansion of solid Ni-base superalloys. *Mater. Sci. Eng. A* **1998**, *245*, 135–141.

[131]Pollock, D.D. *Physical Properties of Materials for Engineers*, CRC Press, **1993**.

[132]Mills, K.C.; Youssef, Y.M.; Li, Z.; Su, Y. Calculation of Thermophysical Properties of Ni-based Superalloys. *ISIJ Int.* **2006**, *46*, 623–632.

[133]Arblaster, B.J.W. Crystallographic Properties of Platinum. *Platin. Met. Rev.* **1997**, *41*, 12–21.

[134]Mel'nikova, T.N.; Trakhtengerts, M.S.; Yakimovich, K.A. Thermal expansion and density of solid alkali metals: isotopic effects. *High Temp. - High Press.* **1987**, *19*, 407–410.

[135]Garai, J. Correlation between thermal expansion and heat capacity. *Comput. Coupling Phase Diagrams Thermochem.* **2006**, *30*, 354–356.

[136]James, J.D.; Spittle, J.A.; Brown, S.G.R.; Evans, R.W. A review of measurement techniques for the thermal expansion coefficient of metals and alloys at elevated temperatures. *Meas. Sci. Technol.* **2002**, *12*, R1–R15.

[137]T. W. Clyne, P.J.W. *An Introduction to Metal Matrix Composites*; Cambridge University Press, **1993**.

[138]Xie, J.; Chen, S.P.; Brand, H. V.; Rabie, R.L. High-pressure thermodynamic, electronic and magnetic properties of Ni. *J. Phys. Condens. Matter* **2000**, *12*, 8953–8962.

[139]Andersson, J.-O.; Helander, T.; Hoglund, L.; Shi, P.F.; Sundman, B. Thermo-Calc & DICTRA, computational tools for materials science. *Calphad: Comput. Coupling Phase Diagrams Thermochemistry*, **2002**, *26*, 273–312. (TTNI8 database: http://www.thermocalc.com/).

[140]Mohan Rao, P. V.; Suryanarayana, S. V.; Satyanarayana Murthy, K.; Nagender Naidu, S. V. The high-temperature thermal expansion of Ni3Al measured by X-ray diffraction and dilation methods. *J. Phys. Condens. Matter* **1989**, *1*, 5357–5361.

[141]Chen, Y.; Prasath Babu, R.; Slater, T.J.A.; Bai, M.; Mitchell, R.; Ciuca, O.; Preuss, M.; Haigh, S.J. An investigation of diffusion-mediated cyclic coarsening and reversal coarsening in an advanced Ni-based superalloy. *Acta Mater.* **2016**, *110*, 295–305.

[142]Tiley, J.; Viswanathan, G.B.; Hwang, J.Y.; Shiveley, A.; Banerjee, R. Evaluation of gamma prime volume fractions and lattice misfits in a nickel base superalloy using the external standard X-ray diffraction method. *Mater. Sci. Eng. A* **2010**, *528*, 32–36.

[143]Wusatowska-Sarnek, A.M.; Blackburn, M.J.; Aindow, M. Techniques for microstructural characterization of powder-processed nickel-based superalloys. *Mater. Sci. Eng. A* **2003**, *360*, 390–395.

[144]Karunaratne, M.S.A.; Kyaw, S.; Jones, A.; Morrell, R.; Thomson, R.C. Modelling the coefficient of thermal expansion in Ni-based superalloys and bond coatings. *J. Mater. Sci.* **2016**, *51*, 1–14.

[145]Zhang, R.Y.; Qin, H.L.; Bi, Z.N.; Li, J.; Paul, S.; Lee, T.L.; Zhang, S.Y.; Zhang, J.; Dong, H.B. Temperature-Dependent Misfit Stress in Gamma Double Prime Strengthened Ni-Base Superalloys. *Metall. Mater. Trans. A* **2020**, *51*, 1860–1873.

[146]Callister, W. D.; Rethwisch, D. G. *Materials science and engineering: an introduction*; Hoboken, NJ: Wiley, **2014**.

[147]Herring, C. Effect of change of scale on sintering phenomena. *J. Appl. Phys.* **1950**, *21*, 301–303.

[148]Collins, D.M.; Stone, H.J. A modelling approach to yield strength optimisation in a nickel-base superalloy. *Int. J. Plast.* **2014**, *54*, 96–112.

[149]Baldan, A. Review progress in ostwald ripening theories and their applications to nickel-base superalloys Part I: Ostwald ripening theories. *J. Mater. Sci.* **2002**, *37*, 2171–2202.

[150]Svoboda, J.; Fischer, F.D. Model for coarsening of intergranular precipitates in multicomponent systems. *Scr. Mater.* **2010**, *62*, 754–757.

[151]Hopgood, A.A.; Martin, J.W. Coarsening of γ′-precipitates in single-crystal superalloy SRR 99. *Mater. Sci. Technol.* **1986**, *2*, 543–546.

[152]Peca, F. de la; Prestat, E.; Fauske, V.T.; Burdet, P.; Jokubauskas, P.; Nord, M.; Ostasevicius, T.; MacArthur, K.E.; Sarahan, M.; Johnstone, D.N.; et al. hyperspy/hyperspy: HyperSpy v1.5.2. **2019**.

[153]Rose, M. Spacing measurements of lattice fringes in HRTEM images using digital darkfield decomposition, [MSc Thesis, University of Missouri - St. Louis], **2006**.

[154]Malm, J.O.; O'Keefe, M.A. Deceptive "lattice spacings" in high-resolution micrographs of metal nanoparticles. *Ultramicroscopy* **1997**, *68*, 13–23.

[155]Tsen, S.C.Y.; Crozier, P.A.; Liu, J. Lattice measurement and alloy compositions in metal and bimetallic nanoparticles. *Ultramicroscopy* **2003**, *98*, 63–72.

[156]Hu, X.B.; Niu, H.Y.; Ma, X.L.; Oganov, A.R.; Fisher, C.A.J.; Sheng, N.C.; Liu, J.D.; Jin, T.; Sun, X.F.; Liu, J.F.; et al. Atomic-scale observation and analysis of chemical ordering in M_3B_2 and M_5B_3 borides. *Acta Mater.* **2018**, *149*, 274–284.

[157]Nash, P. *Phase diagrams of binary nickel alloys*. ASM International, 1991.

[158]Zhang, H.R.; Ojo, O.A.; Chaturvedi, M.C. Nanosize boride particles in heat-treated nickel base superalloys. *Scr. Mater.* **2008**, *58*, 167–170.

[159]Hong, H.U.; Kim, I.S.; Choi, B.G.; Yoo, Y.S.; Jo, C.Y. On the Mechanism of Serrated Grain Boundary Formation in Ni-Based Superalloys with Low γ′ Volume Fraction. *Proc. Int. Symp. Superalloys 2012,* **2012**, 53–61.

[160]Frank, F.C. Grain Boundaries in Metals. *Nature* **1958**, *181*, 976–977.

[161]Hondros, E.D.; Seah, M.R.; Hofmann, S.; Lejček, P. Chapter 13 - Interfacial and Surface Microchemistry. In *Physical Metallurgy (Fourth Edition)*; CAHN, R.W., HAASEN†, P., Eds.; North-Holland: Oxford, **1996**; pp. 1201–1289.

[162]Guo, J.; Haberfehlner, G.; Rosalie, J.; Li, L.; Duarte, M.J.; Kothleitner, G.; Dehm, G.; He, Y.; Pippan, R.; Zhang, Z. In situ atomic-scale observation of oxidation and decomposition processes in nanocrystalline alloys. *Nat. Commun.* **2018**, *9*, 1–9.

[163]Katona, G.L.; Erdélyi, Z.; Beke, D.L.; Dietrich, C.; Weigl, F.; Boyen, H.-G.; Koslowski, B.; Ziemann, P. Experimental evidence for a nonparabolic nanoscale interface shift during the dissolution of Ni into bulk Au(111). *Phys. Rev. B* **2005**, *71*, 115432.

[164]DENSsolutions Company. Guide to Nano-Chip Technology.

[165]Ren, K.; Cheng, Y.; Xia, M.; Lv, S.; Song, Z. In-situ observation of Ge2Sb2Te5 crystallization at the passivated interface. *Ceram. Int.* **2019**, *45*, 19542–19546.

[166]Mallikarjuna, H.T.; Caley, W.F.; Richards, N.L. Oxidation Kinetics and Oxide Scale Characterization of Nickel-Based Superalloy IN738LC at 900 °C. *J. Mater. Eng. Perform.* **2017**, *26*, 4838–4846.

[167]Schaffer, B.; Spillane, L.; Thomas, P.J. Model-Based EELS Quantification and ELNES Phase Mapping Using Experimentally Measured Cross-Sections. *Microsc. Microanal.* **2019**, *25*, 648–649.

[168]Bertoni, G.; Verbeeck, J. Accuracy and precision in model based EELS quantification. *Ultramicroscopy* **2008**, *108*, 782–790.

[169]Brewer, L. Thermodynamic Properties of the Oxides and their Vaporization Processes. *Chem. Rev.* **1953**, *52*, 1–75.

[170]Sharma, R. Experimental set up for in situ transmission electron microscopy observations of chemical processes. *Micron* **2012**, *43*, 1147–1155.

[171]Dong, Z.H.; Sergeev, D.; Kobertz, D.; D'Souza, N.; Feng, S.; Мьller, M.; Dong, H.B. Vaporization of Ni, Al and Cr in Ni-Base Alloys and Its Influence on Surface Defect Formation During Manufacturing of Single-Crystal Components. *Metall. Mater. Trans. A Phys. Metall. Mater. Sci.* **2020**, *51*, 309–322.

[172]Clausius, R. Ueber die bewegende Kraft der Wärme und die Geseitze, welche, sich daraus für die Wärmelehre selbst ableiten lassen. *Ann. Phys.*, **1850**, *155*, 500–24.

[173] Clapeyron, E´. Memoire sur la Puissance Motrice de la Chaleur, *J. l'E´c. polytech.*, **1834**,*23*, 153–90.

[174]Anjabin, N.; Salehi, M.S. Dissolution Kinetics of Spheroidal-Shaped Precipitates in Age-Hardenable Aluminum Alloys. *Metall. Mater. Trans. A Phys. Metall. Mater. Sci.* **2018**, *49*, 3584–3591.

[175]Aaron, H.B.; Fainstein, D.; Kotler, G.R. Diffusion-limited phase transformations: A comparison and critical evaluation of the mathematical approximations. *J. Appl. Phys.* **1970**, *41*, 4404–4410.

[176]Aaron, H.B.; Kotler, G.R. Second phase dissolution. *Metall. Trans.* **1971**, *2*, 393–408.